國 立 中 央 大 學

水文與海洋科學研究所
博 士 論 文

使用高頻海岸雷達進行海浪和船隻探測

USING HIGH-FREQUENCY COASTAL RADAR FOR OCEAN WAVES AND VESSEL DETECTION

研 究 生　　: Dao Duy Toan (陶瑞全)

指導教授　　: Dr. Chien Hwa (錢樺)

中 華 民 國 一 一 一 年 六 月

USING HIGH-FREQUENCY COASTAL RADAR FOR OCEAN WAVES AND VESSEL DETECTION

ABSTRACT

Hundreds of high-frequency (HF) coastal radar systems are operated in the world for purposes related to marine salvage, oil spill response, coastal zone management, and understanding of upper ocean layer dynamics. At present, 25 HF coastal radar stations consisting of both cross/loop monopole and phased array systems were installed along Taiwan's coastline and are primarily operated modes for observing ocean currents. In the next period, 21 phased array HF and very high-frequency (VHF) radar stations are on-going to install at the end of 2022 to monitor the evolution of ocean surface waves around the Taiwan island's coastal area in the long term. In order to fulfill the demands for high-frequency radar application exploitation, this study focuses on two HF radar applications' essential topics, which are assessing the uncertainty of ocean surface wave parameters under various sea-states and developing algorithms for coastal vessel monitoring.

First, the simulation of radar Doppler spectra was implemented to understand the theoretical relationship between radar cross-section (RCS) and sea-state parameters. Based on Barrick's theory, the Doppler spectra of HF radar cross-section are simulated from the given directional wave spectrum, which can be generated by applying the wind-wave spectra model for steady wind conditions or using the 3rd generation wave spectra model for monsoon and typhoon conditions. As preliminary results, various sensitivity tests of the simulated Doppler spectra are implemented under different wind speeds, wind directions, operating radar frequencies, and spreading parameters. The result showed that the simulated Doppler spectra agree

well with those in the literature. This indicated that our simulation toolbox works well.

To estimate the wave parameters. i.e., significant wave height, mean period, and wave spectrum from HF radar sea-echoes, existing methods are implemented to establish estimators for testing and evaluating the method's performance. In the beginning, the numerical simulation is used to assess the bias estimation of wave parameters under various weather conditions, such as the steady homogenous wind, monsoons, and typhoons. The results showed that the uncertainty of wave parameters estimated from simulated Doppler spectra under typhoon conditions is lower than those in monsoon conditions. In addition, to assess wave parameters' bias from the actual HF radar data, the backscattered signal of the 27.75 MHz HF radar (LERA MKIII) system is used. This system consists of 16 Rx antennas in a linear array installed at the northern of the Taichung harbor, Taichung City, Taiwan, in late November 2018 for wave monitoring in the long term. Estimation results are compared with those of in-situ data observed by an acoustic wave and current profiles (AWAC) deployed in the radar's footprint. The comparison results indicated that the radar system and estimators perform very well. Furthermore, it is found that the connection coefficients of wave parameters (which might be the function of radar-to-wave angle, smallness parameters, and spectral width parameters) have existed. Correction algorithms are proposed to estimate the scaling factor for calibrating radar-deduced wave parameters. The results demonstrated the dependence of wave height scaling factor on the radar-to-wave angle, while wave period scaling factors are mainly influenced by smallness parameters.

On the other hand, this study implements two approach methods to identify coastal vessel locations using HF radar backscattered signals: the rang-Doppler (RD) (or Doppler-Range, D-R) spectra and range-Angle brightness distribution methods. The estimated position of coastal vessels is compared with ship's information from

Automatic Identification System (AIS) data for assessing the performance of the radar system and the efficiency of detection methods. The results showed that both approaches work well. Furthermore, while the RA method can monitor ships' trajectories, the RD approach can provide the radial speed of those targets. Besides, we also found the influence of the ship's characteristics, including the length, the direction, and the heading, on the detection number of targets. Overall, this study illustrated the advantages and the limits of the HF radar technique for wave monitoring and ship detection.

***Key words**: high-frequency coastal radar, Barrick's theory, wave parameters, wave parameter correction, ship detection.*

使用高頻海岸雷達進行海浪和船隻探測

摘要

高頻雷達可應用於用於與海洋打撈、溢油響應、近岸區域管理，理解上層海洋動力等方面，目前全世界已有數百座高頻 (HF) 岸基雷達系統正在運作。目前，台灣海岸線安裝了二十五個高頻海岸雷達站，包括交叉/環路單極子和相控陣列雷達系統，主要用於觀測洋流。下一階段，二十一座相控陣列高頻（HF）和甚高頻 (VHF)雷達站將於 2022 年底建成，將被用於台灣近岸海域海浪之長期監測。為滿足高頻雷達應用軟體開發需求，本研究將聚焦於兩個高頻雷達應用議題，其一是評估不同海況下海表波浪參數反演結果之不確定性，其二是開發近岸船舶偵測算法。

首先都普勒頻譜模擬結果將被用於理解雷達截面積（RCS）與海況參數之理論關係。基於巴里克理論（Barrick’ s theory），高頻雷達截面積之都普勒頻譜可以從指定的方向波譜中模擬出來。方向波譜可由海浪譜計算得來，穩定風速（steady wind）可採用風波譜模型計算，季風或熱帶氣旋條件下可採用第三代海浪波譜模型計算。目前的初步結果為，已完成在不同風速、風向、雷達運行頻率、波譜分散度參數等狀況下都普勒頻譜模擬之敏感性測試。測試結果與文獻中譜型結果吻合良好，這表明我們的模擬軟體運行良好。

為從高頻雷達海洋回波估算波浪參數，如即示性波高、平均週期和海浪譜，研究採用已有方法來建立測試和評估方法表現之估算系統。最初，數值模擬被應用於評估不同天氣狀況下波浪參數之偏差。結果顯示，估算自都普勒頻譜之波浪參數，其不確定性在颱風條件下要低於季風條件。另外，為獲得來自實際運作之高頻雷達之波浪參數偏差，本研究採用頻率為 27.75MHz 接收後向散射訊號之高頻雷達系統（LERA MKIII）。該系統於 2018 年 11 月建於台灣臺中港北方，擁有 4 根發射天線及 16 根接收天線，是用於觀測海浪參數之高頻陣列雷達系統。

估算結果與位於雷達覆蓋區之聲波波流剖面儀（AWAC）實地觀測數據進行比對，比對結果顯示雷達系統運作良好，估算系統表現良好。此外，研究發現波浪關聯參數（connection coefficient of wave parameter）是存在的，此關聯參數是雷達徑向-波向夾角、微小參數（smallness parameter）以及譜寬參數（spectral width parameters）之函數。研究提出修正算法來估算比例因子（scaling factor），比例因子將被用於校驗（calibrate）雷達推算之波浪參數。結果顯示波高比例因子具有與雷達觀測方向-波向夾角之相依性，而波浪週期比例因子則主要受微小參數（smallness parameter）之影響。

本研究應用兩種方法從高頻雷達後向散射訊號偵測近岸海域船舶位置，即都普勒-距離（DR）方法與方位角-距離（AR）頻譜方法。船舶位置估算訊

息已經與船舶自動偵測系統（AIS）提供之訊息比對驗證，結果顯示兩種方法均有良好估算效果。AR 方法可以偵測船隻軌跡，RD 方法可以提供這些目標物之雷達徑向速度。此外，我們也發現船舶長度、方向及航向等特征將影響目標物數量之偵測。整體上，本研究討論了將高頻雷達技術應用於海浪監測及船舶偵測之優點與限制。

關鍵詞：高頻岸基雷達，巴里克理論，波浪參數，波浪參數校正，船舶偵測.

ACKNOWLEDGEMENTS

I would like to express my deepest gratitude to my advisor Dr. Hwa Chien who gave me a chance to study here. He gave me the motivation, valuable advice, helpful support, and precious guidance for my Ph.D. research.

I would like to thank Chairman and Assoc. Prof. Zhi-Cheng Huang, Prof. Lie-Yauw Oey, Prof. Ming-Hsu Li, Assoc. Prof. Tso-Ren Wu, Assis. Prof. Iam Fei-Pun, and Assis. Prof. Pei-Yuan Chen gave me many suggestions and guidance when I was doing my Ph.D. program at the Institute of Hydrology and Oceanic Sciences (IHOS), National Central University. Besides, I would like to thank Mrs. Hsio-Fen Lu and Ms. Huei-Lin Huang, who supported me in completing official documents when I was studying at IHOS and the procedure papers for my final defense.

I would like to thank the committee members, including Prof. Jenn-Shyong Chen, Dr. Jian-Wu Lai, and Assis. Prof. Yu-Ren Chung. They gave me plenty of suggestions for my research proposal and the dissertation. I would like to thank Prof. Jenn-Shyong Chen again for his help in the cooperation work of papers and projects. I would like to thank Dr. Pierre Flament, who is a Professor at the Radio Oceanography laboratory, the University of Hawaii at Manoa, and the Institute of Habor and Marine Technology allowing me to use the actual HF radar data and in-situ wave data near the Taichung harbor, Taichung City, Taiwan. I would like to thank Dr. Pierre Flament and his group again for many helpful codes and discussions on the steps of radar data processing.

Dear lab mates, Dr. Hao-Yuan Cheng, Dr. Yao-Zhao Zhong, Mr. Huan-Meng Chang, Mrs. Sun-Pei Shen, Mr. Shih-Tung Wei, Mr. Chih-Chiang Chang, Mr. Wei Chang, Ms. Pei-Yuan Chen, Ms. Lin Zhang, Ms. Nguyen Thi Thanh Hang, Mr. Cheng-Ta Lee, Mr. Ya-Di, Mr. Jack, Mr. Steve, Mr. Cheng-An, I would like to say thank you with all of you for being my friends in addition to just discussing in

research and projects. Your kindness and friendliness gave me the motivation, excitement, and happiness to study at the Marine Physical Observation Research Group laboratory.

I would like to thank Dr. Tran Dinh Trong, Assoc. Prof. Vu Van Thang, and all colleagues at the Department of Geodesy, Hanoi University of Civil Engineering, Vietnam, who encouraged me to study abroad and gave me the chance to complete the Ph.D. program in Taiwan.

Dear Vietnamese who have been international students at National Central University (NCU), Taiwan, I would like to thank all of you who are friends with me while studying overseas. I hope that you will soon complete your studies at NCU and return to serving our country. Also, I hope to meet you soon and cooperate to improve the scientific research quality in Vietnam.

And special thanks to my family, including my grandmother, parents, elder brother, younger sister, and lovely wife, Mrs. Nguyen Thi Mai, who always encouraged and assisted me when I was doing my Ph.D. They save time for me to do research and write my Ph.D. dissertation. Moreover, they usually comfort and remind me to be patient and try harder to accomplish the selected goal when I left down.

TABLE OF CONTENTS

LIST OF FIGURES

LIST OF TABLES

CHAPTER I INTRODUCTION

1.1 Motivation and Aims

1.1.1 Motivation

Over the development of four decades, the HF surface wave radar is becoming a robust technology for monitoring the coastal environment in terms of the ocean surface current, wave field, and wind mapping. There are around 400 HF radar stations installed globally and are being used in various applications [1]. In addition, more than 110 radar stations are being used in Asia and Oceania countries for different purposes related to marine safety, coastal zone management, tsunami warning, oil spill response, and understanding of upper ocean dynamics [1]. In Taiwan, 25 HF coastal radar stations, both cross/loop monopole and phased-array systems, were installed along the coastline and are primarily operating modes for observing ocean currents. In the next phase, more than 20 phased-array HF and VHF radar stations mainly for monitoring the wave field are ongoing to install at the end of 2022. Therefore, it is necessary to understand the knowledge for improving the efficiency of HF radar data processing as well as effectively exploiting HF coastal radar applications.

There are two most popular phased-array HF radar systems: the Wellen Radar (WERA) system developed by the University of Hamburg in the 1990s and the phased-array HF radar system developed by the University of Hawaii in 2008. The HF radar systems that are going to install in Taiwan in 2022 are the later features with compact size, low cost, and easy installation and maintenance. As a preliminary system for testing, a 27.75 MHz linear phased array HF radar system consists of 16 receiver antenna elements installed at Taichung harbor for multi-purposes related to monitoring the sea state in the middle of Taiwan Strait and navigating marine vessels

near the Taichung harbor's entrance in the long-term. The procedure for data processing needs to be established. In order to fulfill the part processing HF radar data for various applications, this study focuses on HF radar applications for retrieving sea state parameters and vessel detection.

1.1.2 Aims

This work aims to implement estimators to retrieve ocean wave information and vessel tracking from the HF radar sea-echo data. Based on the mechanism between HF radar cross-section and research objects, and the experimental data, this dissertation focuses on the following goals:

(1) Establish the estimator for evaluating the method's performance in retrieving wave parameters as well as the directional wave spectrum from HF radar Doppler spectra.

(2) Assess the uncertainty of wave parameters estimated from the backscattered data of a single phased-array HF radar system. Then, propose the platform for assessing and controlling the quality of HF radar products.

(3) Propose a new direction of arrival (DOA) estimation method to improve the uncertainty of the azimuthal angle of HF radar backscattered signals.

(4) Propose a new method for detecting marine vehicles from HF radar sea-echo. The influence of the ship's characteristics on the performance of the HF radar system is assessed.

With these goals, the study applied both simulation and experimental data to demonstrate the advantage of the HF radar system in monitoring ocean wave information and coastal vessels.

1.2 Literature review

1.2.1 HF radar system and applications

The marine weather condition information is essential in numerous marine engineering topics related to sea vessel navigation, marine salvage, coastal zone management, oil spill response, coastal erosion, designing offshore structures, supporting maritime activities, and understanding the coastal process [2, 3]. At present, approximately 1.2 billion people, who are living and working within 150 km of the coast [1], can be influenced by the severe weather conditions corresponding to the dynamic of upper ocean layers, such as tropical cyclones, extreme wind, heavy wind, and rain from storms, etc. Therefore, it is necessary to apply a new coastal management technique for monitoring ocean surface layers as well as navigating marine traffic in the coastal zone. To meet the demand for higher spatial and temporal resolutions, low cost, and convenience in installation and maintenance, the high frequency (HF) ocean radar becomes a promising technique for the above purposes. After almost five decades of development, the HF radar technique is widely used, with hundreds of radar systems have been installed worldwide. Accordingly, many applications from HF radar product is implemented, such as search and rescue, hazard detection, coastal circulation, environment management, ocean model validation and assimilation, and beyond [1].

This remote sensing technique can help predict marine pollution and maritime traffic control in the coastal zone for search and rescue. Meanwhile, the HF radar can also detect tsunami waves. In another respect, from the long-term monitoring, the ocean surface current retrieved from HF radar systems can provide a unique view of seasonal and interannual variability in surface circulation in the coastal waters. Thus, it helps analyze inshore and offshore circulation differences.

The HF Radar data can support environmental management, including short-term pollution events and long-term resource management. Specifically, the data can be used in tracking the fate of runoff, wastewater discharges, residence time, and source-sink of water parcels. Further, HF radar data have been used in identifying circulation features that account for plankton blooms, including harmful algal blooms and phytoplankton delivery to the rich ecosystems. Also, the surface current data from HF radar systems are used to design networks for marine protected areas and assess the transport of juvenile salmonids in coastal waters. The HF radar data is also an essential component of an index of the environmental condition for ecosystem health and fishery oceanography.

Lastly, for Ocean model validation and assimilation, the HF radar products consisting of currents and waves are the essential data in the assessment of operational and retrospective. The HF radar-derived surface current data can be assimilated into the numerical model for simulating 3-dimensional circulation and water properties in the coastal ocean.

1.2.2 The HF radar Doppler spectra and ocean surface wave parameters

In order to derive the relationship between the radar cross-section of the HF radar system and ocean surface wave parameters, numerous theoretical methods have been developed. Initially, an empirical relationship was proposed between 2^{nd}-order sidebands surroundings 1^{st}-order peaks of the Doppler-range (D-R) spectra and the ocean wave spectra measured from in-situ wave instruments [4]. Then, Barrick [5, 6] successfully described the relationship between the characters of radar cross-section (RCS) and the directional wave spectrum based on the Bragg scattering mechanism investigation [7] and the perturbation theory. At present, this theory is widely used in developing algorithms for the directional wave spectrum inversion. In 2001, a new analysis was investigated by Gill and Walsh [8] based on a generalized function

theory [9] and focused on the scattering electric field from the time-varying, good conducting ocean surface and involves pulsed dipole, and applied to the bistatic case. Later, Gill and his group have been tested the ability to install the HF radar system on a floating platform [10]. In another similar approach, Barrick, Hardman, Wyatt, and Engleback had derived and proposed a new relationship for retrieving the directional wave spectrum from simulated bistatic HF radar data [11]. Besides, Voronovich & Zavorotny [12] and Ding et al. [13] derived formulas for the sea echo from Airborne HF/VHF radar. This means that both mono- and bi-static models for coastal, shipborne, and airborne have been developed and tested at present.

1.2.3 Methods of wave field estimation

In order to retrieve wave information on the sea surface from HF radar sea echo, Barrick [14] first proposed an analytical approach to estimate significant wave height (Hs) and mean period (Tm) from radar Doppler spectra. The formula described the relationship between wave parameters and the ratio of the second-order weighted energy over the total first-order power. Then, some modified methods by adding one or two empirical parameters were proposed to determine the value of Hs and Tm [15-20]. In addition, Long and Trizna [21] first suggested that the wind direction could be extracted by using the ratio of the approaching over receding energies located at Bragg frequency in positive and negative parts of radar Doppler spectra, respectively. Subsequently, many methods of wind direction estimation were proposed [22-25].

On the other hand, numerous inversion methods have been proposed for estimating the directional wave spectrum from HF radar Doppler spectra. While the Fourier method is the only parametric method [26, 27], the nonparametric methods are widely developed, such as Wyatt's and Hisaki's methods [28, 29], the Bayesian method [30, 31], the Neural Network [32], and the Nonlinear Optimization-Based

Method [33]. In each inversion approach, there exist advantages, limitations, and abilities for application. At present, the most popular one is Wyatt's method, which is used to establish commercial software and is called Seaview sensing.

1.2.4 Methods of ship detection

For the operating frequency range of 3 MHz to 30 MHz, the HF radar signal can propagate thousands of kilometers over the sea surface. Therefore, the HF radar system can detect targets such as vessels at a range up to 200 nautical miles from the coastline [34]. Many applications on the horizontal sea surface, including marine traffic (detection and tracking marine vehicles, search and rescue of marine casualties), pollution mitigation, and research in coastal oceanography, are all exciting topics. Based on the Law of the Sea that establishes 200 nautical miles as the Exclusive Economic Zone (EEZ), HF radar appears to be an excellent tool to monitor maritime activities within the EEZ of a country. Therefore, the radar system is becoming an active tool for ship detection and tracking in the coastal zone and the Automatic Identification System (AIS).

In order to detect coastal vessels from the HF radar backscattered signal, various commercial radars such as the cross-loop CODAR SeaSonde system and the phased-array antennas WERA system have been applied [35, 36]. Accordingly, numerous detection algorithms have also been proposed and put in use, e.g., constant false alarm rate (CFAR) [37-39], curvilinear regression analysis [34], morphological component analysis [40], adaptive detection technique [41], range-Doppler spectra enhancement and clutter suppression [42], and some extended and advanced procedures or methods such as machine learning based on vector regression [43] and others [44, 45].

On the other hand, different from the range-Doppler (RD) (or Doppler-range, D-R) methods, a new approach for detecting ship echoes from the range-Angle (RA)

brightness distribution method was proposed [46]. The technique was implemented to compute the so-called power density (also called brightness) as a function of the azimuthal angle for each range cell. It directly allows showing ship echoes on the 2D range-Angle brightness distribution map. Later, the new method's performance is assessed by comparing the estimated location of targets from both the RA and RD methods and AIS information.

1.3 The Scope of the Dissertation

This dissertation focuses on several topics: the relationship between HF radar cross-section and sea-state parameters, methods of wave parameter retrieval, and methods of ship detection. The content of this dissertation is arranged as follows:

Chapter 2 introduces a theory describing the relationship between monostatic radar cross-section and the directional spectrum of ocean waves. Then, the End-to-End simulation (E2ES) test-bed consists of a self-developed toolbox for simulating the radar Doppler spectra from the given directional wave spectrum and estimating wave parameters are built.

Chapter 3 represents the work of E2ES. The performance of wave estimators is tested under the steady homogenous wave field. It is found that the bias of estimation results is significantly influenced by the angle between radar bearing and wave direction and sea-states.

Chapter 4 assesses the uncertainty of wave parameters such as significant wave height and the mean period obtained from simulated radar Doppler spectra under the condition of monsoon and typhoon wave fields. Based on the analyzed results, the author investigated factors that may play the role-key in improving the accuracy of wave parameters estimated from HF radar sea-echo. Also, the author found the typhoon wavefield condition that HF radar system can perform better.

Chapter 5 presents the procedure of wave processing from the backscattered signal of a single HF radar system. Two contributions are already proposed: (1) a new method for separating Doppler spectra components; (2) algorithms of wave parameter correction. The comparison results demonstrated the efficiency of correction methods.

Chapter 6 introduces the method for ship detections. In addition to the RD methods, the RA method is first proposed to identify ship echo. The comparison result between the estimated position of targets and AIS information demonstrated the performance of the RA method. Furthermore, the percentage of target detection with respect to the ship's characteristics is assessed.

Chapter 7 summarizes our contributions and presents potential ideas that can be investigated in future works.

CHAPTER II FUNDAMENTAL THEORY FOR OCEAN RADAR SCATTERING

2.1 The Scattering of High-frequency radio waves from an ocean surface

Radar scattering is the radar signal scattered when the incident radio (electromagnetic - EM) wave at a given radar frequency encounters a target, cluster of targets, or surface. Typically, the incident radar signal is scattered in all directions. And the radar receiver element can acquire a part of scattered signals (called the radar backscattered signals) that is significantly weaker than the transmitted signal. The strength and characteristics of the backscattered signal depend on the transmitter power, the background noise level, receiver antenna gain, and the feature of the target, including the size and number of targets or the roughness feature of the interacted surface. The radar backscattering signal is called the radar sea-echo when the object is the sea (ocean) surface. Those radar sea-echoes are powerfully relevant to the dynamic of ocean surface layers and ocean surface features. Due to objects moving on the ocean surface, such as waves, currents, and marine vehicles, the intensity of sea echoes scattered from objects can be recognized on the domain of range and Doppler-shift in any radar-looking direction.

For radar applications in oceanography, the incident radar signal is typically scattered over the free surface of the ocean when the radio wave interacts with ocean surface waves. Since World War II, two common radar types located at shorelines have been used to study the physic of ocean parameters. In which, the microwave radar with less than 15 cm radar wavelength (S-band) [47, 48] has been successful in retrieving the information of surface wave parameters (spectral shape, dominant direction, wave height, periods, and beyond) and surface currents. However, microwaves interact primarily with very short ocean waves and limit in terms of range for sight measurement. In contrast, the dominant energy of ocean waves is

located at longer wavelengths like those in gravity bands. Therefore, it is difficult to estimate the energy content of long waves by considering the modulation of short waves located within microwave bands. On the other hand, the characteristics of the ocean surface layer were also measured by the high frequency (HF) radar system working at the frequency band of 3-30 MHz. Overcome the disadvantages of microwave systems, the HF radar system having a wavelength of 10-100 meters, which can propagate thousands of kilometers along the curved surface of the earth, is able to measure ocean parameters over the exclusive economic zone (EEZ) as well as the shelf continental with thousand of square kilometers. In addition, these HF radar systems have been developed successfully in both skywave and ground wave modes that allow looking at the exciting area of the ocean, even in single-site operations. The resolution of oceanic measurements from HF radar systems ranges from a few hundred meters to a few kilometers, depending on the radar system configuration, such as operating frequency, bandwidth, and the primary purpose for radar applications. The radio waves at HF bands can interact with the ocean waves carrying the bulk of the spectral energy. Therefore, ocean surface information can be interpreted more easily from HF radar sea-echo than those from microwave radar signals.

In 1955, Crombie [7] was the first to apply the backscattered signal of HF radar to measure ocean physical parameters. He had identified the radar scattering from the ocean surface in a radar Doppler spectrum, which was extracted from the data of an HF radar system working at 13.4 MHz. He also used that data to explain the difference between the expected surface gravity wave and measured Doppler frequencies caused by the current velocity at ocean surface layers. In that study, two main features were identified on the Doppler spectrum. First of all, a narrow and robust peak was reproduced and located at a Doppler frequency with respect to an ocean wave having a wavelength, $L = \lambda/2$. Here, λ is the wavelength of the

transmitted EM wave. That greater peak was called the first-order Doppler spectra peak. Meanwhile, another smaller peak is located at a Doppler frequency of approximately $\sqrt{2}$ the Bragg frequency was suggested to relate to an ocean wavelength, $L = \lambda$.

Generally, the interaction between an ocean surface wave having a half wavelength of incident EM wave creates a phase-coherent reinforcement (constructive interference) that sexists in the backscattered radio signal (Figure 2-1). This effect is well known as Bragg scattering, and the corresponding surface waves are called Bragg waves. This effect is labeled “first-order” or “linear” in the literature because the EM-ocean wave interaction is simplified as a linear equation. The reflected signal is evident by significant peaks in the radar spectra at a Doppler frequency twice that of the transmit frequency. This Doppler shift in the radar spectra was first reported by Crombie [7]. Later, the phase of the coherence varying with Doppler frequency was found by Crombie [49]. It implies that signals having different Doppler shifts were coming from different directions and caused by the corresponding ocean current. That led to the development of HF radar for current ocean retrieval, typically the Coastal Ocean Dynamic Applications Radar (CODAR) [50].

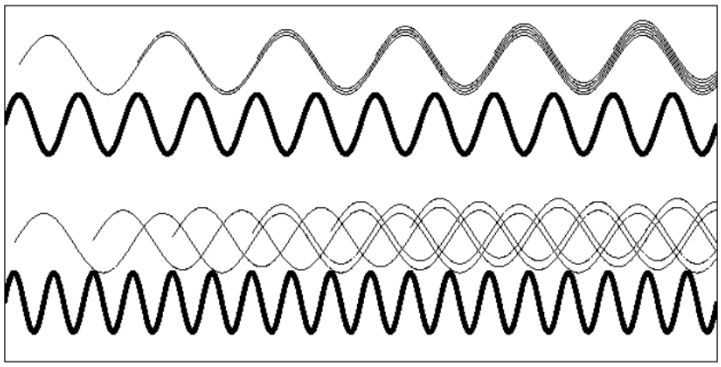

Figure 2-1 The Bragg scattering mechanism. It is the coherent reflection of the EM wave (thin black lines) by ocean waves (the thicker black line) with a half wavelength of λ (upper); while incoherent reflections, i.e., cancellation of the EM energy, occur for arbitrary ocean wavelengths (lower) [50].

In addition, the second- and higher-order Doppler spectra are the continuous energy from first-order peaks produced by two independent effects; an electromagnetic and a hydrodynamic. Accordingly, the electromagnetic effect explains the twice times scattering of radar waves from ocean waves, where the geometry of the double scattering causes coherent reflections, while the hydrodynamic effect describes the scatter of radar waves due to the double bounds effect of water waves. Therefore, both electromagnetic and hydrodynamic components could be represented in the scattering equation of the second-order Doppler spectra based on the perturbation expansion. And any ocean waves can contribute to the value of electromagnetic and hydrodynamic terms. Thus, information about the entire wave directional spectrum is contained in the second-order continuum. As with first-order scattering, the necessary condition for both the EM and hydrodynamic components is the coherence of the reflected signal [50]. Therefore, it implies that the directional wave spectrum and ocean wave parameters can be estimated from the second-order radar Doppler spectra.

2.2 Barrick's theory

2.2.1 Introduction

The sea surface can be seen as a slightly rough surface for the HF band; the HF radar signal backscattered from the sea surface can be analyzed based on the perturbation theory [51]. Firstly, the ocean is assumed to be in deep-water regions and unbounded surfaces in the derivation. Secondly, the seawater provides high conductivity and less diffraction propagation attenuation of vertical polarization HF radio waves. It means the sea surface is considered as an ideal conductive surface, and the backscatter coefficients of vertical polarization can be deduced by the perturbation method. The vertical polarization part should focus on because the horizontally polarized scattering component from the sea is several orders of magnitude lower than the vertical component [6].

Based on the E-M scattering theory from a rough surface, the radar cross-section (RCS) from the ocean surface was developed using two methods, i.e., the perturbation method and the Kirchhoff method [52]. Typically, the RCS of HF radar data is defined as the combination of the first-order, $\sigma^{(1)}$, and higher-order (the second-order, $\sigma^{(2)}$) spectra of Doppler-Range spectra. The first-order cross-section represents the interaction between radio waves and ocean waves, having a wavelength of one-half of the incident EM wave based on the Resonance Bragg scattering theory [5, 52]. These peaks are related to ocean waves approaching or receding the radar site along the radar bearing. The second and higher orders represent the double bounce effects, radio waves' interactions with pairs or more ocean waves. It implies that the shape of the ocean wave spectrum dominates the second-order Dopper spectra. In addition, the nature of the scattered signal also depends on the radar operating frequency, beamwidth polarization, and the distance between the radar transmitter and receiver elements (monostatic or bistatic types) [8].

Barrick first proposed the first-order of the monostatic cross-section for plane wave incidence based on the boundary perturbation theory, which casts the Bragg peaks as weighted delta functions [5]. After that, he extended this theory to the second-order Doppler spectra to investigate and explain the higher-order observed signals [6]. Besides, he detailed interpretation of two coupling coefficients of the second-order Doppler spectra: the contribution of the hydrodynamic component due to the small nonlinear terms in the boundary conditions at the freeway water surface and the contribution of the electromagnetic component due to the previously neglected high-order term of the boundary perturbational scatter theory [6]. Lastly, the mathematical formulation of the first- and second-order Doppler spectrum will be represented in the next part.

2.2.2 The Radar Cross Section

The Doppler-range (or range-Doppler, RD) spectrum is the level one product of the HF radar system. It is extracted from the time-series HF radar backscattered signal recorded by receiver antenna elements using Fourier transform algorithms. It shows the energy distribution of radar sea-echo over the range and Doppler frequency shift. It results from backscattered intensity due to the interaction of electromagnetic (EM) waves in the HF band and ocean surface waves. Typically, D-R spectra exhibit two dominant first-order peaks and two minor second-order peaks at positive and negative Doppler frequencies.

A. The first-order Doppler spectrum

The first-order Doppler spectra peaks are induced by the direct backscattering of transmitted EM waves with gravity waves traveling on the ocean surface [5]. The ocean wave component that induces backscattering features has a one-half wavelength of the EM wave and is called the Bragg wave (Figure 2-2). The

magnitude of the first-order peak is related to the Bragg wave's amplitude, direction, and spreading factor. The Doppler frequency shifts of the first-order peaks correspond to the combined effects of surface current velocity and the celerity of the waves propagating in approaching or receding directions with respect to the radar site along the radar-looking direction. The formulation of the first-order peak is given as follows:

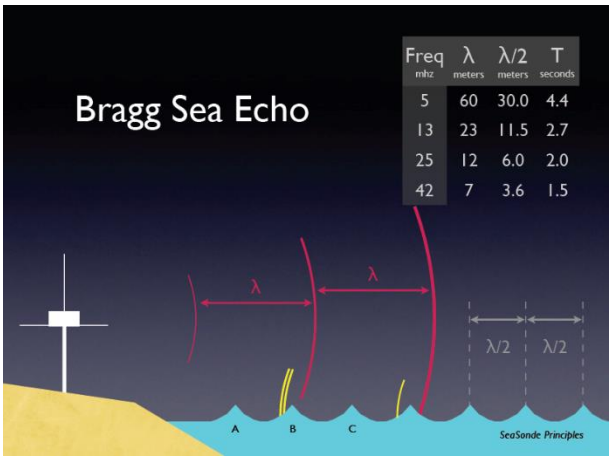

Figure 2-2 EM waves and backscattered signal from Bragg waves [53].

$$\sigma^{(1)}(\omega) = 2^6 \pi k_0^4 \sum_{m_2=\pm 1} S(-2m_2\boldsymbol{k}_0)\,\delta(\omega - m_2\omega_B) \tag{2.1}$$

In (2.1), m_2= ±1 denotes the sign of the Doppler shift frequency, ω, that correspond to the receding and advancing Bragg waves, $\boldsymbol{k}_0$ is the EM wavenumber vector having the magnitude of k_0, $S(.)$ represents the directional wave spectrum, $\omega_B = \sqrt{2gk_0}$ is the Bragg Doppler frequency, the delta function constraint is denoted by $\delta(.)$.

As mentioned before, two first-order peaks are related to the backscattered signal from Bragg waves, which range from a few to 10 s meters in wavelength depending on the radar frequency and exhibit responses to directional changes in the local wind field [21]. Thus, Figure 2-3 illustrates an example of the Bragg wave

directionalities with the radar-looking direction. The colored cardioid curves denote the patterns of the directional spreading distribution of the Bragg waves with respect to spreading parameter *s*. The spreading parameter, *s*, can be defined following the form of direction spread function in [54], in which small values indicate broad directional spreading and vice versa.

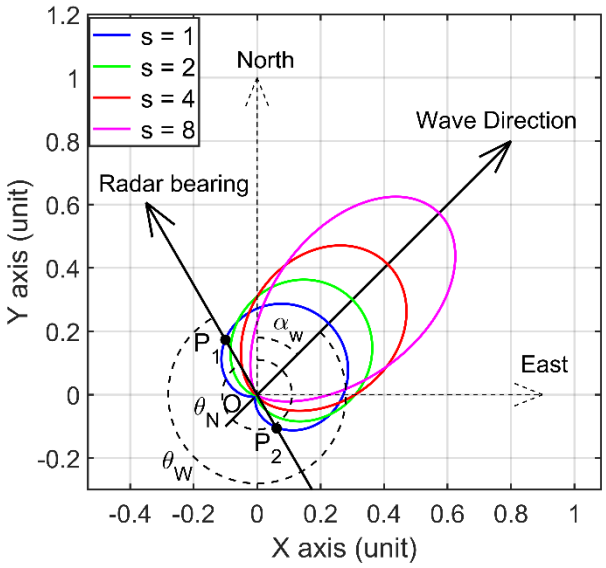

Figure 2-3 Wave directional distribution in relation to the radar-looking direction.

In Figure 2-3, the lengths of OP_1 and OP_2 are the magnitudes of the two first-order peaks of the Bragg waves traveling in opposite directions, respectively. And the ratio between OP_1 and OP_2 is associated with the Bragg wave propagating direction (or wind direction) and the directional spreading characteristics [21]. Furthermore, it is found that this ratio becomes sensitive to the noise level when the directional spreading parameter becomes narrow (increasing s).

B. The second-order Doppler spectrum

The second-order Doppler spectrum consists of broader spectral components representing the summation of the double-bounce effects of the EM signal. The double-bounce means that the radio wave has been twice Bragg-scattered with any

possible pairs of ocean surface wave spectral components in specific wavenumber vectors before receiver elements obtain it. Applying boundary perturbation theory [51], the mathematical form of the second-order Doppler spectra can be represented as follows [6, 55, 56]:

$$\sigma^{(2)}(\omega) = 2^6\pi k_0^4 \sum_{m_1,m_2=\pm 1} \int_{-\infty}^{\infty}\int_{-\infty}^{\infty} S(m_1\boldsymbol{k}_1)S(m_2\boldsymbol{k}_2) \times |\Gamma|^2\delta\left(\omega - m_1\sqrt{gk_1} - m_2\sqrt{gk_2}\right)dpdq \tag{2.2}$$

In (2.2), $\boldsymbol{k}_1$ and $\boldsymbol{k}_2$ are wavenumber vectors of two ocean waves containing magnitudes k_1, k_2 and directions $\theta_{k_1}, \theta_{k_2}$, respectively on the coordinate p–q plane as in Figure 2-4. The double integration in (2.2) is used to superimpose the effects of the double-bounce of the EM wave with any possible pairs of ocean waves that satisfy the condition of $\boldsymbol{k}_1 + \boldsymbol{k}_2 = -2\boldsymbol{k}_0$. Due to the nonlinear quadruplet wave-wave interactions, the ocean wave wavenumber $\boldsymbol{k}_1 + \boldsymbol{k}_2$ is coupled. Γ_T is the total coupling coefficient. From (2.2) and Figure 2-4, it is understood that the energy of each 2nd-order component is the integral of 2nd-order energy at each contour line over direction contributed by multiple wave spectrum from a pair of ocean waves with the condition given above. It means that we can simulate the 2nd-order Doppler spectrum from a given directional wave spectrum and radar frequency following this expression. Furthermore, the left panel of Figure 2-4 indicates that there are singularities in the radar Doppler spectrum at Doppler frequencies $|\omega_d| = \sqrt{2}\omega_B$ and $|\omega_d| = \sqrt[4]{2^3}\omega_B$ [55, 56]. In addition, the dashed circle in both panels of Figure 2-4 presents points satisfying $\boldsymbol{k}_1.\boldsymbol{k}_2 = 0$ **,** which is the denominator in the electromagnetic coupling coefficient, is zero. It implies the integral in (2.2) has singularities that will cause small peaks in the sea echo spectrum at the value of frequency [56].

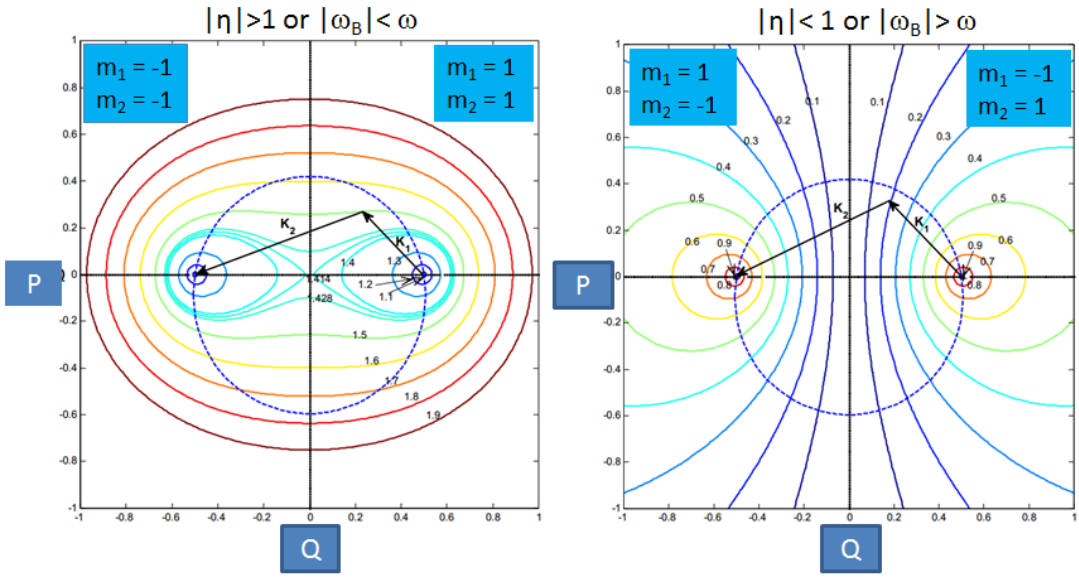

Figure 2-4 The normalized frequency contours of the 2nd-order Doppler frequency for the cases of $m_1 = m_2$ (the left panel) and $m_1 \neq m_2$ (the right panel).

2.2.3 The Coupling coefficients

In (2.2), the total coupling coefficient, Γ_T, represents the contribution of ocean wave-wave interactions between a pair of ocean waves ($\boldsymbol{k}_1$, $\boldsymbol{k}_2$) and the effect of the EM wave reflection from the seawater surface. It can be expressed as the summation of the hydrodynamic (Γ_H) and electromagnetic (Γ_{EM}) second-order coupling coefficients. Herein, the electromagnetic component relates to radio waves twice scattered from the ocean wavefield, where the geometry of the double scattering produces coherent reflections (Figure 2-5). In another respect, the hydrodynamic component corresponds to nonlinear surface waves, which satisfy the condition of $\boldsymbol{k}_1 + \boldsymbol{k}_2 = \boldsymbol{k}_B$ [57] with $\boldsymbol{k}_1$, $\boldsymbol{k}_2$ are two ocean wavenumber vectors, and $\boldsymbol{k}_B$ is the wavenumber vector of the second-order Doppler frequency (Figure 2-6). Figure 2-6 shows the mechanism of the hydrodynamic coupling coefficient. Here, the black lines show the crestline for $\boldsymbol{k}_1$, $\boldsymbol{k}_2$, and the red line shows $\boldsymbol{k}_B$, the second-order crestline ($\boldsymbol{k}_B$) connects points of $\boldsymbol{k}_{1,2}$ maximum constructive and destructive

interference, i.e. crestline and trough intersects. The formulation of the electromagnetic and hydrodynamic coupling coefficients are given as follows:

$$\Gamma_{EM} = \frac{1}{2}\left[\frac{\frac{(\boldsymbol{k}_1.\boldsymbol{k}_0)(\boldsymbol{k}_2.\boldsymbol{k}_0)}{k_0^2} - 2\boldsymbol{k}_1.\boldsymbol{k}_2}{\sqrt{\boldsymbol{k}_1.\boldsymbol{k}_2} + k_0\Delta}\right] \tag{2.3}$$

$$\Gamma_H = \frac{-i}{2}\left[k_1 + k_2 + \frac{(k_1k_2 - \boldsymbol{k}_1.\boldsymbol{k}_2)(\omega_d^2 + \omega_B^2)}{m_1m_2\sqrt{\boldsymbol{k}_1.\boldsymbol{k}_2}(\omega_d^2 - \omega_B^2)}\right] \tag{2.4}$$

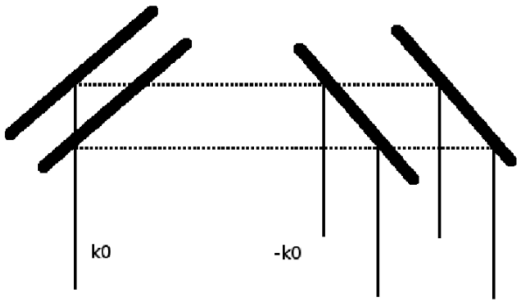

Figure 2-5 The electromagnetic double-scattering [50]. The thin solid line represents on the left represents the incident radar wavevector, k_0, while the multiple coherent received radar wave vectors, $-k_0$, show on the right, the thicker black lines represent two ocean wavevectors, and the dotted line represents the scattering of radio waves due to ocean waves.

In (2.4), $\Delta = 0.011 - 0.012\mathrm{i}$ is the normalized seawater impedance value [56]. In the present study, an End-to-End simulation is established based on (2.1) to (2.4) to simulate the Doppler spectra from the given ocean wave directional spectrum.

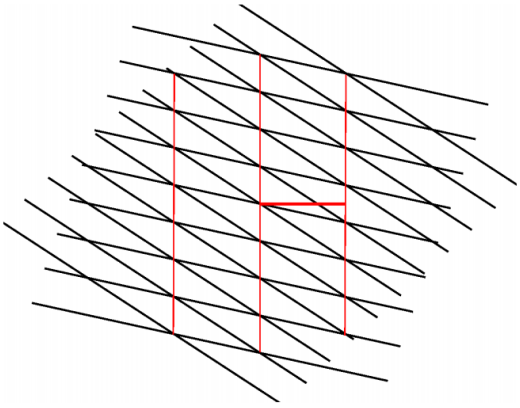

Figure 2-6 The hydrodynamic coupling coefficient [50]. This figure shows a nonlinear effect wherein a second-order component (red) is produced from the interaction of two first ocean waves (blacks).

The derivation of Barrick's theory is based on the perturbation-theory expansion of the nonlinear hydrodynamic and electromagnetic equations for water and waves. Meanwhile, the perturbation theory has a finite radius of convergence in the "smallness parameters." The multiple between the radar wave number and the root-mean-square height of ocean waves, $k_0 h_{rms}$, is one of these. When this smallness parameter is unity, the entire theory becomes invalid. This limitation was pointed out by many authors [56, 58, 59]. Based on this saturation limit, the maximum significant wave height Hs is suggested to be $\mathrm{H_{sat}} = 2/k_0$. In extreme cases, when the wave is greater than the saturation limit, the estimation result of wave height will be underestimated.

2.3 Simulation of Monostatic Radar Cross-Section

To simulate the Doppler spectrum of monostatic HF radar systems, (2.1) and (2.2) were derived under various water conditions [56]. The detailed formulation of Doppler spectrum components in the deep water region was also represented many times [55, 56]. Whereby, the Doppler frequency and wavenumber are first

normalized by dividing ω_B and $2k_0$, respectively; the form of Barrick's equation for the first and second-order components of monostatic radar cross-section is rewritten as follows [56]:

$$\sigma^{(1)}(\eta) = 4\pi \sum_{m_2=\pm 1} S\left(-m_2 \hat{\boldsymbol{k}}_0\right) \delta(\eta - m_2) \tag{2.5}$$

$$\begin{aligned} \sigma^{(2)}(\eta) = 8\pi \sum_{m_1, m_2=\pm 1} \int_0^{\infty} \int_{-\pi}^{\pi} & S(m_1 \boldsymbol{K}_1) S(m_2 \boldsymbol{K}_2) \\ & \times |\gamma|^2 \delta\left(\omega - m_1\sqrt{K_1} - m_2\sqrt{K_2}\right) K_1 dK_1 d\theta_1 \end{aligned} \tag{2.6}$$

where η is the normalized Doppler shift, $\hat{\boldsymbol{k}}_0$ is the unit vector of radio wavenumber, $\boldsymbol{K}_1$ and $\boldsymbol{K}_2$ are two normalized wavenumber vectors of two ocean waves, respectively, γ is the normalized coupling coefficient, and θ_1 is the direction of the wavenumber vector $\boldsymbol{K}_1$. In (2.6), the value of m_1, m_2 define four side-bands of the second-order component of DR spectra: $m_1 = m_2 = 1$ corresponds to $\eta > 1$, $m_1 = m_2 = -1$ corresponds to $\eta < -1$, $m_1 = 1$ and $m_2 = -1$ corresponds to $-1 < \eta < 0$, and $m_1 = -1$ and $m_2 = 1$ corresponds to $0 < \eta < 1$.

Then, the two-dimensional nonlinear integral of (2.6) can be simplified by transforming it into a single variable because the integrand includes the Dirac delta function. Then, the algorithm of second-order components is rewritten as:

$$\sigma^{(2)}(\theta_1, \eta) = \int_0^{\theta_L} G(\theta_1, \eta) d\theta_1 \tag{2.7}$$

$$\begin{aligned} G(\theta_1, \eta) = 16\pi \Big[& |\gamma|^2 \{ S(K_1, \alpha_1) S(K_2, \alpha_2) \\ & + S(K_1, -\alpha_1) S(K_2, -\alpha_2) \} \left| \frac{dy}{dh} \right| y^3 \Big]_{y=\hat{y}} \end{aligned} \tag{2.8}$$

where,

$$\left| \frac{dy}{dh} \right| = \left| 1 + m_1 m_2 \frac{y(y^2 + \cos\theta_1)}{(y^4 + 2y^2 cos\theta_1 + 1)^{3/4}} \right|^{-1} \tag{2.9}$$

with $y = \sqrt{K_1}$. $\hat{y}$ can be obtained by solving the following nonlinear equation:

$$\eta - m_1\hat{y} - m_2(\hat{y}^4 + 2\hat{y}^2 cos\theta_1 + 1)^{1/4} = 0 \tag{2.10}$$

Furthermore, other parameters can be calculated as:

$$K_2 = \sqrt{{K_1}^2 + 2K_1 cos\theta_1 + 1} \tag{2.11}$$

$$\theta_2 = sin^{-1}\left(\frac{K_1 sin\theta_1}{K_2}\right) + \pi \tag{2.12}$$

$$\alpha_1 = \theta_1 \pm (1 - m_1)\pi/2 \tag{2.13}$$

$$\alpha_2 = \theta_2 \pm (1 - m_2)\pi/2 \tag{2.14}$$

The value of θ_L denotes the upper limit of integration and can be given by $\theta_L = \pi$ when $|\eta| \leq \sqrt{2}$, and $\theta_L = \pi - \cos^{-1}(2/\eta^2)$ when $|\eta| > \sqrt{2}$, respectively. In addition, the normalized coupling coefficient can be calculated as follows:

$$\gamma_H = \frac{-i}{2}\left[K_1 + K_2 + \frac{(K_1K_2 - \boldsymbol{K}_1.\boldsymbol{K}_2)(\eta^2 + 1)}{m_1 m_2\sqrt{K_1K_2}(\eta^2 - 1)}\right] \tag{2.15}$$

$$\gamma_{EM} = \frac{1}{2}\left[\frac{\left(\boldsymbol{K}_1.\hat{\boldsymbol{k}}_0\right)\left(\boldsymbol{K}_2.\hat{\boldsymbol{k}}_0\right) - 2\boldsymbol{K}_1.\boldsymbol{K}_2}{\sqrt{\boldsymbol{K}_1.\boldsymbol{K}_2} + \Delta/2}\right] \tag{2.16}$$

Based on the expression of Lipa & Barrick [56], we computed the component of the total coupling coefficient in the domain of normalized Doppler frequency and direction by implementing (2.10) to (2.16). The results are shown in Figure 2-7. In this figure, the horizontal and vertical axes are the normalized Doppler frequency and the first ocean wave direction. The black dashed lines denote the normalized Doppler frequency; blue and magenta dashed lines represent the location of two singularities at the normalized Doppler frequency of $2^{0.5}$ and $2^{0.75}$.

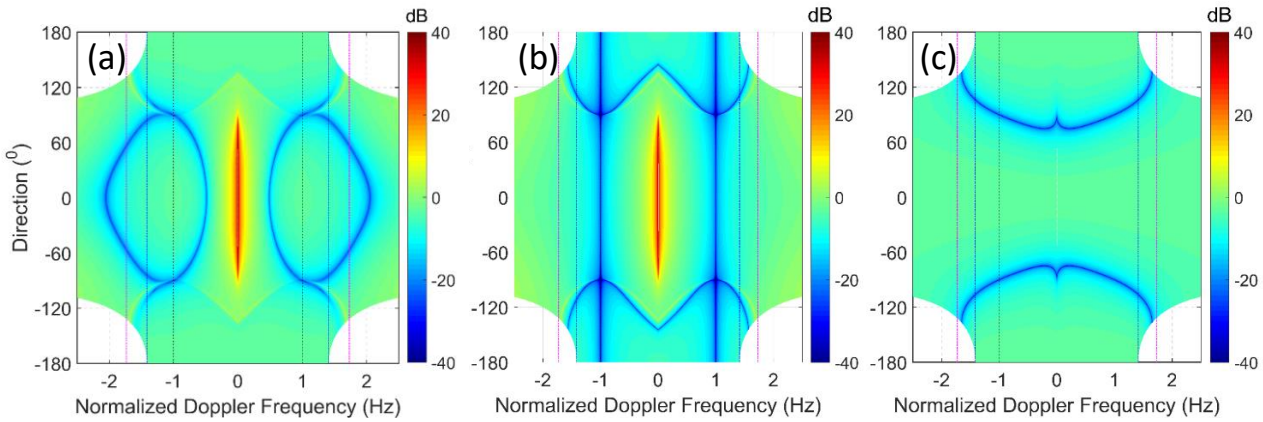

Figure 2-7 The total, electromagnetic, and hydrodynamic coupling coefficients. Panel (a) represent the total coupling coefficient over normalized Doppler frequency and direction domains, while panels (b) and (c) show the pattern of electromagnetic and hydrodynamic terms, respectively.

Based on the above expression, the HF radar sea echo RCS can be simulated using a numerical simulation with given sea-stage parameters. In this process, the directional wave spectra are essential inputs that can be obtained following two approaches. For simple homogeneous wave fields in the open sea, the analytical wave spectra such as the PM spectrum [60] or the JONSWAP spectrum [61], Longuet-Higgins' directional spreading model [54], and Mitsuyasu's formula [62] were chosen to generate the directional spectra with respect to various wind speeds, fetched limit, wind directions, and spreading factors. For more realistic and complicated sea states, such as those during monsoon fronts and typhoons, the directional spectra were generated from the 3rd-generation wave model over the spatial domain with the input of high-resolution surface wind fields. The flow chart of the 2nd-order Doppler spectrum simulation can be implemented as follows (Figure 2-8):

(1) Determine the magnitudes and directions of the coupled wavenumber vectors corresponding to a given normalized Doppler frequency by solving the nonlinear equations.

(2) Compute the magnitudes of the spectral components of the two coupling waves in the wavenumber domain.

(3) Compute the normalized coupling coefficients that correspond to a pair of wavenumber vectors.

(4) The results of the previous three steps are substituted into the normalized equation and then compute the second-order Doppler spectrum by taking integration over the wavenumber domain.

(5) Repeat steps (1)-(4) for each normalized Doppler frequency to obtain the entire DR spectrum.

(6) Obtain the simulated Doppler spectrum by summing the first- and second-order Doppler spectrum.

(7) Add background noise on the simulated D-R spectrum.

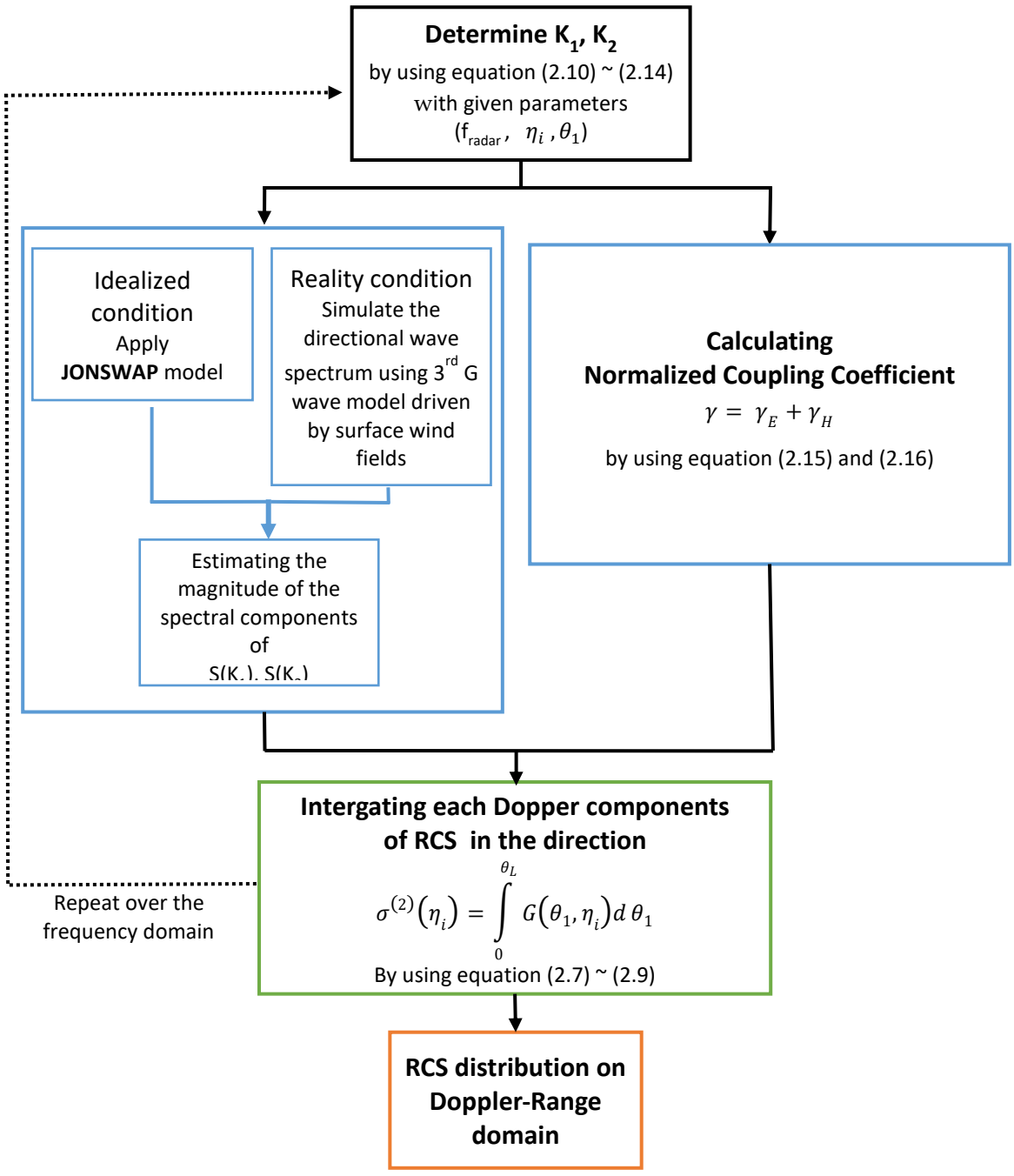

Figure 2-8 The flowchart of the second-order Doppler spectra simulation.

Based on the expressed equation, a toolbox can be established to simulate the HF radar Doppler spectra from the given directional wave spectrum, operating radar

frequency, radar-looking direction, and other radar parameters. The simulation results will be represented and depicted in the next section.

2.4 Description of Radar Cross-Section Results

In order to validate the End-to-End simulation (E2ES) toolbox, idealized examples using various wind speeds at 10 meters high from the sea surface (U_{10}), the non-dimensional fetch, $\tilde{\chi}$, and wind direction are given, and the simulation results are characterized with respect to the inputs. The minimum spreading factor 's' in Longuet-Higgins' formula is assumed to be 1 for the shortest wave component having a 1-meter wavelength. Figure 2-9 illustrates an example of noise-free cases from the simulation toolbox, depicting the effects of changing the wave direction, wind speed, and radar operating frequency to a Doppler spectra shape.

The simulation is implemented under various wave directions to verify the influence of wave direction on the shape of radar Doppler spectra. In this test, the values of input parameters are selected as follows: U_{10} = 10 m/s, $\tilde{\chi}=10^4$, the operating radar frequency, f_{Radar}= 27.5 MHz, the radar-looking direction, θ_N=0°; the wind direction, α_w = 0°, 45°, and 90°. As the initial results, Figure 2-9(a) illustrates the shifting of spectral shape from asymmetric to symmetric, corresponding to the increase of the angle between the wave direction and radar beam azimuthal orientation, which is also called the radar-to-wave angle, θ_w. When the alignment of the wave propagating direction and the radar bearing is formed, one side of the spectral power will be reduced. The symmetry of the two first- and second-order components could also be influenced by wave directionality.

Secondly, the influence of changing sea-states on radar Doppler spectra is tested. Where, f_{Radar} = 27.5 MHz, $\theta_N = 0°$, $\alpha_w = 90°$, and U_{10} = 6, 8, 10 m/s. Figure 2-9(b) shows the effect of wind speed on the energy of the 2nd-order component. The

power of radar signals significantly increases at the second-order components with increasing wind speed. The dominant peaks of the 2nd-order components also move toward the 1st-order peaks as the wavelength grows longer with the increasing wind speed. Those characteristics of the simulated first- and second-order spectrum in Figures 2-9(a) and (b) agree with the previous study [56]. Since the wave direction and its directional spreading width strongly influence the ratio between the spectral powers of two second-order sidebands surrounding a stronger Bragg peak. The rotating and inhomogeneous wind fields of typhoons and the corresponding complexity of wave directionality play crucial roles in the inversion of wave parameters.

Thirdly, the radar Doppler spectrum is simulated using different operating radar frequencies. In this test, U_{10} = 10 m/s, $\theta_N = 0°$, $\alpha_w = 90°$ and f_{Radar} = 27.5 MHz, 15 MHz, and 5 MHz. Consequently, Figure 2-9(c) shows the magnitudes and the shape of radar Doppler spectral corresponding to various operating radar frequencies. Obviously, the second-order peaks are shifted away from the first-order peaks and reduce the magnitude corresponding to the decrease of the transmitted radar frequency. This separation identifies the 1st- and 2nd- order peaks easier on the Doppler spectra for lower HF radar frequency bands with the absence of noise. However, there is no doubt that the background noise will be present in reality, making the selection of the radar frequency band a trade-off process. For example, too high a radar frequency band results in a blurred gap between the 1st- and 2nd-order peaks; meanwhile, the second-order peaks would be too weak and vanish in the noise for the lower-frequency radar system. Screening of background radiofrequency and preliminarily understanding wave the ocean wave characteristics in the target area are thus essential prior to the determination of radar frequency and radar station installation.

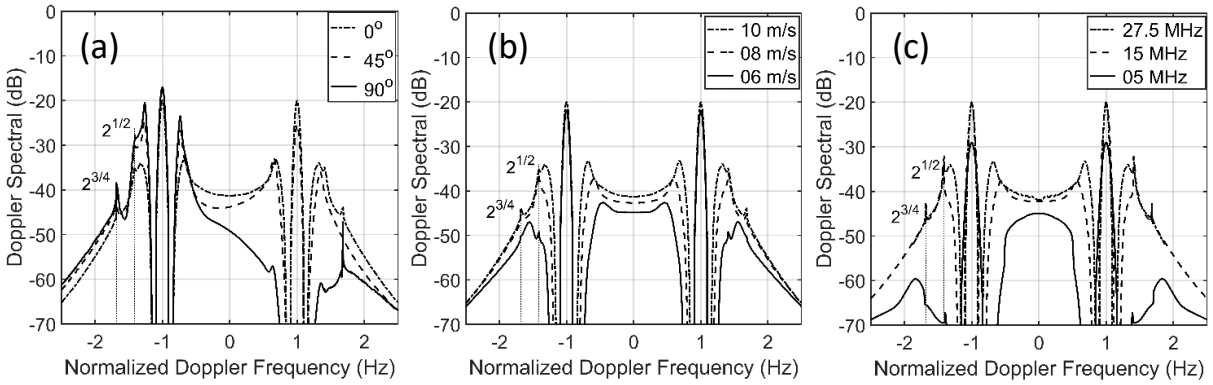

Figure 2-9 The simulated HF radar Doppler spectral under various weather conditions and radar settings. Herein, (a), (b), and (c) show the shape of the simulated Doppler spectra with respect to different wind directions, wind speeds, and operating radar frequencies, respectively.

In Figure 2-9, the leading singularities are located at the frequencies $\pm 2^{1/2}\omega_B$ and $\pm 2^{3/4}\omega_B$. They are caused by the characteristics of the hydrodynamic and electromagnetic coupling coefficients. In short, those phenomena mentioned above are consistent and agree well with the known behavior of the DR spectra. The current simulation toolbox can thus be used in the next section to evaluate the errors from estimation methods.

2.5 Summary

Based on the work of Lipa and Barrick [55, 56], the monostatic radar cross-section is conducted. As a result, the first-order spectrum is only a single peak corresponding to the Bragg waves propagating toward or away along radar bearing. In contrast, the second-order Doppler spectrum is affected by the energy of coupled ocean waves, which causes the double bounds for scattering radio waves. This chapter illustrated the effect of different inputs of wind speed, wind direction, and operating radar frequency on the simulation results. In addition, we have successfully

established the toolbox for simulating the radar cross-section of HF radar sea-echo. It is not only helpful for understanding the relationship between radar RCS and sea-state parameters but also provides the tool for testing estimators and implementing the inverse problem. In the next step, this simulation will be implemented to assess the performance of wave estimators and to investigate the advantages and limitations of the HF radar technique.

CHAPTER III ESTABLISHMENT OF THE END-TO-END SIMULATION

3.1 Introduction

Since 1955, the HF coastal radar has been developed as an oceanographic research tool [7], and is now widely applied based on its performance [1]. Based on the electromagnetic and hydrodynamic theory, the ocean surface information consists of the shape and velocity that can be extracted from the radar Doppler spectrum [51]. Thus, the synoptic measurement of physical oceanographic properties such as maps of surface-current velocity, the surface wave directional spectrum, wave parameters, and surface wind field information can be retrieved using features of radar Doppler spectra. There, the advantages of the HF radar technique over other ocean remote sensing techniques as well as traditional-situ techniques are the ability to retrieve ocean measurement over a larger area within hundred kilometers from the coastline with a very high temporal and spatial resolution, low cost, and flexible in installation and maintenance.

In order to retrieve the parameter of ocean surface waves from HF radar sea echo, numerous theories have been developed to describe the relationship between the characteristics of HF Doppler spectra and the sea-state information (represented in Chapters 1 and 2). Then, inversion algorithms for retrieving wave parameters and wave spectrum are developed (reviewed in Chapter 1). Finally, empirical methods robust in the computation are adopted to establish wave parameter estimators with no empirical constant included and non-requirement of Doppler spectrum signal-to-noise ratio (SNR). In this simulation, Barrick's analytical formulas [14] are applied to build up the End-to-End Simulation (E2ES) toolbox, which is used to assess the performance of estimators in wave height and mean period retrieval with the input of simulated HF radar Doppler spectra. Barrick's formulas will be represented in the following section.

3.2 Methods of Wave Parameter Estimation

3.2.1 Significant wave height

In 1977, Barrick first proposed that the root-mean-square wave height, h_{rms}, is proportional to the ratio of the weighted 2nd-order spectral energy over the 1st-order power, as in (3.1) [14]. The weighting calculation is essential so that the shape of the 2nd order sideband can be altered to present the corresponding wave spectrum.

$$h_{rms} = \frac{1}{k_0}\sqrt{\frac{2\int_{-\infty}^{\infty}\sigma^{(2)}(\omega)/w(\eta)d\omega}{\int_{-\infty}^{\infty}\sigma^{(1)}(\omega)d\omega}} \tag{3.1}$$

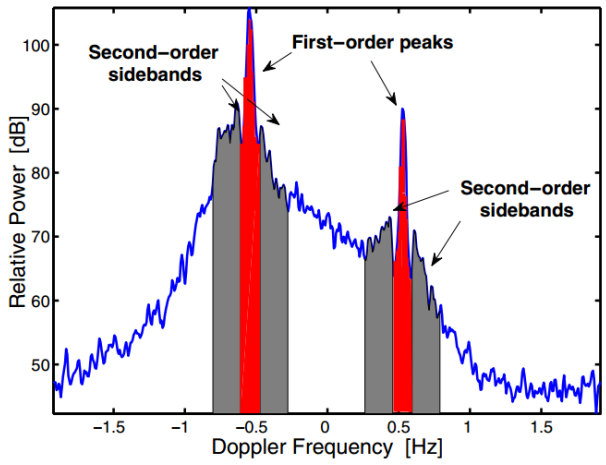

Figure 3-1 An example of the Doppler spectrum observed by a 27.65 MHz linear phased-array system [63].

Where, $\sigma^{(1)}$ and $\sigma^{(2)}$ are the first- and second-order Doppler spectrum, respectively (Figure 3-1), η and ω are normalized- and Doppler frequency, k_0 is the radio wavenumber, and $w(\eta)$ is the weighting function. The 2nd-order Doppler spectrum results from a double-bounce effect, upon which the transmitted signal interacts twice with a pair of wave components of two specific wavenumbers before being received. In such conditions, two mechanisms dominate the return signal

characteristics, i.e., the diffractive resonant scattering of electromagnetic waves and the quadruplet wave-wave nonlinear interaction. The coupling coefficient was introduced by Barrick [6] to represent the combined effects of the two above mechanisms. Later on, Barrick [14] reduced the dimensionality of the coupling coefficient from two dimensions (k_x, k_y) to a single dimension (Doppler frequency) by taking the averaged value over the normalized directional distribution. This approximation is called the weighting function $w(\eta)$. To obtain the value of the weighting function, it is first necessary to calculate the coupling coefficient; but its calculation is extremely tedious, though. Lipa and Barrick [56] have demonstrated the step-by-step procedures of the coupling coefficient computation. On the other hand, Alattabi [64] digitized the values directly using the original figure from Barrick's publication [14, 57] (Figure 3-2). In Figure 3-2, $w(.)$, $w_e(.)$, and $w_h(.)$ are the total, the electromagnetic, and the hydrodynamic weighting function, respectively, η (or ν in [14]) is the normalized Doppler frequency. Subsequently, the significant wave height H_s can be computed based on the fundamental theory of ocean waves. Furthermore, (3.1) illustrates the retrieval of root-mean-square wave height from the ratio of Doppler spectra energy, which means the influence of losing power in the term of transmitted range can be ignored, except for the low second-order spectrum SNR condition.

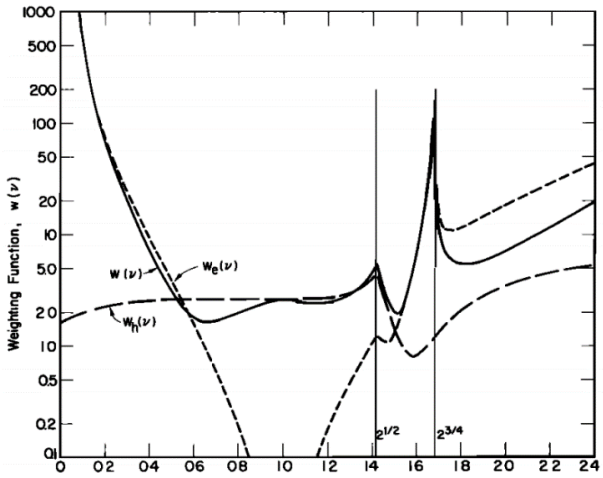

Figure 3-2 The weighting function is derived from the normalized coupling coefficient [14]. In this figure, the horizontal and vertical axes represent the normalized Doppler frequency (in unit) and the weighting function value (in unit), respectively.

Thus, the accuracy of the estimator in (3.1) is influenced by the theoretical error, statistical such as sampling error, and noise contamination [50]. Two first errors can be estimated and avoided, but the influence of noise could be detected and prevented only to a limited extent. From practical experience, it was confirmed that the accuracy of significant wave height mostly depends on the value of $k_0 h_{rms}$ [14, 17, 59, 65, 66], the favorable range for which is $0.1 \leq k_0 h_{rms} \leq 1$ (Figure 3-3) [14, 65]. It implies that the frequency of the HF band should be carefully selected based on the regional sea state [58, 65-67].

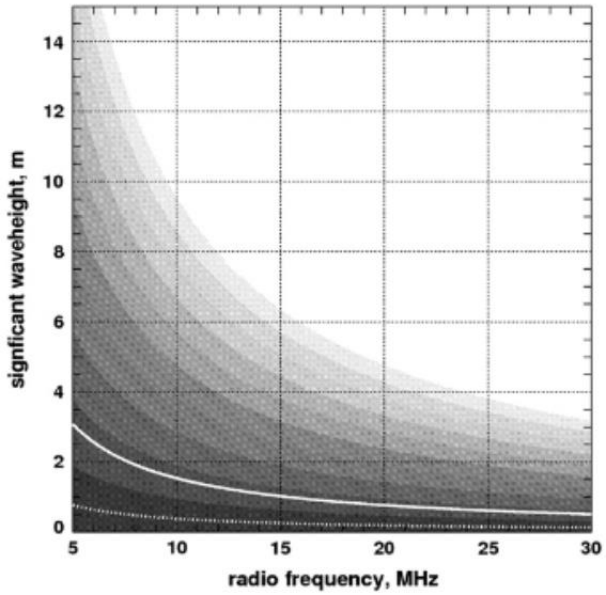

Figure 3-3 The contoured perturbation parameter with respect to radar frequency and significant wave height [66]. The contoured perturbation parameter is plotted with ten equal levels from less than 0.1 (black color) to greater than 1 (white color).

Later, a relationship between the root-mean-square wave height and the unweighted energy ratio of two Doppler spectra components was proposed by Maresca & Georges [15]. Accordingly, two empirical parameters were determined by fitting the ratio value and in-situ measurements of h_{rms}. The optimal values of two empirical parameters, which are the scale and power values, were found as 0.8 and 0.6, respectively, with a 7% error of the root mean square wave height [15]. In another study, the value of h_{rms} was calculated using an empirical formula in the half-power law [18], a modified form of (3.1). This method was applied in the DUCK94 experiment on the North Carolina coast, United States, and featured a 0.38 m root mean square error of significant wave height in the range of 0.5-6 m.

In 1998, a comparative study using three different algorithms of wave height retrieval was implemented by Heron & Heron [68]. After regressed of two phased-array radars data with 7 days of in-situ buoy data in the vicinity of the DUCK pier,

the author had concluded that Barrick's method performed better than two other methods, which were developed by Maresca & Georges [15] and Heron et al. [69]. In addition, a revised version of (3.1) consisting of noise removal was proposed.

$$h_{rms} = \frac{\xi_H}{k_0} \sqrt{\frac{2 \int_S (\sigma(\omega) - N)/w(\eta) d\omega}{\int_F (\sigma(\omega) - N) d\omega}} \tag{3.2}$$

In (3.2), N is the background noise, and the region of the first- and second-order Doppler spectrum for integral calculation were denoted as F and S, respectively. In this formula, two modifications were made. First, the background noise should be subtracted from the 1st- and 2nd-order Doppler spectra components. Second, a scaling factor ξ_H was introduced for better fitting the sea truth based on their data. This scaling factor, which was called the correction factor by Barrick [14], was suggested to be a constant of 0.551 by Heron & Heron [68]. Also, those authors mentioned that (3.2) is invalidity when the angle between the wind direction and the radar beam direction tends to be within 15° of orthogonal. In reality, it can be seen from (3.1) that the wave height results would not be influenced by the range but will be degraded with decreasing SNR in the frequency bands of the second-order spectrum. This method has no empirical constant to be tuned and has been widely used in previous studies [14, 68, 70, 71]. In this chapter, (3.1) was adopted to establish the estimator of the E2ES toolbox for determining significant wave height from the simulated Doppler spectra under various sea-state conditions.

3.2.2 Mean wave period

Analytical inversion methods for the mean wave period retrieval were proposed by Barrick [14] and Wyatt et al. [17], respectively. Barrick's equation is given as:

$$T_m = \xi_{Tm} \frac{2\pi}{\omega_B} \frac{\int_{0,1}^{1,\infty} \sigma^{(2)}(\omega)/w(\eta)d\eta}{\int_{0,1}^{1,\infty} |\eta - 1|\sigma^{(2)}(\omega)/w(\eta)d\eta} \quad (3.3)$$

where ω_B is the Bragg frequency, ξ_{Tm} represents the correction factor of the mean wave period, the characteristic discussed by Barrick [14], and originally equals 1. The frequency range of the integral in (3.3) could be on either side of the 1st-order peak, i.e., from 0 to 1 or 1 to infinity for normalized Doppler frequency on the side of stronger power density. Due to no empirical constants being included, the accuracy of the radar-deduced mean period mainly depends on the theoretical approach's error, SNR, and the defined Doppler frequency range of the second-order spectrum. Based on Barrick's work, the reported root-mean-square error (RMSE) of the mean wave period was approximately 12.4% for $k_0 h_{rms} > 0.3$ [14]. In practical calculation, Wyatt et al. [66] had discussed the effects of different radar working frequencies and the radar-to-wave angle and suggested the upper and lower frequency limits of the integral in (3.3). This chapter implemented (3.3) to establish the mean period estimator for the E2ES toolbox.

3.3 End-to-End Simulation

In this study, an End-to-End Simulation is established using Barrick's theory (Chapter 2) and existing above estimators to assess the uncertainty of wave estimators under homogenous wave fields and varying operating radar frequencies. This simulation toolbox is designed as a numerical test-bed that simulates the DR spectrum using the given directional wave spectra, HF radar location, operating frequency, and orientation. The radar Doppler spectra simulation flowchart is shown in Figure 2-8. The test is also implemented under noise-free conditions. The wave parameter estimators will then be applied to the simulated DR spectra. Finally, the

results will be compared with known targets for assessing the accuracy under various wave spectral and directional characteristics.

3.3.1 The setting parameters of E2ES

To implement the E2ES test-bed under the homogeneous wave field, the sea state is described using two widely statistical wave models, which are the JONSWAP spectrum [61] for the young sea and the Pierson-Moskowitz (PM) spectrum [60] for the full developed sea. For the young sea, the wind speed at 10 meters high from the sea surface (U_{10}) is set up in the range of 3-20 m/s with the non-dimensional fetch $\tilde{\chi} = 10^4$, while U_{10} is from 8 to 25 m/s for the fully developed sea. Herein, the wind speed range and non-dimensional fetch are selected for satisfying the perturbation theory condition. The wind direction is from 0^o to 90^o. The Longuet-Higgins wave directional spreading model [54] and Mitsuyasu directional spreading factor parameterization [62] are used to generate the directional wave spectrum. Also, it is assumed that the value of spreading factor ‘s’ is not less than 2. The flowchart of E2ES is shown in Figure 3-4.

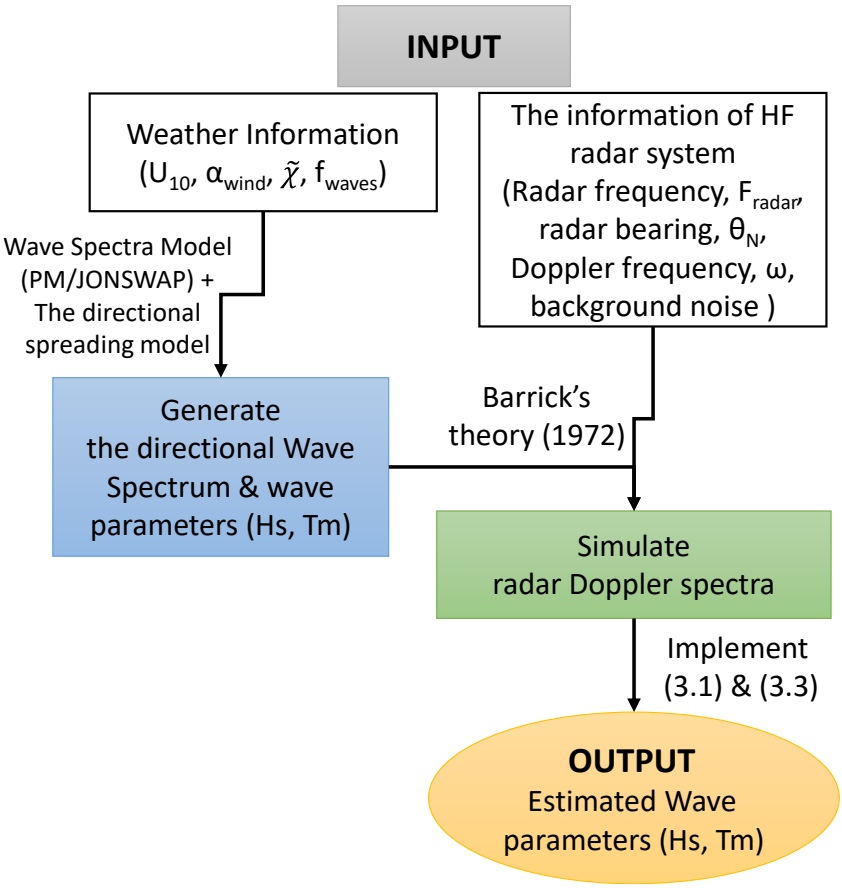

Figure 3-4 The flowchart of the E2E simulation.

The simulation is carried out at three operating radar frequencies, which are 27.5 MHz, 12 MHz, and 5 MHz. Wherein the 5 MHz operating radar frequency is applied to assess the performance of estimators under the fully developed seas, two other operating radar frequencies are deployed under the young sea condition. In summary, the setting parameters of HF radar Doppler spectra simulation are listed in Table 3.1.

Table 3-1 Setting parameters for Doppler spectra simulation.

Radar frequency	5 MHz	12 MHz	27.5 MHz
Chirplength	1	0.4	0.21666
Doppler bins	1024	2048	2048
Radar-looking direction (^{o})	90	90	90
U10	8-25	3-20	3-20
Wind direction (^{o})	0-90	0-90	0-90
The sea state situation	Fully developed	Young sea ($\tilde{\chi} = 10^4$)	Young sea ($\tilde{\chi} = 10^4$)
Wave spectra model	PM	JONSWAP	JONSWAP
Ocean current	-	-	-
Water depth	-	-	-

To retrieve wave parameters from those simulated Doppler spectra, (3.1) and (3.3) are adopted. Thus, it is necessary to identify and separate regions of first- and second-order components on simulated Doppler spectra for implementing those two retrieval algorithms. In the work of the E2E simulation, we did not add the Doppler frequency shift caused by the ocean current. It means that the location of the simulated first-order peak is precisely the theoretical value of Bragg frequency. Therefore, the null denotes the boundary between the 1st- and 2nd-order components can be identified by searching the minimum spectra value within the area, which is limited by a given maximum velocity. Or, it also means that a threshold of maximum current velocity should be assumed and adde into wave estimators. In this E2ES test-bed, the ocean current velocity is given and represented in Table 3-2. In addition, the

integral of (3.1) is calculated over the frequency range of $|0.4|\omega_B \sim |1.6|\omega_B$ [66], while the ocean wave frequency for the integral of (3.3) is taken as in Table 3-2.

Table 3-2 Setting parameters for Wave Parameter Inversion.

Radar frequency	5 MHz	12 MHz	27.5 MHz
Maximum radial velocity (cm/s)	150	100	50
Wave frequency for inversion (Hz)	0.03-0.15	0.045-0.23	0.05-0.35
Wave frequency resolution (Hz)	0.005	0.005	0.005

3.3.2 Results of Wave parameter comparison

First, we focus on the dependency of the errors on wave directionality. Figure 3-5 shows the comparisons of the estimated and target wave parameters under a free-noise condition. To retrieve the estimation result of significant wave height, the scaling factor, ξ_H, is determined as 0.504, which is close to the proposed empirical constant [68]. As the primary result, panels (a), (b), and (c) of Figure 3-5 show that the estimated wave height features a perfect fit to the target values when the angle between the wave direction and radar-looking direction, θ_w, equals to 45^o; it exhibits overestimation and underestimation with the decrease or increase of θ_w. Meanwhile, the bias of wave height estimation reaches the maxima overestimation or underestimation, respectively, when the peak wave direction is aligned or perpendicular to that of the radar beam. The comparisons of the estimated mean period and the target value are represented in the three last panels of Figure 3-5. Generally, there is a robust linear relationship between the estimated and the given mean period for different θ_w. However, the data points do not collapse on the 1-to-

1 diagonal line. The slopes are approximately 0.882, which agrees with reported results in the literature [14, 72]. These results demonstrated that the errors are not uniformly distributed over the spatial domain, even for homogeneous wave fields. The wave direction is crucial information for the correction of the systemic bias. Also, narrower wave directional spreading would rapidly degrade the performance, especially when θ_w is close to 90°. As it is known from the Mistuyasu's parameterization that the wave directional spreading width increases with frequency for those higher than the peak frequency. It implies that the directional spreading features are broader at higher frequency bands of Bragg waves, and can reduce bias estimation. This result agrees with the scenario mentioned in [15] and should be considered to determine the operating frequency of the HF radar system.

On the other hand, the accuracy of the estimated wave parameter is significantly influenced by the SNR of radar Doppler spectra. The higher noise level incurs higher bias and increases the sensitivity of θ_w results. It demonstrated that both above sources tend to cause a higher uncertainty of radar-deduced wave parameters.

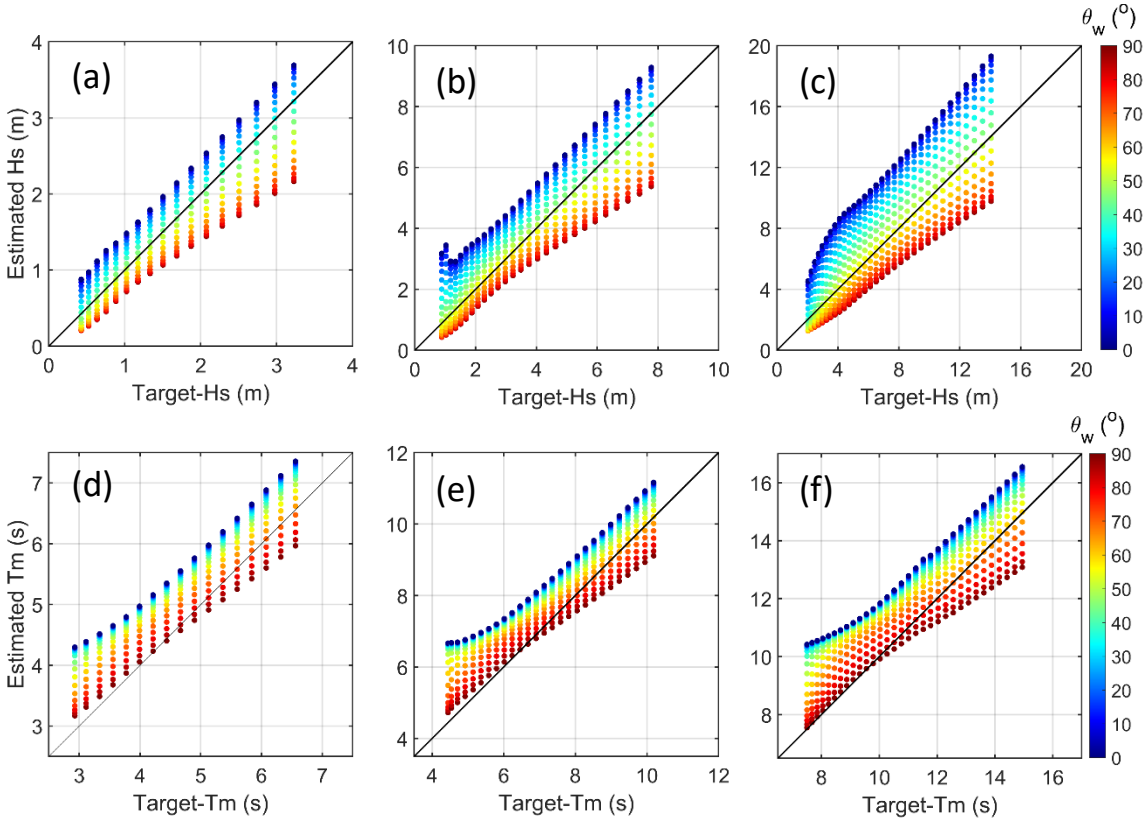

Figure 3-5 This figure illustrates the effect of varying radar-to-wave angle, θ_w, to wave parameters estimated from simulated Doppler spectral. Panels (a), (b), and (c) show the scatter plot of the given end estimated significant wave height with respect to the operating radar frequency of 27.5 MHz, 12 MHz, and 5 MHz, respectively, while panels (d), (e), and (f) shows the those of mean period with respects to three above operating radar frequencies.

It can be concluded that essential factors influencing the radar performance in steady and homogeneous cases are the radar-to-wave angle, SNR, and wave directional spreading characteristics. The wave directionality factors consisting of the angle between peak wave direction and radar bearing and the directional spreading width play critical roles in affecting the uncertainty of estimation results. Maresca & Georges [15] had implemented the sensitivity test and found that 16

would be the threshold of the spreading factor ‘s’ for Bragg waves; when ‘s’ greater than the threshold (narrower spreading width), accurate estimation of Hs would be impaired.

3.4 Summary

In this chapter, wave parameter estimators are implemented based on Barrick’s analytical methods [14, 57] for retrieving significant wave height and mean period from the HF radar Doppler spectra. Then, estimators were assessed under the steady homogenous wave field conditions. Overall, the estimated wave parameters agree well with the target value without depending on the wavefield condition and operating radar frequency.

The bias estimations of wave height and mean period are significantly influenced by the radar-to-wave angle and spreading parameters for the homogenous wave field condition. For significant wave height retrieval, the estimation results reach maximal overestimation when radar bearing is co-line to the main wave direction. A constant empirical value called the scaling factor was found as 0.504, which is close to the value of 0.551 in the literature [33, 68]. Meanwhile, a slope value between the estimated and the target mean period was found to be 0.882, which is also close to the value in Barrick’s report [14]. It illustrates the accuracy of our self-developed toolbox.

CHAPTER IV NUMERICAL INVESTIGATION OF THE UNCERTAINTY OF MONSOON AND TYPHOON WAVE PARAMETERS SIMULATION ON HF RADAR OBSERVATION

4.1 Introduction

Tropical cyclones (TCs) cause devastating losses to life and property and have significant socioeconomic effects worldwide. In particular, East and Southeast Asian countries are severely affected due to the frequent attack of typhoons. Since 1980, the intensity of TCs that have struck the North West Pacific region has increased by 12%–15%, and the proportion of category 4 and 5 TCs has doubled owing to climate change [73]. To improve the accuracy of typhoon forecasting using atmosphere-wave-ocean coupled models, the characteristics of waves that dominate air-sea interactions and comprise air-sea heat, moisture, and momentum fluxes [74, 75] should be subject to real-time monitoring and data assimilation into forecasting models [76]. However, information on the directional spectra of typhoon waves remains limited because of the rigors of instrument deployment and inadequate in situ data.

On the other hand, the characteristics of ocean surface waves, which mainly influence the process of air-sea interaction, and play crucial roles in the intensification of typhoons, can be retrieved from the Doppler spectra components of the HF radar cross-section. At present, the HF radar system consisting of size compact, flexible installation and maintenance, working in challenging environments such as heavy wind and rainfall, and meeting demands for affordability, is a promising alternative for ocean wave monitoring under various weather conditions. Therefore, this chapter aimed to assess the uncertainties of retrieved wave parameters, such as significant wave height and mean period, using simulation data

of HF radar Doppler spectra under monsoon and typhoon conditions. For quantitative investigation, a numerical test-bed is ongoing to establish. In this test-bed, Barrick's approach in 1972 is used first to simulate the radar Doppler-range spectra with the inputs of directional wave spectra, which can be hindcasted from the third-generation wave model. Then, those simulated radar Doppler spectra are used to estimate the wave parameters using wave estimators built up from existing methods in Chapter 3. In this study, the Typhoon Dujuan (2015) and the monsoon front in May 2018 are carried out as examples. The results could provide useful information for assessing the performance of HF radar-deduced wave parameters under monsoon and typhoon conditions.

4.2 Simulation of Monsoon and Typhoon Waves

In order to assess the uncertainty of wave parameters estimated from HF radar sea echo under monsoon and typhoon conditions, the radar Doppler spectra will be simulated using the directional wave spectrum, which is generated by the third-generation wave model. Hindcast directional spectrum data of monsoon conditions from May 23 to 31, 2018, and Typhoon Dujuan from September 23 to 29, 2015, are first represented and discussed in this section.

4.2.1 Monsoon waves

The first case study is the reversal of wind direction from northeast to southwest caused by the passage of the summer monsoon front on May 29, 2018. Wave directional spectra were obtained using the WaveWatch-III model driven by ECMWF reanalysis of wind fields for the southwest monsoon event from May 23 to 31, 2018. In this model, a three-layer nested grid system was implemented over the computational domain of the entire Northern Pacific, and the highest spatial and temporal resolution is 9 km and 1 hour, respectively. To reduce the complexity of

the monsoon wave directional spectrum simulation using WaveWatch-III, the option of wave-current interaction, which could affect the simulated directional spectrum as well as wave height [77, 78], was turned off.

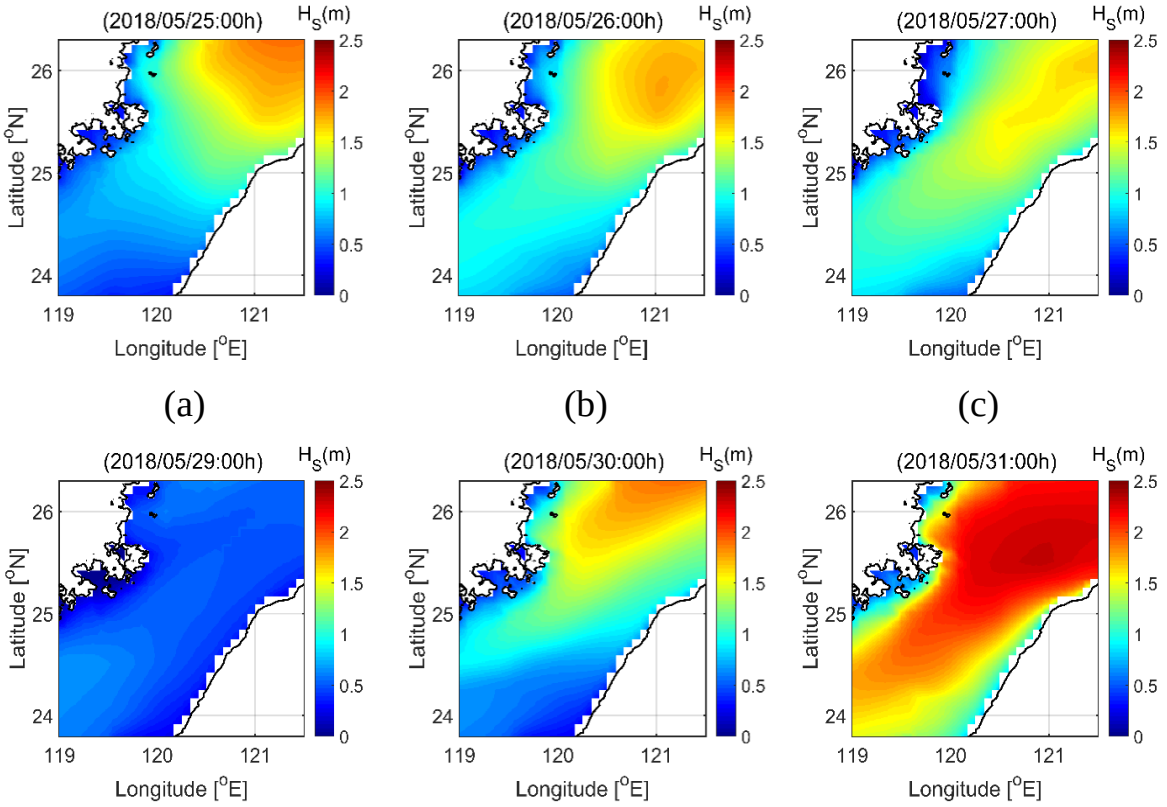

Figure 4-1 The temporal evolution of significant wave height during the passage of a northwest monsoon front at the northern Taiwan Strait in late May 2018.

As a result, the evolution of the wave height field during the onset of monsoon events in the Northern Taiwan Strait is represented in Figures 4-1. The figure shows that the highest significant wave height caused by the monsoon wind field during those six days reached 2.4 m. For more understanding of monsoon wave characteristics, the temporal evolution of the directional spectra at a fixed position near the center of the Taiwan Strait (120.50° E, 24.85° N) for the corresponding six days is shown in Figure 4-2. It illustrated that the wave direction and directional

spreading experienced dramatic changes from an east & north-east (ENE) main direction with broader spreading to south & south-west (SSW) with narrower spreading during the front passage.

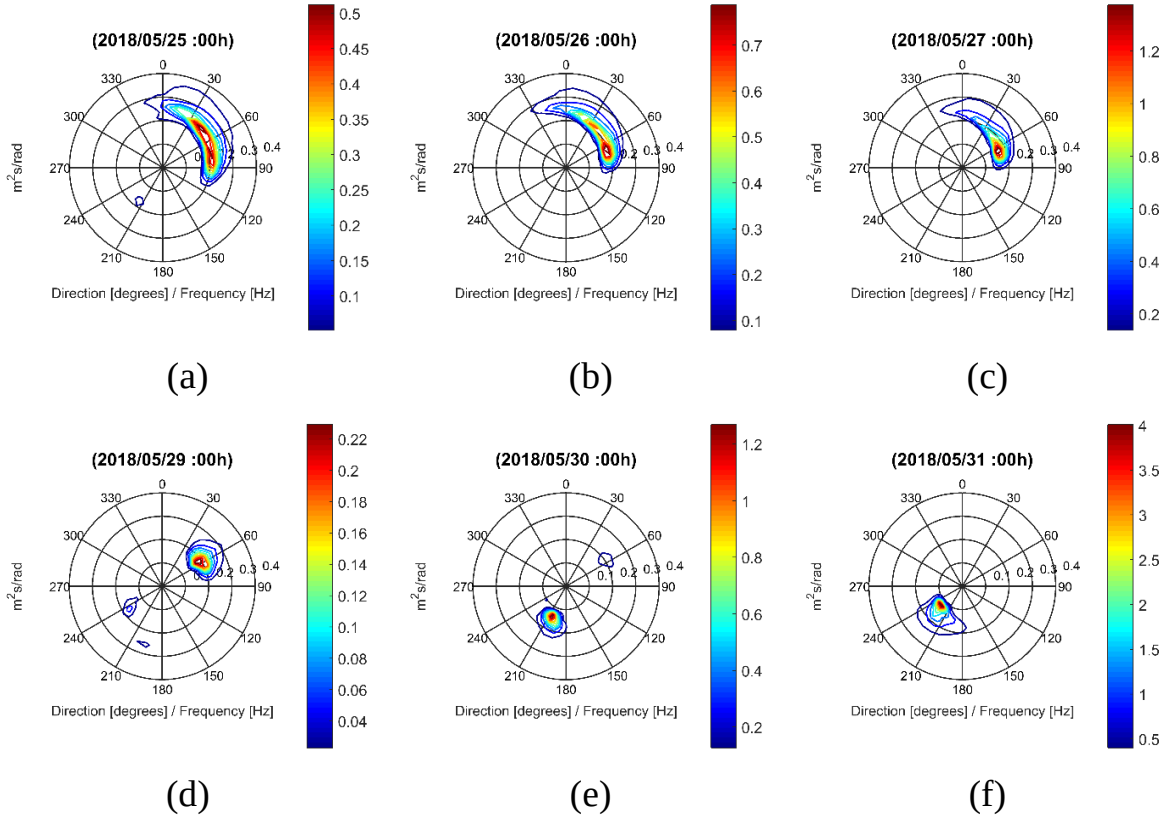

Figure 4-2 Daily evolution of monsoon wave directional spectra at the center of the Taiwan Strait (120.50° E, 24.85° N) in late May 2018.

4.2.2 Typhoon waves

In order to assess the uncertainties in wave parameters estimated from HF radar Doppler spectra under the passage of typhoons, the non-parameterized directional wave spectra generated using the third-generation wave model are used as inputs of the test-bed. Hindcast directional spectra from September 23 to 29, 2015, during Typhoon Dujuan (category 4) made landfall on the eastern coast of Taiwan (Figure 4-3) are chosen as typhoon cases. In reality, a 16 m significant wave height was measured by a data buoy station on the northeast coast of Taiwan during the

influence of Typhoon Dujuan [79] and caused substantial damage to coastal structures. The trajectory, intensity of Typhoon Dujuan, and the simulated max Hs over the northwestern Pacific are shown in Figure 4-3.

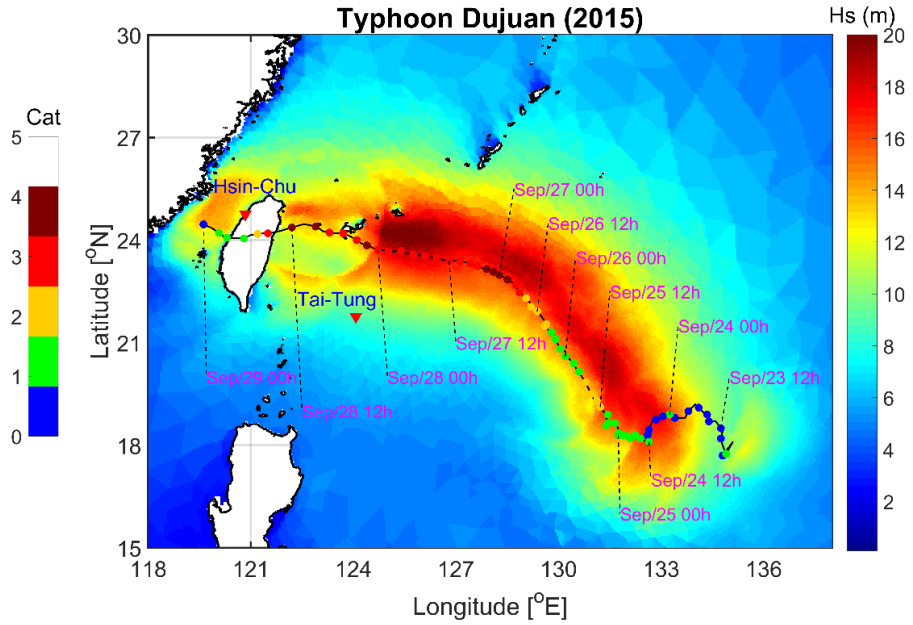

Figure 4-3 The spatial distribution of the maximum significant wave height during Typhoon Dujuan in 2015.

For simulating the unsteadiness and spatial heterogeneity of the typhoon wave characteristics near the maximum wind radius, the directional spectra were hindcasted using the DHI MIKE-21 3rd-generation Spectral Wave (SW) model on an unstructured grid domain that covered the entire Northwestern Pacific. The wave model was driven by an ultra-high-resolution (1×1 km) wind field, which was data assimilated and provided by the typhoon research group at the Department of Atmospheric Sciences, National Central University, Taiwan. In addition, an unstructured grid was designed to be finer than 3 km in spatial resolution along the typhoon trajectory to reconstruct the unsteady and heterogeneous wave field around and maximum wind radius near the typhoon eye. To validate the uncertainty of the

modeled wave height, in-situ wave data at Hsin-Chu coastal and Tai-Tung offshore buoys (Figure 4-3) is used. Subsequently, the Hs comparisons of the model output to the observation are shown in Figure 4-4. The comparison results illustrate the uncertainty of model outputs and demonstrate the simulation results close to the wave field's actual situation under typhoon conditions.

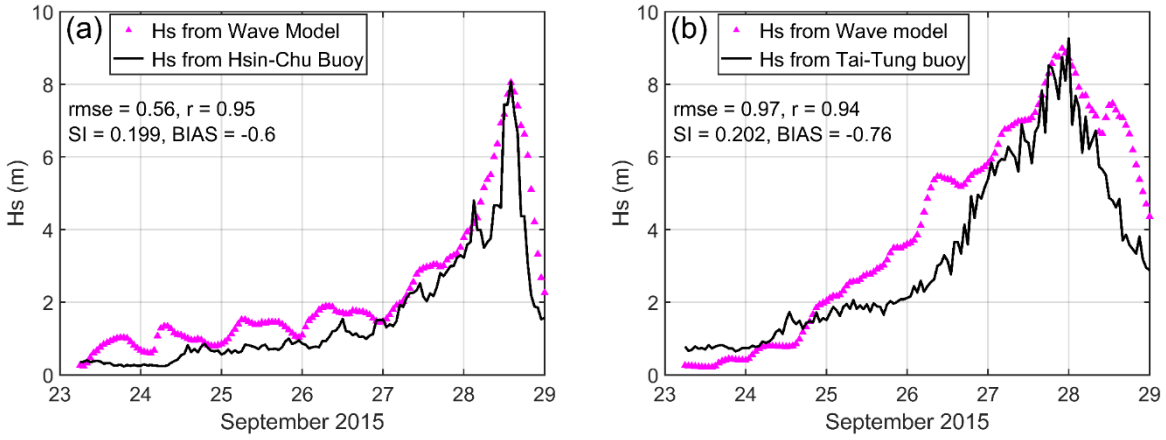

Figure 4-4 The comparison of time-series significant wave height from the in-situ data of (a) Hsinchu buoy and (b) Tai-Tung buoy and the simulated values from the Wave model.

Examples of the directional wave spectra (DWS) near the maximum wind radius of about 50 km from the typhoon eye in 8 corresponding quadrants and at the typhoon center are shown in Figure 4-5. Whereby penal (e) shows DWS at the typhoon center, while the other eight panels show DWS at the locations 50 km from the eye relative to the typhoon translation direction, details (b) and (h) aligns in the direction of typhoon translation direction; (b) is in the front and (h) in the rear; panels (c), (i), (a), (g) represent the directional spectra at the middle of the upper-right, lower-right, upper-left and lower-left quadrates; panels (f), (d) represent the directional spectra on the right- and left-hand-sides of the eye, respectively.

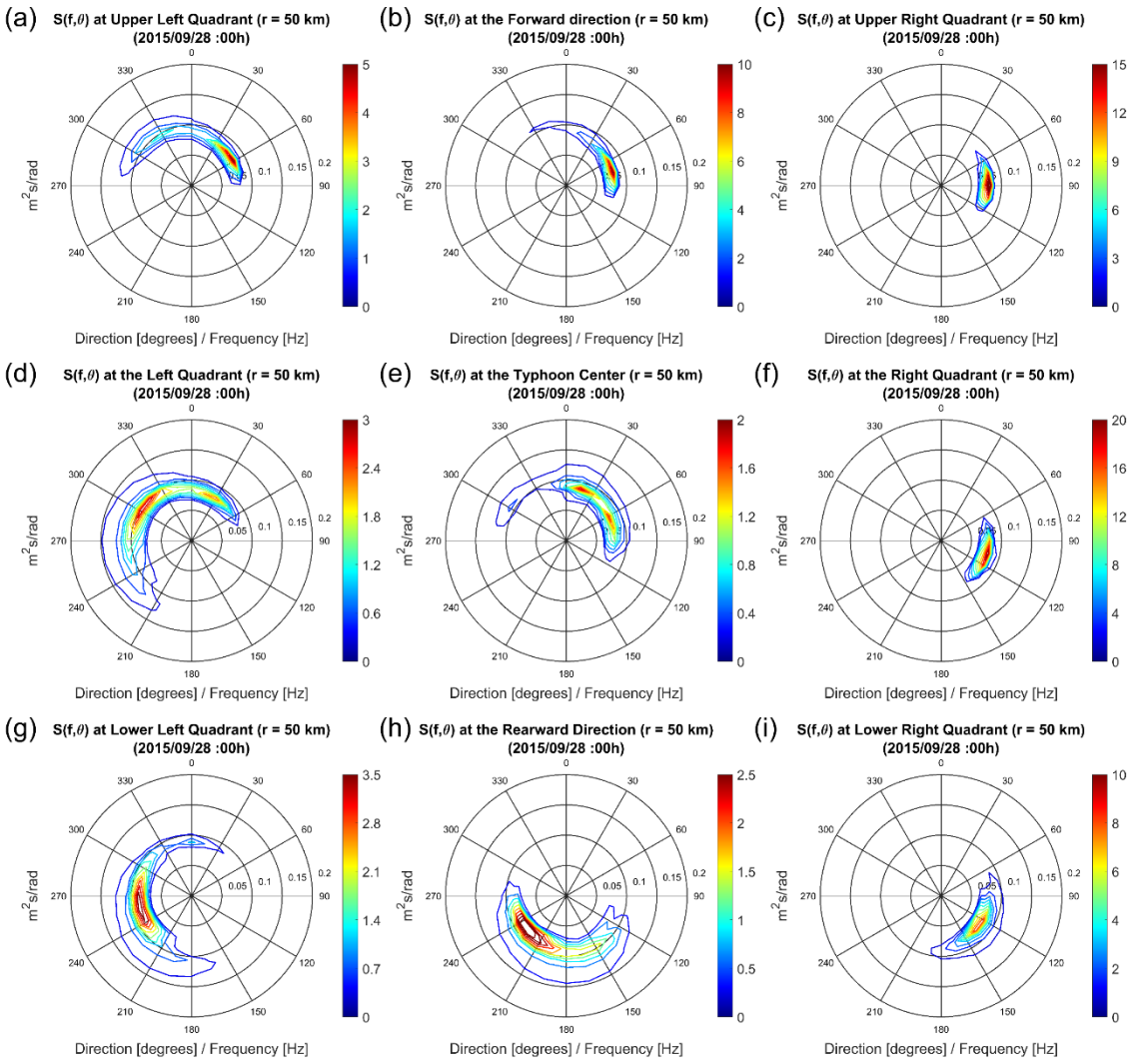

Figure 4-5 The directional wave spectra at 00UTC on September 28, 2015, at nine positions relative to the eye and the typhoon translation direction. Wherein, penal (e) shows the directional wave spectrum at the typhoon center, while the other eight panels are at the locations 50 km from the eye relative to the typhoon translation direction, details (b) and (h) aligns in the direction of typhoon translation direction; (b) is in the front and (h) in the rear; (d) and (f) are the left- and right-hand sides of the eye relative to the typhoon translation direction, respectively; (a), (c), (i), (g) represent the directional spectra at the center of the upper-left, upper-right, lower-right, and lower-left quadrates, respectively.

Figure 4-5 illustrates that the typhoon wave directional spectra exhibited extreme spatial heterogeneity, bimodality, and varying directional spreading. It is also found that the most intensified wave power density was accompanied by narrower directional spreading in the upper-right quadrant relative to the typhoon trajectory and eye. By contrast, the directional spectra show broader directional spreading in the left two quadrants relative to the typhoon trajectory. In addition, the bimodal wave spectrum caused by the simultaneous presence of swell and wind waves can be observed in the left-hand quadrants. As the wave characteristics near the typhoon center are complex, we will investigate whether these complexities impair the wave parameter inversion for HF radar.

4.3 Reviewing area estimation of HF radar observation

In order to simulate the radar Doppler spectra under the monsoon wave field condition, two virtual HF radar stations, R_1 and R_2, 20 km apart on the northwest coast of Taiwan, are designed (Figure 4-6). Herein, R_1 is ongoing to install at the Observatory of National Central University, Xinwu district. The second radar station, R_2, will also be installed at the end of 2022 in the Dayuan district. This radar network would be applied for multi-purposes consisting of dynamic coastal monitoring, marine traffic management, and beyond. In this research, a 27.5 MHz HF radar system with radar coverage of 40 km from the coastline is designed. Then, the Doppler spectra data of two HF radar sites are simulated using the modeled directional spectra of monsoon waves as input at their locations denoted by black dots in Figure 4-6.

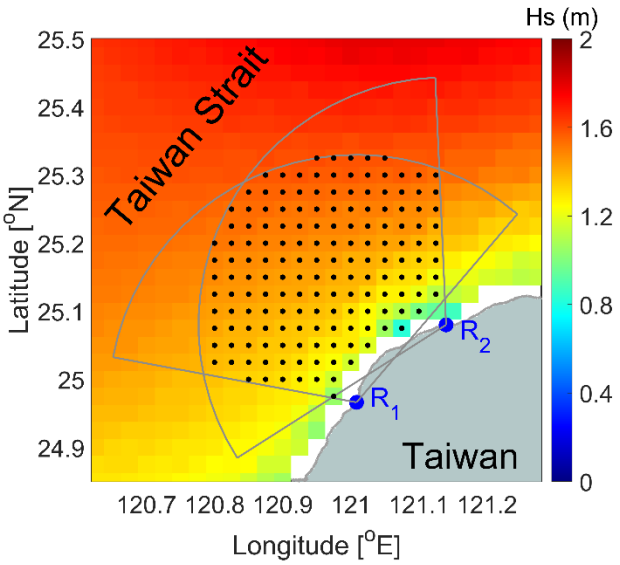

Figure 4-6 This figure shows the HF radar network with the attendance of two virtual radar sites (R_1, R_2) at the coastline of Taoyuan city, Taiwan, for the case study under monsoon conditions. The grey line shows the coverage area of the two virtual HF radar stations, and black points denote the location of the modeled monsoon directional wave spectra.

For the typhoon case study, 5 MHz is selected as the operating frequency of the HF radar system. The observation range for wave measurement is assumed to be 120 km. Two types of virtual radar networks are located on the coastline and be mobile, and moving with typhoon translation are designed. For the first type, the coastal HF radar network with the attendance of two virtual radar sites, R_1 and R_2, is located on the coastline and 50 km apart, as shown in Figure 4-7. In this figure, the grey line shows the coverage area of two virtual HF radar stations; the magenta point and magenta line represent the typhoon eye and typhoon trajectory, respectively; black points denote the location of the modeled typhoon directional wave spectra. Later, the hourly Doppler spectra from two HF radar stations are simulated using the input of the modeled typhoon directional wave spectra within the radar's footprint.

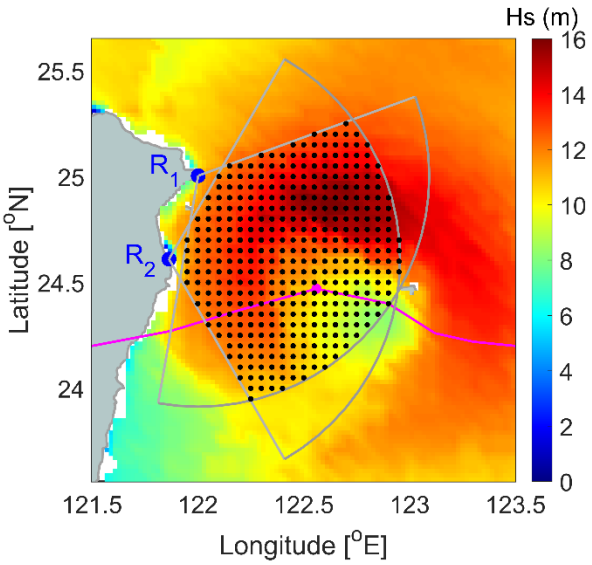

Figure 4-7 The configuration of a coastal HF radar network with the attendance of two virtual radar stations is set up for the testbed under typhoon conditions. Herein, the grey line shows the coverage area of two virtual HF radar stations (R_1, R_2); the magenta point and magenta line represent the typhoon eye and typhoon trajectory, respectively; black points denote the location of the modeled typhoon directional wave spectra.

For the mobile Hs radar networks and moving with the typhoon translation, their configuration is designed as follows: The network consisted of 2 or 3 radar stations and focused on the area of typhoon quadrants with respect to the typhoon trajectory (Figure 4-8). In Figure 4-8, panels (a)-(d) represent the HF radar network with the attendance of two virtual radar sites viewing the upper-right, upper-left, lower-right, and lower-left quadrants of the typhoon; panels (e)-(h) represent the HF radar network with the attendance of three virtual radar sites focusing the desired area as those of panels (a)-(d); and panels (i)-(l) show the HF radar network with the attendance of two virtual radar sites viewing the right- and left-hand sides, and front and rear quadrants of Typhoon Dujuan. There are many concerns about the

practicality of the above virtual HF radar networks for monitoring wave and wind fields at various typhoon quadrants. However, the theory and experiments of HF radar systems installed on platforms have been developed for more than ten years [10, 80, 81]. Of course, it is still a long way to perfect the HF radar technology to reach the setting condition, as shown in Figure 4-8, but those experiments are still possible. Furthermore, aircraft [12] and sky radar used HF bands are also actively being tested and implemented [15, 82-84]. Therefore, it demonstrates that in addition to radar stations on the ground or fixed platforms, the sea, air, and skywave radars [85] using HF bands can be deployed for monitoring the dynamic of upper ocean layers in the future.

In Figure 4-8, the grey line shows the coverage area of two virtual HF radar stations, blue polygons covering black points show the focusing area of designed HF radar networks, black points denote the location of the modeled typhoon directional wave spectra, the magenta point, and magenta line represent the typhoon eye and typhoon trajectory, respectively. Then, the hourly Doppler spectra on each black point are simulated for analysis. The monsoon and typhoon waves retrieved from the Doppler spectra simulation of HF radar networks in Figures 4-6, 4-7, 4-8 will be assessed and compared in the next section.

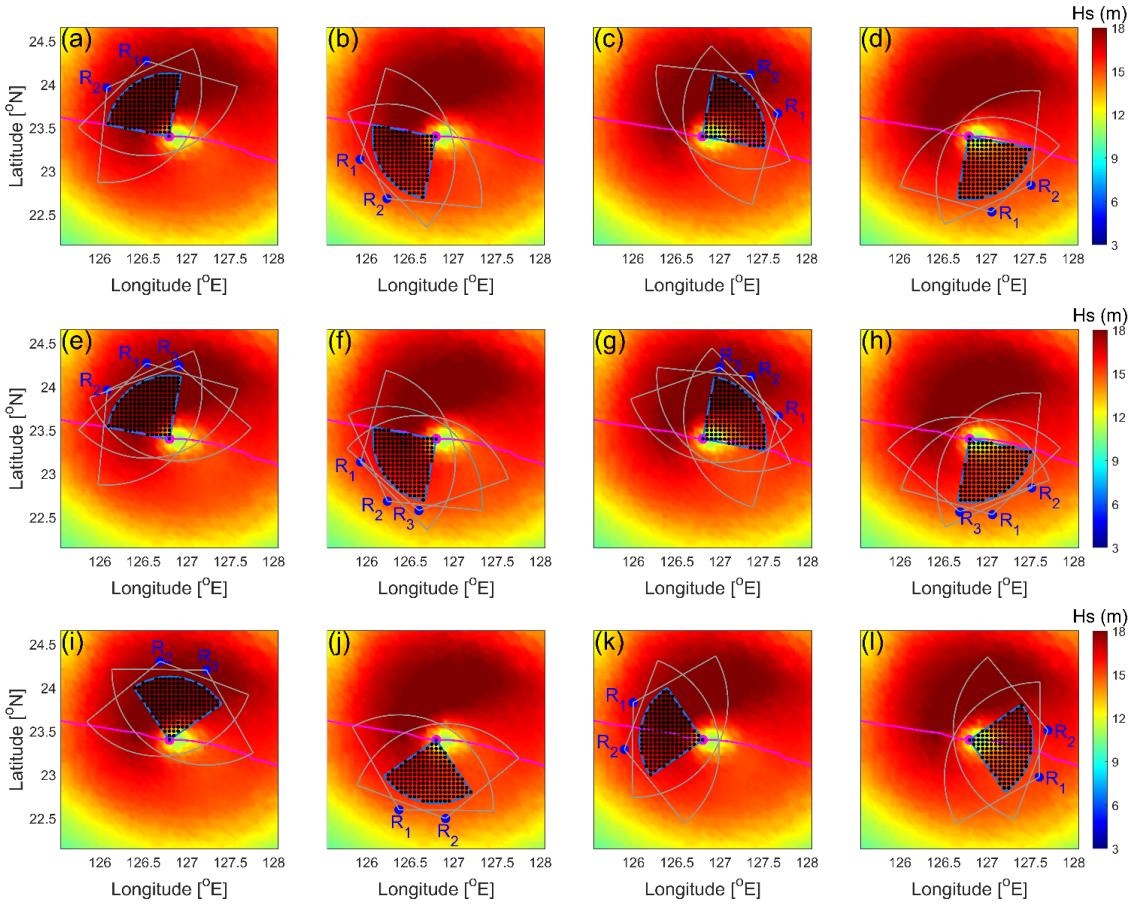

Figure 4-8 The configuration of virtual HF radar networks concerning the trajectory of Typhoon Dujuan and focusing on typhoon quadrants is set up for the testbed when the typhoon is on the ocean. Panels (a)-(d) represent four virtual HF radar networks with the attendance of two radar sites looking to the upper-right, upper-left, lower-right, and lower-left quadrants of the typhoon; panels (e)-(h) represent the virtual HF radar network consisting of three virtual radar sites focusing on the desired area as those of panels (a)-(d); panels (i), (j), (k), and (l) represent the virtual HF radar network consisting of two radar sites looking the right, left, front, and rear typhoon quadrants, respectively.

4.4 Results and Discussions

4.4.1 Background of statistic parameters

This study analyzes the comparison between estimated and target values to assess the bias estimation of wave parameter retrieval using HF radar Doppler spectrum. The widely used statistical values, which are the correlation coefficient (r), root-mean-square error (RMSE), the mean bias (BIAS), and the scatter index (SI), are used to show the uncertainty of estimation results. The formulas of those statistical parameters are given as follows:

$$
\begin{aligned}
r &= \frac{\mathrm{cov}(x, y)}{\sigma_x \sigma_y} \\
\mathrm{RMSE} &= \left[\frac{1}{N}\sum_{i=1}^{N}(y_i - x_i)^2\right]^{1/2} \\
\mathrm{BIAS} &= \frac{1}{N}\sum_{i=1}^{N}(y_i - x_i) \\
\mathrm{SI} &= \sqrt{\frac{\sum_{i=1}^{N}[(x_i - \bar{x}) - (y_i - \bar{y})]^2}{\sum_{i=1}^{N} {y_i}^2}}
\end{aligned}
\tag{4.1}
$$

where x and y represent the estimated and target values, $\bar{x}$, $\bar{y}$, σ_x and σ_y are their mean values, and standard deviations, $\mathrm{cov}(x, y)$ is the covariance value of x and y, and N is the number of synchronized data between x and y variables, respectively.

4.4.2 Wave Parameters Simulations of HF Radar Observation Under Monsoon Conditions

To quantitative the uncertainty of wave parameters estimated from the simulation data of HF radar Doppler spectra under monsoon conditions, the comparisons between estimated monsoon wave height and mean period and the

target values will be carried out. First of all, Figure 4-9 represents the targets and estimated wave parameters at 0300LT on May 31st, 2018. In this figure, panels (a) and (b) describe the map of significant wave height and mean period generated from the Wave model, respectively, while (c) and (d) represent maps of radar-deduced Hs and Tm from simulated HF radar Doppler spectra, respectively. Panels 4-9(a) and (c) show that the radar-deduced Hs is over-estimated in the northeast region, and underestimated in other areas. It is noted that a 0.504 wave height scaling factor was applied in the process of E2ES. It means radar-deduced Hs can be overestimated over the radar's footprint if the additional wave height scaling factor does not use. Notably, after the arrival of the monsoon front on May 29, 2018, the directional spreading of ocean surface waves became narrower; and it may cause the bias estimation of results. Meanwhile, the spatial distributions of the mean wave period at panels (b) and (d) show that the estimated mean period agrees pretty well with the target value under the passage of the monsoon front. It implies that the variation of the spreading factors may not play a key role in affecting the uncertainty of the radar-deduced mean period. Instead, the radar-to-wave direction would be the critical factor influencing Hs and Tm estimation. The overestimation of Hs and Tm in the northeast area in Figures 4-9(c), (d) has demonstrated the above discussion.

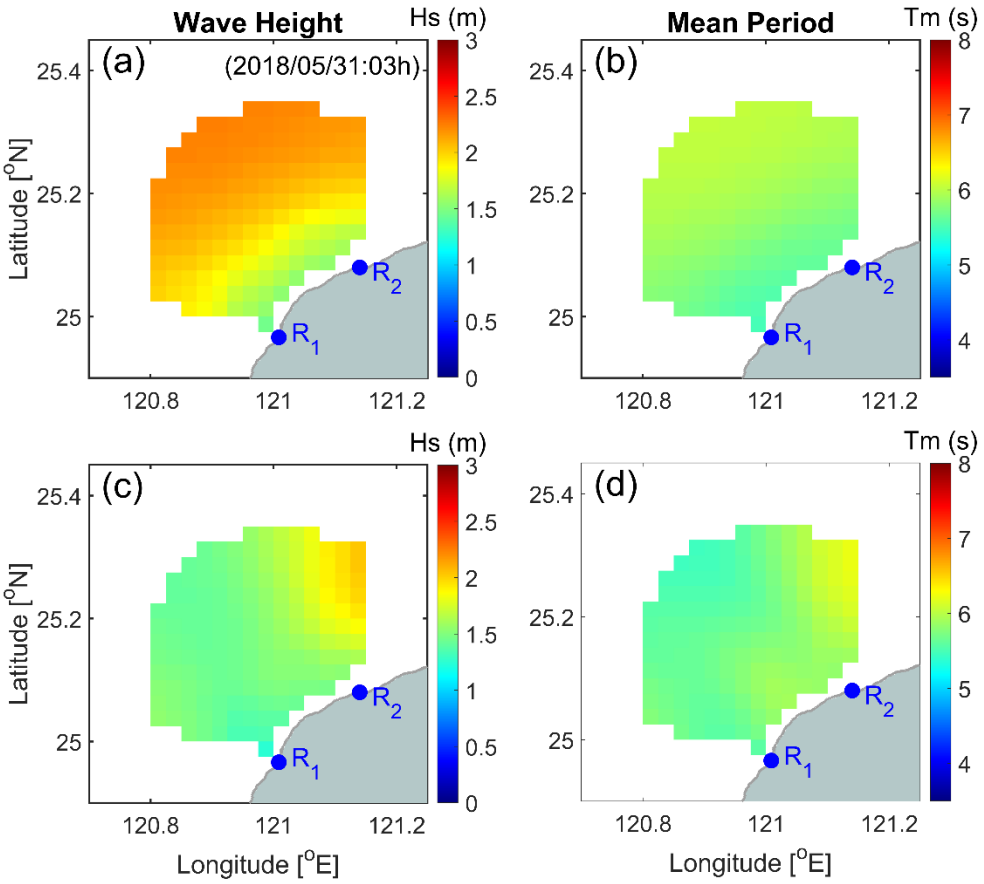

Figure 4-9 The spatial distributions of target and estimated wave parameters under a northeast monsoon condition. Herein, panels (a) and (b) represent the map of modeled significant wave height and mean period, respectively, at 0300LT on May 31st, 2018, while (c) and (d) represent maps of retrieved Hs and Tm from simulated radar Doppler spectra, respectively.

The results in Figure 4-9 only show an example of the difference between estimated and target wave parameters over the spatial domain of radar coverage. However, the uncertainty of radar-deduced wave parameters under monsoon front conditions has not been shown yet. Therefore, comparison results of wave parameters and Hs and Tm estimation error indexes are computed and shown in Figures 4-10, 4-11 & 4-12. The comparison results in Figure 4-10 indicated that the

estimated Hs & Tm agree well with the target values. Figure 4-10(a) shows that the radar-deduced wave height is almost underestimated under higher sea states. The scatter plot also indicates that the bias estimation of Hs increase when the monsoon wave field increases. It implies that a value of 0.504 for the wave height scaling factor may not be the correct value for calibrating radar-deduced wave height under monsoon conditions. On the other hand, the comparison results in Figure 4-10(b) demonstrated the performance of the mean wave period estimator. And the estimated Tm is comparable to the target value.

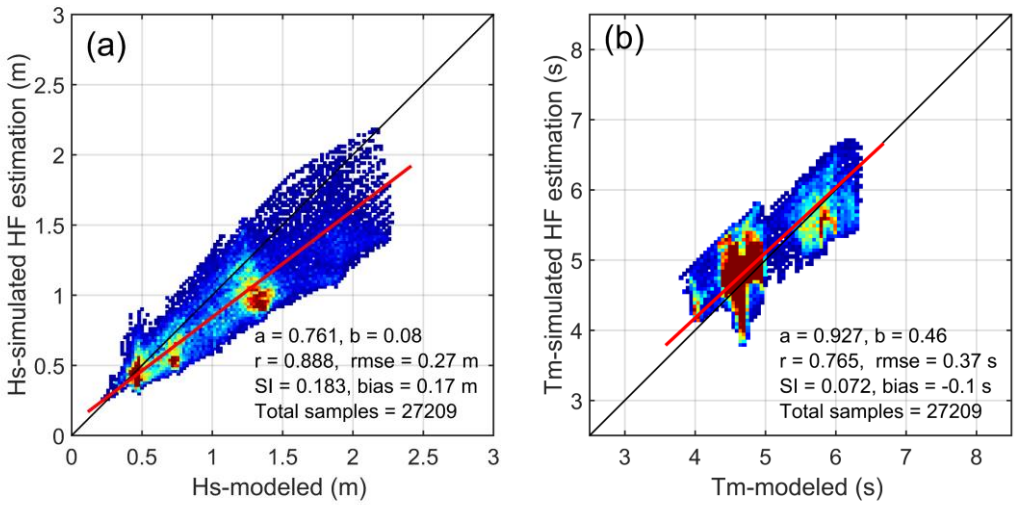

Figure 4-10 The scatter comparisons of (a) significant wave height estimation and (b) mean period estimation of the constellation of the virtual HF radar network and the modeled values under monsoon conditions.

Figures 4-11 and 4-12 show the distribution of error indexes (root-mean-square error (RMSE), Scatter Index (SI), BIAS, and correlation coefficient) for wave parameter estimations. In two of those figures, panels (a) and (c) represent the error indexes of radar-deduced significant wave height, while panels (b) and (d) represent the error indexes of mean period estimation. The corresponding value of those statistic parameters for Hs and Tm estimation are also listed in table 4.1. First of all,

the spatial distribution of the RMSE for Hs in Figure 4-11(a) shows that the bias estimation of Hs is small in the nearshore region and becomes significant in the offshore zone where the sea-state is strong. Similar to RMSE's pattern, the spatial variation of SI of Hs estimation increases gradually with the increase of wave height in the offshore area. The averaged RMSE and SI for significant wave height over the coverage area are 0.26±0.10 in meters and 0.142±0.042, respectively. This bias estimation is sizeable for the simulation work. Furthermore, panel (a) of Figure 4-12 demonstrated the underestimation of radar-deduced wave height, which is related to the unfit of the scaling factor; while the correlation coefficient between estimated and modeled significant wave height in Figure 4-12(c) shows the pretty good performance of Barrick’s analytical formula for wave height retrieval.

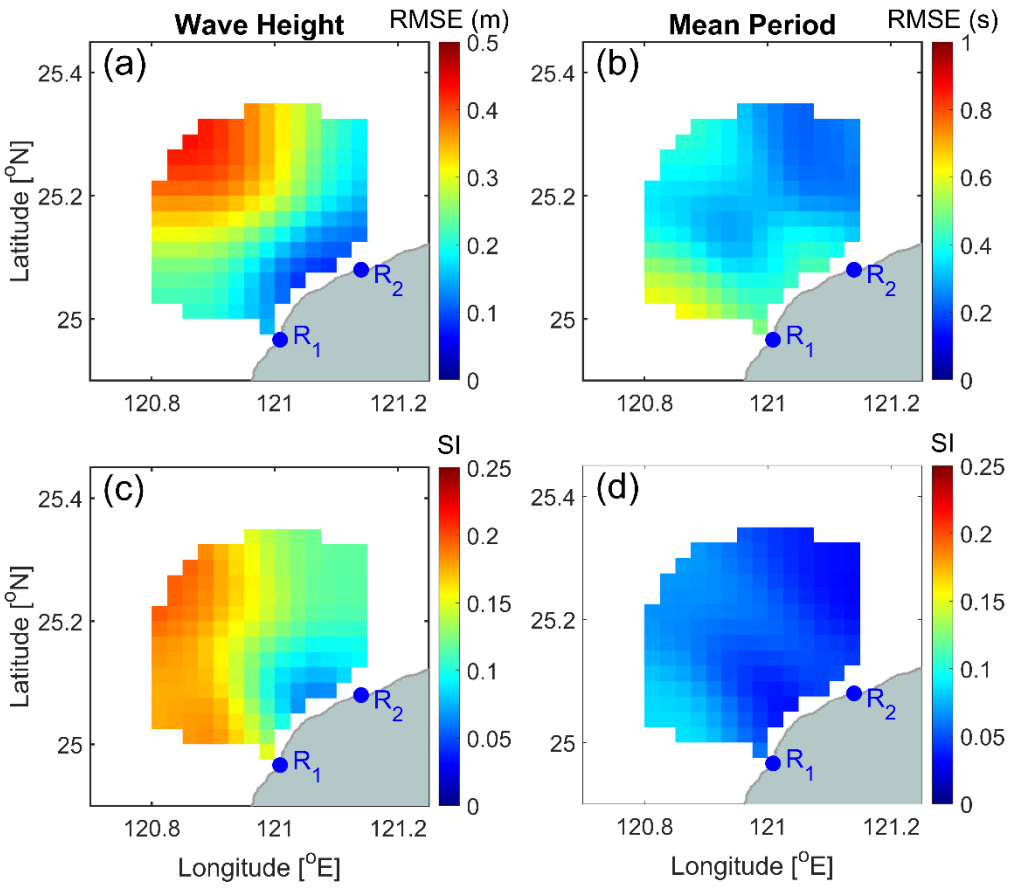

Figure 4-11 The spatial distribution of error indexes (RMSE & SI) of significant wave height and mean period estimations from the constellation of the virtual HF radar network under monsoon conditions. Wherein panels (a) and (c) represent the map of RMSE and SI for Hs, respectively, while panels (b) and (d) represent the map of RMSE and SI for Tm, respectively.

The analysis of the mean wave period shows that the RMSE of Tm estimation is less than 0.5 s except for the southwest area where radar bearing is almost co-line with wave direction. And, the SI of the mean period estimation is not over 0.1. Obviously, the result of RMSE and SI of Tm estimation in Figures 4-11(b) and (d) is reasonable compared to error indexes in Figure 4-10. The comparison results in Figure 4-10(b) show the agreement between the estimated and target mean period.

However, the spatial distribution of BIAS in Figure 4-12(b) indicates that the results of Tm estimated from the radar Doppler spectra simulation exhibit overestimation in the nearshore area and underestimation in the offshore region. This has also been also discussed in section 3.3.2.

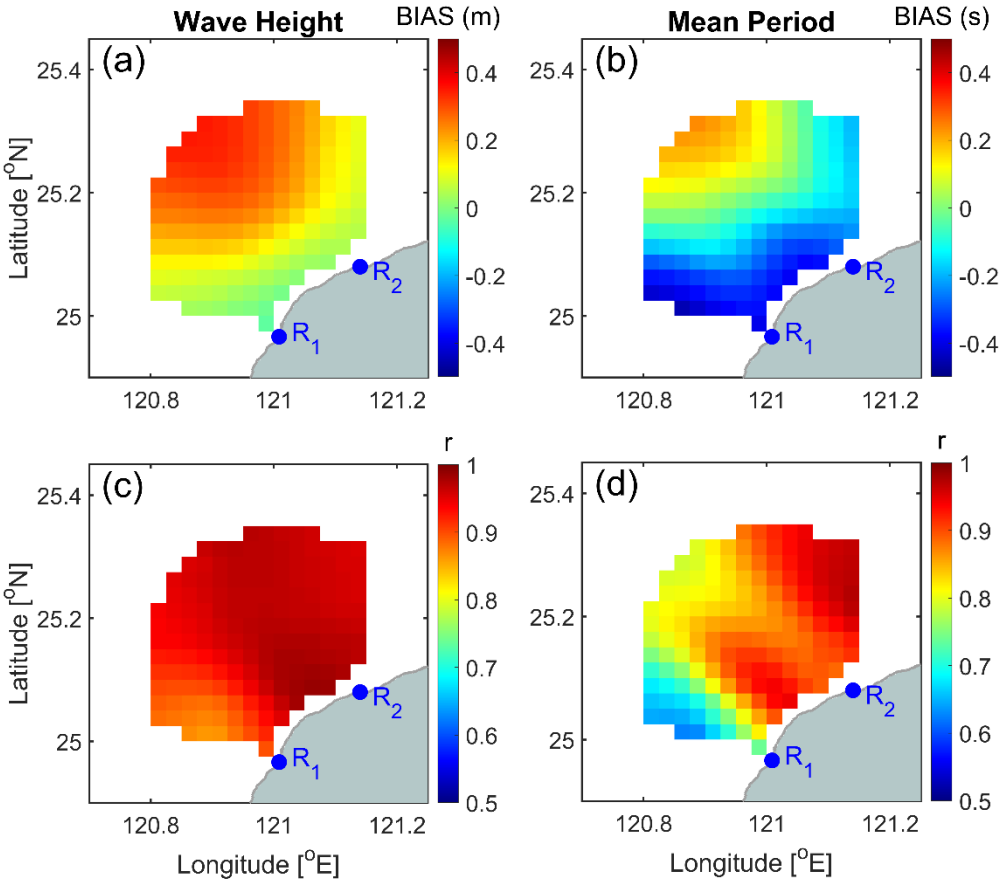

Figure 4-12 The spatial distribution of BIAS and correlation coefficient (r) of significant wave height and mean period estimations from the constellation of the virtual HF radar network under monsoon conditions. In this figure, panels (a) and (c) represent the map of BIAS and *r* for the significant wave height, respectively, while panels (b) and (d) represent the map of BIAS and r for the mean period, respectively.

Table 4-1 Statistical parameter of waves height and mean period estimations under the NE monsoon wavefield condition.

Statistic Parameters	Hs	Tm
r	0.95 ± 0.04	0.85 ± 0.12
RMSE	0.26 ± 0.10	0.36 ± 0.13
BIAS	0.175 ± 0.123	-0.109 ± 0.218
SI	0.142 ± 0.042	0.055 ± 0.018
Number of points	27209	

In another respect, the uncertainty of the estimation results can be computed over the space domain at each time period. As a result, the temporal variation of Hs and Tm estimation error indexes from the coastal virtual HF radar network under monsoon conditions is shown in Figure 4-13. In Figure 4-13, the variation of RMSE is represented by red dots, while the value of SI is shown in blue bars. Figure 4-13 shows the averaged uncertainty of wave height estimation, which are 0.25 m and 0.152 for RMSE and SI, respectively, and they are 0.4 sec and 0.059 for RMSE and SI of mean wave period, respectively. The RMSE for Hs varies around 0.3 m for normal sea-states and reaches over 0.5 m when the monsoon front passage radar's footprint. However, the maximum SI was over 0.24 on May 29, 2018, under the calm sea condition (see Figure 4-1). Besides, the maximum SI of the mean period estimation was approximately 0.1 in the middle of May 28, 2018, when the sea state was low. But the value of SI under the passage of the monsoon front is still less than 0.06 even though the RMSE of Tm is slightly increased. This indicated that the mean period estimator is more stable than the wave height estimator in terms of bias estimation. The variation of error indexes for wave parameter estimation demonstrated the excellent performance of estimators for mapping wave height and mean period under monsoon conditions.

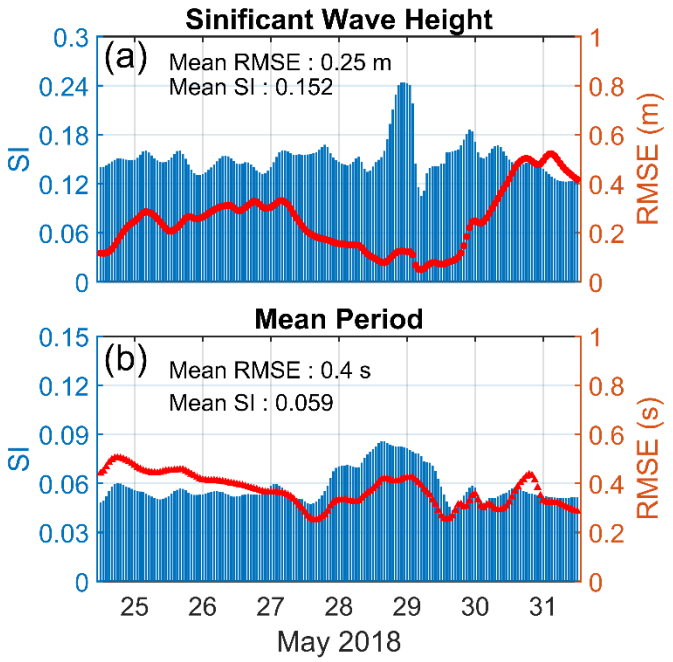

Figure 4-13 Temporal Variation of error indexes for (a) significant wave height and (b) mean period from the constellation of the virtual HF radar network under monsoon conditions. In this figure, the value of RMSE is denoted by red rectangles corresponding to the right axis, while the blue bar corresponding represents SI to the left axis.

Overall, the results in Table 4.1 and Figures 4-11 to 4-13 indicate that the performance of the estimator for mean period retrieval is good, while those for wave height retrieval are under-expected. Therefore, a suitable scaling factor is necessary for improving the efficiency of the wave height estimator. In Figure 4-14, the spatial distribution of the wave height scaling factor is mapped. This figure indicates that the value of the wave height scaling factor varies over space depending on radar bearing, wave direction, and sea-states.

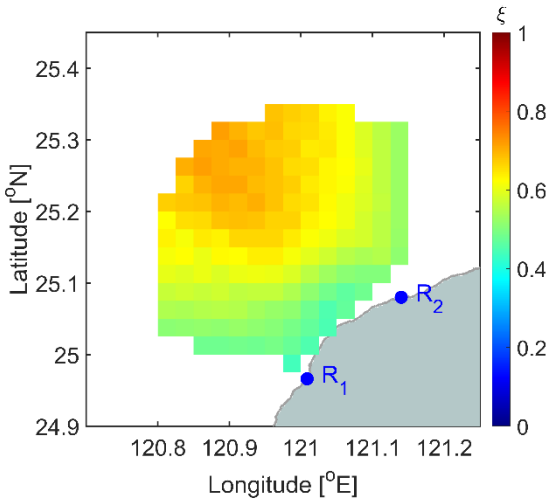

Figure 4-14 The spatial distribution of wave height scaling factor within the footprint of the constellation of the virtual HF radar network.

4.4.3 Wave Parameters Estimations of HF Radar Observationunder Typhoon Conditions

A. The case study of the coastal virtual HF radar network

As typhoon waves feature complicated patterns in the directional wave spectrum, such as the bimodality and azimuthal asymmetry, it is necessary to assess the error indexes of radar-deduced typhoon wave parameters. First of all, the spatial distribution of wave parameters estimated from the Doppler spectra simulation of the virtual HF radar network at the northeast coast of Taiwan island and the modeled value are shown in Figure 4-15. Whereby, two upper panels show the spatial variation of wave height and the mean period from the numerical simulation wave model at 1200UTC on September 28, 2015, while two lower panels are the corresponding maps of estimated wave height and the mean period.

Figures 4-15(a) and (c) show that the estimated Hs are mostly overestimated compared to the targets. But the maps of estimated and given Hs provided the same pattern of the high and low wave fields. This means the overestimation of Hs is only

due to the given input of the scaling factor, which may not be suitable for retrieving typhoon wave height. In addition, during the landfall of Typhoon Dujuan, the limited fetch caused small wave-age and provided the broader distribution of the directional spreading. This may benefit the estimation of significant wave height. For comparing the mean wave period, Figure 4-15(b) indicates that the mean period from the numerical wave model slightly varies over the space when Typhoon Dujuan starts to attack Taiwan's east coast. In contrast, there is a significant difference in the estimated mean period values over radar footprint (see Figure 4-15(d)). This variation is mainly due to the change of the radar-to-wave angle as well as the complexity of the typhoon wave directional spreading. To evaluate the uncertainty of wave height and mean period estimation for this case study, the error indexes are assessed since the period when Typhoon Dujuan starts to influence Taiwan's coast (from September 27-29, 2015) and shown in Figure 4-16 and 4-17. A summation of statistic values is also represented in Table 4-2.

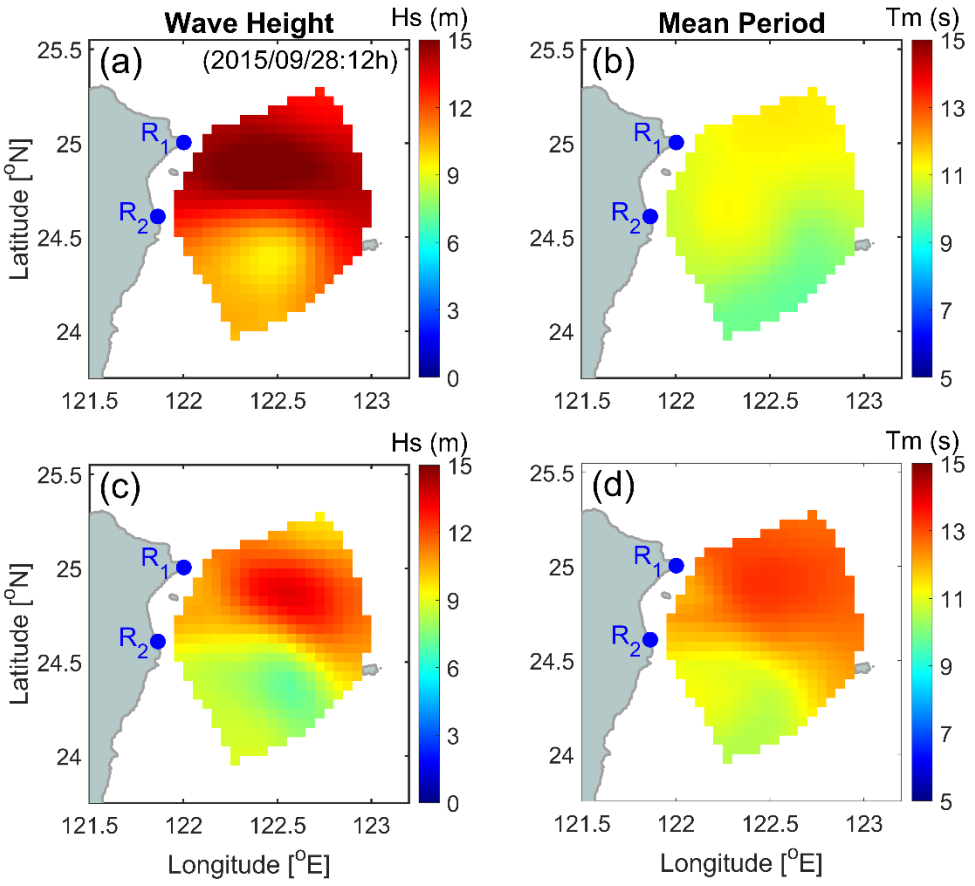

Figure 4-15 The spatial distribution of estimated wave parameters from the constellation of the coastal virtual HF radar network under typhoon conditions and the modeled values. Herein, panels (a) and (b) show the maps of wave height and the mean period from the numerical simulation wave model, respectively, at 1200UTC on September 28, 2015, while panels (c) and (d) are the maps of radar deduced wave height and mean period, respectively.

Firstly, the error indexes of significant wave height estimation are analyzed. Thus, the spatial distributions of RMSE and SI of wave height are described in panels (a) and (c) of Figure 4-16, respectively, while those of Figure 4-17 represent the map of BIAS and correlation coefficient, respectively. Also, the averaged RMSE of Hs is 2.32±0.56 in meters, while the mean SI is 0.170±0.057 (table 4.2). It is seen that the

error-index for Hs can exceed 4.0 m and 0.25 for RMSE and SI, respectively. This implies that the uncertainty of significant wave height estimated from Doppler spectra simulation under typhoon conditions is significant. First, it is because of the unfit wave height scaling factor for typhoon waves. Figure 4-16(a) describes that the RMSE of wave height is small in the region, staying in the middle of two virtual radar stations and increasing in other areas. The radar-to-wave angle may play a key role to the variation of wave height RMSE. The distribution of SI indicates the favorable or difficult area for wave height retrieval. It implies that the wave height scaling factor for typhoon conditions should vary in space. The map of BIAS in Figure 4-17(a) shows the total overestimation of radar-deduced wave height, while, Figure 4-17(c) illustrates the estimator's performance. It is demonstrated based on the comparison of estimation and target values in Figure 4-18. Then, Figure 4-19 represents the wave height scaling factor map for the constellation of the coastal virtual HF radar network under typhoon conditions. However, the scaling factor for the case study in Figure 4-7 is slightly lower than Heron & Heron's scaling factor, which is 0.551.

Secondly, panels (b) and (d) of Figures 4-16 & 4-17 represent the error indexes and correlation coefficient of the mean wave period estimated from the Doppler spectra simulation of the coastal virtual HF radar's constellation under Typhoon Dujuan condition. The averaged RMSE, BIAS, and SI of mean period estimation are 1.54±0.44, -1.43±0.04 in seconds, and 0.050±0.019, respectively. It is obvious the RMSE is mostly smaller than 1.5 seconds except for the north area where typhoon wave direction travels to the north of Taiwan Strait. At that location, the wave direction could be co-line with radar bearing and causing bias of Tm estimation. The maximum RMSE can be 2.5 seconds, while SI is approximately 0.1. The BIAS and correlation coefficient of Tm estimation in the north area (see Figure 4-17) illustrates the disagreement and overestimation of the radar-deduced mean period compared to

target values. The narrowness of the directional spreading may be one of the negative factors that cause the larger error of Tm estimation. In other regions, the uncertainty of Tm estimation can be acceptable.

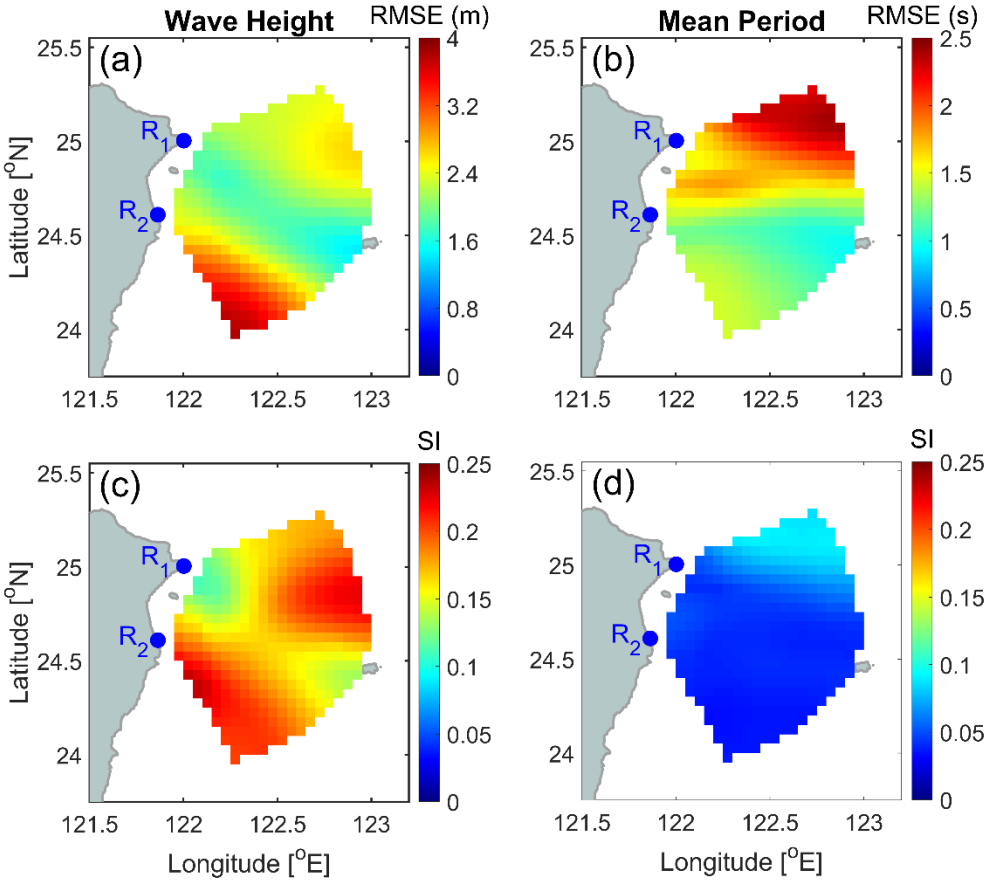

Figure 4-16 The spatial distribution of error indexes (RMSE & SI) of significant wave height and mean period estimations from the constellation of the coastal virtual HF radar network under typhoon conditions. Herein, panels (a) and (c) represent the spatial distribution of RMSE and SI for Hs, respectively, while panels (b) and (d) represent the spatial distribution of RMSE and SI for Tm, respectively.

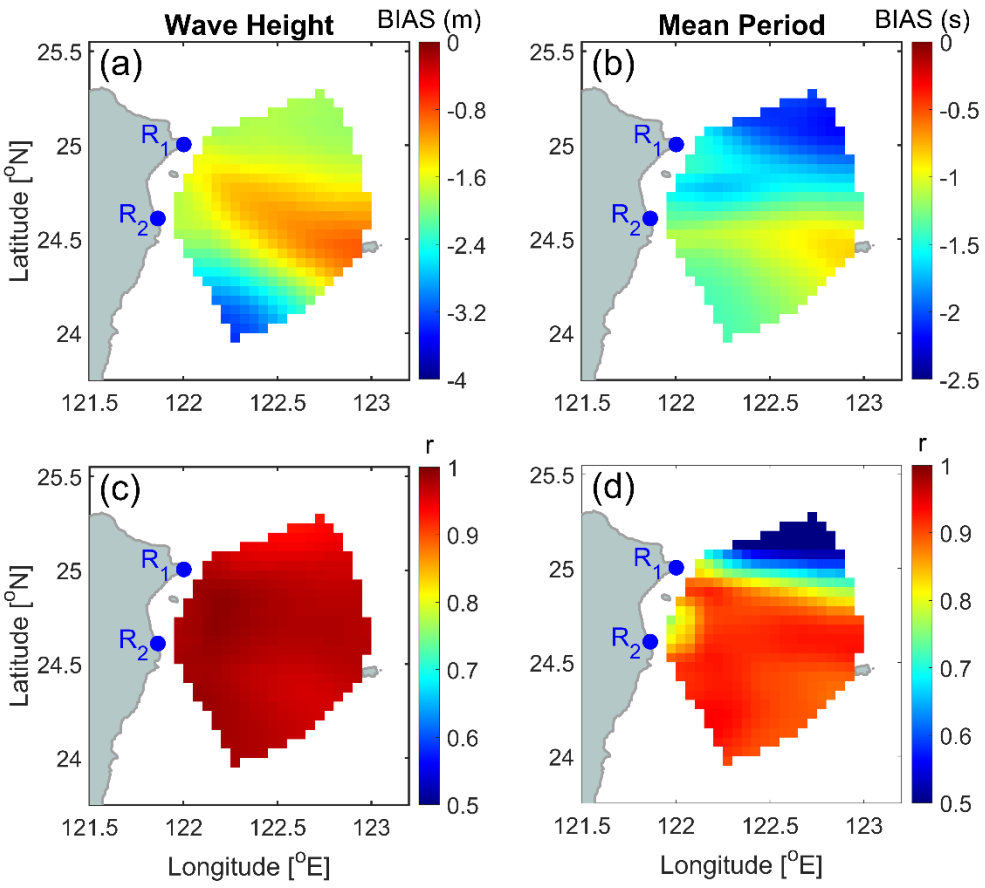

Figure 4-17 The spatial distribution of BIAS and correlation coefficient (r) of significant wave height and mean period estimations from the constellation of the coastal virtual HF radar network under typhoon conditions. Panels (a) and (c) show the distribution map of BIAS and r for Hs, respectively, while the distribution map of two those statistic parameters for Tm are shown on panels (b) and (d), respectively.

Table 4-2 Statistical parameters of wave height and mean period under the wave field condition of Typhoon Dujuan in 2015.

Statistic Parameters	Hs	Tm
r	0.97 ± 0.02	0.83 ± 0.16
RMSE	2.32± 0.56 (m)	1.54 ± 0.44 (sec)
BIAS	-1.70 ± 0.57 (m)	-1.43 ± 0.4 (sec)
SI	0.178 ± 0.031	0.050 ± 0.019
Number of points	18192	

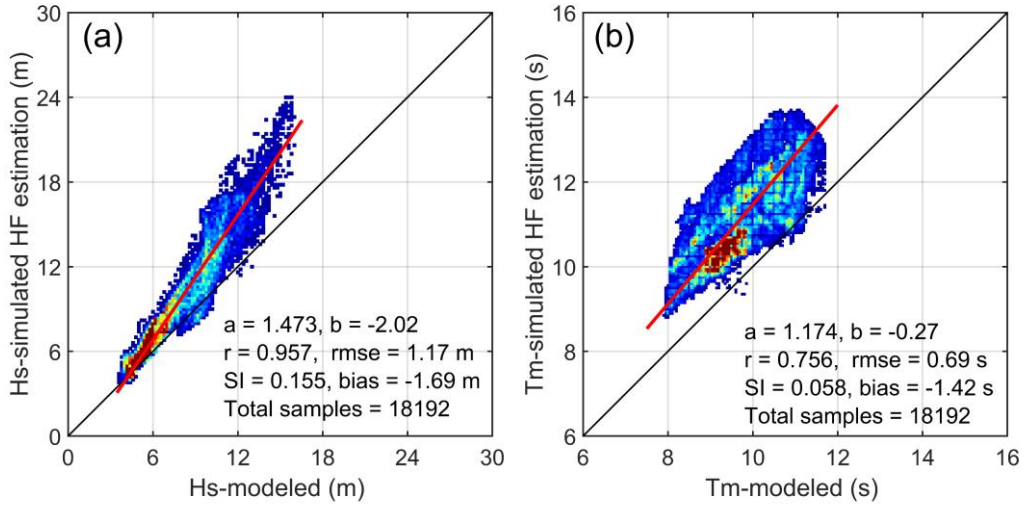

Figure 4-18. The scatter comparisons of (a) significant wave height estimation and (b) mean period estimation from the constellation of the virtual HF radar network and the modeled values under typhoon conditions.

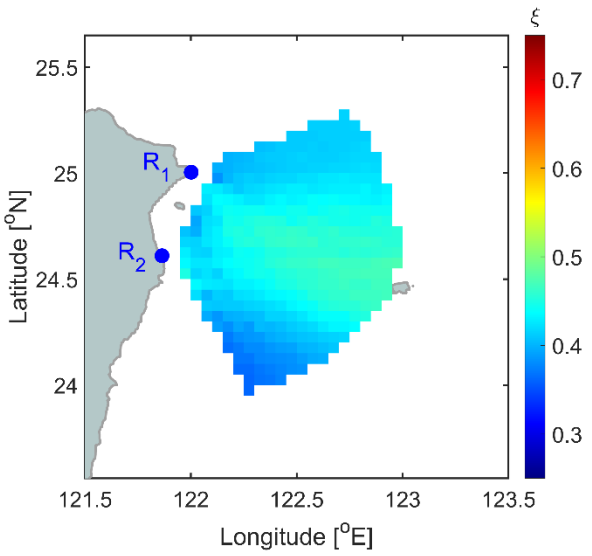

Figure 4-19. The spatial distribution of wave height scaling factor within the footprint of the coastal virtual HF radar network.

In another respect of analyzing the error indexes of wave parameters estimation from the constellation of the coastal virtual HF radar network under typhoon conditions, the temporal variation of Hs and Tm error indexes are shown in Figure 4-20. In that figure, the variation of RMSE is represented by red dots corresponding to the right axis, while the value of SI is shown in blue bars corresponding to the left axis. Figure 4-20 indicates that the averaged uncertainty of mapped wave height using HF radar Doppler spectra simulation is 2.01 m for RMSE and 0.123 for SI, while they are 1.6 sec and 0.064 for RMSE and SI of the radar-deduced mean period. It can see that the RMSE for Hs estimation is less than 2.0 meters when Typhoon Dujuan is in the open ocean, and RMSE and SI significantly increase when the typhoon passage to the shallow water region and attacks Taiwan island at 1200UTC on September 28, 2015. At that period, the maximum value of RMSE can reach approximately 5.0 meters. Furthermore, the value of SI still increases and reaches 0.18 when Typhoon Dujuan moves to the west of Taiwan island. The fact is that the modeled wave heigh reduced while the RMSE of Hs

estimated from radar Doppler spectra simulation is still large. For analyzing the temporal variation of mean period error indexes, SI is smaller than 0.1, and RMSE does not reach over 2.0 seconds even when the typhoon land on Taiwan island. In addition, the value of RMSE and SI are reduced when Typhoon Dujuan passage to shallow water regions. It is because the dominant wave is wind waves instead of swells as in the previous period.

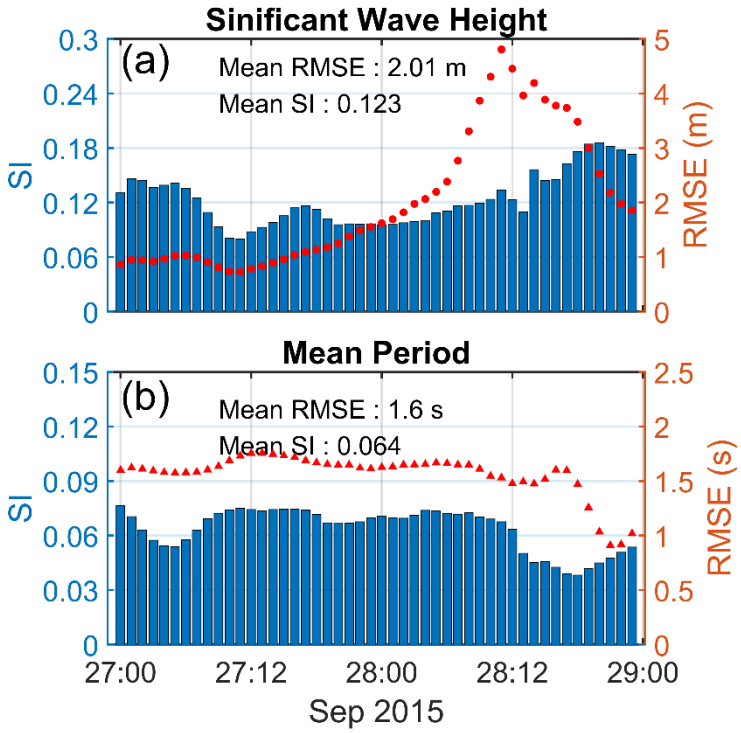

Figure 4-20. Temporal variations of error indexes for (a) significant wave height and (b) mean period estimations from the constellation of the coastal virtual HF radar network under typhoon conditions. The variation of RMSE is represented by red dots with respect to the right axis, while the value of SI is represented in blue bars with respect to the left axis.

It can be concluded that the bias estimation of typhoon wave height causes by unfavorable conditions, including rough sea and the small value of the radar-to-wave angle, while the error of mean period estimation is mainly caused by the directional

spreading width and swells dominant wave field. However, the error indexes of wave parameter estimation still illustrate the performance of the HF radar technique, which can work well for mapping wave fields under typhoon conditions.

Based on the analyzed results, it can be roughly concluded that error indexes of radar-deduced significant wave height and mean period under typhoon conditions are smaller than those in monsoon conditions. Overall, the estimation results have shown the excellent performance of estimators for retrieving wave height and period under both monsoon and typhoon conditions.

B. The case study of the virtual HF radar network at various typhoon quadrants

This section focuses on the effects of the radar station location relative to the typhoon. Based on the test of HF radar networks with the attendant of two or three virtual radar stations, as shown in Figure 4-8, the uncertainty of radar-deduced wave parameters is assessed. Figures 4-21 and 4-22 show the scatter plot between estimated wave parameters and the target values for the twelve constellations of the virtual HF radar network, focusing on eight typhoon quadrants around the eye. The error indexes also are represented in Table 4-3. Herein, panel (a), (b), (c), and (d) of Figure 4-21 represents the scatter plots of wave height comparison corresponding to four constellations of the virtual HF radar network with the attendant of two radar stations staying and focusing the upper-right, lower-right, upper-left, and lower-left quadrants of Typhoon Dujuan, respectively, while panels (e) to (h) show those of Hs comparison corresponding to other four constellations of the virtual HF radar network with the attendant of three radar stations. And four last panels of this figure show the scatter plot of Hs comparison following the four last constellations of the virtual HF radar network with the attendant of two radar stations staying and focusing

on the right, left, front, and rear typhoon quadrants. And a similar sequence for wave period comparison is represented in Figure 4-22.

Regarding Hs estimation errors, the results of radar-deduced wave height are almost overestimated compared to the modeled values. This is caused by the unsuitable input of the scaling factor for typhoon waves. Overall, Hs's scatter indexes, defined as the RMSE normalized to the target value, are 5.6-7.8% for left quadrants, 6.4-10.1% for right quadrants, and 7.0% & 9.1% for front and rear quadrants, respectively. It illustrates that the uncertainties of Hs estimation are reduced for the typhoon case compared to the monsoon case. The comparison results also show that the bias estimation of wave height retrieved from the Doppler spectra simulation at the left quadrants is smaller than those of the right quadrants. The fact is that the directional spreading width in the left-hand quadrants is broader than those in the right-hand quadrants. This evidence implies that the complexities of typhoon wave directional spectra include extreme spatial heterogeneity, multiple peaks, and especially broadened spreading, which might reduce the uncertainty of wave height estimation. In addition, the SI of radar-deduced wave height can also be reduced by approximately 20% by introducing information from additional stations.

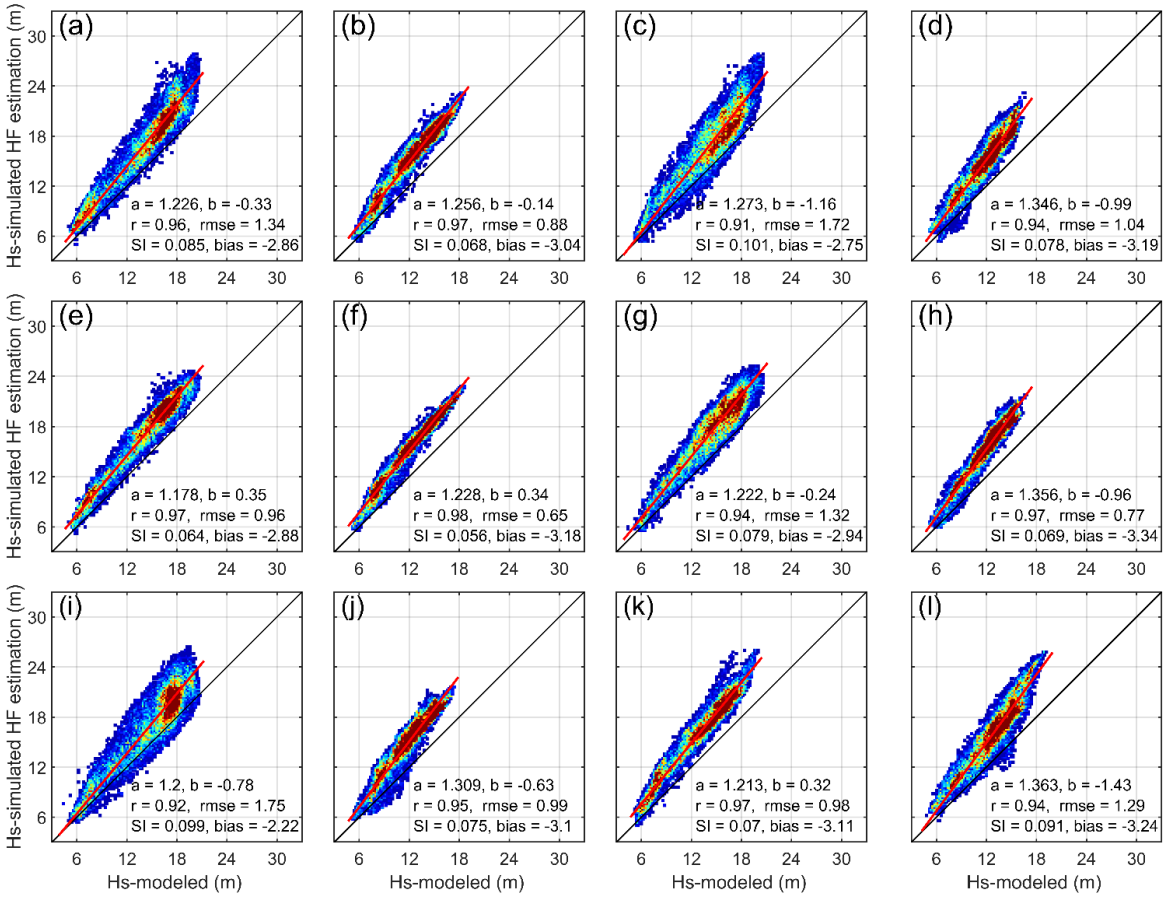

Figure 4-21 The comparisons between wave height estimation of the constellations of the twelve virtual HF radar networks under typhoon conditions and the modeled values. Panels (a) to (d) show scatter plots of wave height comparison corresponding to four constellations of virtual HF radar networks with the attendance of two radar stations looking to the upper-right, lower-right, upper-left, and lower-left quadrants of the typhoon region, while panels (e) to (h) show those of Hs comparison corresponding to other four constellations of the virtual HF radar network with the attendance of three radar stations, and panels (i) to (l) show the scatter plot of Hs comparison following four last constellations of the virtual HF radar network with the attendance of two radar stations looking to the right, left, front and rear quadrants of the Typhoon Dujuan region.

Regarding Tm estimation errors, the radar-deduced mean wave period results are also overestimated compared to the modeled values (Figure 4-22). The scatter indexes of mean period estimation from those above constellations of the virtual HF radar network under typhoon conditions are 3.1-4.1% for left quadrants, 3.2-4.6% for right quadrants, and 4.4% and 3.6% for the front and rear quadrants, respectively. The uncertainty of the radar-deduced mean period retrieved from the virtual radar network moving together with the typhoon center is gradually smaller than those of the mean wave period retrieved from the coastal virtual HF radar network as in Figure 4-8 and those of the monsoon case. The comparison results also indicate that the bias estimation of the mean period at the left and right quadrants are the same. It implies that the influence of the sea-state and the directional spreading width around the typhoon center on the error of mean period estimation has not seemed evident under typhoon conditions. Also, it is found that the SI of mean period estimation is slightly reduced by introducing information from additional stations.

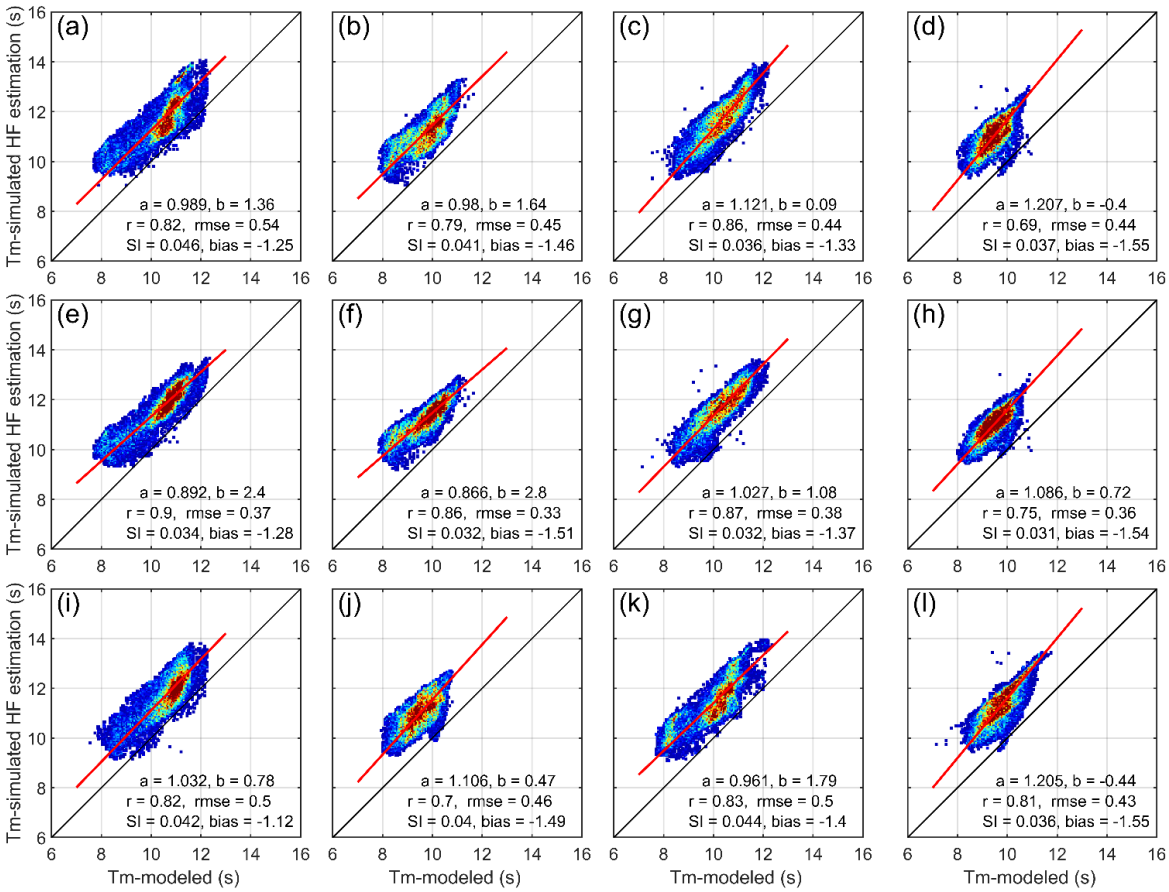

Figure 4-22 The comparisons between the mean period estimation of the constellations of the twelve virtual HF radar networks under typhoon conditions and the modeled values. Panels (a) to (d) show scatter plots of mean period comparison corresponding to four constellations of the virtual HF radar network with the attendance of two radar stations looking to the upper-right, lower-right, upper-left, and lower-left quadrants of the typhoon region, while panels (e) to (h) show those of Tm comparison corresponding to other four constellations of the virtual HF radar network with the attendance of three radar stations, and panels (i) to (l) show the scatter plot of Tm comparison following four last constellations of the virtual HF radar network with the attendance of two radar stations looking to the right, left, front and rear quadrants of the Typhoon Dujuan region.

Table 4-3 Statistical parameters of the comparison between wave parameters estimation of the twelve constellations of the virtual HF radar network under typhoon conditions and the modeled values.

Wave Parameters		Case 1	Case 2	Case 3	Case 4	Case 5	Case 6	Case 7	Case 8	Case 9	Case 10	Case 11	Case 12
Hs	r	0.96	0.97	0.91	0.94	0.97	0.98	0.94	0.97	0.92	0.95	0.97	0.94
	RMSE	1.34	0.88	1.72	1.04	0.96	0.65	1.32	0.77	1.75	0.99	0.98	1.29
	BIAS	-2.86	-3.04	-2.75	-3.19	-2.88	-3.18	-2.94	-3.34	-2.22	-3.10	-3.11	-3.24
	SI	0.085	0.068	0.101	0.078	0.064	0.056	0.079	0.069	0.099	0.075	0.070	0.091
Tm	r	0.82	0.79	0.86	0.69	0.90	0.86	0.87	0.75	0.82	0.70	0.83	0.81
	RMSE	0.54	0.45	0.44	0.44	0.37	0.33	0.38	0.36	0.50	0.46	0.50	0.43
	BIAS	-1.25	-1.46	-1.33	-1.55	-1.28	-1.51	-1.37	-1.54	-1.12	-1.49	-1.40	-1.55
	SI	0.046	0.041	0.036	0.037	0.034	0.032	0.032	0.031	0.042	0.040	0.044	0.036
Number of points		16648	16872	16647	16882	16648	16872	16647	16882	16683	16853	16722	16706
Focusing region		*Upper Right*	*Upper Left*	*Lower Right*	*Lower Left*	*Upper Right*	*Upper Left*	*Lower Right*	*Lower Left*	*Right side*	*Left side*	*Front side*	*Rear side*
Number of virtual radar site		2	2	2	2	3	3	3	3	2	2	2	2

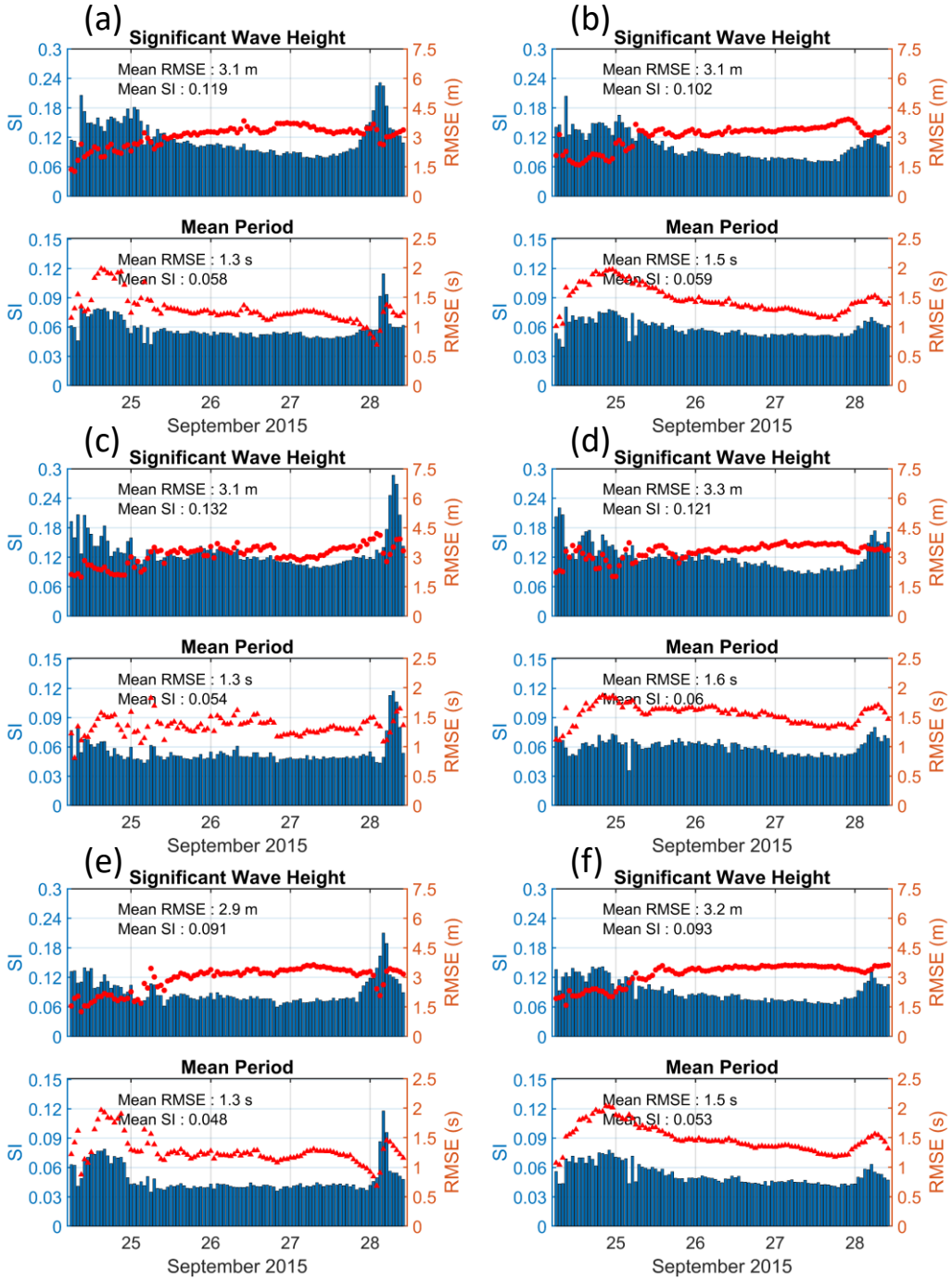

Figure 4-23 Temporal variations of error indexes of significant wave height and mean period estimations from the twelve virtual HF radar networks are shown in Figure 4-8. The temporal variation of RMSE is represented by red dots concerning the right axis, while those of SI are shown in blue bars with respect to the left axis.

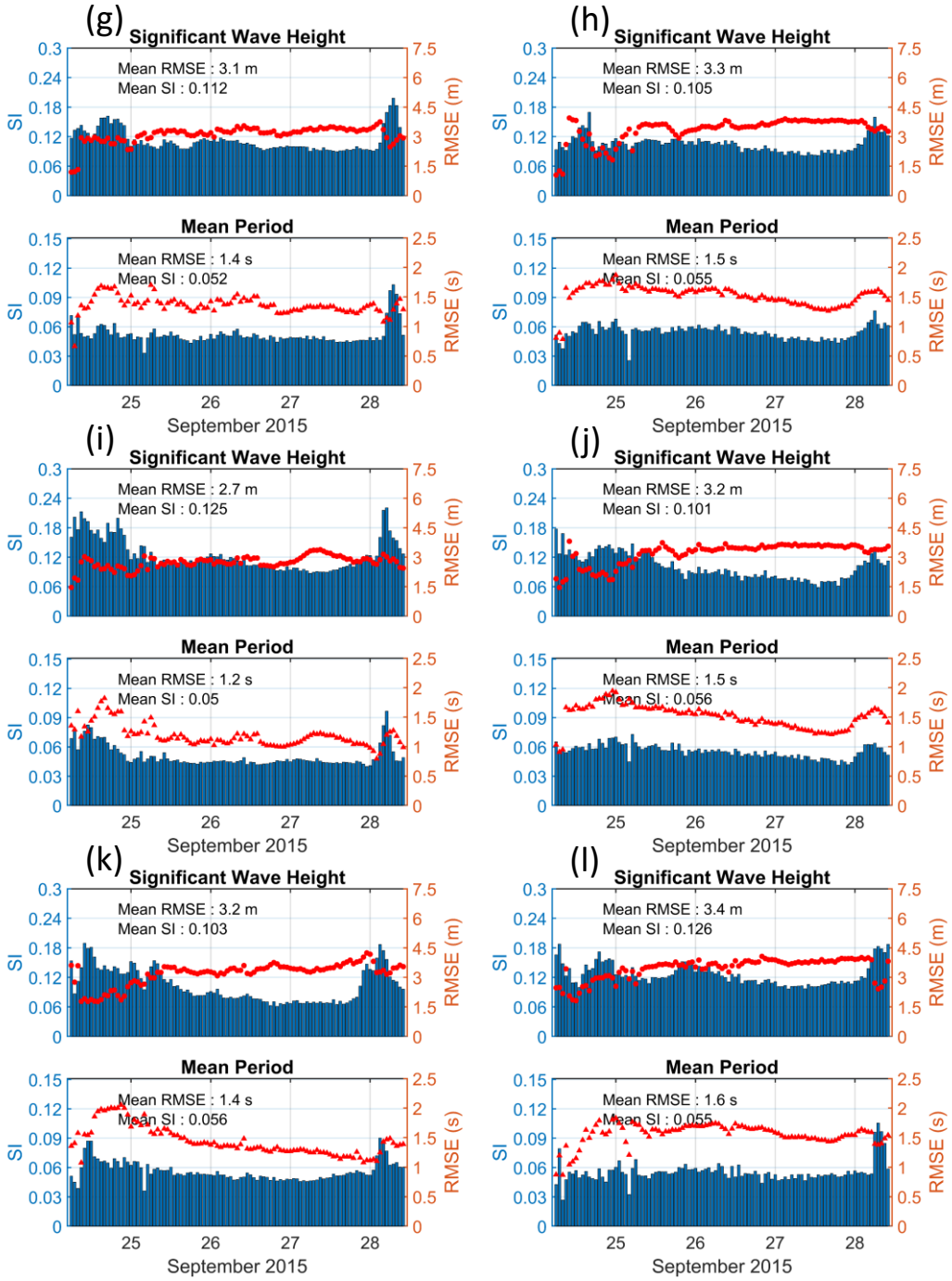

Figure 4-23 Continued.

As one of the respects for data analyses, Figure 4-23 represents the temporal variation of error indexes of wave parameters estimation from the twelve constellations of the virtual HF radar network under typhoon conditions. The

sequence of error index results in Figure 4-23 corresponds to the sequence of twelve virtual HF radar networks in Figure 4-8. In each panel of Figure 4-23, the temporal variation of RMSE is represented by red dots with respect to the right axis, while those of SI are shown in blue bars concerning the left axis. The variations of SI show that the uncertainty of wave parameters estimation is normal when the typhoon is on the open ocean and increases when the typhoon passage the shallow water region. While the bias estimation of both Hs and Tm in the right quadrants is slightly greater than those in the left quadrants, their differences become significant when Typhoon Dujuan attacks Taiwan island. It implies that the shallow water regions may be one of the negative factors that caused the higher uncertainty of wave parameters estimation under typhoon conditions.

Overall, the uncertainty of typhoon wave parameters estimated from the Doppler spectra simulation is compared with those of wave parameters estimation under monsoon conditions. Based on the comparison results, it could be concluded that the error indexes of wave height and mean period under typhoon conditions are smaller than those in monsoon conditions. Finally, the estimation results of wave parameters illustrated the performance of estimators for retrieving wavefield information under various conditions.

4.5 Summary

In this chapter, estimators were implemented based on Barrick's analytical method [14, 57] for retrieving wave height and mean period from the HF radar Doppler spectra simulation. Then, those estimators were applied under two wave field conditions: monsoon waves and typhoon waves. Overall, the estimated wave parameters agree well with the target values without depending on the wavefield condition and radar operating frequency.

In order to assess the uncertainty of wave parameters estimated from the HF radar sea-echo under monsoon and typhoon conditions, two types of HF radar networks consisting of at least two radar stations were implemented. The result indicated that the heterogeneity and rapid changes in the spatial distribution of the wavefield under the influence of high wind speeds might be an advantage for HF radar wave monitoring. In particular, the broadened directional spreading in typhoon cases benefits the second-and first-order backscattering ratio compared with those of monsoon cases.

This chapter assessed the uncertainty of wave parameters estimated from HF radar sea-echo under monsoon and typhoon conditions based on the self-developed E2ES toolbox and numerical testbeds. The comparison results indicated less bias of wave height and mean period estimations under typhoon conditions, which is the broadened Bragg wave spreading widths, compared with those in monsoon conditions. It indicated that the directional spreading parameter of ocean surface waves is a special factor affecting the results of wave parameter estimation. Furthermore, the bias estimation of wave parameters can be reduced by introducing information from additional stations. In terms of improving the uncertainty of radar-deduced wave parameters as well as retrieving the directional wave spectrum from HF radar Doppler spectral under various conditions, the theoretical method, such as a Bayesian method, is suggested to be implemented and tested in future studies.

CHAPTER V DETERMINATION AND VALIDATION OF WAVE PARAMETERS ESTIMATED BY A SINGLE HF RADAR SYSTEM

5.1 Introduction

Over five decades of development, the HF radar technique has achieved many remarkable signs of progress. At present, hundreds of HF & VHF coastal radar stations have been installed worldwide and are operated to monitor the variability of sea surface layers in the coastal region [1]. Accordingly, a new type of HF radar system, consisting of linear phased-array receiver antenna elements, has been developed to retrieve ocean wave information since the 1990s. At present, there are the two most popular phased-array systems, which are the Wellen Radar (WERA) system developed by the University of Hamburg [86] and the compact HF Doppler radio scatterometer system that the University of Hawaii has built since 2008 [87]. In Taiwan, there are now a total of 25 HF radar systems were installed and in operating mode. In which, 20 HF stations are operated by Taiwan Ocean Radar Observing System (TOROS), a research center in Taiwan Ocean Research Institute; the Naval Academy manages two stations, and three phased-array systems were deployed by the Harbor and Marine Technology Center. However, two WERA systems were broken several years ago. Also, most of those systems are mainly used for mapping ocean surface currents. Only a phased-array HF radar (LERA MK-III) system consists of 16 receiver antenna elements installed at the northern Taichung harbor in late November 2018 in the operational mode for wave monitoring. Therefore, wave monitoring using the HF radar technique is still limited; even Taiwan island is one of the most frequently attacked by severe typhoons worldwide. In terms of launching the new project, more than 20 HF and VHF radar stations are ongoing to install along the coastline of Taiwan island at the end of 2022. However, to practice with the HF radar data for wave processing, only the data of the HF radar

system near the Taichung harbor is used in this study. Thus, the HF radar system at the HTCN station operated at 27.75 MHz central frequency and 300 kHz bandwidth and was set up to obtain sea echoes within 40 km from the coastline with 500 m spatial resolution. After two years, the system performed very well and is still in operational mode. Besides, the second HF radar station, located in the south of Taichung harbor, was installed in September 2021, and is still in testing mode. In the schedule, two those HF radar stations are used to monitor the wavefield outside Taichung harbor and aim to provide early warning of extreme weather phenomena such as freak waves, large swells, etc. However, due to various reasons, only the radar backscattered data of the HTCN station is used in this study. Therefore, processing and validation of wave parameters deduced from the sea-echo data of a single HF radar station still need to be taken care of.

In order to retrieve the information on ocean surface waves from HF radar Doppler spectra, numerous theoretical and empirical methods have been developed (review in Chapter 1). Although the theoretical approaches provide adequate wave information with high accuracy, the condition of a dual-radar system, the high signal-noise ratio (SNR) of the second-order spectrum, and powerful computers are required. However, only one radar station might be installed for some reasons, such as the limitation of space for the radar installation, within the period of radar testing, the delay in disbursement of funds, etc. Therefore, there are many challenges in implementing theoretical methods for retrieving the directional wave spectrum and wave parameters. It means that empirical methods, which are robust in computation and less requirement of Doppler spectrum SNR, can be applied to process the D-R spectrum data of a single radar system. As known, Barrick's empirical formulas are the most common in various empirical methods for estimating wave parameters without wave spectrum and empirical constants. However, this method was simplified by adding given assumptions or ignoring minor factors, such as adding

the weighting function computed from averaging the coupling coefficients over direction [14]. It is also possible that the effect of radar-to-wave angle was abandoned. Consequently, the time-series estimated results still agree well with in-situ measurement in terms of the correlation coefficient, but the distribution of wavefield maybe not be reliable; see Figure 3 in [70]. The high instabilities of wavefield maps can significantly influence the accuracy of rouge wave identification. They also increase the uncertainty of early warning systems if the estimated results are used. Therefore, calibrating wave parameters deduced from a single radar station is necessary.

The calibration is implemented based on the location consisting of both radar and in-situ measurements. Typically, the linear relationship model is used to calibrate wave parameters in the area where the in-situ data is available. Also, some other approaches were proposed using wave direction [88], the power-law [14], or frequency spectrum connection coefficients [64, 89]. However, while the experimental data in Barrick's report is limited, a dual radar system is essential for Gurgel's approach, and the empirical parameters are changed depending on location. Moreover, the factors related to wave height [70, 90] and wave direction [91] were not taken into account while making the empirical constant of correction coefficients. The fact is that empirical constants can apply effectively to single points, but it exists uncertainty for mapping the surface wavefield. Besides, the limitation of in-situ data in the space domain also affects the accuracy of calibrated wavefield mapping. Therefore, it is necessary to assess and propose an efficient method for calibrating wave parameters estimated from the spectra data of a single HF radar system.

This chapter presents the procedure of wave processing from the backscattered data of a linear phased-array HF radar system. Here, a new approach is first implemented to separate Doppler spectrum components for wave inversion. Then, the empirical methods are applied to estimate wave parameters and the non-

directional wave spectrum. Next, the estimated wave parameters are compared to in-situ wave data recorded by an Acoustic Wave and Current profiler (AWAC). After that, correction methods for calibrating radar-deduced wave parameters are introduced and implemented. Finally, the calibration results are compared to in-situ wave data again to assess the performance of those correction methods. The comparison result could help to find out a better correction method that satisfies the condition of a single radar station, variable current and waves, and limited in-situ data with a minimum of bias estimation.

5.2 The Radar system and Data collection

In late November 2018, a linear phased-array HF radar system consisting of 16 receiver elements, working at 27.75 MHz and 300 kHz bandwidth, was installed northern of Taichung harbor (24^{o} 18.591'N, 120^{o} 31.389'E), named HTCN. The system has been used for long-term monitoring of sea-state evolution in the middle of the Taiwan Strait for navigation purposes outside the Taichung harbor. The location of this HF radar system is shown in Figure 5-1(a). The HTCN station was installed on the western coast of Taiwan, 2.5 km north of the Taichung harbor entrance. Nearby, an Acoustic Wave and Current profiler (AWAC) for measuring in-situ current and wave data was deployed (the black triangle). This radar system uses a 2×2 antenna array arranged in a rectangle shape with edges of a half and a quarter wavelength of the radio transmitted wave (Figure 5-1(b)). The transmitted signal is set up in the mode of frequency-modulated continuous-wave (FMCW). For the receiving system, 16 active antennas were arranged in a linear phased array with a distance adjacent antenna of 4 m (Figure 5-1(c)). Based on the beamforming algorithm, ocean surface current, waves, winds, and swells can be obtained from the HF radar Doppler-Range spectrum data with the range and bearing resolutions of 0.5

km and 10°, respectively. The radar products are currently archived every 30 minutes. Further, the parameters of this radar system can be found in Table 5-1.

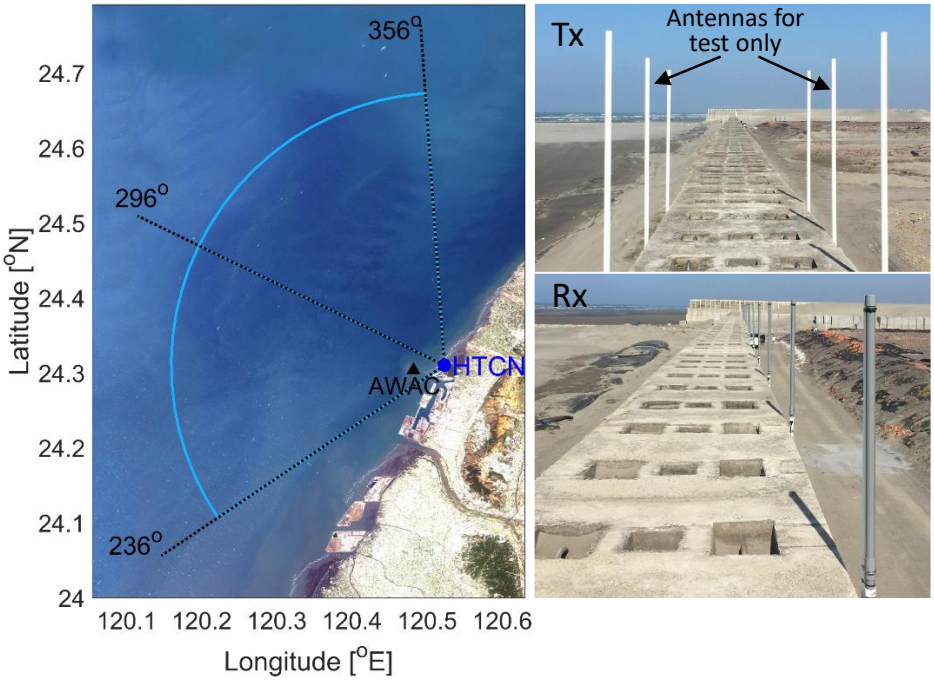

Figure 5-1 This figure shows the HF Radar system used in the present study. In the left panel, the blue dot shows the installation location of the radar station, on the western coast of Taiwan, 2.5 km north of the Taichung harbor entrance. The black triangle indicates the location of AWAC, from which the in-situ data are used for comparison. The azimuth of the boresight beam of the Rx antenna array is 296o. The upper right panel shows the transmitting antennas, and the lower right panel shows the 16 receiving antennas.

Table 5-1 The configuration setting of the HTCN station.

Manufacturer	The Radio Oceanography Laboratory, UH	Number of receiver antenna elements	16
Type	MK-III	Temporal resolution (minutes)	30
Transmit power (Watts)	10	Total samples	8192
Transmit frequency (MHz)	27.75	Range resolution (km)	0.5
Bandwidth (KHz)	300	Maximum range (km)	40
Number of transmitter antenna elements	4	Nominal bearing resolution (degree)	10
Transmitted waves	FMCW chirps	Bearing angle (degree)	296 ± 60
Chirp-length (sec)	0.21666	The technique of azimuthal resolution	Beamforming algorithm
Transmit sweep rate (Hz)	4.6	Complicating issues: variable current and waves, intense background noise.	

5.3 Extraction of Doppler-Range spectrum

5.3.1 Methods of Direction of Arrival

Typically, the time series backscattered sea-echo is the HF radar system's output, called the level 0 product. For the HF radar system near Taichung harbor, the raw data is acquired and saved into I and Q channels with the chirp length of 0.21666 sec for each sample, meaning more than 8192 samples were recorded within 30 minutes (Table 5-1). Meanwhile, surface current radial velocity, wave, and wind information are estimated from the first- and second-order Doppler spectra components [14, 92]. Therefore, the I and Q data need to transfer to the Doppler-Range (D-R) spectrum, which presents the radar echo intensity distribution over the domain of range and Doppler frequency, and called the level 1 product.

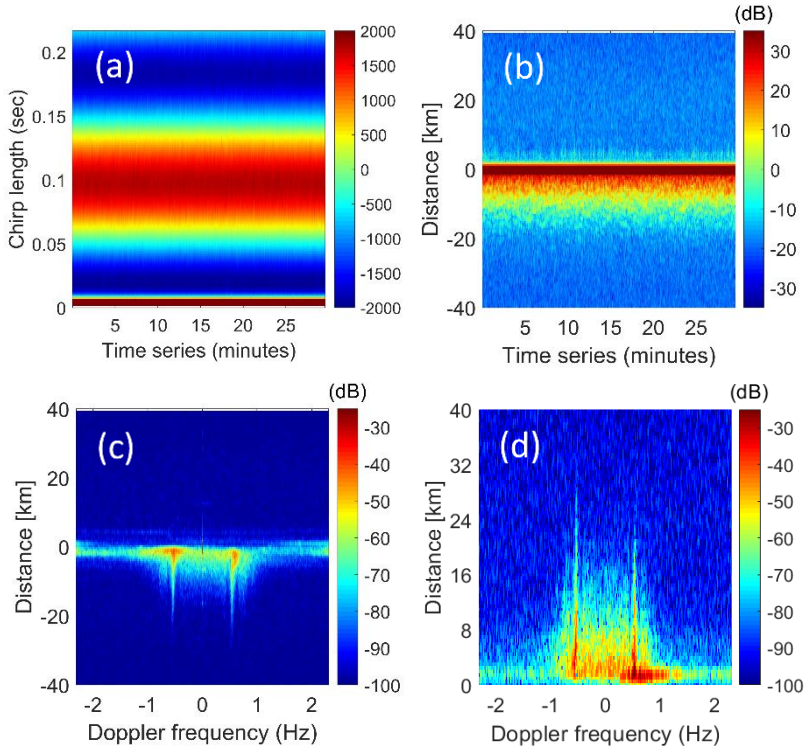

Figure 5-2 An example of the staged intermediate products at different levels in the step of time-series to Doppler spectra transformation. In this figure, panel (a) is the temporal sequence of the original chirp signal intensity of the I channel for one observation lasting for 29 mins and 40 sec with for one selected antenna, panel (b) is the result after applying FFT and Blackman-Harris window to each chirp signal, (c) is the Doppler-Range spectrum for the selected antenna after the second FFT and Blackman-Harris window over the observation time of (b), and (d) is the Doppler-Range spectrum with respect to an azimuthal direction after beamforming and Hamming window over the signal from 16 Rx antennas.

Generally, the Fast Fourier Transform (FFT) and the Direction of Arrival techniques are implemented to extract the D-R spectra in different azimuthal directions. This process includes three steps: firstly, the 1st FFT is used to transfer the IQ data over radar chirp-length to the first spectra data in the range domain. Next,

the 2nd FFT is used to convert the 1st FFT spectra data over the time series to the new spectra in the Doppler frequency domain. Then, the spectra power at the RFI and SORT parts was obtained. Here, RFI means radio frequency interference representing the system noise, while the received sea-echo signals are described in the SORT part, which corresponds to the spectra at range cells in the negative distance of panel (c) of Figure 5-2. Finally, the suitable side of the Doppler-Range spectrum, which shows the reasonable echo signal from the sea, is selected to represent the backscattered sea-echo signal received by an element of receiver antennas. The flowchart of this processing is represented in Figure 5-2.

In fact, to estimate the DOA of the backscattered signal of HF radar sea-echo, amount of methods were developed, such as the least square method [93], direction-finding methods [94, 95], and beamformer methods [96-100]. Regarding spatial scanning, Multiple Signal Classification (MUSIC) is often applied to determine the azimuthal direction of the backscattered signal from the CODAR system [94, 95, 101]. The advantage that the cross-loop monopole system doesn't need large land space for installation is favorable for many agencies.

On the other hand, the DOA of signals from sea-echo data of the linear phased-array system is estimated by using the conventional beamforming algorithm (or called the Ballet beamformer method) [102], the directionally constrained minimum power (DCMP) (or called the capon method) [96, 99, 100], and the norm-constrained DCMP (NC-DCMP) algorithm [103]. Later, those algorithms will be represented in this section.

A. The Bartlett beamformer algorithm

For an HF radar phased array system consisting of M receiver antenna elements spaced linearly with a constant distance, the spatial spectrum is formed using the output values obtained by orienting the antenna array in all directions.

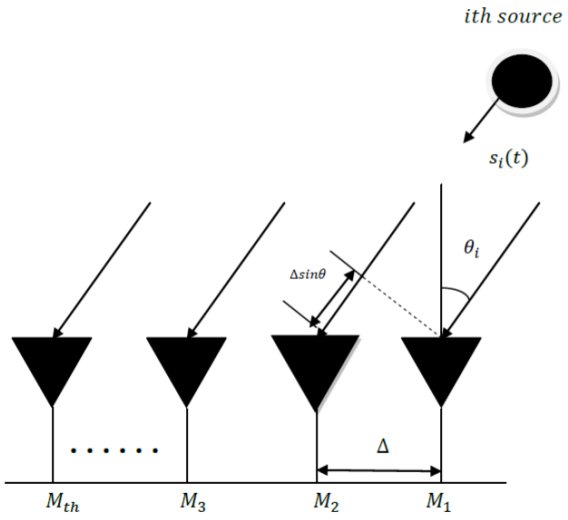

Figure 5-3 System model for DOA estimation using a uniform linear array of M elements [98].

In which, Δ is the distance between each antenna, and is restricted to a half wavelength of received signals, θ_i represent the coming direction of the source i. Then, the incident signal travels at a speed of c over a distance D and reaches the first rightmost elements (Figure 5-3). If we assume that all the signals generated by all the d sources, $Si(t)$, $1 \leq i \leq d$, the total signal and noises received by the M[th] element at time t can be expressed as [98]:

$$x_m(t) = S_i(t) \sum_{i=1}^{d} e^{j(M-1)\mu_i} + n_M(t), for\ M = 1 \quad (5.1)$$

Equation (4) can be written in the form as:

$$x = \boldsymbol{A}S(t) + n(t) \quad (5.2)$$

In which, x is the total signal, S is the data column vector received by M antenna elements, n is the noise of those antennas, and $\boldsymbol{A}$ is the steering matrix, including the steering vector of the antenna array response to a specific direction. The idea is to steer the array in a given direction during a period and measure the output power. The steering direction coincides with the DOA of backscattered

signals providing a maximum output power that yields the DOA estimates. In this case, an HF radar phased array system can be treated as an array electronically. Then, a weight vector, w, can be designed and applied to linearly combine the data received by the receiver antenna elements to form a single output signal $Y(t)$,

$$Y(t) = \sum_{i=1}^{M} w_i^* x_i(t) = w^+ X(t) \tag{5.3}$$

The total averaged output power of the phase array system over K snapshots can be expressed as:

$$P(w) = \frac{1}{K}\sum_{k=1}^{K} |Y(t_k)|^2 = \frac{1}{K}\sum_{k=1}^{K} w^H X(t_k) X(t_k)^H w \tag{5.4}$$

or $$P(w) = w^H R_{xx} w$$

In which, w_i is the weight at the i^{th} source, * shows the complex conjugate, H represents the conjugate transpose of the vectors, and R is the covariance matrix of the input signal. The value of w_i can vary under applying different beamforming algorithms.

For the conventional (Bartlett or Delay & Sum) beamformer method, the steering vector, $A(\theta)$ with a scanning angle θ is chosen as the weight vector.

$$w = A(\theta) \tag{5.5}$$

Replacing (5.5) to (5.4), the output power of spectra is considered as the function of DOA, and given as follows:

$$P(\theta)_{BA} = A(\theta) R_{xx} A(\theta)^H \tag{5.6}$$

Then, the direction that produces the most significant output power is the estimation of the desired signal's direction [97, 98, 100].

B. The Capon beamformer algorithm

The Capon beamformer method, also called Minimum Variance Distortionless Response (MVDR) method, was proposed to overcome the poor resolution problems

associated with the conventional method [96, 98]. In this method, the array weights vector can be obtained by minimizing the mean output power with the constraint gain for the input signals from the specific direction. The optimized weight vector is given as [96]:

$$w = \frac{{R_{xx}}^{-1} A(\theta)}{A(\theta) {R_{xx}}^{-1} A(\theta)^H} \tag{5.7}$$

Replacing (5.7) to (5.4), the output power of spectra is expressed as:

$$P(\theta)_{CA} = \frac{1}{A(\theta) {R_{xx}}^{-1} A(\theta)^H} \tag{5.8}$$

The angle, θ, in the spectrum corresponding to the peak value gives the accurate DOA estimation.

C. The NC-DCMP algorithm

To improve the robustness of the Capon beamformer, the diagonal-loading technique with a norm-constrained condition has been developed [103-105], and given as follows:

$$\mathbf{w} = \frac{(\mathbf{R} + \sigma \mathbf{I})^{-1} \mathbf{e}}{\mathbf{e}^H (\mathbf{R} + \sigma \mathbf{I})^{-1} \mathbf{e}} N \tag{5.9}$$

$$|\mathbf{w}^H \mathbf{w}| \leq \delta N \tag{5.10}$$

Where, σ is the diagonal-loading value, $\mathbf{I}$ is the identity matrix, and δ is the norm constraint parameter. Given a proper number of δ and by increasing the value of σ progressively in (5.9) until the vector $\mathbf{w}$ satisfies the constraint (5.10), then the vector $\mathbf{w}$ at this moment is a suitable steering vector, denoted $\mathbf{w}_{\mathrm{NC}}$, for computation of the brightness with following modified expression:

$$B(\mathbf{k}) = \mathbf{w}_{\mathrm{NC}}^H (\mathbf{R} + \sigma \mathbf{I}) \mathbf{w}_{\mathrm{NC}}. \tag{5.11}$$

A larger δ value makes the condition (5.10) satisfied more quickly and results in a better angular resolution, which is beneficial for ship detection and tracking.

However, the brightness in (5.11) decreases with increasing δ value, and the roll-off rate may depend on the direction of **k** [46]. That paper also discussed the issue of δ and presented a way to reduce the time-consuming calculation. The report suggested that a larger Δσ value takes less time to complete the calculation. Also, the brightness and computation are almost constant when the δ value is larger than 10. Suitable values of δ and Δσ for practical operation of NC-DCMP beamformers and the performances of the three beamformers will be examined in more detail in the results of D-R spectrum extraction.

5.3.2 Results of The Doppler-Range spectrum

It is implementing three DOA methods for the extraction of the D-R spectrum from HF radar backscattered signal. The results are shown in Figures 5-4 to 5-6. It can see that the D-R spectrum extracted from the three above beamformer algorithms are almost the same. Thus, it demonstrated that the conventional beamforming algorithms are good enough in terms of accuracy for extracting Doppler spectra of sea-echo from the time-series data.

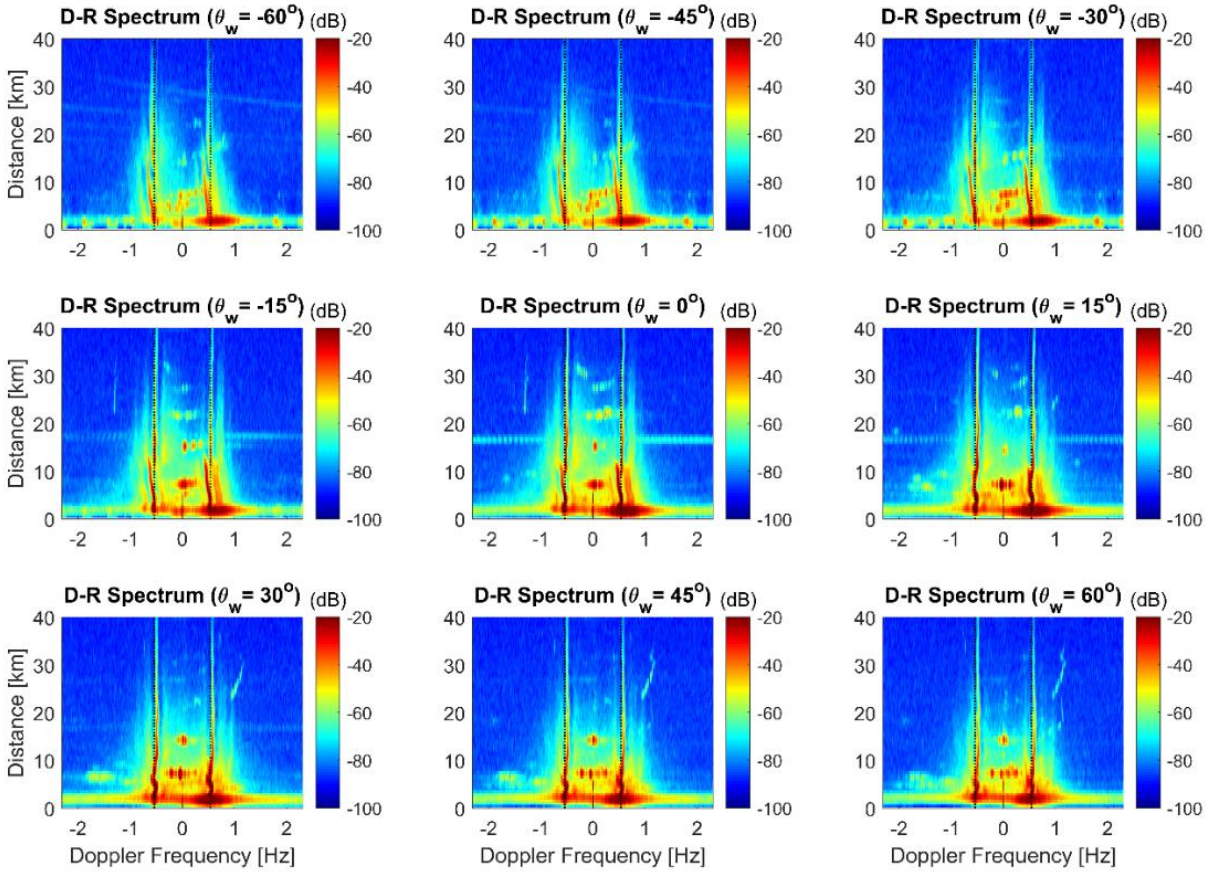

Figure 5-4 The Doppler-Range spectra are extracted from the backscattered data of the HTCN station using the conventional beamforming method.

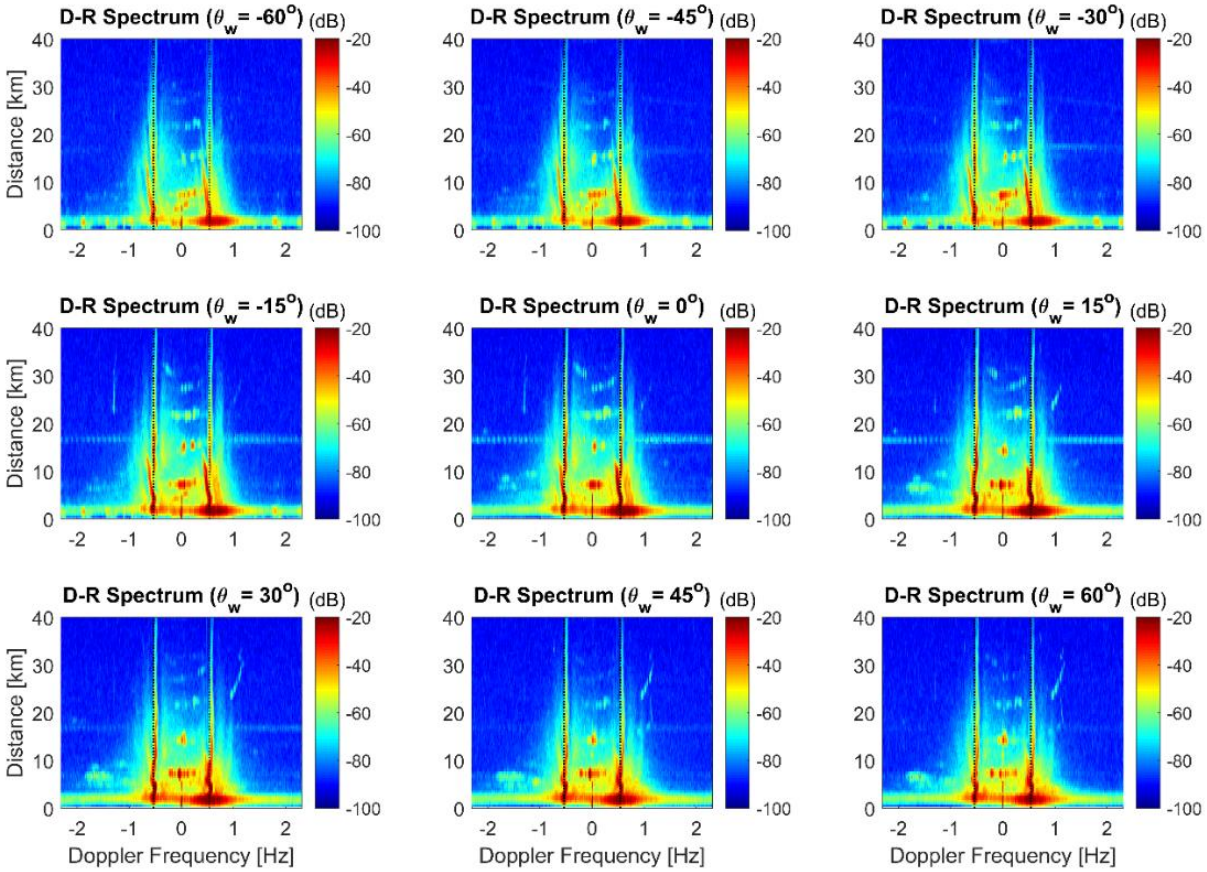

Figure 5-5 The Doppler-Range spectra are extracted from the backscattered data of the HTCN station using the Capon method.

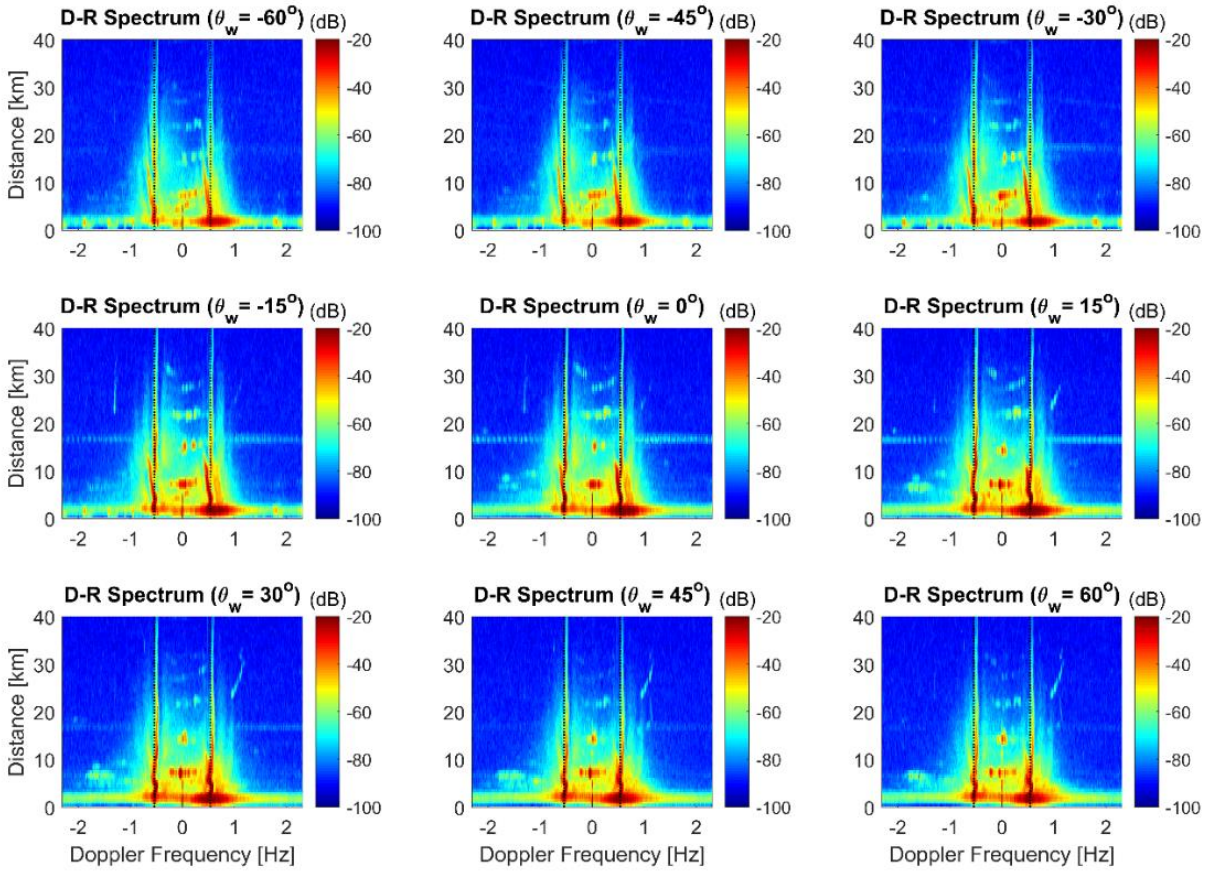

Figure 5-6 The Doppler-Range spectra are extracted from the backscattered data of the HTCN station using the NC-DCMP method.

5.4 Wave Parameter Estimation

5.4.1 Methods

The methods of significant wave height and mean wave period retrieval were represented in section **3.2**. This section introduces the method of determining peak wave period and frequency spectrum from HF radar Doppler spectrum.

A. Peak wave period

In the present study, Young's [106] formulation for estimation of T_p from wave spectrum is adopted. Combining the initial idea of Hasselmann [4], the peak

wave period nondirectional spectrum can be estimated from one of the weighted second-order sidebands and given as follows:

$$T_{p_{(m)}} = \xi_{Tp} \frac{\int_{0,\omega_B}^{\omega_B,\infty} {\sigma_{w(m)}^{(2)}}^{n}(\omega)d\omega}{\int_{0,\omega_B}^{\omega_B,\infty} |\omega - \omega_B| {\sigma_{w(m)}^{(2)}}^{n}(\omega)d\omega} \quad (5.12)$$

where, $\sigma_{w(m)}^{(2)}$ is the weighted second-order spectrum by dividing the weighting function at the sideband m^{th} with m = 1, 2, 3, and 4, n is the weighting exponent and suggested to be 5 [107], ξ_{Tp} is called as the correction factor of peak wave period. The Doppler frequency range of the second-order spectrum for peak period computation is the same as those for mean period estimation. Also, the inversion computation was carried out using only the Doppler spectrum's dominant side unless two Bragg peaks differ by less than 3 dB [64]. Otherwise, an average of both sides is used.

B. Wave spectrum

To obtain wave frequency spectrum from the Doppler spectra data of a single HF radar system, various approaches, including the theoretical method [27] and empirical approaches [64, 89], were proposed. Howell and Walsh [27] applied the Fourier series method to retrieve the power wave spectrum. Grugel et al. [89] used unweighted normalized 2nd-order sidebands from the Doppler spectrum and divided them by the in-situ wave spectrum to determine the transfer function for a specific radar frequency at 27.65 MHz. The authors suggested that the transfer function could be applied to any other radar frequency just by multiplying a factor, which is the square of the ratio between the 27.65 MHz to the given radar frequency. Alattabi et al. [64], on the other hand, considered the weighting function essential and included the weighting calculation before estimating the transfer function. In this study, we use weighted 2nd-order sidebands to retrieve the wave power spectrum.

From (3.1) in Chapter 3, the significant wave height for the deep-water condition can be given:

$$\mathrm{H}_s \simeq 4.004\mathrm{h}_{rms} = 4.004\sqrt{\frac{2}{{k_0}^2}\frac{\int_{-\infty}^{\infty}\sigma^{(2)}(\omega)/w(\eta)d\omega}{\int_{-\infty}^{\infty}\sigma^{(1)}(\omega)d\omega}} \tag{5.13}$$

Therefore,

$$\int_0^{\infty} S(f)df = \frac{\alpha(f)}{0.5{k_0}^2\int_{-\infty}^{\infty}\sigma^{(1)}(\omega)d\omega}\int_{-\infty}^{\infty}\sigma_w^{(2)}(\omega)d\omega \tag{5.14}$$

Where, $\alpha(f)$ is the transfer function [64, 89]. The last term in the right-hand side of (5.14) can be rewritten as:

$$\begin{aligned}\int_{-\infty}^{\infty}\sigma_w^{(2)}(\omega)d\omega &\\ = \int_{-\infty}^{-\omega_B-\Delta\omega}\sigma_w^{(2)}(\omega)d\omega &+ \int_{-\omega_B-\Delta\omega}^{0}\sigma_w^{(2)}(\omega)d\omega \\ + \int_{0}^{\omega_B-\Delta\omega}\sigma_w^{(2)}(\omega)d\omega &+ \int_{\omega_B+\Delta\omega}^{\infty}\sigma_w^{(2)}(\omega)d\omega\end{aligned} \tag{5.15}$$

or,

$$\int_{-\infty}^{\infty}\sigma_w^{(2)}(\omega)d\omega = E_{w(1)}^{-} + E_{w(2)}^{-} + E_{w(3)}^{+} + E_{w(4)}^{+} \tag{5.16}$$

Here $E_{w(1)}^{-}, E_{w(2)}^{-}, E_{w(3)}^{+}, E_{w(4)}^{+}$ are the weighted energy of four second-order sidebands; the minus and plus signs denote the location of those sidebands [64]. In addition, the relationship between ocean wave frequency, f, and radar Doppler frequency, ω, is represented as $f = |\omega - \omega_B|$. From (5.14), the transfer function can be determined using the synchronized data of radar- and in-situ measurements. Then, the radar-deduced-wave frequency spectrum estimated can be computed using (5.17).

$$S(f) = \frac{\alpha(f)}{0.5{k_0}^2\int_{-\infty}^{\infty}\sigma^{(1)}(\omega)d\omega}\sum_{i=1}^{4}\sigma_{w(i)}^{(2)}|\omega \mp \omega_B| \tag{5.17}$$

Where, *i* represents the index of the second-order sideband, "-" or "+" is used when ω is positive or negative, respectively.

In this paper, all retrieval methods are implemented to estimate significant wave height, periods, and frequency spectrum from the level 1 product at the HTCN station. For data processing, ocean wave frequencies are given in the range of 0.05-0.5 Hz. Also, a threshold of 7 dB for data quality control is set up in our program. This means that wave parameters can only be calculated if the 2^{nd}-order Doppler spectrum SNR is greater than the given threshold. Otherwise, the NaN value will replace the invalid data, and the radar-derived wave parameters have not been further quality-controlled. Later, the estimation results will be compared to those of in-situ data to assess the method's accuracy and the radar system's performance.

5.4.2 Identification of Doppler spectra components

A. The existing method

Generally, the Doppler spectrum's first-order peaks are identified based on the strong peaks surrounding the theoretical Bragg frequency [55, 86, 108]. For example, identifying the first-order peaks on the Doppler spectra was shown in Figure 5-7. The Doppler spectrum in this figure was taken out at the range 20^{th} in the D-R spectrum map with 296^{o} bearing and at the time of 16h 30' Jan 26, 2019 LT, when the significant wave height at the mouth of Taichung harbor is approximately 2.1 m. In Figure 5-7, the thin solid black line represents the Doppler spectra power acquired at the HTCN station; two dashed black lines show Bragg frequencies' theoretical location. In horizontal, two dashed black lines represent the background noise at the positive and negative sides of the Doppler spectra; the thicker black solid represents the averaged spectra power over Doppler frequency, while the solid red line is used as a threshold for identifying the first-order peaks. Based on the given threshold above, the possible Bragg peaks can be identified as magenta segments. The location

and strength of practical Bragg frequencies (two red dots) can be determined using the weighted method [55]. Also, the first-order regions (green segments) are limited by using two dashed-dotted cyan lines. Lastly, four blue segments represent the valuable area of the second-order components.

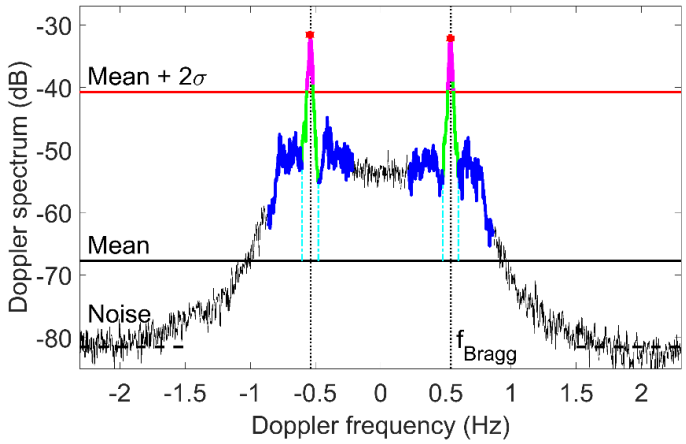

Figure 5-7 An example of spectra component identification. Herein, the thin solid black line represents the Doppler spectra power deducing from the radar sea echo data at the HTCN station; two dashed black lines show Bragg frequencies' theoretical location. In horizontal, two dashed black lines represent the background noise of two Doppler spectra sides; the thicker black solid represents the averaged spectra power over Doppler frequency; the solid red line is used as a threshold for identifying the first-order peaks (magenta segments); two red dots represent the location and strength of two practical Bragg frequencies; blue segments show the valuable power of four second-order Doppler sidebands.

To separate the region of Doppler spectral components, constant threshold methods were first implemented. In these methods, the nulls' location, which denotes the boundary between the first- and second-order components, needs to be identified. For simplicity, the range of the second-order spectrum in the spectral domain could be determined according to the lowest and highest frequencies of ocean waves [27, 109, 110]. Accordingly, the null location was set to $\pm 0.1\omega_B$ for the 25.4 MHz HF

radar system [27], and $\pm 0.15\omega_B$ for the 24.5 MHz HF radar system [110]. Wyatt [66, 111, 112] discussed the effects of using different frequencies as the null thresholds, and 0.05 Hz was suggested as the null location. A similar range of the null locations, ranging from 0.04 Hz to 0.07 Hz, was used at [64, 89, 113] using different radar working frequencies. However, the null location might change depending on the D-R spectrum characteristics associated with sea states, surface current spatial variability, SNR, and radar frequency. An adaptive method for the determination of null location is necessary for higher operating frequency HF radar system under variable surface current and wavefield, and strongly background noise [114].

B. The adaptive method - ImageFOL

In fact, the existing method would be accepted for specifying spectra component areas under simple current field and low sea-state conditions. However, it may not be accurate enough for processing the D-R spectrum data of the higher operating frequency HF radar system under variable surface current and wavefield and strongly background noise. The truth is that the above condition is similar to those of the middle Taiwan Strait. Besides, the existing method's performance can be influenced by other factors induced by intermittent radio frequency, ionospheric scattered, ship echo, and moving offshore wind energy structures [114]. Therefore, adopting an alternative method, which is more robust in the isolation of spectra components under various weather conditions, is necessary.

In this study, a new technique is applied to split the spectral energy area relevant to useable measurements for current retrieval from the spectral energy dominated by wavefield and background noise and called the ImageFOL method [114]. The technique concept consists of a single and globally relevant smoothing length scale for reducing the number of user-defined parameters, D-R spectra pretreatment, maker-controlled watershed segmentation (MCWS), and an image

processing technique. This method provides an intuitive view of range-dependent spectra as naturally seeing "by eye" and correcting Bragg energy's complex pattern into the reasonable area of first-order peaks. In this method, the most crucial step is the MCWS technique that allows segmenting the image or isolating image elements, which may be attractive objects on the D-R spectra map. According to Kirincich's discussion [114], watershed segmentation is the most viable technique for isolating the Bragg regions on the spectra power map. Therefore, it can be performed better for capturing the usable Bragg peaks on the complex D-R spectrum under severe sea-state conditions with the highly varying surface current.

Table 5-2 The parameter of the ImageFOL method.

Center frequency of the transmitter (MHz)	27.75	vel_scale (cm/s)	20
Number of Doppler bins	2048	max_vel (cm/s)	120
Radial velocity resolution,v_incr (m/s)	0.012	SNR_min of the first-order components (dB)	5
complicating issues	Highly variable surface current, variable waves, strong background noise, severe sea-state generated by winter monsoons.	smoothing length scale N = vel_scale/v_incr	16

In the ImageFOL method, the D-R spectra at each azimuthal direction will be treated as an image to identify the first-order regions. To implement this method,

three essential parameters are required. Herein, two thresholding parameters, which are the minimum signal-to-noise ratio of the first-order Doppler spectra and the maximum current velocity possibly measured with the HF radar system, are given. They are taken based on the radar operating frequency, the variable range of current velocity, and expert experiences, see table 2 [114]. The remaining one is the smoothing length scale, which is defined to set the smoothing disk's size and smooth out small variations such as ship’s echoes for guiding object identification. It is also the critical factor for identifying the first-order limit spectra' proper delineation. Accordingly, Table 5-2 represents the initial setting parameters of the ImageFOL method, which is used to process the D-R spectra data at the HTCN station. The method’s sequential process consists of pretreatment, adjusting the length scale, screening for radiofrequency noise contamination, the MCWS application, and postprocessing; see the detail in [114].

C. Present settings of the modified ImageFOL method

Theoretically, the first-order component on the Doppler spectrum with respect to a certain azimuthal angle has a single energy peak around Bragg frequency. In reality, the multi-peaks or widened first-order components appear when there are varying surface currents or in complicated wave fields.

The original ImageFOL method was designed only for the identification of the first-order peaks with the aim of improving the accuracy of the surface current radial velocity estimation. For the determination of the null location, this method needs some modifications because it has a tendency to delimit part of the second-order area into the first-order range when the first- and second-order areas overlap, which occurs in the conditions of severe sea state or when using high radar operating frequencies. The Doppler-Range spectra in Figure 5-8(b) is shown as an example. Also there, Figure 5-8 are the results of using constant threshold and ImageFOL

methods for identifying the first-order component of the Doppler-Range (D-R) spectrum in various sea states. Panel (a) and (b) of Figure 5-8 illustrate the D-R spectrum under a severe sea state with a measured significant wave height of 3.86 m and a calm sea state with 0.78 m significant wave height, respectively. At each panel, black lines represent the detected regions using the constant threshold method, and white lines for the original ImageFOL method. It can be seen in Figure 5-8(a) that compared to the calm sea state Figure 5-8(b), the original ImageFOL results over-estimate the range of the first-order region. And this leads to a persistent under-estimate of the significant wave heights as well as the periods. In order to eliminate the bias, a simple solution with two steps is proposed.

+ Determination of the centroid Bragg frequency: At an individual range cell, the upper and lower Doppler frequencies are first set as a search window using the results of ImageFOL. Then the geometric center of Doppler frequency is calculated in this window by taking a weighted average of over 25% of the substantial peaks in the widened first order components. Also, Doppler frequencies relevant to the ship echo, interference can be identified and filtered out if the Doppler frequency shift for those peaks to the estimated centroid frequency is greater than a given statistic value, which is normally two times the standard deviation. This procedure can be implemented in an iterative loop to reduce the bias estimation of the centroid frequency.

+ Re-identification of First-order regions: Based on the above geometric center and the usable of significant peaks, two outer left- and right substantial peaks are marked. Then, it is assumed that there is a significant decline from the usable Bragg peak to the nulls located in the middle of the first- and second-order areas, the local minima of the spectral components are searched for, towards the higher and lower frequencies using the normalized spectrum, one of the ImageFOL method's output. The local minima will be used as null locations. Finally, the watershed

transform technique's smoothing disk is applied to smooth the new bound of first-order regions over the range cell domain.

The two above steps show the main difference between the original and modified ImageFOL methods. The example of first-order identification under two different sea states proving the efficiency of the modified ImageFOL method will be represented later.

D. Examples of identified first-order areas

In order to demonstrate the achievement of the proposed solution for detecting areas of Doppler spectra components, the results of spectra component identification are also shown in Figure 5-8. In the first case, the D-R spectra under the condition of the winter surface current and the severe sea-state driven by a typical local winter monsoon are processed (Figure 5-8(a)). Meanwhile, Figure 5-8(b) illustrates the D-R spectra under the complex surface current condition and low sea-states. As the results, Figure 5-8 shows the detected area of the first-order component estimated from three different approaches. Figure 5-8(a) shows that the results of the modified ImageFOL method are slightly different from those of the constant threshold method, while it is highly different from the result of the original ImageFOL method, which might be influenced by the intense energy of the second-order components near the first-order spectrum. On the other side, there is a significant difference between the detected area from ImageFOL and the constant threshold methods (Figure 5-8(b)). While the former provides an area that exceeds the expectation result, the latter delivers an underestimated result. The application of the modified ImageFOL method shows that it is effective in correcting the first-order area; the result is relatively close to the expectation.

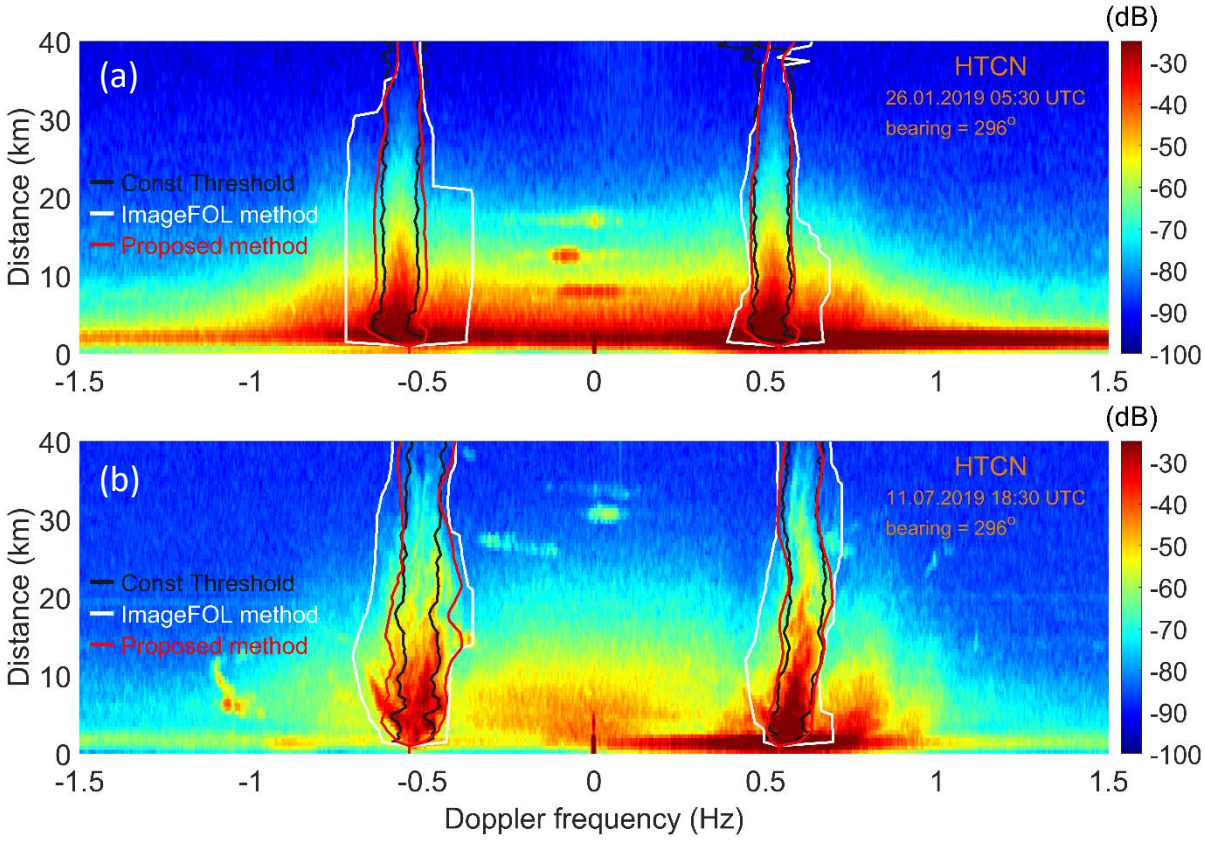

Figure 5-8 Comparisons of methods for identifying the first-order component of Doppler-Range (D-R) spectra in various sea states. Here, panel (a) illustrates the spectra under a severe sea state (Hs = 3.86m), while panel (b) shows the spectra under the low sea state (Hs = 0.78 m) and varying surface currents. Black lines represent detected regions using the constant threshold method, and white and red lines are used for the original and the modified ImageFOL methods, respectively.

The first-order area results determined from the original ImageFOL method are usually more extensive than those of the constant threshold method. It indicated two issues: firstly, the complex surface current strongly affects the expansion of Bragg peak regions under low and middle sea-state; secondly, the instability of wave components at low-frequency bands such as swell is significant due to the mix between swell backscattered signals and the Bragg wave signals. The modified

ImageFOL method performed better than two other methods in both high and low wave conditions. In this study, the modified ImageFOL method is implemented to separate Doppler spectra components of approximately 385 days of data. Comparison results between estimated and in-situ wave parameters will be represented in a later section.

5.4.3 Validation of estimation results

A. In-situ for validation

In the study area, the in-situ data of ocean surface parameters are currently recorded by an AWAC, which was deployed at approximately 30 m depth in water, and located outside the mouth of the Taichung harbor (24^{o} 18.199'N, 120^{o} 28.916'E) (Figure 5-1). The AWAC stays in the HTCN station's footprint at a bearing of 267^{o} and a range of 4.59 km. The device operates at 600 kHz and has a Janus configuration with four beams, one vertical beam, and three beams located at 25^{o} from the vertical axis. It acquires the data at 1 Hz in 34 minutes for every hour. The collected data is frequently processed by the Storm, a commercial software developed by the manufacturer. In data processing, the directional wave spectrum over 49 frequency components and 90 directions were determined using the maximum likelihood method (MLM). Then, ocean surface waves' parameters were calculated from the frequency spectrum over the range of 0.02-0.49 Hz. In this study, the data of in-situ wave parameters representing the sea-truth will be compared with estimated wave parameters retrieved from the HF radar system.

B. Validation results on wave parameters

First, the ten days comparisons of three typical weather scenarios, such as winter monsoon, typhoon, and calm sea state with significant diurnal land-sea breeze phenomena, are shown in Figures 5-9, 5-10, and 5-11, respectively. In those three

figures, black lines show the time-series of wave parameters obtained by the AWAC, and blue dots represent the estimated Hs, Tm, and Tp using (3.2), (3.3), and (5.12) with the original scaling factor ($\xi_{Hs} = 0.551$, $\xi_{Tm} = 1$, $\xi_{Tp} = 1$). In the present study, the scaling factors of wave parameters are calibrated using one-year continuous in-situ data, which gives the values as $\xi_{Hs} = 0.786$, $\xi_{Tm} = 0.896$, $\xi_{Tp} = 0.965$. Using these revised scaling factors, the radar-deduced data are shown as the red diamonds in Figures 5-9, 5-10, and 5-11. Overall, it is a good agreement between Hs estimated from radar and those of in-situ data, while the agreement between estimated and in-situ periods is still limited.

For the two cases of winter monsoon cases, the left three panels (a), (c), and (e) of Figure 5-9 shows a typical monsoon condition in January 2020, and the right panels for the passage of a cold front in October 2020. Firstly, the results agree well for Hs, Tm, and Tp in case I, as shown in the left panels of Figure 5-9, using present scaling factors, compared to using previous scaling factors. This implies the scaling factor could vary due to the radar frequency, local conditions, and the systems used. Secondly, as can be seen from the graph on the right of Figure 5-9 for case II, the wave conditions change significantly and rapidly during the cold front's passage. This rapid growth of waves can be captured by radar in terms of wave height. However, there exists a bias in estimation results both for Tm and Tp, especially around the duration of the passage of the front. The radar-deduced wave periods were over-estimated for short waves and under-estimated for long waves or swell. This result indicates that there might be a deviation in wave spectral shape estimation and will be discussed later.

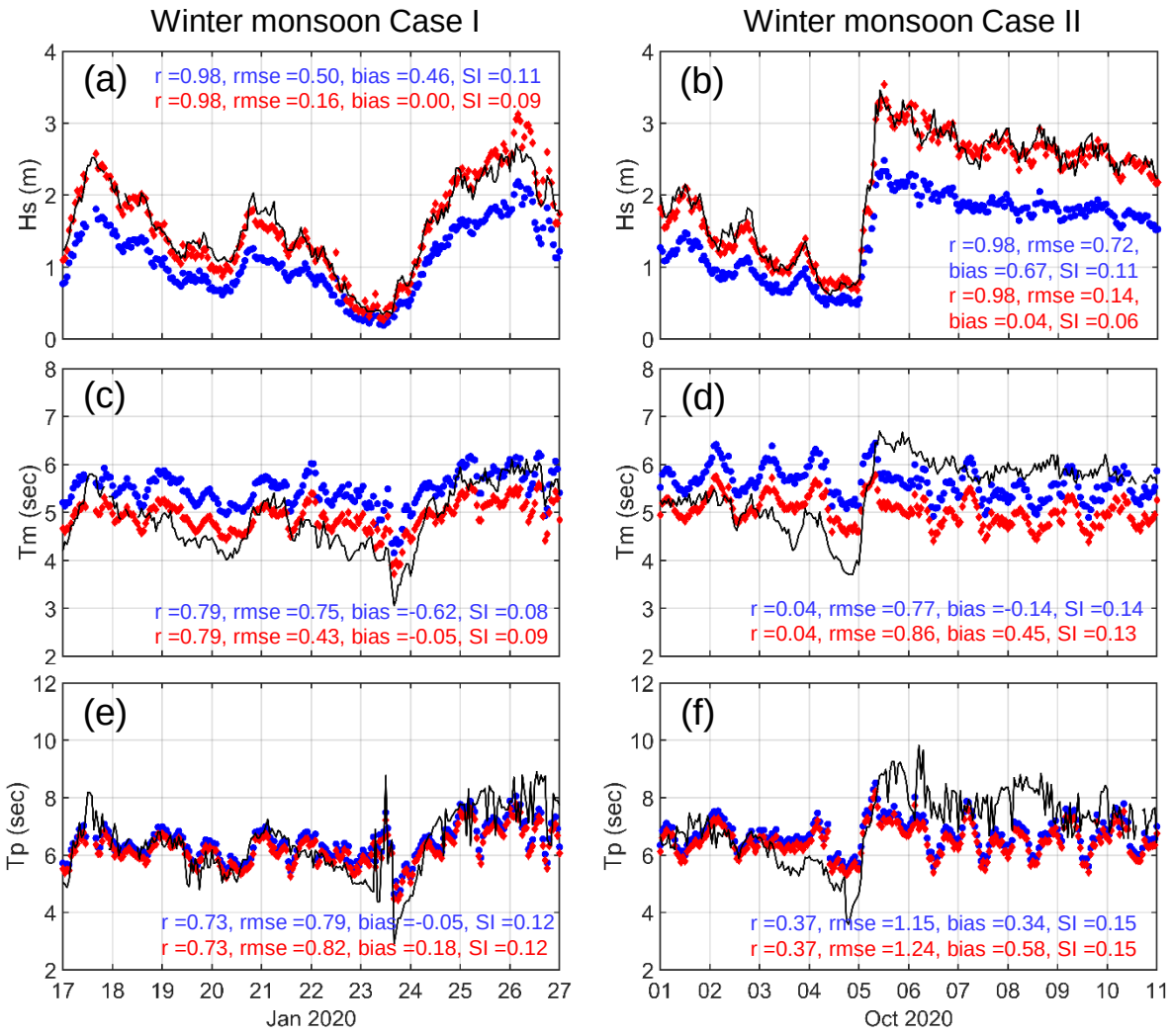

Figure 5-9 The ten days comparisons of wave parameters obtained from HF radar and in-situ measurement in two winter monsoon cases. In this figure, case I (January 2020), as shown on the left three panels (a), (c), and (e) are typical local winter monsoon conditions, whereas Case II in the right panels (b), (d), and (f) illustrate the time series during a passage of a cold front in October 2020. Black lines denote the in-situ measurement from AWAC, and blue dots for estimated wave parameters with original scaling factors ($\xi_{Hs} = 0.551$, $\xi_{Tm} = 1$, $\xi_{Tp} = 1$), red diamonds for present calibrated constant scaling factors ($\xi_{Hs} = 0.786$, $\xi_{Tm} = 0.896$, $\xi_{Tp} = 0.965$).

Figure 5-10 shows the comparison during typhoon conditions, where DANAS case in Figure 5-10(a), (c) and (e), and super typhoon LEKIMA case in Figures 5-10(b), (d), and (f). The shaded area denotes the duration of typhoons. The trajectories of the two typhoons were on the north-western Pacific, translating northward and north-westward toward Jeju, Korea, and Shanghai, China, respectively, and both did not bring direct impacts to the study area near Taichung, Taiwan. The sea state observed by the radar was mostly mixed wind sea and swell condition. Comparing the wave heights during typhoon DANAS, the radar data reasonably agree with the sea truth. The maximum error occurred during the peak value from 1200LT-1700LT, July 17, 2019, coincides with the nearest distance from the typhoon eye to the study area, as shown in Fig. 5(a). The wave height was measured by AWAC around 3 m, and the smallness parameter was 0.8. The maximum bias reached 50% using newly calibrated scaling factors. For typhoon LEKIMA as in Figure 5-10(b), the bias of wave height was smaller. The discrepancy between these two cases might indicate that the presence of swell in the wave field will influence the strength of HF radar Doppler spectra and might play a critical role in wave height determination. For the results of Tm and Tp, features of oscillations can be identified both in in-situ data and radar data, and these variations of Tm and Tp signals are in phase. However, during the peak periods of both typhoons DANAS and LEKIMA, the maximum periods were under-estimated, as seen in Figures 5-10(c) and (f).

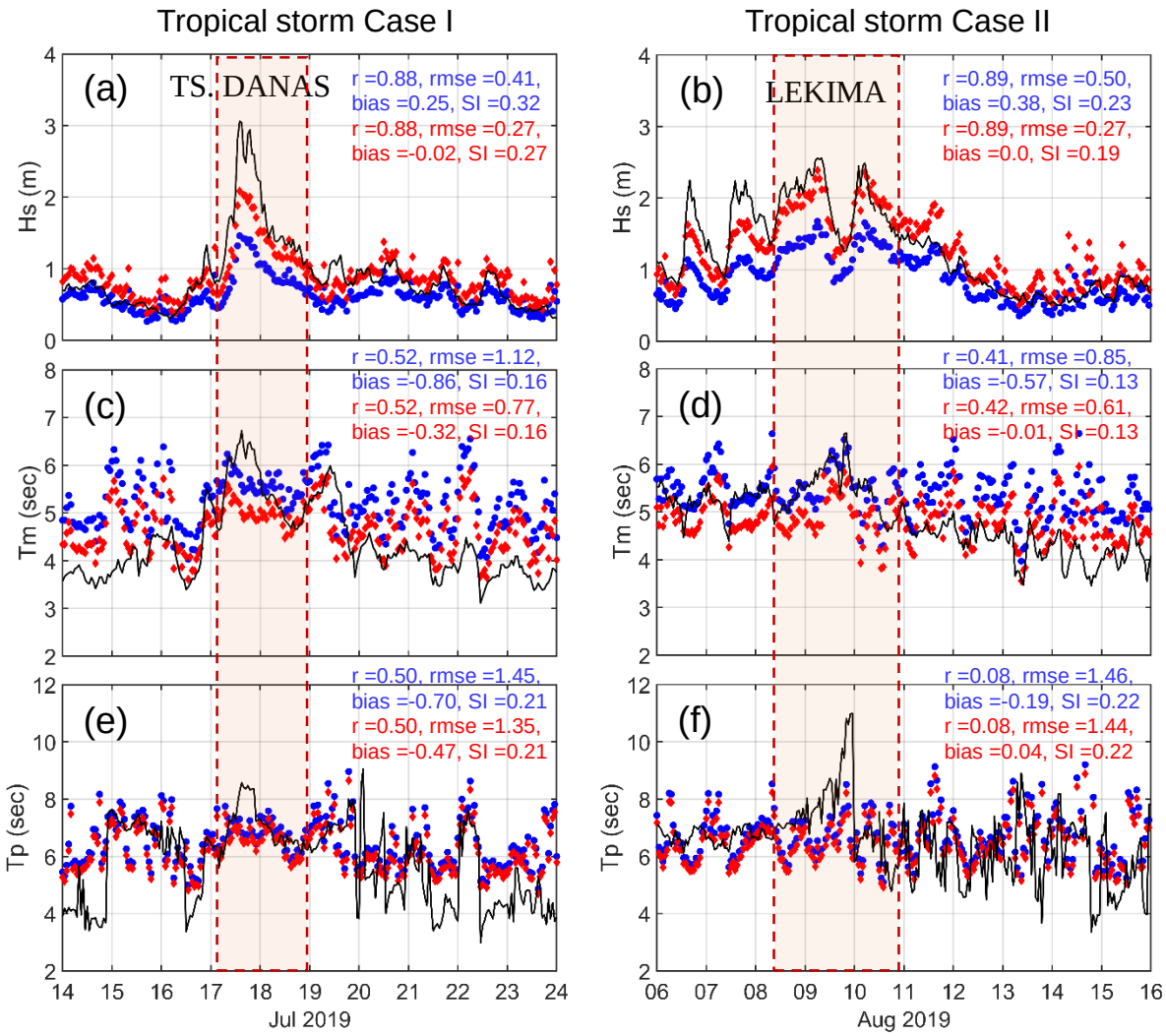

Figure 5-10 The ten days comparisons of wave parameters obtained from HF radar and in-situ measurement in two tropical storm cases. The significant wave height, mean period, and peak period during the passage of TS DANAS are shown as Case I in the left three panels (a), (c), and (e), respectively. Corresponding figures during super typhoon LEKIMA are shown in the right panels (b), (d), and (f) as Case II. Black lines denote the in-situ measurement from AWAC, and blue dots for estimated wave parameters with original scaling factors ($\xi_{Hs} = 0.551$, $\xi_{Tm} = 1$, $\xi_{Tp} = 1$), red diamonds for present calibrated constant scaling factors ($\xi_{Hs} = 0.786$, $\xi_{Tm} = 0.896$, $\xi_{Tp} = 0.965$).

Thirdly, the inter-comparison of wave parameters under the weather condition when the diurnal oscillations were significant, shown in Figure 5-11, is discussed. The diurnal oscillation of coastal wave height is usually associated with the land-sea breezes effects and becomes notable in the summer when the insolation and surface heating is intensified. The amplitude of such oscillation in wave height could reach to 1.5 m, as seen in Figures 5-11(a) and (b). Due to the highly growth rate of wave height, it is regarded as a rapidly changing wave field, which is necessary to be cautious for maritime activities. The short fetch of land-sea breeze limits the growth of wavelength, and therefore the wave energy contributes to the higher frequency component in the spectrum. And this results in the intensity enhancement of the 2^{nd} order component in the Doppler spectra. In both cases, as shown in Figure 5-11, with the clear 2^{nd} order signal, the radar-deducted wave heights and periods agree well.

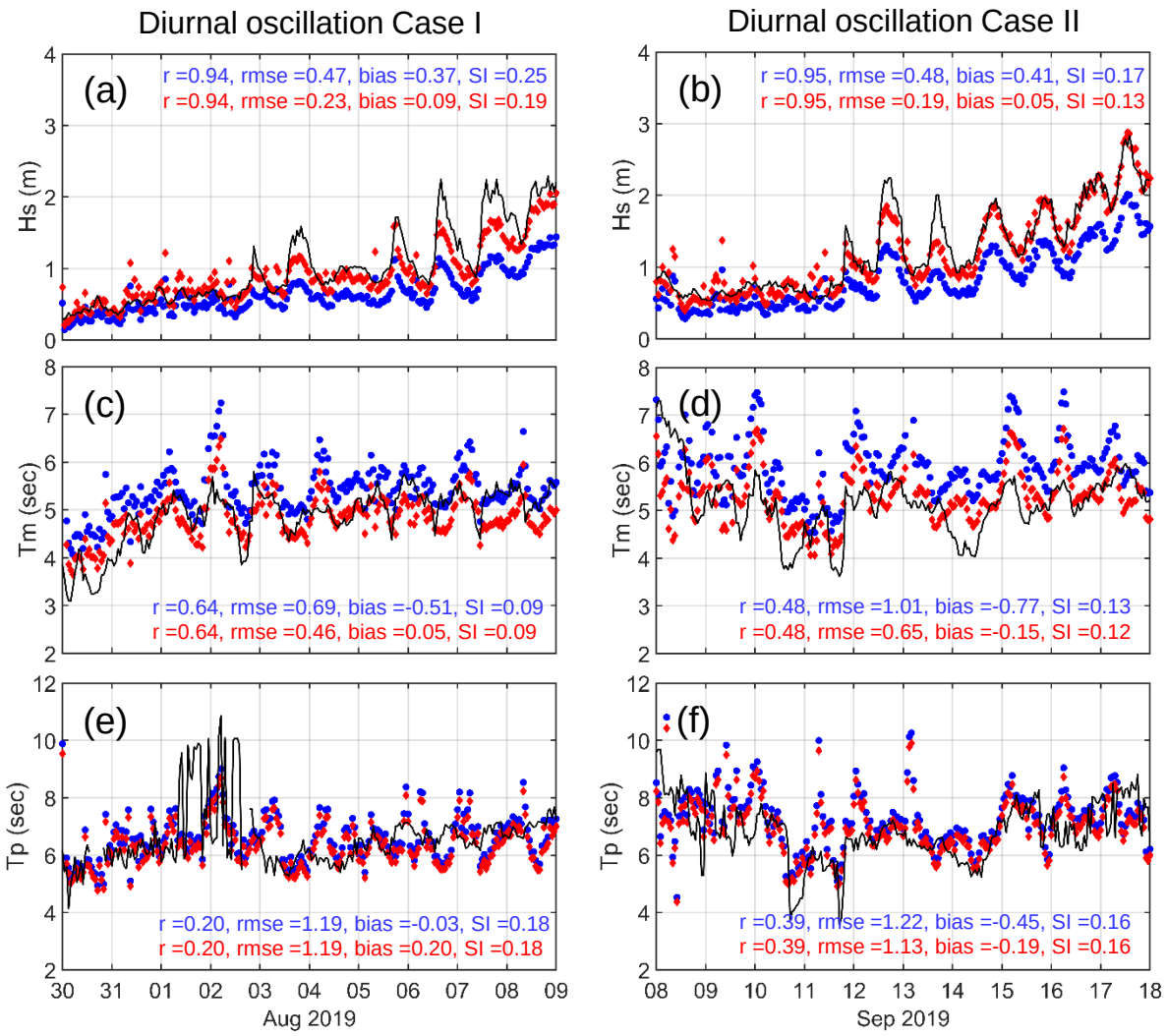

Figure 5-11 The ten days comparisons of wave parameters obtained from HF radar and in-situ measurement in later summer when the diurnal oscillations were significant. Three panels (a), (c), and (e) in the left column show the significant wave height, mean period, and peak period of early August 2019, respectively, whereas the right panels (b), (d), and (f) for the second duration in mid-September 2019. Black lines denote the in-situ measurement from AWAC, and blue dots for estimated wave parameters with original scaling factors ($\xi_{Hs} = 0.551$, $\xi_{Tm} = 1$, $\xi_{Tp} = 1$), red diamonds for present calibrated constant scaling factors ($\xi_{Hs} = 0.786$, $\xi_{Tm} = 0.896$, $\xi_{Tp} = 0.965$).

The above discussions are made based on selected cases of 10 days durations. In order to enlarge the sample size for assessing the uncertainty of radar-deduced wave parameters, 385 days of continuous and synchronized radar and AWAC data from 2019 to 2020 is used for the present intercomparison. After the implementation of data quality control, approximately 6800 match-up data pairs were yielded. Among the match-up pairs, the occurrence probability of wave direction, 73.3% were from the north-east (330^{o}-60^{o}) associated mostly with winter monsoons, 23.5% from the south-west (210^{o}-300^{o}), and the rest was 3.2%, which has the wave incident angle near perpendicular to the coastline and exhibits small wave heights. Error indexes with respect to the above-mentioned wave directions are listed in Table 5-3. Scatter plots between the radar-deduced to the AWAC data of significant wave height, mean period, and peak period are shown in Figures 5-12(a), (b), and (c), respectively.

As can be seen in Table 5-3, the error indexes from this study, the correlation coefficient (r), root-mean-square error (RMSE), and scatter index (SI) of significant wave height are 0.96, 0.24 m, and 0.15, respectively; while they are 0.68, 0.75 s, 0.15 for the mean period, and 0.49, 1.42 s, 0.22 for peak period. Detail error indexes are listed in Table 5-3. Alattabi et al. [64] reviewed and summarized the error indexes from the literature. Based on the work of Alattabi et al. [64], the error indexes from various studies, e.g., Wyatt [115], Ramos et al. [71], Wyatt et al. [66], Chen et al. [16], Hisaki [116] and etc., as well as the present study are reorganized as listed in Table 5-5. Using Table 5-5 as the reference, the error indexes from the present study are comparable or even smaller. The current radar data quality and estimators are acceptable for wave parameters retrieval at a single point. Further, significant differences in the correlation coefficients (r) and the scatter indexes (SI) among the categories of different wave directions can be identified. This indicates that wave direction and its spreading might play crucial roles affecting the estimation results.

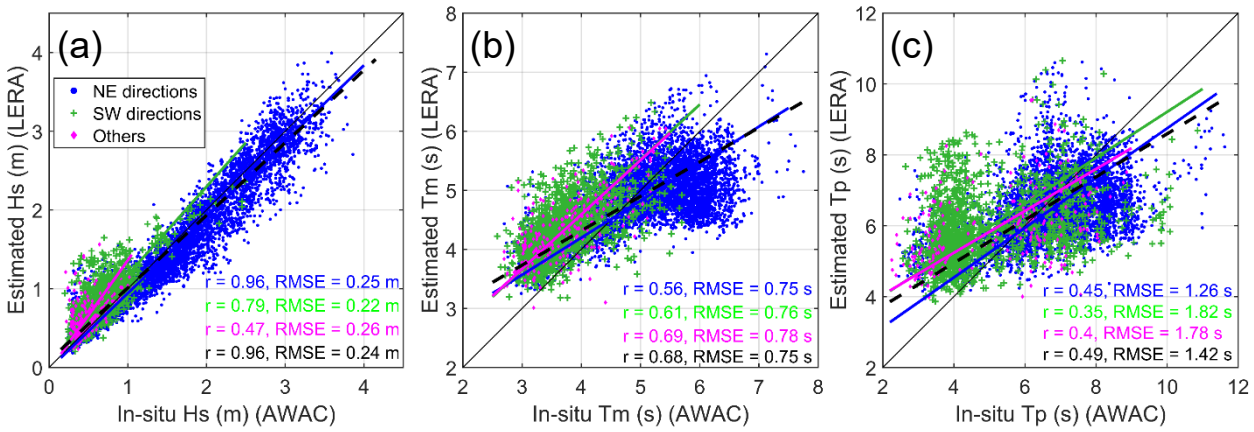

Figure 5-12 This figure shows the scatter plot of radar-deduced (a) significant wave height, (b) mean period, and (c) peak period calibrated from the newly constant scaling factors and in-situ wave data. In each panel, blue circle, green plus, and diamond magenta represent wave parameters corresponding to their directions: north-east (N-E) monsoon waves, southwest (S-W) monsoon waves, and waves from other directions. The red lines are the regression line for the whole dataset, and three other lines are regression lines corresponding to the three above sources of waves.

Regarding the error indexes for the above three weather scenarios, the average RMSE of wave height is 0.15 m for winter monsoon cases, 0.27 m for typhoon cases, and 0.21 m for summer diurnal oscillation cases. Other error indexes are listed in Table 5-4. The majority of the indexes are smaller for the winter monsoon and summer diurnal oscillation cases, and are greater for typhoon cases. For the error indexes of Tm, the RMSE and SI features the least for diurnal oscillation cases and then followed by winter monsoon cases. Again, the typhoon cases have the greatest error indexes. From the above results of comparisons and discussion, it could be concluded that the radar performance also depends on the shape of the second-order Doppler spectrum.

Table 5-3 Comparison of wave parameters from the LERA system and AWAC.

Statistical parameters	**Significant Wave height (m)**				**Mean Wave Period (s)**				**Peak Wave Period (s)**			
	N-E directions	**S-W** directions	Others	Total	**N-E** directions	**S-W** directions	Others	Total	**N-E** directions	**S-W** directions	Others	Total
r	0.96	0.79	0.47	0.96	0.56	0.61	0.69	0.68	0.45	0.35	0.40	0.49
RMSE	0.25 m	0.22 m	0.26 m	0.24 m	0.75 s	0.76 s	0.78 s	0.75 s	1.26 s	1.82 s	1.78 s	1.42 s
BIAS	0.08 m	-0.14 m	-0.15 m	0.02 m	0.25 s	-0.61 s	-0.61 s	0.02 s	0.32 s	-0.99 s	-0.72 s	-0.02 s
SI	0.13	0.24	0.41	0.15	0.13	0.12	0.13	0.15	0.17	0.30	0.29	0.22
Slope	0.965	1.118	1.399	0.921	0.627	0.930	0.920	0.582	0.70	0.65	0.59	0.61
Intercept	-0.02	0.06	-0.04	0.09	1.69	0.87	0.91	1.99	1.74	2.73	2.87	2.52
N	*5032 (73.3 %)*	*1614 (23.5 %)*	*218 (3.2 %)*	*6864*								

Table 5-4 The error indexes of wave parameters under three weather scenarios.

Wave parameters	**The weather scenario**	***r***	**RMSE**	**BIAS**	**SI**
Hs	Monsoon	0.98	0.14 – 0.16 m	0.00 – 0.04 m	0.06 – 0.09
	Typhoon	0.88 – 0.89	0.27 m	-0.02 – 0.0 m	0.19 – 0.27
	Summer Diurnal oscillation	0.94 – 0.95	0.19 – 0.23 m	0.05 – 0.09 m	0.13 – 0.19
Tm	Monsoon	0.04 – 0.79	0.43 – 0.86 s	-0.05 – 0.45 s	0.09 – 0.13
	Typhoon	0.41 – 0.52	0.61 – 0.77 s	-0.32 – -0.01s	0.13 – 0.16
	Summer diurnal oscillation	0.48 – 0.64	0.46 – 0.65 s	-0.15 – 0.05 s	0.09 – 0.12
Tp	Monsoon	0.37 – 0.73	0.82 – 1.24 s	0.18 – 0.58 s	0.12 – 0.15
	Typhoon	0.08 – 0.50	1.35 – 1.44 s	-0.47 – 0.04 s	0.21 – 0.22
	Summer diurnal oscillation	0.20 – 0.39	1.13 – 1.19 s	-0.19 – 0.20 s	0.16 – 0.18

Table 5-5 Comparison of the method's performance in this study with other results reported in the literature for different methods and different radar frequencies.

Inversion type	**Study**	f_{radar} **(MHz)**	**The type of radar system**	**Hs (m)**		**Tm (s)**		**Tp (s)**	
				RMSE	r	RMSE	r	RMSE	r
Theoretical	Howell & Walsh [27]	**25.4**	single & dual-radar	**0.14–0.49**	**0.87–0.99**	–	–	**0.63–0.88**	**0.91–0.96**
	Wyatt et al. [117]	7–10	dual-radar	0.30–0.74	0.55–0.96	0.84–4.56	0.13–0.82	–	–
	Wyatt et al. [118]	16	dual-radar	0.41–0.46	0.96–0.97	–	–	–	–
	Wyatt et al. [66]	7–12 12–13 **25**	dual-radar	0.45 0.44 **0.41**	0.91 0.80 **0.97**	–	–	–	–
	Hisaki [116]	**24.5**	single & dual-radar	**0.22–0.44**	**0.68–0.82**	–	**0.56–0.69**	–	–
	Lopez et al. [112]	12.3	dual-radar	0.40–1.51	0.77–0.93	0.85–2.53	0.80–0.85	1.47–3.18	0.75–0.83
	Lopez & Conley [119]	12.3	dual-radar	0.30–0.45	0.87–0.94	0.50–1.35	0.65–0.9	1.72–3.20	0.49–0.76

Empirical	Wyatt [115]	**27.65** 7–12	single & dual-radar	**0.33–0.67** 0.52–2.82	**0.76–0.90** 0.74–0.95	–	–	–	–
	Ramos et al. [71]	**25.4**	dual-radar	**0.21–0.70**	**0.68–0.96**	–	–	–	–
	Chen et al. [16]	8.3 14.2 18.5–19.5 **22.5**	single radar	0.53–1.83 0.31–0.58 0.23–0.35 **0.22–0.35**	0.45–0.46 0.67–0.70 0.81–0.84 **0.82–0.83**	–	–	–	–
	Gomez et al. [120]	12	dual-radar	0.39–0.69	0.78–0.93	0.81–2.81	0.52–0.81	2.25–4.23	0.33–0.76
	Lopez et al. [113]	12	dual-radar	0.26–0.44	0.90–0.96	0.65–1.20	0.67–0.86	–	–
	Middleditch et al. [121]	8.512	dual-radar	0.31–0.57	0.83–0.94	0.92–1.10	0.66–0.76	1.21–1.77	0.57–0.75
	Cai et al. [70]	7.8	single radar	0.57–1.48	0.40–0.91	–	–	–	–
	Alattabi et al. [64]	48	single radar	0.16–0.25	0.86–0.94	0.79–0.84	0.80–0.95	1.38–2.16	0.51–0.84
	Present study (using newly calibrated scaling factors)	**27.75**	single radar	**0.14–0.27**	**0.88–0.98**	**0.43–0.86**	**0.04–0.79**	**0.82–1.44**	**0.08–0.73**

The wave spectrum is one of the essential wave information that could be estimated from the HF radar data. To illustrate the radar-deduced wave spectra under different sea states, cases of three weather scenarios, including the winter monsoon, typhoon, and the wave height diurnal oscillation, are selected. To determine transfer function values, (4.14) for the radar-deduced wave spectrum retrieval is implemented. The estimation results of the wave spectra at AWAC's location are presented in Figure 5-13. In this figure, panels (a), (b), and (c) show the five days time series data of estimated wave spectra under three sea-state scenarios, while panels (d), (e), and (f) show the in-situ wave spectra recorded by AWAC. To re-determine the practical value of the transfer function of the wave spectrum, the ratios of the estimated spectrum over the in-situ spectrum with respect to three sea-state scenarios are shown in panels (g), (h), and (i). The correlation coefficients of 5 days time series between the estimated and in-situ wave spectral components under three weather conditions are estimated and shown in panels (j), (k), and (l).

Firstly, the panels of the left column in Figure 5-13 show results during the passage of a cold front in early winter in 2020. The rapid increase of wave spectral intensity caused by strong wind can be recognized in both panels (a) and (d). The down-shift of peak frequency during the peak wave height was obvious in AWAC's data in Figure 5-13(d). However, not visible in radar-deduced spectra in panel (a). Also, the spectral width is narrower in sea-truth data in panel (d), indicating swell dominant sea-state, whereas in panel (a) the low-frequency component is over-estimated and widens the spectral width.

Secondly, the panels in the middle column in Figure 5-13 show the case under the influence of the DANAS typhoon in 2019. In both panels (b) and (e), the peaks of wave height driven by the typhoon are clearly recognized. Again, the lowered wave frequency that accompanied the peak wave height can be seen in AWAC's data in panel (e), but not clear in radar data in panel (b). The radar-deduced spectrum over-

estimates the spectral width. Then, the panels of the right column in Figure 5-13 illustrate the wave spectra under significant land-sea breeze conditions, where the wave height features diurnal oscillation. The spectral width is also widened.

The ratio between radar-deduced wave spectra to the sea truth can be regarded as the inverse of the transfer function. The temporal variation of the transfer functions in three sea-state scenarios is shown in Figures 5-13(g), (h), and (i). In order to determine the transfer function, the probability density distribution of the ratio between the estimated spectrum to in-situ data with respect to all wave frequency bands is shown as the shaded dots cloud in Figure 5-14(a). The darker the shading indicates the higher probability of occurrence, on the basis of which, the mean and median values of the ratio at a different frequency can be determined accordingly, as illustrated by red and blue lines, respectively. These two curves can be regarded as the transfer function. Local maxima in both the red and blue lines can be identified at 0.365 Hz, which reflects the effect of the singularity in the electromagnetic coupling coefficient at $\pm\omega_B\sqrt[4]{2^3}$. Also, it can be noted that the distribution of the shaded dots cloud is narrower in the range 0.12 Hz < f_i < 0.4 Hz, where the red and blue lines agree well. In this spectral range, the transfer functions have a higher degree of confidence owing to the better SNR of the 2nd-order spectrum compared to those of swell and short wind waves. In the rest of the spectral band, the deviation between the red and blue lines increases. A similar phenomenon can be seen in Figures 5-13(j), (k), and (l), which are the correlation coefficients of the time series of the spectral power density between the radar-deduced data and the sea-truth. Such correlation coefficient with respect to the wave frequency is shown as the dotted black line in Figure 5-14(a) using one-year data. In panel (a) of Figure 5-14, the black-while color shape represents the probability density distribution of the ratio between in-situ spectrum over the estimated spectrum at each wave frequency component; the two red and blue lines connect the average and median values of

each probability distribution, respectively, and they can be called as the transfer function. The dotted black line is the connection of correlation coefficient values between the estimated and in-situ spectrum, while panel (b) shows the comparison of the present transfer function and those of literature. In this panel, the red line shows the inversion of the transfer function that is averaged and transferred from the present operating radar frequency (27.75 MHz) to a 48 MHz radar frequency using Gurgel et al.'s formula [89], dashed-dotted, and dashed blue lines show the transfer function at shallow and deepwater regions for an operating radar frequency of 48 MHz published by Alattabi et al. [64]. From Figure 5-14(a), the correlation coefficient is greater than 0.6 for most of the spectral bands except for the singularity point, but it starts to decrease at frequencies below 0.10 Hz. This result coincides with the transfer function characteristics.

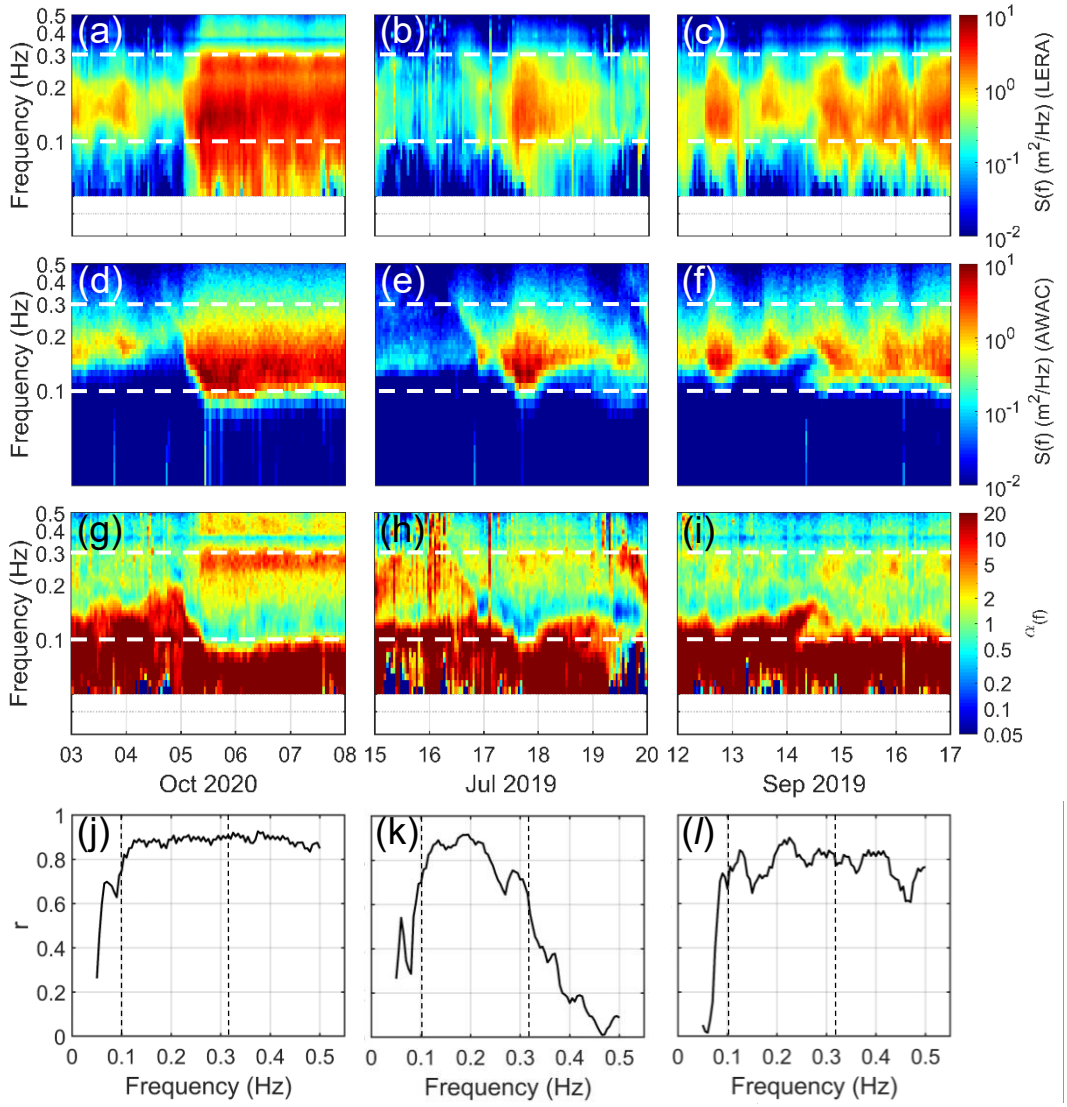

Figure 5-13 The five days comparisons of wave spectrum obtained from HF radar and in-situ measurement in winter monsoon, typhoon, and the diurnal oscillations cases. Panels (a), (b), and (c) show the wave spectrum estimated from radar Doppler spectra using the empirical method, while panels (d), (e), and (f) are the in-situ frequency spectrum measured by AWAC. Panels (g), (h), and (i) are the corresponding ratio between estimated over the in-situ wave spectrum. Panels (j), (k), and (l) are the corresponding correlation coefficient between the two above spectrum.

C. The transfer function

Relevant empirical studies of the transfer function are scarce, the present transfer function characteristics are compared with the result of Alattabi et al. [64], which was obtained from a 48 MHz very high-frequency (VHF) radar system. In order to convert the value of the transfer functions to the same basis of radar working frequency, an adjusting formula proposed by Grugel et al. [89] is applied. Figure 5-14(b) shows the comparison where the red line shows the inverse of the transfer function in the present study, while dashed-dotted and dashed light blue lines represent those of Alattabi et al.'s results for shallow and deep water conditions, respectively. This panel shows the similar properties of the two transfer functions. First, the peaks of both studies occur around 0.075 Hz. Second, the variation patterns are almost identical and slightly different in the value. It implies that the shape of the transfer function is universal and independent of radar frequencies, radar manufacturers, and weather conditions. The presently proposed transfer function extends over the spectral range to 0.5 Hz and exhibits a decreasing trend with frequency, from 0.673 to 0.086, when the wave frequency increases from 0.265 Hz to 0.50 Hz if the effect of electromagnetic singularity is temporarily ignored.

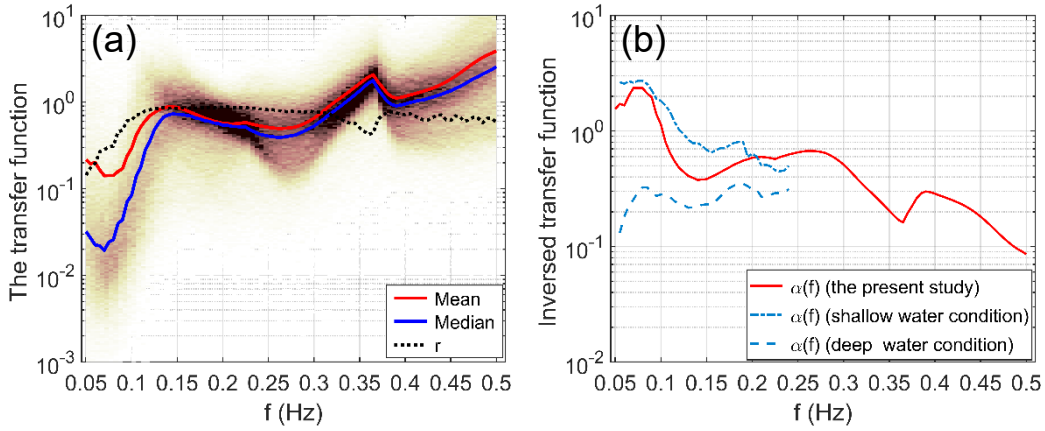

Figure 5-14 This figure shows the ratio between radar-deduced wave spectrum and in-situ data. Panel (a), the color shape represents the probability density distribution of the ratio between in-situ spectrum over the estimated spectrum with respect to each wave frequency component, red and blue lines are two lines that connect average and median values of each probability distribution, respectively; those connection lines can be called the transfer function. The dotted black line is the connection of correlation coefficient values between the estimated and in-situ spectrum. Panel (b) shows the comparison of the present transfer function and those of literature. In this penal, the red line shows the inversion of the transfer function that is averaged and transferred from the present operating radar frequency (27.75 MHz) to 48 MHz radar frequency using Gurgel et al.'s formula [89], dashed-dotted and dashed blue lines show the transfer function at shallow and deepwater regions for an operating radar frequency of 48 MHz [64].

If the above transfer function is applied to the analysis, then the radar-deduced wave parameters are identical to those using scaling factors. Inter-comparisons of radar-deduced Hs, Tm, and Tp using newly scaling factors and those of results using the estimated transfer function are shown in Figures 5-15(a), (b), and (c), respectively. In each panel of Figure 5-15, the horizontal axis shows calibrated wave parameters

using constant scaling factors ($\xi_{Hs} = 0.786$, $\xi_{Tm} = 0.896$, $\xi_{Tp} = 0.965$), while the vertical axis represents estimated wave parameters using the transfer function in Figure 5-14(a), and three red lines are the regression line for the comparison of wave parameters (Hs, Tm, and Tp). Based on the error indexes in Figure 5-15(a), (b), it is shown that the transfer function plays a good role in the correction of the spectral shape; the corrected results are also equivalent to the results of the wave parameters calculated after correction through the scaling factor.

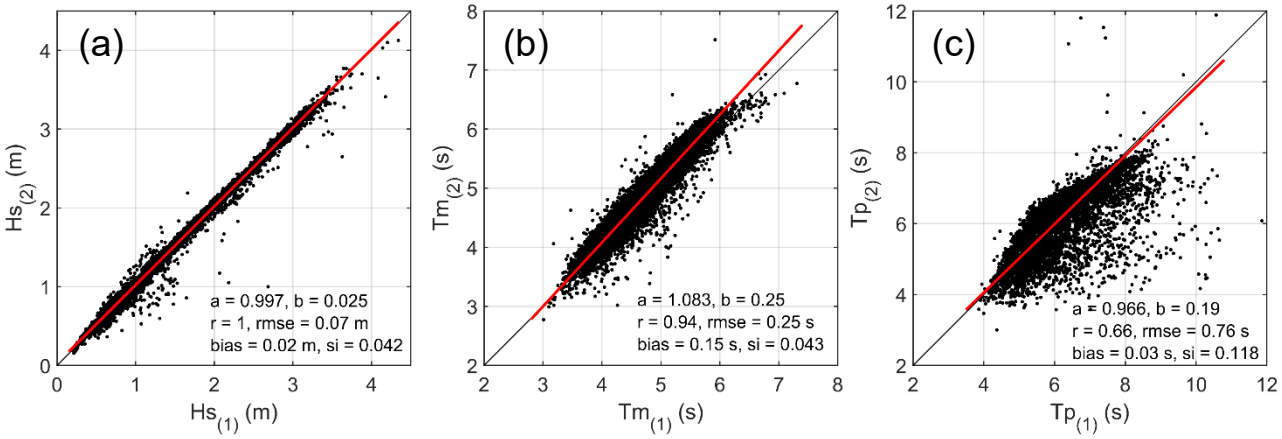

Figure 5-15 The comparison of the calibrated wave parameters using three constant scaling factors and the transfer function. Herein, calibrated significant wave height, mean period, and peak period comparisons are shown in (a), (b), and (c), respectively. In each panel, the horizontal axis shows the calibrated wave parameters using the newly scaling factors, while the vertical axis represents radar-deduced wave information using the transfer function. Black dots show the entire dataset, and red lines are regression lines.

C. The variability of wavefield mapping

It has been proved in the previous section that the radar-deduced wave parameters from a single HF radar system agree well with sea-truth data for one specific point. In this section, the spatial variability of the errors in the radar-deduced

wave field is focused. Spatial patterns of wave parameters, estimated using identical methods in chapters 3 and 5, will be examined.

Cai et al. [70] and Tian et al. [122] had demonstrated that the error indexes of significant wave height deduced by a single radar feature systematic bias depending on the radar-looking direction. In order to examine this issue, one-day averaged maps of wave parameters are illustrated in Figure 5-16. Figures 5-16(a), (b), and (c) are the spatial distribution of 1-day averaged radar-deducted wave height, mean period, and peak period with newly constant scaling factors ($\xi_{\mathrm{Hs}} = 0.786$, $\xi_{\mathrm{Tm}} = 0.896$, $\xi_{\mathrm{Tp}} = 0.965$) under the passage of a cold front winter monsoon, respectively. The averaged in-situ wave parameters from AWAC over one day are 2.91m of Hs, 5.3s of Tm, and 8.0s of Tp. In Figure 5-16(a), there is a symmetric pattern of extremely inhomogeneous wave height over the space domain with lower wave height near the radar boresight and significantly larger on outer bearings. The bathymetry is a gentle, mild slope with no shoal in the middle of the radar footprint. It indicated that the variability of estimated wave height at different radar bearings might be caused by retrieval algorithms, where radar-to-wave angle, θ_w, was not taken into account. Figure 5-16(b) and (c) show the estimated mean and peak period spatial distribution, respectively. It can see that the map of wave periods also exhibits a similar issue. To better view wave height variability, three intermediate factors for wave height estimation are shown in Figure 5-17. Herein, panel (a) represents the distribution of angle between radar beam and in-situ wave direction under winter monsoon conditions, panel (b) shows the distribution of total 1st- and 2nd-order energies, and the ratio between the 2nd-order over the 1st-order power is described in panel (c).

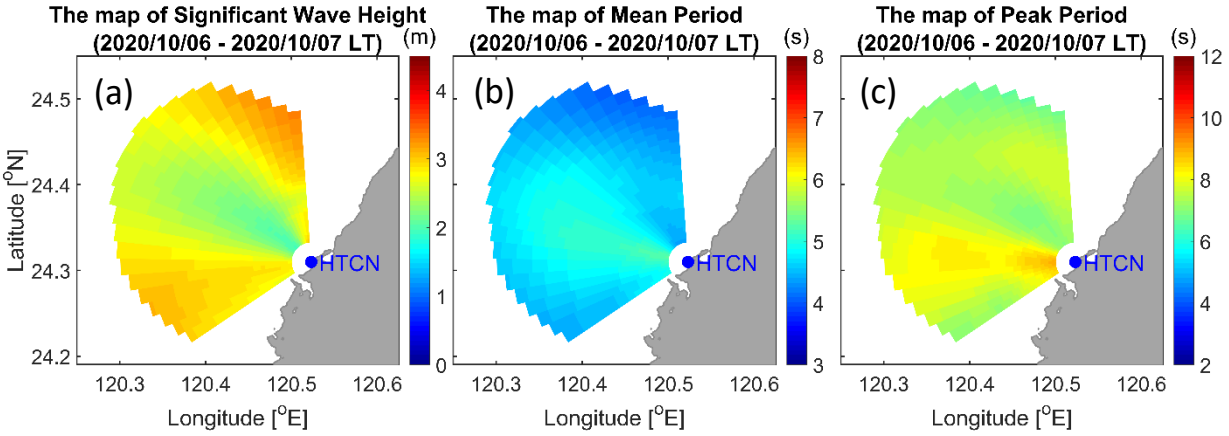

Figure 5-16 The spatial pattern of 1-day averaged radar-deducted Hs, Tm, and Tp under prevailing winter monsoon. Significant wave height, mean period, and peak period are estimated using Heron's formula with present scaling factors ($\xi_{Hs} = 0.786$, $\xi_{Tm} = 0.896$, $\xi_{Tp} = 0.965$) and illustrated in (a), (b), and (c), respectively. The 1-day averaged in-situ wave parameters from AWAC are 2.91m of Hs, 5.3s of Tm, and 8.0 s of Tp.

The colormap in Figure 5-17(a) shows the spatial distribution of θ_w, in which the variation of incident angles of waves due to the refraction effect in shoaling bathymetry has been considered. The value of θ_w nearly reaches 90° at the radar boresight and decreases gradually to the left and right sides. In panel (b), the solid and dashed lines represent the spatial variability of the 1st-order and weighted 2nd-order total energies, respectively. Then, the ratio of the weighted 2nd-order total energy over the 1st-order total energy is used to estimate significant wave height using (3.2) is shown in panel (c).

Similar to the wave height distribution in Figure 5-16(a), the value of the spectra energy ratio in Figure 5-17(c) is small in the orthogonal direction of the linear phased-array of radar receiver elements and significant increases in both outer bearings, which means that the issue of mapping wavefield is identified.

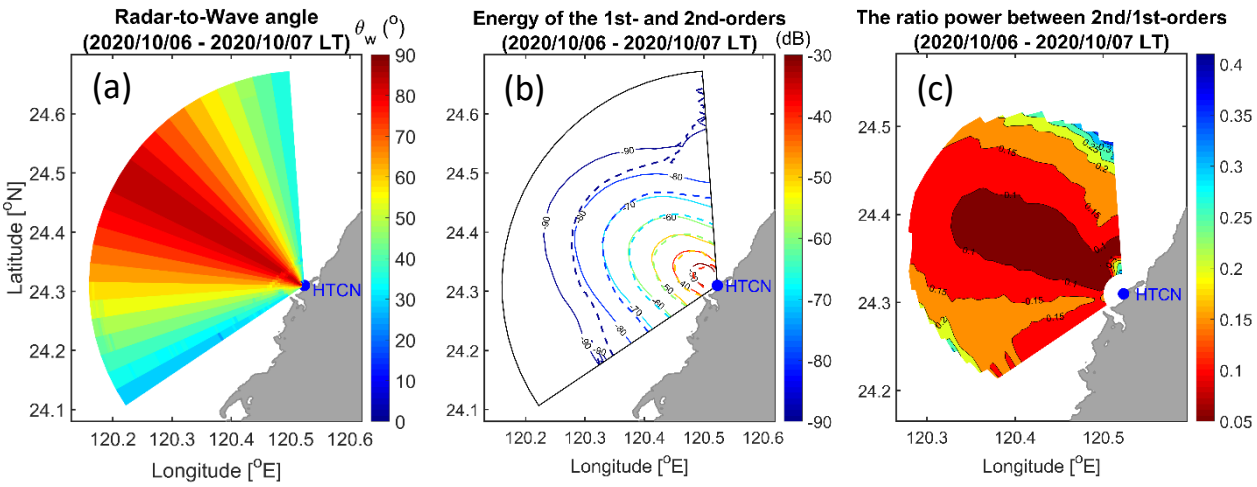

Figure 5-17 The spatial pattern of 1-day averaged value of intermediate factors for wave height estimation. Panel (a) shows the distribution of angle between radar beam and in-situ wave direction under winter monsoon conditions, panel (b) shows the distribution of total first- and second-order components, and panel (c) represents the ratio between the second-order over the first-order powers.

It has been mentioned already by Ulaby et al. [123] in the integral equation model (IEM), the backscattered sea-echo signals with respect to a given radar frequency are related to sea-surface roughness that is influenced by wind speed and vary under different wind directions such as upwind, downwind and crosswind. Accordingly, any geophysical model function (GMF) should consider sea water properties, radar parameters, observation geometry, and radar-looking direction. One of the important keys in the GMF is the angle between the radar bearing and wind or the Bragg wave direction. However, it has not yet been considered in existing estimators for wave parameters retrieval. As the maps of calibrated radar-deduced wave parameters using newly constant scaling factors need further correction, the scaling factor of wave parameters is assumed to be functions of additional factors instead of just constants. Relevant literature will be reviewed in the next section.

5.5 Wave Parameter Calibration

5.5.1 Introduction

Numerous correction methods have been proposed such as Barrick [14], Graber and Heron [18] & Heron and Heron [68], Essen et al. [88], Gurgel et al. [89], Alattabi et al. [64], and Shahidi & Gill [91]. The basic idea was to multiply the wave parameter by a factor to better fit the sea truth. The factor, called a scaling factor, was initially regarded as a constant, and then further considered as a function of smallness parameters, $\varsigma = k_0 h_{rms}$, and θ_w. Correction methods that use transfer function is the alternative of scaling factor, still, the consideration of the angle effects is not included.

Barrick [14] was the first to propose the scaling factors of Hs, and Tm as functions of smallness parameters using the power law. The angle between radar-looking direction and wave direction, θ_w, was also considered as the secondary factor. Theoretical values of the scaling factors with respect to certain values of θ_w were computed using numerical simulation and illustrated graphically. Barrick [14] addressed the importance of the wave direction in terms of the correction of the radar-deduced parameter to reduce the uncertainty. Due to the limited observation data, however, formulations of the scaling factors were not proposed.

Since then, methodologies of wave parameters retrieval had continued to progress in the next two decades, but did not focus on scaling factors until the late ’90s, when the WERA system became available, and the DUCK94 experiment and SCAWVEX Experiment were conducted. Graber and Heron [18], using one-week DUCK94 data, proposed the constant value equivalent to 0.682 of the scaling factor aiming for the significant wave height mapping using radar Doppler spectra. Using the same dataset from DUCK94 but in a different period, a value of 0.551 was

suggested by [68, 90] for the significant wave height scaling factor. The data from Shahidi and Gill [91] agreed with the results of Heron and Heron [68] under a calmer sea state. For moderate to severe sea states, Shahidi and Gill [91] gave a modified version of the scaling factor ranging from 0.55 to 1 depending on significant wave height. Among the above methods, the effects of wave direction were still not considered in the retrieval formula of the wave height scaling factor.

On the other hand, Gurgel et al. [89] and Alattabi et al. [64] used the spectral domain transfer function to estimate wave parameters from the Doppler spectra of HF radar data. However, the transfer functions were independent of the wave direction and smallness parameters. In 1999, Essen et al. [88] used a dual-radar system and proposed an empirical approach allowing retrieve wave height and mean wave direction at the footprint. In this process, the calibrated significant wave height was computed from an empirical formula consisting of the angle between estimated wave direction and radar bearing. However, the data from a dual-radar system is required for estimating both above wave parameters.

In conclusion, the scaling factor of wave parameters, may be influenced by the angle between the radar beam and the main wave direction, θ_w, especially for the single radar case, and smallness parameters. Both θ_w and ς play critical roles in the correction formulations for wave parameter scaling factors. Therefore the scaling factor of wave parameters cannot be ordinarily simplified as a constant over the sea states and wave direction. One of the aims of this study is to investigate the properties of the scaling factors using long-term data and to provide, if applicable, the correction formula that could be applied with different radar frequencies and sea states. In order to obtain a more detailed behavior of the scaling factor variation with respect to various wave fields, the numerical simulation will be implemented in the next section.

5.5.2 Correction methods

A. The E2E Simulation of wave parameter retrieval under Barrick's approach

In order to investigate the relationship between wave parameter scaling factors and the two above factors from a theoretical viewpoint, forward simulations of Doppler spectra based on Barrick's theory [5, 6, 56] are carried out. These simulated Doppler spectra are then used as inputs to the estimators for comparative study. This End-to-End Simulation (E2ES) toolbox is designed to simulate the Doppler spectra from the given input parameters, including the directional wave spectra, HF radar location and orientation, system parameters, and the signal-to-noise ratio (SNR). Then, existing estimators shown in section 2 are applied to retrieve Hs, Tm, and Tp from simulated Doppler spectra in the next step. The output results are compared to target values to obtain the scaling factors. The flowchart of the HF radar Doppler spectra simulation was already represented in chapter 2.

To simulate the Doppler spectra, the JONSWAP spectrum [61] and the cardioid directional spreading model [54] with Mitsuyasu's parameterization of the spreading factor [62] were adopted to generate the directional wave spectra as inputs. In the simulations, the wind speed at 10 meters height from the sea surface (U10) ranges from 2-15 m/s with the non-dimensional fetch limited, $\tilde{\chi}$ =10^4, wind direction is set as 30^o north, and the Mitsuyasu's wave spreading parameters are set from 2 to 15 for wind sea condition. For radar information, the radar frequency is operated at 27.75 MHz; the radar-looking direction is given in the range of 120^o-300^o, which makes θ_w is within the range of -90^o to 90^o. Examples of simulated Doppler spectra with respect to different θ_w and U10 were shown in Figure 2-9. The results of simulated Doppler spectra are comparable to those of Barrick & Lipa's results [56]. The comparisons of radar-deduced wave parameters retrieved from simulated Doppler spectra and target values are shown in Figure 3-5. Accordingly, the scaling

factors of Hs, Tm, and Tp as functions of θ_w are shown in Figures 5-18(a), (b), and (c), respectively. In Figure 5-18, dots denote simulated values every 5 degrees of θ_w using a self-developed E2ES toolbox, the color dots indicate the value of smallness parameters, and the solid lines represent the fitted curve using the $\cos^2(\theta_w)$ function.

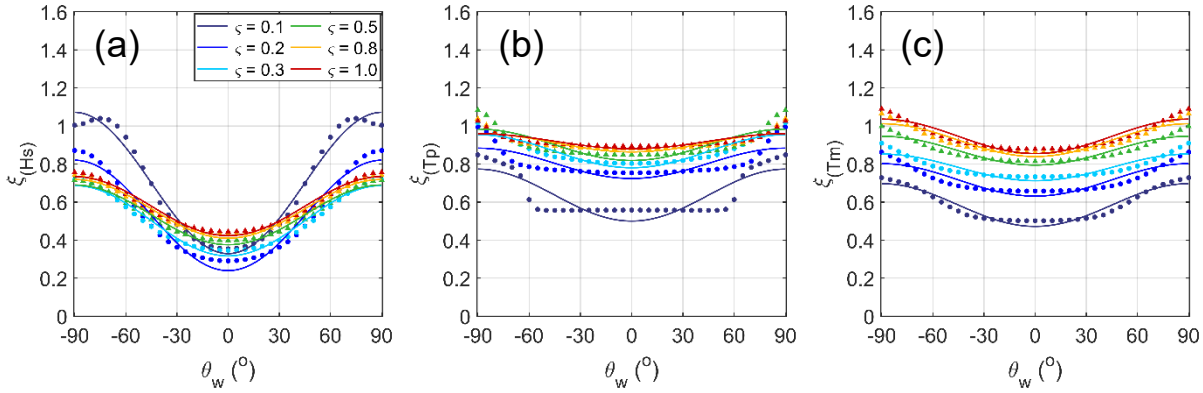

Figure 5-18 The scaling factors of simulated wave parameter estimations. Herein, the wave height, mean period, and peak period scaling factors with respect to radar-to-wave angle and smallness parameter are shown in (a), (b), and (c), respectively. Dots denote simulated values every 5 degrees of θ_w using self-developed E2ES toolbox. The curves are fitted based on the simulation results using the cos2 (θ_w) function.

To obtain the estimator for radar-deduced wave height nondirectional spectrum, as shown in (3.2), Barrick [14] has rewritten the form of the second-order spectrum of HF radar cross-section using the approximation of two following quantities. First, the coupling coefficient, which is the function of radar Doppler frequency and integration parameters, was replaced by an approximation that still remains functional for Doppler frequency but was averaged over the variable of integration, called the weighting function. The weighting function, determined from the theoretical model, can allow reducing the dependency of results on both the wave

spectrum directionality form and the radar-to-wind angle. Second, the double integrand of the 2nd-order spectrum equation can be derived in the single integrand form when the delta function is eliminated by integrating the entire equation with respect to Doppler frequency. The new form allows computing the root-mean-square wave height from the ratio when dividing the weighted 2nd-order Doppler sidebands by the 1st-order spectral energy. Due to the two above approximations, the effect of directionality caused by the variation of changing the radar-to-wind angle and the spectrum shape has been minimized, but not completely disappeared from Barrick's results. As a sec of results, Figure 5-18 shows the effect of θ_w to wave parameter scaling factors, which were retrieved from the End-to-End simulation under various weather conditions.

Figure 5-18 first shows that the wave parameter scaling factors are symmetric to $\theta_w = 0^o$. All those scaling factors feature the minimum value when the radar-looking direction and the wave direction are parallel, and reach the maximum when the two above directions are orthogonal. Figure 5-18(a) shows that the significant wave height deduced from simulated radar Doppler spectra is overestimated compared to the target value. It is consistent with Barrick's discussion [14]. The variation of wave height scaling factors is significantly changed when the smallness parameters are less or greater than 0.3. For $0.1 < \varsigma < 0.3$, ξ_{H_S} is close 1 when $|\theta_w|$ is in the range of 60^o-90^o, and becomes minimum when $\theta_w = 0^o$. Meanwhile, ξ_{H_S} is stable with $\varsigma \geq 0.3$, and is significantly changed with respect to the value of θ_w. It indicated that the scaling factor of significant wave height is influenced by both θ_w and ς under low sea-states, and only is dependent on θ_w for moderate and severe sea-states.

Figures 5-18(b) and (c) show the change of simulated wave period scaling factors with respect to radar-to-wave angle and smallness parameter. The results

show that wave periods deduced from simulated Doppler spectra are almost overestimated compared to the target values. In addition, the tendency of wave period scaling factors under the change of θ_w is identical with those of the wave height scaling factor, which is minimum when θ_w=0°, and it increases to maximum when radar bearing is perpendicular to wave direction. The fitted regression curves relevant to different smallness parameters are almost parallel to each other. It demonstrated the crucial role of sea-states in the uncertainty of wave period estimated from radar Doppler spectra.

It is found that the scaling factor of the three above radar-deduced wave parameters is dependent on both the angle between the radar-looking direction and the main wave direction and sea-state conditions. Figure 5-18 shows that the $\cos^2(.)$ function presents well the relationship between radar-to-wave angle and wave parameter scaling factors, while the power function had been demonstrated as a good model describing the relationship between wave parameter scaling factors and smallness parameters. In this study, we aim to test and assess the performance of numerous empirical formulas for choosing a better fit model, which is used to calibrate radar-deduced wave parameters using θ_w and ς.

B. The correction method for the wave height scaling factor

1. The cosine function

In 1999, Essen et al. [88] first proposed an empirical formula for computing radar-deduced wave height from in-situ wave height weighted a $\cos^2(.)$ function of half of the angle between radar-looking direction and mean wave direction. The mean wave direction at peak frequency could be estimated from the Doppler spectra of a dual-radar system; the Hs deduced from the radar Doppler spectra is assumed in a linear relationship with the total variance composed from both Bragg lines. This

means that the angle between radar-looking direction and mean wave direction play the main key role in the exact determination of significant wave height.

On the other hand, Ulaby et al. [123] found that the backscattering coefficient of the ocean surface, σ^0, observed from microwave radar under the upwind is slightly greater than those in the downwind. Therefore, a cos2(.) function was suggested to represent the relationship between σ^0 and radar-to-wind angle. However, the radio wavelength of the microwave radar only interacts with the ocean waves having a short wavelength of centimeters or capillary waves based on the Bragg scattering mechanism, while the EM wave at HF bands resonances to surface waves with a few tens of meters wavelength, which are gravity waves traveling over the ocean. The fact that the HF radar Doppler spectra under upwind and downwind conditions are equivalent. This discussion can be demonstrated by using the E2ES toolbox. Though, there exists a relationship between cos2(.) and $\cos^2(.)$. Therefore, the cos2(.) function could be used as a potential function for calibrating radar-deduced wave height using the radar-to-wave angle.

Based on the literature review as well as the E2ES's result in the previous section, the $\cos^2(.)$ function was the best fit for describing the change of the wave height scaling factor, ξ_{H_S}, under the variation of the radar-to-wave angle. The correction function form could be given as follows:

$$\xi_{H_S} = a_1 + a_2 \cos^2(\theta_w) \tag{5.18}$$

In which, a_1 and a_2 are two empirical parameters of (5.18), and $\theta_w = \alpha_w - \theta_N$ is the angle between the radar-looking direction and the main wave direction. The value of empirical parameters in (5.18) can be determined using the synchronized data of in-situ and radar measurements. The most crucial advantage of (5.18) is that this function can be used to calibrate wave height in the space domain, such as the wavefield in Figure 5-16(a). The disadvantage is that the input wave direction

collected by in-situ instruments is limited in the space domain due to the high investment cost.

2. The power function

In 1977, Barrick [14] proposed a formulation describing the relationship between ξ_{H_S} and ς based on the power law. In the previous section, it was discussed that the scaling factors of radar-deduced wave parameters are influenced by smallness parameters. Therefore, the form of correction function for wave height scaling factor can be proposed as:

$$\xi_{H_S} = b_1 + b_2 \varsigma^{b_3} \tag{5.19}$$

In equation (5.19), b_1, b_2, and b_3 are three empirical parameters. Herein, b_1 represents the independent empirical parameter, b_2 and b_3 are the scale and the power value of the power function. It can be seen that significant wave height has existed on both sides of (5.19). To solve the above issue, an iteration procedure can be implemented to get the optimal value of Hs. This loop can stop when ΔHs between two consecutive loops is less than 0.1% of the estimated wave height. This method might reduce the uncertainty of estimated wave height under low sea states compared to corrected wave heights using a constant scaling factor. It was found that this correction method is not able to solve the issue of wave height variability over the space domain, as shown in Figure 5-16(a), using the in-situ data recorded at a single point.

3. Evaluation of correction algorithm

To validate the correctness of equations (5.18) and (5.19), we computed the value of empirical parameters in the two above equations by fitting the co-location and co-time wave data measured from AWAC and the HF radar station. Figure 5-

19(a) and (b) show the variation of wave height scaling factor (vertical axis) under the change of θ_w and ς (horizontal axis), respectively. In Figure 5-19(a), each square dot represents one observation with its averaged smallness parameter showing in color. The blue- to dark-red solid curves are the regression curves of E2ES data regarding the smallness value of 0.1, 0.2, 0.3, 0.5, 0.8, and 1.0, shown in Figure 5-18. Red triangles denote the average value of ξ_{Hs} in every 5° radar-to-wave angle, and the thicker red dashed line is the regression curve using (5.18) fitted on those red triangles. Meanwhile, each square point in panel (b) represents one observation with its density that is shown in color; the red line shows the fitted curve using (5.19), black solid, dashed- and dashed-dotted lines show E2ES results of the wave height scaling factor concerning $\theta_w = 0^o$, 45°, and 90°, respectively.

Figure 5-19(a) shows that the value of θ_w is separated into two main groups of wave direction, as shown in Figure 5-12 when the wave field is controlled by the wind from north-east and south-west directions. It was also found that the smaller wave height was overestimated, while most of the larger wave height was underestimated. The wavefield from the S-W direction is co-line with the bearing from radar to AWAC's location, making the strongest overestimation of radar-deduced wave height. In contrast, the wave height scaling factor is close to 1 when the angle between the radar-looking direction to AWAC and the wavefield from the N-E direction is in the range of 40° to 90°. By fitting (5.18) with red triangles, the tendency between the model function and the data is highly correlated with a 0.8 correlation coefficient. This means the proposed formula is fitted well with the wave height scaling factor variation corresponding to radar-to-wave angle. In another respect, Figure 5-19(b) shows that the radar-deduced wave height was extremely overestimated under low sea-states (ς < 0.3), and they were matched to each other under middle and severe sea-states (ς > 0.3). This is consistent with the E2ES results in the previous section. In this study, the value of the smallness parameter is over

10% compared to the threshold value of the perturbation theory, but those data are limited. It means that Barrick's approach [14, 66] is still correct.

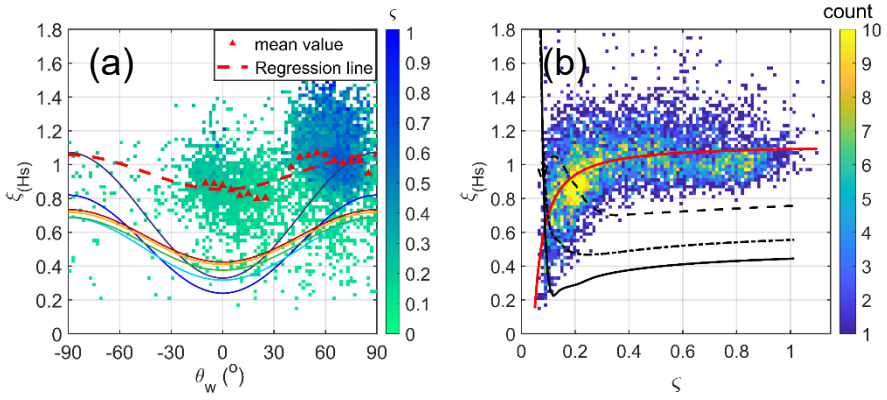

Figure 5-19 The relationship between radar-to-wave angel (θ_w), smallness parameter (ς), and the wave height scaling factor. In panel (a), each dot on the graphs represents one observation, and its color denotes the corresponding smallness parameter. The red triangles are the bin-average value of the data, based on which, the thick-dash red curves were fitted. Solid lines with various colors are the fitting curves from simulations, which are identical to those in Figure 5-18. For panel (b), each dot on the graph represents one observation, and its color denotes the density value (count). The solid red line shows the fitting curves based on the whole data, and solid, dashed- and dashes dots lines show the theoretical value of wave height scaling factor at the radar-to-wave angle value of 0°, 45°, and 90°, respectively.

Meanwhile, Figure 5-19(b) shows the well fit between real observation and the power law (the solid red line). A value of 0.52 for the correlation coefficient demonstrated the minor dependence of the wave height scaling factor on the sea state condition. It can be seen that the red curves are almost parallel to black lines, which is the result of the E2E simulation for different radar-to-wave angles, for ς > 0.2. The difference between red and black lines is only an offset value. It may be caused by

the normal distribution width of the simulated first-order Doppler spectrum. Similarly, both simulation and actual data provide the high uncertainty of radar-deduced wave height under low sea states.

Based on synchronized data of in-situ and radar measurements, the values of empirical parameters in (5.18) were calculated and listed in Table 5-6. It can be seen that the meaning of a_1 in (5.18) and b_1 in (5.19) are similar. In addition, the scaling factor of wave height is dependent on both θ_w and ς. It means (5.18) and (5.19) can be combined to deduce a better value of ξ_{Hs}. Following that idea, we proposed a multivariable function showing the relationship between ξ_{Hs} and both θ_w and ς, which can be formed as follows:

$$\xi_{Hs} = a_1 + a_2\cos^2(\theta_w) + b_2\varsigma^{b_3} \tag{5.20}$$

Herein, only a_1 is used to represent the independent parameter, a_2 is the scale value of the harmonic function, b_2 and b_3 are the empirical parameters of the power function. As a result, the values of the four above empirical parameters were calculated and tabulated in the last column in Table 5-6.

Table 5-6 The estimated empirical parameter values for the correction function of wave height scaling factor.

Statistical parameters	$\xi_{Hs} = f(\theta_w)$	$\xi_{Hs} = f(\varsigma)$	$\xi_{Hs} = f(\theta_w, \varsigma)$
r	0.80	0.55	-
a_1	1.058	-	1.115
a_2	-0.204	-	-0.101
b_1	-	1.116	-
b_2	-	-0.025	-0.010
b_3	-	-1.225	-1.557

This section introduced the relationship between two source variables (θ_w and ς) and the scaling factor of radar-deduced significant wave height. Accordingly, three correction algorithms were proposed. The estimated values of empirical parameters in (5.18), (5.19), and (5.20) were tabulated in Table 5-6. Later, the error indexes of calibrated wave height will be assessed to prove the performance of the three above formulas. In another respect, equation (5.18) provides a tool for calibrating wave height in the space domain if wave direction is given. Although the wave direction from hindcast models can be taken, its resolution is lower than those of the HF radar system at the HTCN station. In this article, the direction of ocean waves over the radar's footprint can be estimated from the in-situ wave data based on the wave refraction phenomenon in narrow water areas using the snell law. In addition, it is only computed the wave direction under the middle and severe sea states $\left(\mathrm{H_s} > \frac{1}{\mathrm{k_0}}\right)$ when the wavefield in the middle of the Taiwan strait is mainly driven by monsoon winds. Another issue is that the Taiwan Strait area is too tiny for typhoon conditions compared to the typhoon's domain. In that case, typhoon wind can be considered homogeneous, except the typhoon trajectory pass to the study area. On the other hand, equation (5.19) could be applied to correct radar-deduced wave heigh under low sea states.

C. The correction method for radar-deduced wave period

1. The cosine function

Similarly, the results of E2ES indicated that the scaling factors of mean and peak periods are the function of radar-to-wave angle following the Hamonic law. Accordingly, two formulas representing the relationship between mean and peak period scaling factors and θ_w are proposed as follows:

$$\xi_{T_m} = a_1 + a_2 cos^2(\theta_w) \tag{5.21a}$$

$$\xi_{T_p} = a_1 + a_2 cos^2(\theta_w) \quad (5.21b)$$

In which, a_1 and a_2 in (5.21a) and (5.21b) can be determined based on the corresponding data of mean and peak wave periods.

2. The power function

As discussed in the previous section, sea-states play a crucial role in correcting radar-deduced wave periods. In a similar way, the formula shows the relationship between wave period scaling factors and smallness parameters can be given as follows:

$$\xi_{T_m} = b_1 + b_2 \varsigma^{b_3} \quad (5.22a)$$

$$\xi_{T_p} = b_1 + b_2 \varsigma^{b_3} \quad (5.22b)$$

Herein, b_1, b_2, and b_3 in (5.22a) and (5.22b) can be determined from the synchronized data of mean and peak wave periods.

3. The relationship between wave period scaling factors and spectra width parameters

Based on the theory of wave period computation, it is clear that the spectrum shape influences the value of the wave period. The correction coefficient of wave period is related to spectra width parameters. Besides, Figure 5-13 demonstrated that radar-deduced wave frequency is highly correlated to in-situ wave frequency under the sea state mainly controlled by the wind field, and is low correlated under typhoon conditions dominated by swells. It indicated that spectral width might be one of the essential factors affecting the accuracy of the radar-deduced wave period. To create the formula showing the relationship between spectral width and the scaling factor of wave period, we fitted the in-situ spectra width and wave period scaling factor using the Matlab toolbox. It was assumed that the scaling factor of the period would

not affect spectra shape if the spectra width reached the threshold value. Then, the proposed formula is given in the form as follows:

$$\xi_{T_m} = \left(\frac{-\sqrt{\ln\left(\epsilon_s / c_1\right)} - c_3}{c_2} \right) \text{for } \ln\left(\epsilon_s / c_1\right) \geq 0$$
$$= \left(\frac{\left|\sqrt{\ln\left(\epsilon_s / c_1\right)}\right| - c_3}{c_2} \right) \text{for } \ln\left(\epsilon_s / c_1\right) < 0 \quad (5.23a)$$

$$\xi_{T_P} = \left(\frac{-\sqrt{\ln\left(\epsilon_s / c_1\right)} - c_3}{c_2} \right) \text{for } \ln\left(\epsilon_s / c_1\right) \geq 0$$
$$= \left(\frac{\left|\sqrt{\ln\left(\epsilon_s / c_1\right)}\right| - c_3}{c_2} \right) \text{for } \ln\left(\epsilon_s / c_1\right) < 0 \quad (5.23b)$$

Whereby, c_1, c_2, and c_3 are empirical parameters of (5.23a) and (5.23b), $\epsilon_s = \sqrt{\frac{m_0 m_4 - m_2^2}{m_0 m_4}}$, is the spectra width parameter [124]. Here, m_0, m_2, and m_4 are the zero-, the second- and the fouth- moments.

The empirical parameters in (5.23a) and (5.23b) can be determined from the wave parameters' synchronized data. It also means that wave period estimated from radar backscattered data can be calibrated using spectral width information. Although the method is capable, the in-situ data are often limited in space due to the high cost. The spectra width parameter deduced from the radar Doppler spectra can be used as a promising alternative.

4. Evaluation of correction algorithm

In order to verify the correctness of (5.21), (5.22), and (5.23) for determining wave period scaling factors, the simulation and actual data were used, as shown in

Figures 5-20 and 5-21. Figure 5-20 shows the relationship between the scaling factor of the mean period and θ_w, ς, and ϵ_s. The concept of Figures 5-20(a) and (b) are similar to those in Figure 5-19, while the horizontal axis of Figure 5-20(c) represents the spectra width parameter, and the vertical axis shows the value of ξ_{T_m}. Herein, each square dot represents one observation with the corresponding density (count). The solid red line is the fitted curves using (5.23).

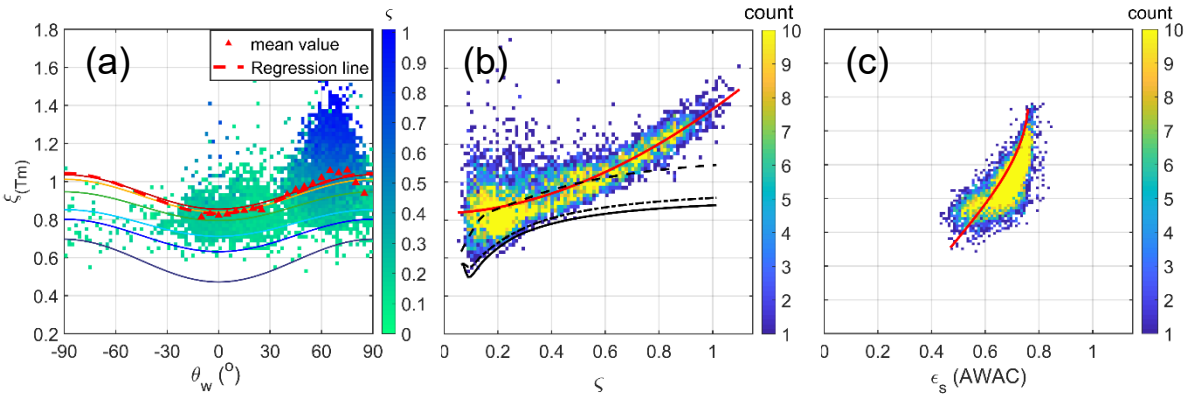

Figure 5-20 The relationship between the radar-to-wave angle (θ_w), smallness parameter (ς) and spectral width parameter (Єs), and the mean period scaling factor. In panel (a), each dot on the graphs represents one observation, and its color denotes the corresponding smallness parameter; the red triangles are the bin-average value of the data, based on which, the thick-dash red curves were fitted; solid lines with various colors are the fitting curves from simulations, which are identical to those in Figure 5-18. For panels (b) and (c), each dot on the graphs represents one observation, and its color denotes the density value (count); the solid red line shows the fitting curves based on the whole data. Solid, dashed- and dashes dots black lines in panel (b) show the theoretical value of the mean period scaling factor when θ_w equals 0°, 45°, and 90°, respectively.

In Figure 5-20(a), the radar-deduced mean wave period is underestimated with increasing sea-state (less than 20-40%). This is because the backscattered signal of

swells could be merged into the first-order regions when smallness parameters reach nearly the saturated condition. It means only backscattered signals relevant to wind-wave components have existed in second-order regions. Although, the observation data is well agreed with the simulation data (r = 0.92). It demonstrates the reliability of our E2ES toolbox and indicates the influence of radar-to-wave angle on the variation of the mean period scaling factor. The value of the empirical parameter in (5.21a) for estimating ξ_{T_m} from θ_w is determined by using the fitting technique.

In another respect, the classification of wave period scaling factors for various smallness parameters could be recognized in Figure 5-20(a). Then, the dependency of the mean wave period scaling factor to the smallness parameter was illustrated in Figure 5-20(b) with a correlation coefficient of 0.81. It can be seen that the simulated data (black lines) agree with the real observation, except for the state of $\varsigma > 0.6$. In this study, the wave period data has crossed the upper range in figure 5 of Barrick's report [14]. We believe that (5.22a) provides a better fit for the relationship between ξ_{T_m} and ς than the plotted curves in the previous litterature [14]. The parameter value of (5.22a) was determined and listed in Table 5-7. In addition, Figure 5-20(c) illustrated the influence of spectra width parameters on the scaling factor of the mean period even though the transfer function was used to adjust the result of radar-deduced wave parameters. The correlation coefficient was 0.76 (see Table 5-7). It can be seen that the red curve for ξ_{T_m} approaches unity asymptotically for a specific value of ϵ_s, where m_2^2 is much smaller than $m_0 m_4$. It means that ξ_{T_m} freed from the influence of ϵ_s when the spectra width is narrow enough. Based on the synchronized data of radar and in-situ measurement, the value of empirical parameters in (5.23a) was estimated and listed in Table 5-7.

Table 5-7 The estimation value of the empirical parameters for correction functions of the mean period scaling factor.

Statistical parameters	$\xi_{T_m} = f(\theta_w)$	$\xi_{T_m} = f(\varsigma)$	$\xi_{T_m} = f(\theta_w, \varsigma)$	$\xi_{T_m} = f(\epsilon_s)$
r	0.92	0.81	-	0.76
a_1	1.044	-	0.887	-
a_2	-0.212	-	-0.075	-
b_1	-	0.837	-	-
b_2	-	0.547	0.514	-
b_3	-	1.825	2.048	-
c_1	-	-	-	0.759
c_2	-	-	-	-0.801
c_3	-	-	-	1.100

Figure 5-21 shows the dependence of the peak wave period scaling factor on source factors, which are θ_w, ς, and ϵ_s. The content of Figure 5-21 is similar to those of Figure 5-20**.** From Figure 5-21, the peak period scaling factor's uncertainty is more prominent than those of the mean period scaling factor (see Figure 5-21(a)). Firstly, this is because the radar-deduced peak period is sensitive due to the ship's echoes, and noise interference. In addition, the extremely underestimation of the peak period under severe sea-states could be due to the lack of lower frequency components mixed into the first-order area in saturated conditions. It can be seen that the dependence of wave period on the radar-to-wave angle is discernible. That is proven by 0.72 for the correlation coefficient between the fitting curves (the red dashed line) and real observation data (red rectangles). Then, the estimation value of empirical parameters in (5.21b) was listed in the second column in Table 5-8.

Figure 5-21(b) shows a high correlation between the scaling factor of peak period and smallness parameter under normal and high sea state conditions, while it is a low correlation under the sea calm condition. The fact is that the peak wave period is easily influenced by radio background noise, active noise, and vessel echoes in low sea-states due to low SNR of 2nd-order components, while the energy of wind waves dominates in 2nd-order sidebands with stronger SNR. Besides, the real observation of ξ_{T_p} is well fit with the theoretical curves when ς is less than 0.4, and becomes overestimated in other cases. It is only because the energy of swells from the real observation was blended in the 1st-order area. Further, the value of 0.48 for the correlation coefficient between actual data and fitting curves using (5.22b) indicated that ς is one of the essential factors for correcting ξ_{T_p} under middle and severe sea states. Notable, the transfer function was used to calibrate the radar-deduced peak period. Therefore, it is perfectly possible that the correlation value is reduced. Later, the empirical parameter value of (5.22b) was tabulated in Table 5-8.

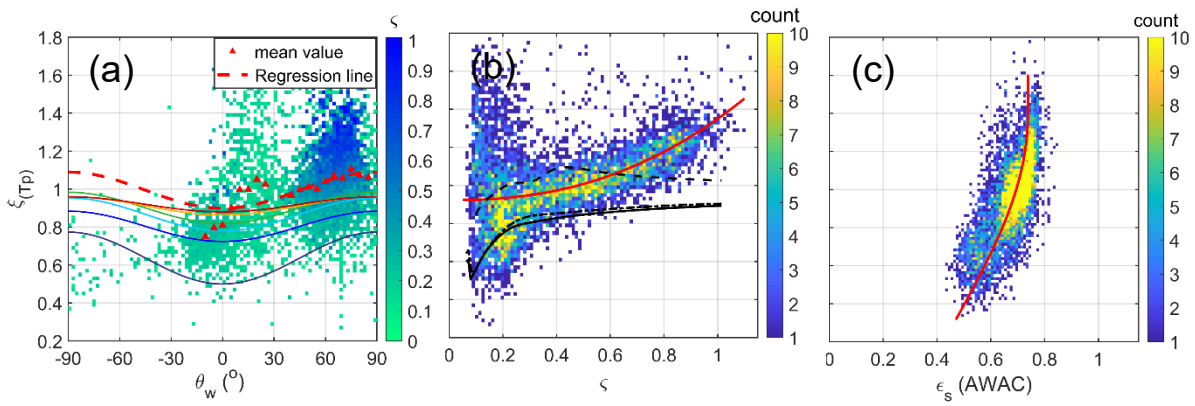

Figure 5-21 The relationship between the radar-to-wave angle (θ_w), smallness parameter (ς), and spectral width parameter (ϵ_s), and the peak period scaling factor. In panel (a), each dot on the graphs represents one observation, and its color denotes the corresponding smallness parameter; the red triangles are the bin-average value of the data, based on which, the thick-dash red curves were fitted; solid lines with various colors are the fitting curves from simulations, which are identical to those in Figure 5-18. For panels (b) and (c), each dot on the graphs represents one observation, and its color denotes the density value (count); the solid red line shows the fitting curves based on the whole data. Solid, dashed- and dashes dots black lines in panel (b) show the theoretical value of the peak period scaling factor when θ_w equals 0°, 45°, and 90°, respectively.

Similar to the mean wave period scaling factor, we look for the relationship between ξ_{T_p} and ϵ_s. Indeed, the correlation coefficient is 0.71 (Table 5-8). The red curve for ξ_{T_p} also approaches unity asymptotically for a specific value of ϵ_s precisely like those of ξ_{T_m}. The value of empirical parameters in (5.23b) was estimated using fitting techniques (see Figure 5-21(c)), and tabulated in Table 5-8.

Table 5-8 The estimation value of the empirical parameter for correction functions of the peak period scaling factor.

Statistical parameters	$\xi_{T_p} = f(\theta_w)$	$\xi_{T_p} = f(\varsigma)$	$\xi_{T_p} = f(\theta_w, \varsigma)$	$\xi_{T_p} = f(\epsilon_s)$
r	0.72	0.48	-	0.71
a_1	1.089	-	0.984	-
a_2	-0.191	-	-0.109	-
b_1	-	0.923	-	-
b_2	-	0.427	0.386	-
b_3	-	2.334	2.809	-
c_1	-	-	-	0.738
c_2	-	-	-	-0.621
c_3	-	-	-	0.868

Due to the lack of in-situ spectra width parameters, we computed the relationship between spectra width parameters estimated from radar data and those of in-situ data. The estimated results are shown in Figure 5-22. We assumed that the spectra width within the radar's footprint correlates to each other, and radar SNR meets the requirement. The spectra width of whole points covered by the radar system at the HTCN station can be computed from the result in Figure 5-22. As sequentially, the wave period is calibrated using (5.23).

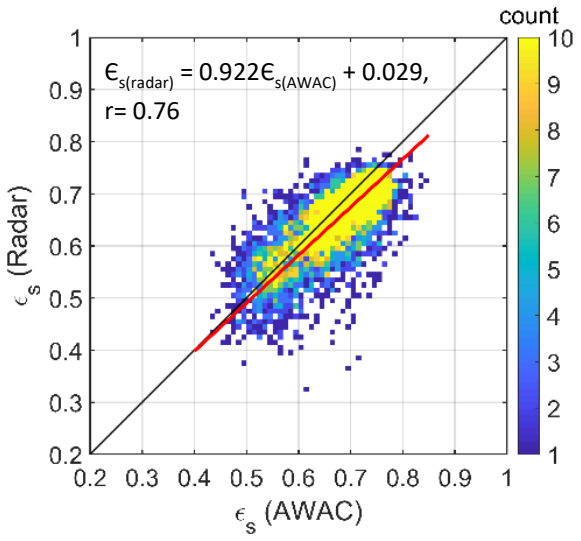

Figure 5-22 The relationship between the spectral width parameter from radar and those of in-situ wave data.

On the other hand, we applied the multivariable function to describe the relationship between wave period scaling factors and both θ_w and ς. The formulas are given as follows:

$$\xi_{T_m} = a_1 + a_2 cos^2(\theta_w) + b_2 \varsigma^{b_3} \quad (5.24a)$$

$$\xi_{T_p} = a_1 + a_2 cos^2(\theta_w) + b_2 \varsigma^{b_3} \quad (5.24b)$$

Herein, a_1, a_2, b_2, and b_3 in are estimated from the synchronized data of mean and peak periods. The estimated values of those empirical parameters were tabulated in Tables 5-7 and 5-8.

This session has illustrated the dependence of correction coefficients of wave parameters on the radar-to-wave angle, smallness parameters, and spectra width parameters. Whereby, the scaling factor of significant wave height is mainly influenced by θ_w and ς, while wave period scaling factors are affected by one more factor, which is spectral width parameters. Based on their relationship, four different correction methods of wave parameter scaling factors were proposed. To assess the

method's performance, error indexes estimated from the wave parameter inter-comparison will be used. The comparison result will be discussed in the next session to select the optimal method for correcting those scaling factors.

5.5.3 Results and Discussions

In order to assess the efficiency of correction methods for calibrating radar-deduced wave parameters, the error indexes between calibrated and in-situ wave parameters are used. The comparison results are shown in Figures 5-23 to 5-25. Overall, the bias estimation of calibrated wave parameters significantly decreases when the correction method is applied.

Accordingly, the value of root-mean-square error (RMSE) and scatter index (SI) was slightly reduced for Hs compared to using the newly wave height scaling factor, and they are approximately 35% and 15% for Tm and Tp, respectively. It was confirmed that the calibration of radar-deduced wave parameters is necessary, especially for the radar-deduced wave period. In detail, Figure 5-23 represents the comparison of significant wave height. Regarding the correction methods, panel (a) shows the value of wave height using a constant empirical value; panels (b) and (c) show the corrected wave height using smallness parameters and in-situ wave direction, respectively; and panel (d) show the calibrated wave height using the multivariable function with the attending of both smallness parameters and in-situ wave direction.

In Figure 5-23, the minimum value of RMSE, mean absolute error (MAE), and SI are 0.231 m, 0.178 m, and 0.140, respectively. This accuracy is much better than the reported results listed in table 7 [64]. Also, the results of wave height error indexes show that the calibration method using radar-to-wave angle performs better than those of others (Figure 5-23(c)).

It can be seen that the correction method's results used radar-to-wave angle values is consistent with the discussion in [88]. Previously, several authors had discussed the effect of wave direction on radar-deduced significant wave height. Though, due to the lack of real measurements, no supporting from simulation results, or using the dual-radar system, the dependence of wave direction is concluded as a minor term and almost ignored [14, 28, 66, 122]. Meanwhile, Cai et al. [70] used the radar-looking direction to calibrate Hs instead of wave direction or radar-to-wave angle. This study demonstrated the importance of θ_w for correcting radar-deduced significant wave height under severe sea-state conditions driven by monsoon winds. Further, the method also allows calibrating wave parameters in the space domain with the limitation of in-situ data. Of course, this method is able for the narrow area, such as the Taiwan Strait, mainly driven by the monsoon wind field. For other regions where the wave field is complicated, a dual-radar system and various locations of in-situ wave data are advised to use for calibrating wave parameters retrieved from radar Doppler spectra.

In this study, the error indexes of calibrated Hs using a constant scaling factor are slightly higher than the method using (5.18) (Figure 5-23(a)). However, the synchronized data of wave height is indeed by the N-E winter monsoon. Therefore, the percentage of waves from other directions is only minor and does not clearly show the dependence of ξ_{H_s} on θ_w. In addition, a slope of 0.92 indicated that the constant correction value of 0.786 is only suitable for calibrating smaller wave heights, while others are underestimated. In contrast, equation (5.19) can be able to correct Hs at different sea states. Figure 5-23(b) shows that the calibrated Hs are overestimated by approximately 5.1% compared to in-situ wave height. The regression curves in Figure 5-19(b) also showed the overestimation of calibrated wave height when $\varsigma > 0.6$. This means only ς maybe not be enough to correct the scaling factor of significant wave height. By applying the multivariable function with

the attending of radar-to-wave angle and smallness parameter and estimated empirical parameters in Table 5-6, the calibrated wave height was computed. Then, the comparison was shown in Figure 5-23(d). The comparison results illustrated that θ_w did not play the key role in (5.20), and ξ_{H_s} is significantly influenced by ς under low sea-states following the power law. However, the effect of the smallness parameter to wave height scaling factor might be reduced under intermediate and severe sea states. This discussion is similar to those in the literature [33]. Finally, it can conclude that the scaling factor of Hs is mainly affected by radar-to-wave angle.

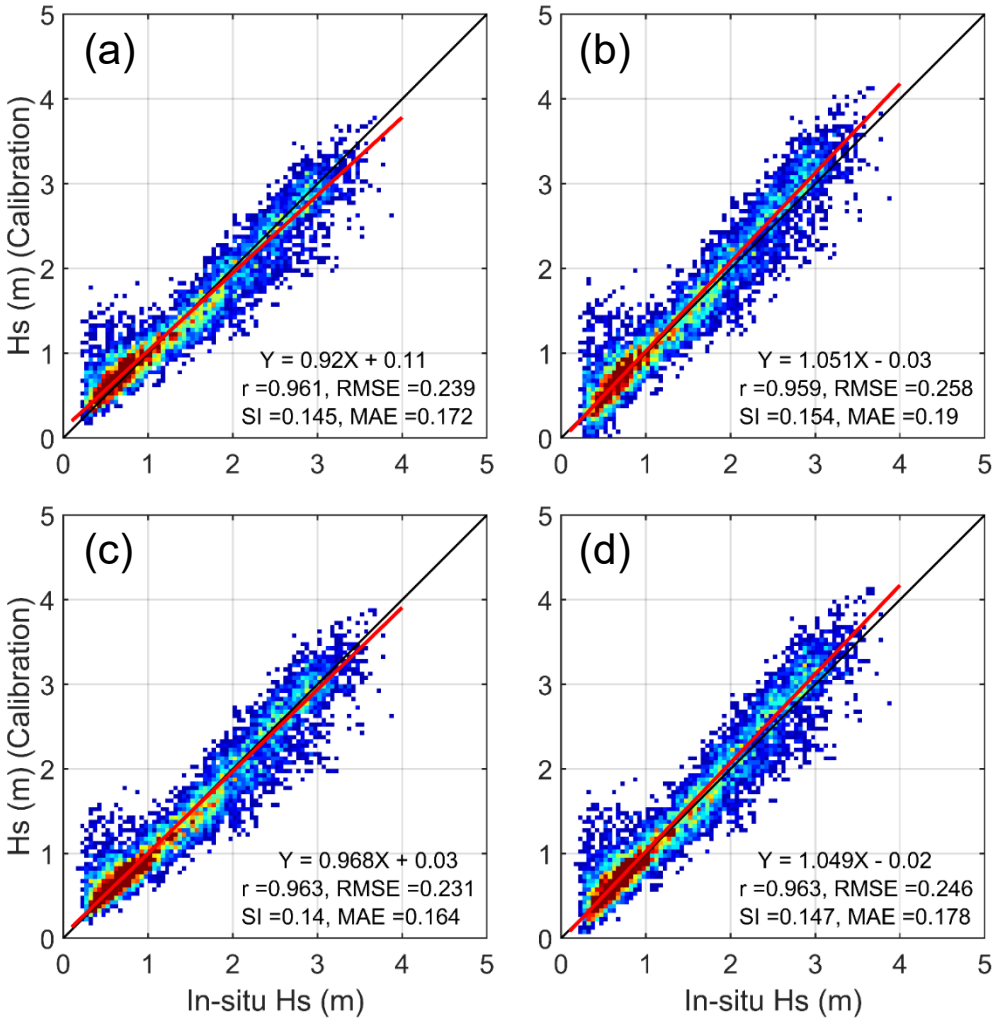

Figure 5-23 Scatter plots of significant wave height between calibrated and in-situ measurements. Regarding the correction methods, panel (a) shows the value of wave height using a constant empirical value, while panels (b), (c), and (d) show the corrected wave height using smallness parameters, in-situ wave direction, and both variables, respectively.

To assess the uncertainty of the calibrated mean period, the results of the mean period comparison are shown in Figure 5-24. Regarding the correction methods, panel (a) shows the comparison of the calibrated mean period using a constant scaling factor, panels (b) and (c) show those of the corrected mean period using

smallness parameters and in-situ wave direction, respectively, panel (d) shows the result of the calibrated mean period using above smallness parameters and wave direction, and panels (e) and (f) show the value of the mean period using in-situ and estimated spectra width parameters, respectively.

The comparison results show that the lowest error indexes of the calibrated mean period are 0.51s, 0.39s, and 0.104 for RMSE, MAE, and SI, respectively (see Figure 5-24(d)). It can be seen that the error indexes at panels (b) and (d) are nearly identical. It means that the bias estimation of calibrating Tm using (5.21a) and (5.24a) are similar. In addition, the new correlation coefficient is approximately 0.87, which is much greater than the initial value, as shown in Table 5-3. This result reaches near the top accuracy of Tm compared to those of the literature, such as in [64]. This means that the calibration of the mean period reduces the bias estimation of the radar-deduced mean period.

It can be seen that the possibility of calibrating Tm using a constant scaling factor (Figure 5-24(a)) is insufficient. Meanwhile, the results in Figures 5-24(b) and 5-24(d) show the reasonableness of calibrated wave period based on the value of the smallness parameter. It means correction methods using ς provide almost the best accuracy of Tm estimation compared to those of other methods. The existence of radar-to-wave angle in (5.21a) is useless for improving the accuracy of the calibrated mean period. Furthermore, combined with the results in Figure 5-24(c), it is believed to suggest that only the radar-to-wave angle is insufficient for determining the scaling factor of the mean period. In addition, the results in Figures 5-24(e) and 5-24(f) show that the spectra width parameter is a potential factor for calibrating the radar-deduced wave period. Although, the uncertainty of estimated spectra width parameters still needs to improve.

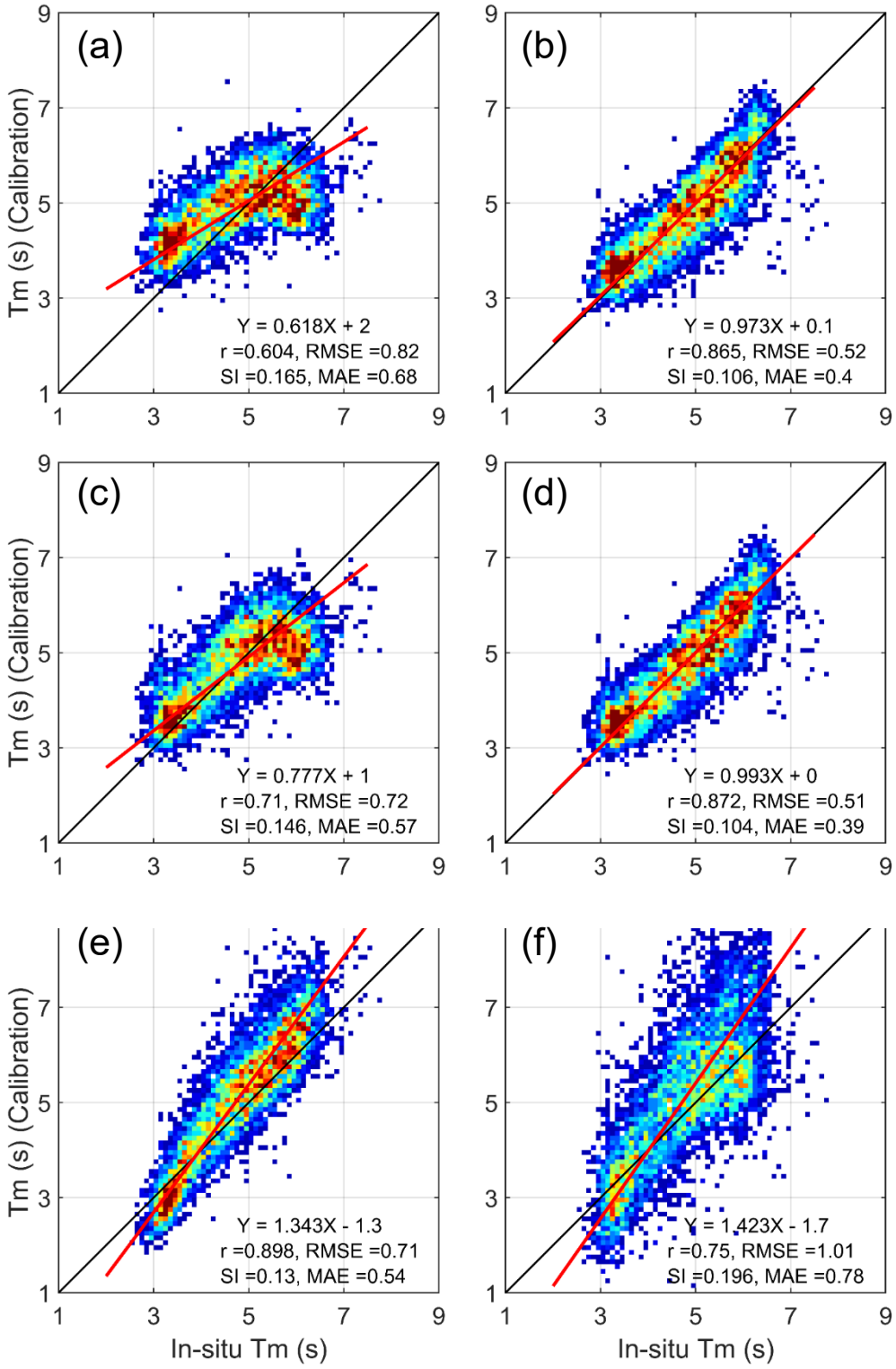
(a)
Y = 0.618X + 2
r =0.604, RMSE =0.82
SI =0.165, MAE =0.68
(b)
Y = 0.973X + 0.1
r =0.865, RMSE =0.52
SI =0.106, MAE =0.4
(c)
Y = 0.777X + 1
r =0.71, RMSE =0.72
SI =0.146, MAE =0.57
(d)
Y = 0.993X + 0
r =0.872, RMSE =0.51
SI =0.104, MAE =0.39
(e)
Y = 1.343X - 1.3
r =0.898, RMSE =0.71
SI =0.13, MAE =0.54
(f)
Y = 1.423X - 1.7
r =0.75, RMSE =1.01
SI =0.196, MAE =0.78
Tm (s) (Calibration)
In-situ Tm (s)
1
3
5
7
9

Figure 5-24 Scatter plots of the mean wave period between calibrated and in-situ observation. Regarding the correction methods, panel (a) shows the value of the mean period using a constant empirical value, while panels (b), (c), and (d) represent the corrected wave height using smallness parameters, in-situ wave direction, and both above factors, respectively. Panels (e) and (f) show the value of the mean period using in-situ and estimated spectra width parameters, respectively.

The comparison of the calibrated peak period and the in-situ data are shown in Figure 5-25. The sequence of this figure is the same as those of Figure 5-24. It can be seen that the highest accuracy of the calibrated peak period is approximately 1.1s of RMSE, 0.8s of MAE, and 0.17 of SI, improving nearly 15% compared to the results in Table 5-3. Like the mean period comparison results, the power-law with the smallness parameter variable provides better accuracy than others. However, the bias of calibrated peak period is still considerable. It is because the peak period estimator is quite sensitive to some factors, such as swell instability, ship echoes, and interference. The theoretical inversion method and the dual-radar system are suggested to implement to improve the peak wave period's uncertainty. On the other hand, Figure 5-25(e) shows a very high value of the correction coefficient between calibrated and in-situ peak periods. It is because we used Young's method [106] to compute the peak wave period from the pseudo spectrum based on Eqns. (5.14) and (5.16) in section 5.2. Therefore, the spectra width parameter significantly influences the estimation result of the calibrated peak period. The comparison results in Figure 5-25(e) indicated that the correction method using ϵ_s is a potential method for improving the uncertainty of the radar-deduced peak wave period.

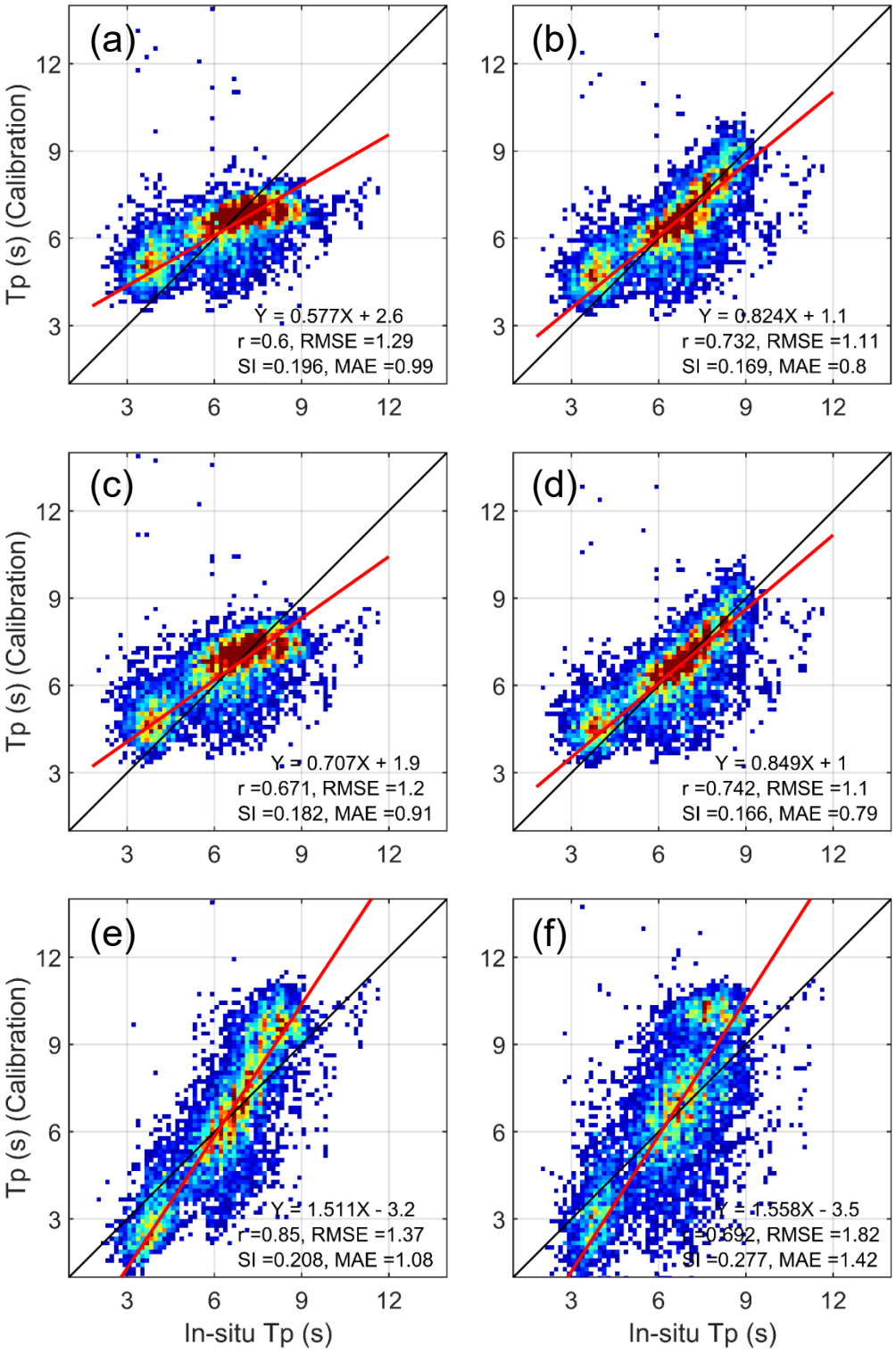
(a)
Y = 0.577X + 2.6
r =0.6, RMSE =1.29
SI =0.196, MAE =0.99
(b)
Y = 0.824X + 1.1
r =0.732, RMSE =1.11
SI =0.169, MAE =0.8
(c)
Y = 0.707X + 1.9
r =0.671, RMSE =1.2
SI =0.182, MAE =0.91
(d)
Y = 0.849X + 1
r =0.742, RMSE =1.1
SI =0.166, MAE =0.79
(e)
Y = 1.511X - 3.2
r =0.85, RMSE =1.37
SI =0.208, MAE =1.08
(f)
Y = 1.558X - 3.5
r =0.892, RMSE =1.82
SI =0.277, MAE =1.42
Tp (s) (Calibration)
In-situ Tp (s)
3
6
9
12

Figure 5-25 Scatter plots of the peak period between corrected and in-situ data. Regarding the correction methods, panel (a) shows the value of Tp using a constant empirical value, while panels (b), (c), and (d) represent the corrected Tp using smallness parameters, in-situ wave direction, and both variables, respectively. And panels (e) and (f) show Tp using in-situ and estimated spectra width parameters, respectively.

In order to correct the value of Hs at the whole radar's footprint using the radar-to-wave angle, we computed wave direction from in-situ wave data based on wave refraction in narrow water areas using the snell law (see Figure 5-17(a)). Then, the value of empirical parameters in Tables 5-6 and (5.18) are used to compute the new value of the wave height scaling factor at all radar points. Then, the radar-deduced Hs are calibrated. The map of corrected wave height is shown in Figure 5-26(d). Later, the calibrated Hs are used to calculate the scaling factor as well as the value of Tm and Tp using empirical parameters in Tables 5-7, 5-8, and (5.22).

As the last discussed, the maps of calibrated wave parameters during the winter monsoon condition were represented in Figure 5-26. In which panels (a), (b), and (c) are three maps of 1-day averaged radar-deduced wave parameters (Hs, Tm, and Tp) using constant scaling factors as in Figure 5-14, while panels (d), (e), and (f) represent the distribution of the calibrated wave parameters using (5.18), (5.22a), and (5.22b), respectively. As a result, the heterogeneity of wave height has been reduced (Figure 5-26(d)). Unfortunately, wave height calibration results have not fully improved due to the lack of in-situ wave data at various locations. Meanwhile, the mean period map is relatively consistent except near the coastal area where wave height is too low (Figure 5-26(e)). Later, the peak period map in Figure 5-26(f) is more reasonable than those in Figure 5-26(c). The reason for lower peak period areas is similar to those of the mean wave period. They all depend on the calibrated wave

height. In summary, although there is only one location of in-situ data, the calibration results of wave parameters are valuable and better accurate than the results estimated from radar sea-echo data.

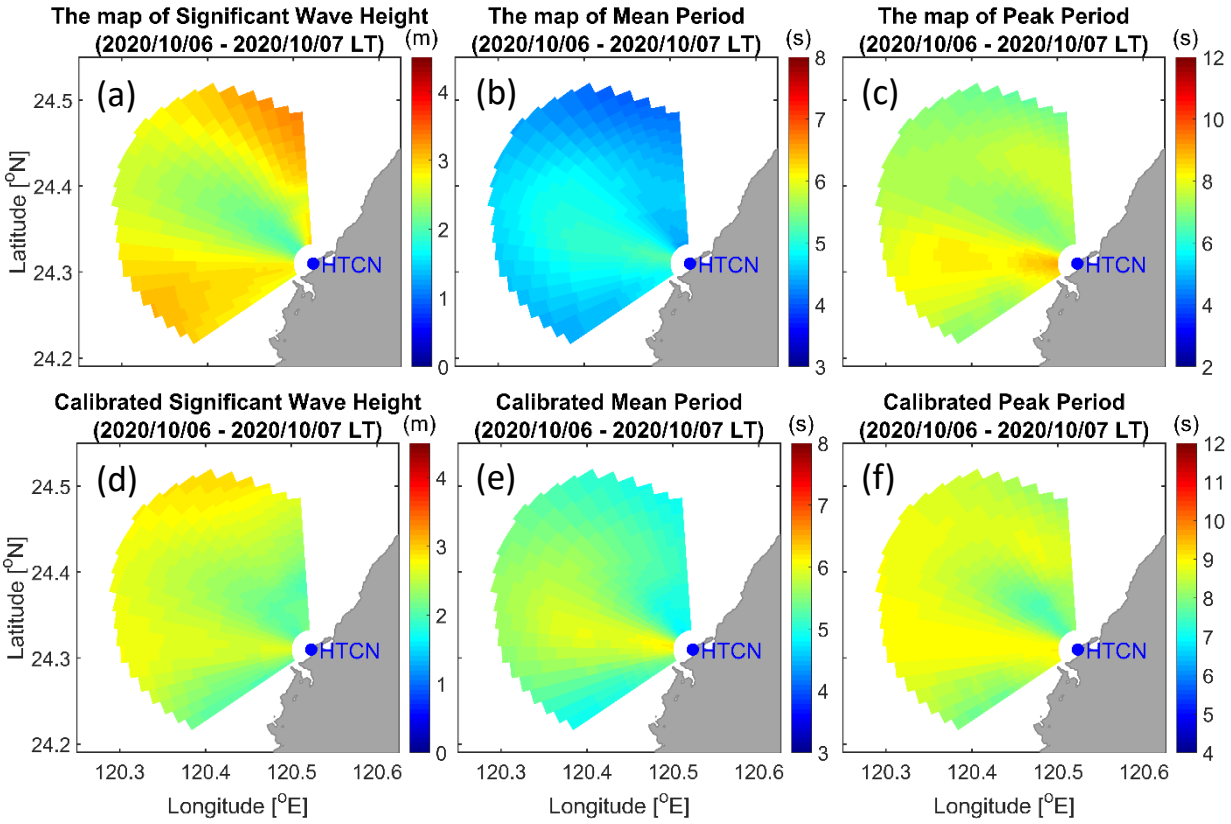

Figure 5-26 The spatial pattern of 1-day averaged radar-deducted and calibrated Hs, Tm, and Tp under prevailing winter monsoon. Herein, panels (a), (b), and (c) show the map of Hs, Tm, and Tp with a single value of their scaling factor as in Figure 5-16, while panels (d), (e), and (f) show the map of Hs, Tm, and Tp computed from corresponding suggested correction algorithms.

The overall procedure of wave parameter correction algorithms using a single radar system's backscattered data is represented in Figure 5-27. The most crucial step is to select the better relationship model among wave parameter ratios with the radar-to-wave angle, smallness parameters, and spectral width parameters by fitting the

radar data to in-situ wave data. As a data preprocessing step, outliers need to be removed from in-situ data. For the radar data, wave parameters are only estimated when the SNR of 2nd-order sidebands is over the given threshold. Besides, the direction of the wavefield can be estimated from the in-situ wave direction and the refraction phenomenon using the snell law. They can also be obtained from the corrected data of the wave model. Further, the output of the wave height corrector will be the input of the wave period correctors. Finally, the calibrated wave parameters will be compared to given thresholds to remove the unrealistic data.

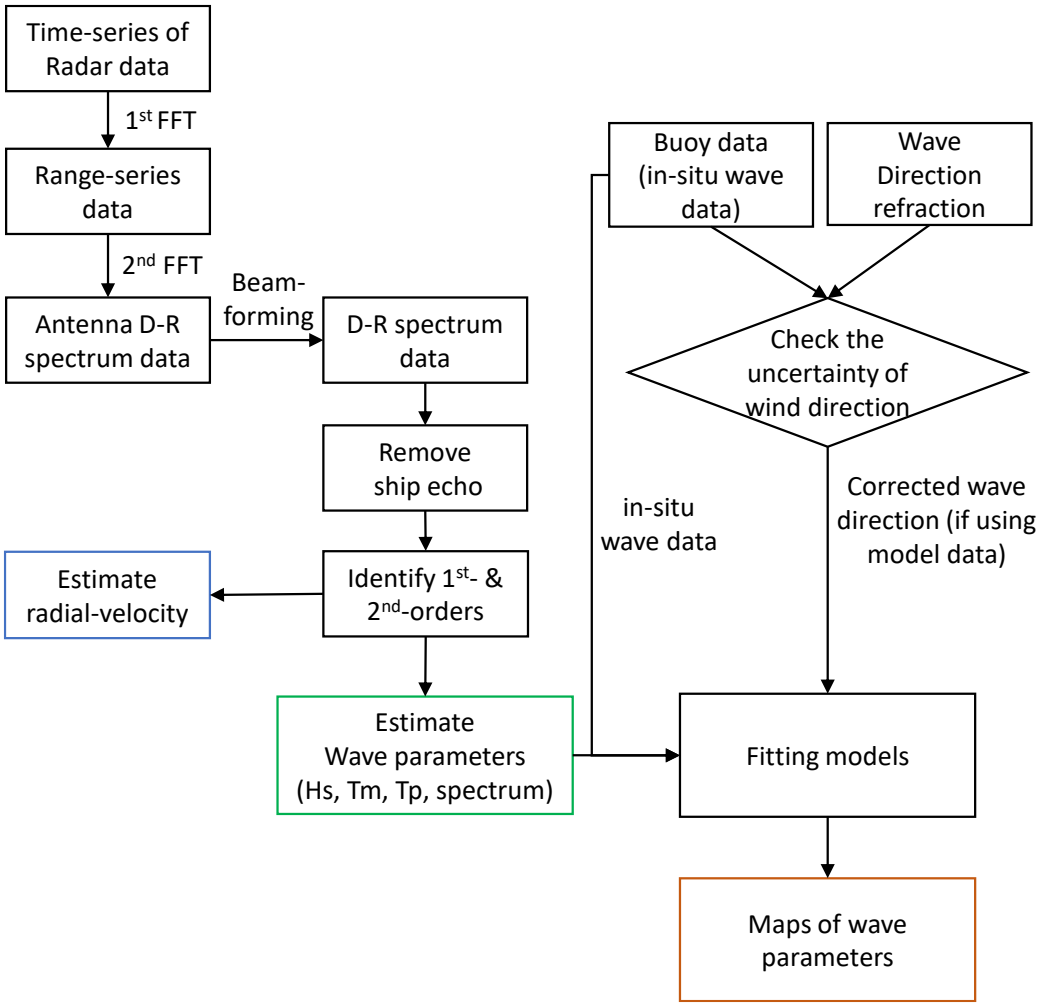

Figure 5-27 Block diagram of wave parameters estimation and calibration.

5.6 Summary

In this chapter, we introduced the data processing of a linear phased-array HF radar system. This system consists of 16 receiver elements, operated at the center frequency of 27.75 MHz and 300 kHz bandwidth, and was installed near the Taichung harbor, Taiwan, to monitor the evolution of ocean surface waves in the middle of the Taiwan Strait in long-term. The system allows extracting the D-R spectrum at different azimuthal directions using beamforming algorithms. Furthermore, existing retrieval methods are adopted to estimate current and wave parameters from a single radar data.

In the work of data processing, the identification of Doppler spectra regions is an essential step that needs to be accurately identified. Unfortunately, a constant empirical value is not enough to mark the boundary between the first-order and second-order components on the Doppler spectra from higher frequency systems under complex surface current and variable wavefield conditions. Therefore, an alternative method was implemented to detect first-order regions of the Doppler-Range spectrum. The method is a careful processing procedure that includes smooth disks of variable size, the D-R spectra pretreatment, the marker-controlled watershed segmentation, and an image processing technique. In practice, this method performed very well in isolating the first-order regions under various weather conditions consisting of variable current, wave, and noise regimes.

Barrick's empirical formulas are the most common estimator and robust in wave parameter estimation under the presence of noise was adopted. In those formulas, no empirical parameters are included. The estimated value was compared to in-situ data to assess the uncertainty of radar-deduced wave parameters. The comparison results indicated that radar-deduced wave height is almost overestimated. In contrast, the wave period results are overestimated under the normal sea-state and underestimated under severe sea-states. The estimated wave height at various radar

bearings is significantly different, especially under extreme conditions of monsoon waves. The comparison results also indicated that the error of radar-deduced wave parameters is still significant and may vary under different wave directions. The estimated and in-situ spectrum are highly correlated in the frequency range of 0.1-0.3 Hz and weakly correlated in other frequency components. The comparison results demonstrated that it is necessary to improve the wave parameter's uncertainty.

An E2E simulation toolbox has been developed to assess wave parameter correction coefficients' sensitivity under various wind speeds and wave directions. The simulation and actual data show that the scaling factor of significant wave height is influenced by both radar-to-wave angle and the smallness parameter for low sea-states ($\varsigma < 0.3$), and is mainly affected by radar-to-wave angle under moderate and severe sea-states ($\varsigma \geq 0.3$). In contrast, the effect of smallness parameters and spectral width parameters on the wave period correction coefficient is more substantial than radar-to-wave angle. Accordingly, the formulas for presenting the relationship between wave parameter correction coefficients and θ_w, ς, and ϵ_s were proposed. In addition, a multivariable function combined with the impact of θ_w and ς was proposed to estimate the value of wave parameter scaling factors. Then, the performance of correction methods and output uncertainty is assessed based on the comparison results of calibrated and in-situ wave data.

The comparison results show the improvement of the error of calibrated wave parameters. For the error indexes of significant wave height, the value of SI is slightly reduced with a value of 3.6%, which are approximately 35% and 15% for the calibrated mean and peak periods, respectively. The results demonstrated that the wave height scaling factor mainly depends on the radar-to-wave angle value, especially under extensive monsoon wavefield conditions. In contrast, it is sufficient to calibrate the mean wave period using calibrated wave height based on the power law. Though, the peak wave period's uncertainty still needs to improve using

theoretical methods and dual-radar system data. Finally, by applying wave parameter correction algorithms, the unrealistic of mapping wavefield from a single HF radar system was reduced.

CHAPTER VI HIGH-FREQUENCY COASTAL RADAR FOR SHIP DETECTION

6.1 Introduction

The coastal radar systems operating at HF and VHF bands have been widely used to monitor the dynamics of upper ocean layers as well as ocean parameters such as surface current, waves, and winds [14, 29, 63, 83, 125, 126]. In addition, these coastal radars have been employed to identify and track coastal vessels on the sea [34, 127-129] and became a powerful supplementary instrument for ship detection and tracking [35, 129, 130] in addition to the Automatic Identification System (AIS). Based on the feature of radio waves propagating over the sea surface, the HF coastal radar can detect targets at a range, which is significantly larger than the microwave marine radar. The HF radar system operates in the frequency range of 3 MHz to 30 MHz, which allows retrieving observations 200 nautical miles away from the coastline [34]. The HF radar system's over-the-horizon capability is one of high interest for many applications, including vessel detection, tracking, and guidance, as well as search and rescue of marine casualties, pollution mitigation, and research in coastal oceanography. These applications of HF radar are exploited based on the United Nations Convention on the Law of the Sea that establishes 200 nautical miles as the Exclusive Economic Zone (EEZ) [35]. The surveillance of maritime activities within a nation’s EEZ is an essential part of protecting national sovereignty. Meanwhile, the radar system recently became an operational tool in coastal monitoring worldwide. For verifying the results of the ship’s location detected from HF radar sea-echo, AIS data is usually used [130].

The performance of HF radar depends on its capability to detect and track targets within its coverage region. For the high-frequency band, the noise level is mainly dominated by the environmental noise, and may vary depending on the

sources of those noises and their characteristics. Accordingly, external noise and interference levels can limit vessel detection capability. In addition, the main contribution of Doppler spectra from HF radar echo is due to scattering from the ocean surface. The feature of the backscattered signal depends on radar frequency, beamwidth, polarization, and the configuration of the HF radar system. For example, the moving of ocean waves can cause Doppler shifts in any radiation scattered from them.

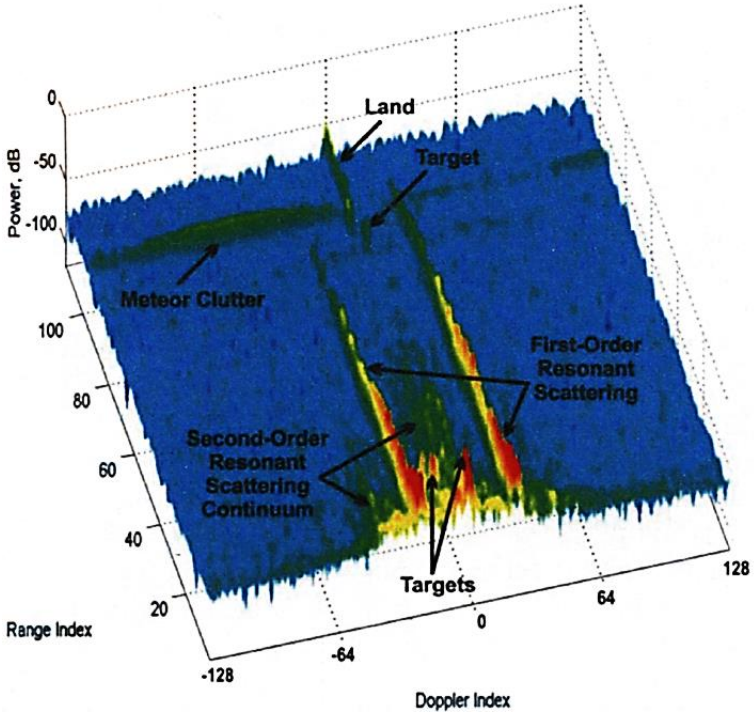

Figure 6-1 Sea clutter and targets appear in the HF radar Doppler-range spectra [35].

In order to detect coastal vessels, various commercial radars such as the cross-loop CODAR SeaSonde system and the phased-array antennas WERA system have been applied [35, 36]. Accordingly, numerous detection algorithms have been proposed and put in use (review in Chapter 1). Furthermore, in late November 2018, a phased-array HF coastal radar was installed at the northern of Taichung Harbor,

Taiwan, to monitor ocean current and waves in the vicinity waters. Besides, the detection and tracking of ships for navigating around the harbor entrance are an objective that needs to be built up. This radar system is operating at the center frequency of 27.75 MHz and 300 kHz bandwidth.

Typically, the ship echo is detected from the map of Doppler-range spectra based on the greater energy of ship echoes compared to the surrounding area. In which, a reference surface generated by smoothing, regression curves, or filtering techniques is used to compute the residual power. Then, a threshold value is applied to identify the possible residual power that may respond to a ship echo. In the next step, constant false-alarm-rate (CFAR) methods can be used to test the statistic for each signal of interest. The CFAR threshold is computed based on the Neyman-Pearson criterion with a fixed probability of false alarm and a maximum probability of target detection [35]. Finally, the bearing from the radar station to targets, which corresponds to the detected signal, is determined using DOA methods such as beamformers, MUSIC, and so on.

On the other hand, different from the use of range-Dopper (RD) (or Doppler-range, D-R) spectra, methods for beamforming with a linear phased-array receiver antenna elements are adopted to compute the so-called power density (called brightness thereafter), which is a function of azimuthal angle for each range cell. This directly allows showing sea and ship echoes on the map of 2D range-Angle (RA) brightness distribution. To implement this approach, three beamforming algorithms were examined: Fourier, Capon, and norm-constrained Capon beamformers. The Fourier beamformer is also called the conventional or the linear approach that is simple to implement but yields a coarser angular resolution and is significantly influenced by the sidelobe effect. Meanwhile, the Capon method is an adaptive beamforming method that is a directionally constrained minimum power (DCMP) algorithm, which can effectively suppress sidelobes and clutter. The disadvantage is

that this beamformer method is sensitive to small errors in amplitude, phase, or position of the received signals and often provides unrealistic results. As an effective solution, a norm-constrained condition can be added to mitigate the sensitivity of the Capon method to improve the Capon beamformer robustness, called the NC-DCMP beamformer [103-105]. In the present study, we will implement the NC-DCMP beamformer to the HF radar data to demonstrate its efficiency for resolving the ship echoes even under multiple target situations. In addition, a band-stop filter can be adopted to remove Bragg echoes before using the beamformers, making the brightness of ship echoes more visible. In this chapter, both RD and RA approaches are implemented to detect vessels from HF radar backscattered signals. The estimation results of ship location will be compared to AIS information to assess the performances of the ship detection methods. In the next section, ship detection methods will be represented.

6.2 Methods of Ship Detection

6.2.1 Methods for range-Doppler spectra

A. The method of curvilinear regression analysis

In order to detect ship echoes from the HF radar Doppler spectra, the technique of curvilinear regression analysis was applied to the WERA radar [34, 35, 131]. This technique can detect the target (ships) in the strong interference environment, which is mainly contributed by the first-order ocean backscattering, and control the false alarm probability. In this method, the authors consider a set of range-Doppler power spectra corresponding to a single snapshot collected by receiver elements of the HF radar system. The RD map statistics may vary from snapshot to snapshot. Therefore, it is possible to detect targets against a background signal, which has an unknown distribution of echo signal amplitudes. The conventional curvilinear regression,

which is the polynomial functions of the 2nd order or more [132], was analyzed to a logarithmically scaled power spectrum and the Doppler range cells, respectively [34]. The examples of regression curves and their confidential upper bounds, along with the range and Doppler cells, respectively, are shown in Figure 6-2. In this figure, the blue line in panels (a) and (b) represents the spectra power over range and Doppler bins, respectively; the red dashed, and solid lines represent the regression curve and the upper confidence bounds, respectively.

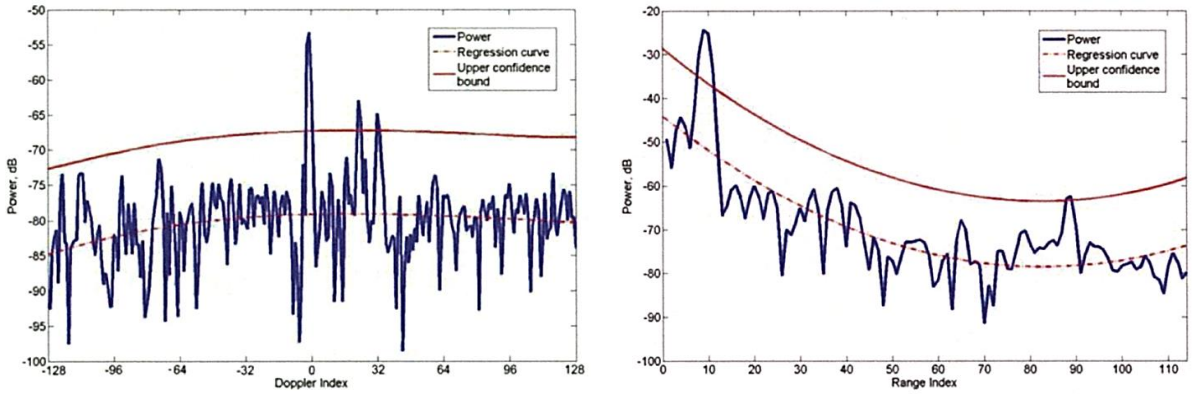

(a) (b)

Figure 6-2 The example of power spectrum with regression curves along with (a) Doppler bin and (b) range cell [35].

On the other hand, an adaptive threshold, T, is used to mark the maximum between 100(1-α)% upper confidential bounds and the regression curve with respect to range and Doppler frequency. The spectra power of cells on the R-D spectra map is compared with those thresholds. All cells whose spectra power are greater than both thresholds in range and Doppler cells are noted for the next process. Next, the CFAR is applied to identify the local peak on the RD spectra map. Finally, the direction of the ship echo is identified using DOA algorithms such as beamformers and MUSIC. The concept of this method is represented as follows:

Step 1: Identify the input variables, which are range cell and Doppler bins, and the confidence level, α. The value of 95% is commonly used.

Step 2. Establish the regression function and calculate its parameters in each range cell as well as Doppler bins. Then, the quadratic polynomial and cubic polynomial functions are implemented to calculate the empirical parameters in terms of range cell and Doppler bin, respectively.

Step 3. Calculate the threshold for each range cell ($T_{\alpha, R}$) and Doppler bin ($T_{\alpha, D}$) based on the empirical parameters of those regression functions and the value of the confidence level. For example, if α equals 95%, the offset value is approximately two times the standard deviation.

Step 4. Identify the adaptive threshold for each pixel by getting the maximum value of the above thresholds, $T = \max(T_{\alpha, R}, T_{\alpha, D})$.

Step 5. Detect the signals that have a power spectrum higher than the threshold.

In addition, the flowchart of this method is shown in Figure 6-3 as follows:

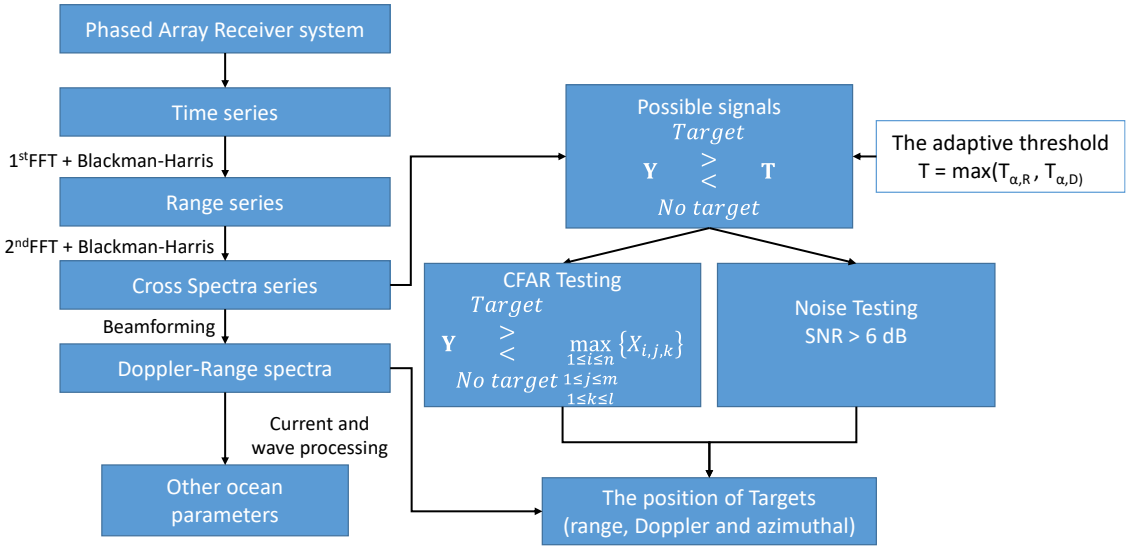

Figure 6-3 The flowchart of the curvilinear regression analysis method.

In this research, we processed the RD spectra map with 128 Doppler frequency bins corresponding to approximately 28 seconds (the radar chirp length equals 0.21666 seconds), which is short enough to consider ships to be stationary or slightly moving. Then, the method will be implemented to detect the ship echoes the HTCN's backscattered data. The estimation results will be compared to the AIS information for assessing the performance of detection algorithms.

B. The adaptive detection method

The adaptive detection method for ship detection was proposed by Chuang e. al. [41]. In this method, the background level, a reference spectrum, is obtained using a 2D Moving Average filter. The window size of the method can be selected based on the sensitivity test of the kurtosis and skewness estimation results, which were retrieved from the histogram of the corresponding residual series [41]. The residual signal is defined as the difference between the power spectra data and the smoothed surface compared to an adaptive threshold in a specific test. Finally, the adaptive value is taken based on a multiple of the standard deviation (1.5σ, 2σ, 2.5σ, and 3σ). The method can be implemented following the flowchart in Figure 6-4.

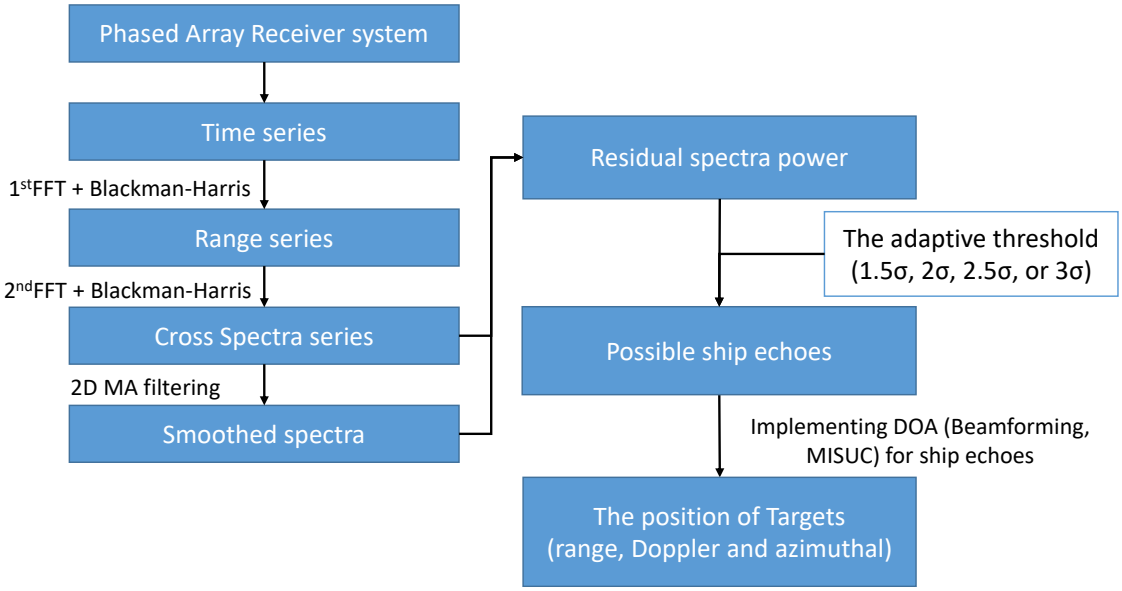

Figure 6-4 The flowchart of the adaptive detection method.

As the final step, the target's position will be identified through the definition of local peaks. The radial velocity of targets can be calculated from the Doppler frequency of the local peaks. For estimating the Direction of Arrival (DOA), the multiple signal classification (MUSIC) [95] and Beamforming [98] algorithms can be applied for cross/loop monopole and phased-array systems, respectively. In this study, the RD spectra with 128 Doppler frequency bins corresponding to approximately a period of 28 seconds are processed. The threshold of 2.5σ is selected for detecting the Ship's echoes. In addition, the conventional beamforming algorithm [98] will be applied to retrieve the bearing or targets. Finally, AIS's database will be used to compare with the estimation results for evaluating the performance of the method.

C. Constant False-Alarm-Rate algorithms

Following the step of detecting possible target positions, the constant false-alarm-rate (CFAR) algorithm, which is calculated based on the Neyman-Pearson

criterion [38], can be applied to identify the local peak in terms of range, Doppler frequency, and azimuth direction. The goal of CFAR algorithms is to set a threshold, which should be high enough to limit false alarms to a tolerable, and low enough to allow detection targets [133]. There is various type of CFAR algorithms, which are Cell-Average (CA), Greatest-of Cell-Averaging (GOCA), Smallest-of Cell-Averaging (SOCA), and Order Statistic (OS) algorithms. As known, the CA-CFAR detector is the most widely used.

In order to verify the possible signals that are a local peak or not, the GOCA-CFAR algorithm should be used [34]. Then, the CFAR algorithm is implemented for each possible target's backscattered signal in terms of range, azimuth, and Doppler shift simultaneously (Figure 6-3). To implement the CFAR techniques, we first set up the upper and lower bounds of the range, Doppler shift, and azimuths, which coverage location of possible signals. Secondly, the local noise level can be identified by taking 33% of the ordered power value [131]. Then, the testing cell can be accepted as a detected target when that cell is located in the center of the farm, highest power spectrum, and its local signal-to-noise level is greater than a given threshold, which was taken as 6 dB (Figure 6-3) [35, 131]. In the case of more than one index being accepted, the quality control, the range, Doppler, and direction of identified peaks are calculated using a center of mass algorithms.

The point was accepted from the CFAR test is considered as an identified radar target. Then, the target information consisting of location, radial velocity, and power spectrum will be calculated and saved into output files.

D. The flowchart of ship detection procedure using HF radar rang-Doppler spectra

Combining the two detection methods and CFAR techniques, we established a flowchart showing the procedure for identifying the target’s position from the RD

spectra of the phased-array HF radar system near the Taichung harbor. The diagram is shown in Figure 6-5.

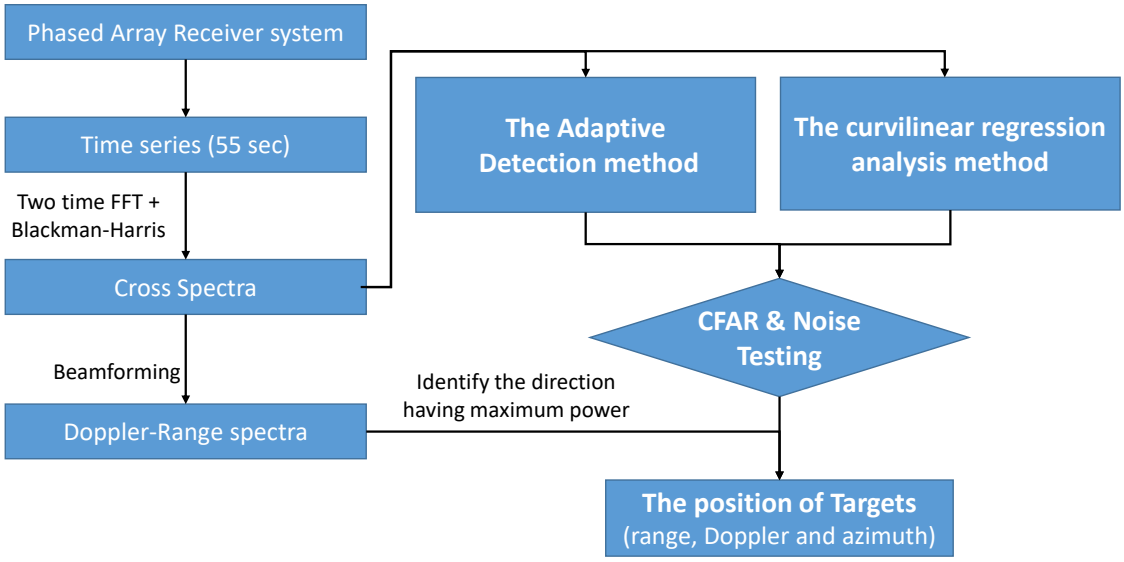

Figure 6-5 The flowchart of the ship detection procedure.

6.2.2 Methods of the range-Angle brightness distribution

A. Beamforming algorithms

For a linear phased-array radar system consisting of M receiver antenna elements, a steering vector, **w**, is used to combine signals of the multichannel, **X**, for producing the output signal, Y, at the desired direction **k**. The formula is given as follows:

$$Y(t) = \mathbf{w}^H \mathbf{X}(t) \tag{6.1}$$

$$\mathbf{w} = [e^{j\mathbf{k}\cdot\mathbf{D}1} \; e^{j\mathbf{k}\cdot\mathbf{D}2} \; \dots \; e^{j\mathbf{k}\cdot\mathbf{D}M}]^T \tag{6.2}$$

Herein, t is the time, the " ^{H} " means the Hermitian operator (conjugate and transpose) of vector or matrix, the multichannel signals are composed in a column matrix, **X**, **k** is the vector of radio wavenumber at the desired direction, and $\mathbf{D}_i$ is the coordinates of the i^{th} receiver antenna.

At the direction **k**, the brightness distribution of the Fourier method is given as (see in section 5.2):

$$B(\mathbf{k}) = \langle Y(t)Y^*(t)\rangle = \mathbf{w}^H\mathbf{R}\mathbf{w} \quad (6.3)$$

where **R** is the matrix of the covariance functions for all signal pairs, and given as:

$$\mathbf{R} = \begin{bmatrix} R_{11} & \dots & R_{1m} \\ \vdots & \ddots & \vdots \\ R_{m1} & \dots & R_{mm} \end{bmatrix} \quad (6.4)$$

Where, R_{ij} is the covariance function of radar signals acquired by two receivers *i* and *j*. Meanwhile, the brightness of the Capon and NC-DCMP methods are given as:

$$B(\mathbf{k}) = N^2/(\mathbf{e}^H\mathbf{R}^{-1}\mathbf{e}) \quad (6.5)$$

$$B(\mathbf{k}) = \mathbf{w}_{\mathrm{NC}}^H(\mathbf{R}+\sigma\mathbf{I})\mathbf{w}_{\mathrm{NC}} \quad (6.6)$$

The detail of those methods has been represented in section 5.2. Whereby the value of σ and δ in parameters in the NC-DCMP beamformer should be investigated [46]. It is suggested that the suitable values of δ and Δσ for the practical operation of NC-DCMP beamformer in each radar system should be examined practically. For the HF radar system at the HFTC station, the values of the two above factors, which are 10 and 0.002 for δ and Δσ, were proposed by Chen et al. [46] for considering the limit of computing time in ship detection and tracking. In the present study, those values are adopted. For other HF or VHF radar systems, the values of δ and Δσ might be changed and should be re-investigated before implementing the NC-DCMP method.

B. Band-stop filter

In terms of identifying ship echoes, the sea echoes are considered clutter. Herein, two first-order spectra are produced by the interaction between incident radio waves and Bragg waves are significant and play a key role in estimating the brightness value. Those sea echoes should be suppressed to highlight the signal of ship echoes. Therefore, a band-stop filter can be applied to remove the effect of Bragg waves and suppress the sea echoes. In this study, the specifications of the

applied band-stop filter are depicted in Figure 6-6. And the effectiveness of the band-stop filter with the following values is given:

A_{pass1} = 1 dB, the amount of ripple allowed in the left passband.

A_{pass2} = 1 dB, the amount of ripple allowed in the right passband.

A_{stop} = 60 dB, attenuation in the stopband (based on practical experiments).

F_{stop1}= f_b - Δf_1 Hz, the first frequency of the stopband.

F_{stop2}= f_b + Δf_1 Hz, the last frequency of the stopband.

F_{pass1} = f_b - Δf_2 Hz, the last frequency of the left passband.

F_{pass2}= f_b + Δf_2 Hz, the first frequency of the right passband, where f_b is the Bragg frequency.

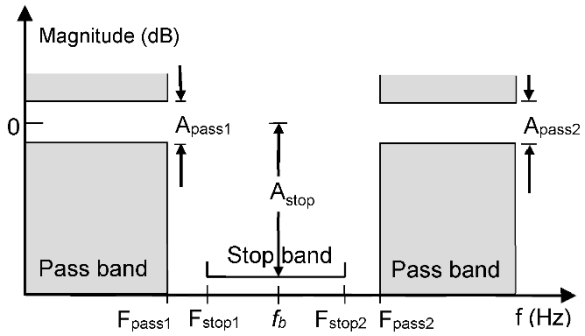

Figure 6-6 Specifications of a band-stop filter [46]. In which, $\Delta f_1 = f_b - F_{stop1}$ (or $F_{stop2} - f_b$) can be defined as the width of the band-stop filter from the center frequency (the Bragg frequency), and $\Delta f_2 = F_{stop1} - F_{pass1}$ (or $F_{pass2} - F_{stop2}$) can be defined as the transition width of the filter. In the present study, Δf_1 and Δf_2 equal Δf, which is fixed as 0.1 Hz.

To demonstrate the effectiveness of the band-stop filter for suppressing sea echoes, the extracted Doppler spectrum and brightness distribution are shown in Figures 6-7(a) and (b), respectively. Where the left panel in Figure 6-7(a) shows the original Doppler spectrum, while the right panel shows the result using the above band-stop filter. It can be seen that at least three possible targets having the Doppler

frequency greater or between the two first-order spectra lines can be recognized in the original spectra map (indicated by the black arrows). Meanwhile, most of the sea wave echoes were removed in the right panel of Figure 6-7(a). Although, if the Doppler frequency of targets is within the transition width of the filter, which is from f_b - Δf_1 to f_b + Δf_2, their echoes will also be filtered. As a result, the backscattered echoes of moving targets may disappear for a while but pop out soon, unless the radial speed of the target is close to those of Bragg waves for a long time. However, it is impossible to treat correctly in that case, neither in RA nor in RD methods.

In addition, Figure 6-7(b) shows the two RA brightness distribution maps produced by the NC-DCMP beamformer with the original and filtered radar echoes. The left panel shows that the target echoes are significantly mixed with the sea echoes, making it challenging to identify the location of the three targets. In contrast, three-target echoes can be recognized in the background echoes on the right panel. This means the band-stop filter was indeed workable to suppress the sea echoes for rising the signal-to-noise of the ship echoes.

In terms of data processing, adaptive band-stop filters for different range cells and time moments might be expected to be proposed due to the variation of f_b caused by several factors, such as changing sea surface wind speed and direction, existing complex surface current [134]. However, it is a challenge to find adaptable band-stop filters for each range cell in each calculation due to the time-consuming issue, making it difficult to identify and track vessels in real-time, unless improving the computing speed of the calculator. Therefore, depending on the calculator capability, this study uses constant parameters for the band-stop filter. Herein, the empirical values of Δf_1 and Δf_2 are selected as 0.1 Hz and 0.2 Hz, respectively, for the 27.75 MHz HF radar system at the HTCN station.

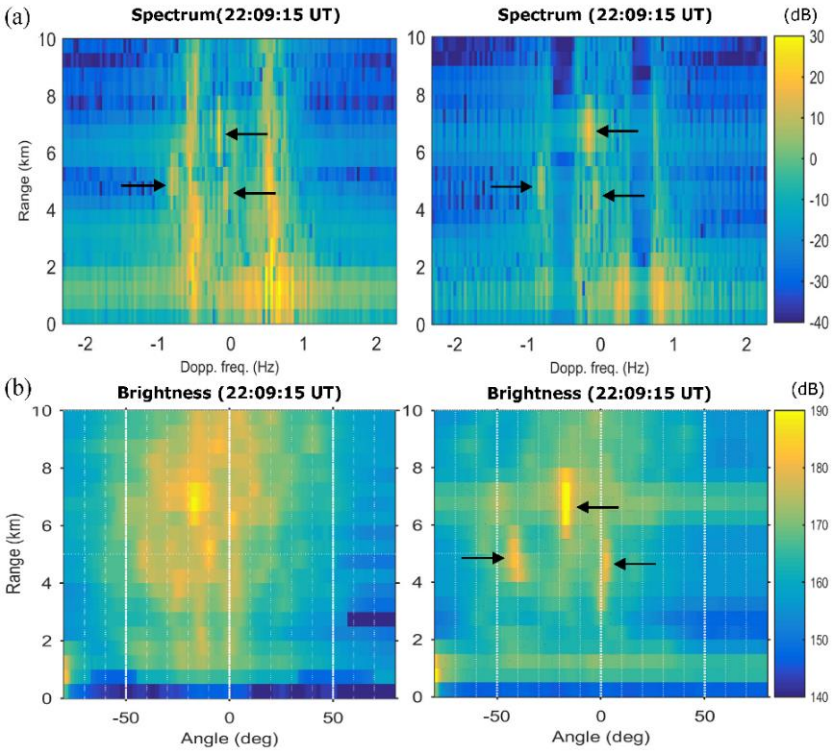

Figure 6-7 The beamforming results in RD spectra (a) and RA brightness distribution (b) obtained from the original and filtered radar echoes [46].

6.3 Data Collection

The information on the phased-array HF radar (LERA MK-III) system installed on the northern protecting embankment of the Taichung harbor, Taiwan, has been introduced in section 5.2 (see Figure 5.1). The receiving system acquired the data with a 0.21666 secs chirp-length, and 8192 chirps raw (I & Q) radar data were assembled in a file corresponding to approximately 30 mins. The bandwidth of the radar system is 300 kHz, proving a 500 m range cell size, and a total of 80 range cells are designed in observation.

Figure 6-8 shows the data processing flowchart of the high-frequency FMCW coastal radar system. It can be seen that the time series backscattered signal (I & Q data) are processed with the first fast Fourier transform (FFT) to retrieve the rang-time spectra, and the second FFT is to produce the range-Doppler spectra. Those

range-Doppler spectra can be used for beamforming in the frequency domain, retrieval of ocean parameters, and target detection. In another approach, the range-time spectra data can be employed directly for beamforming to get the RA brightness distribution maps for ship detection. In this study, the radar data collected on 31 Aug 2019 are presented.

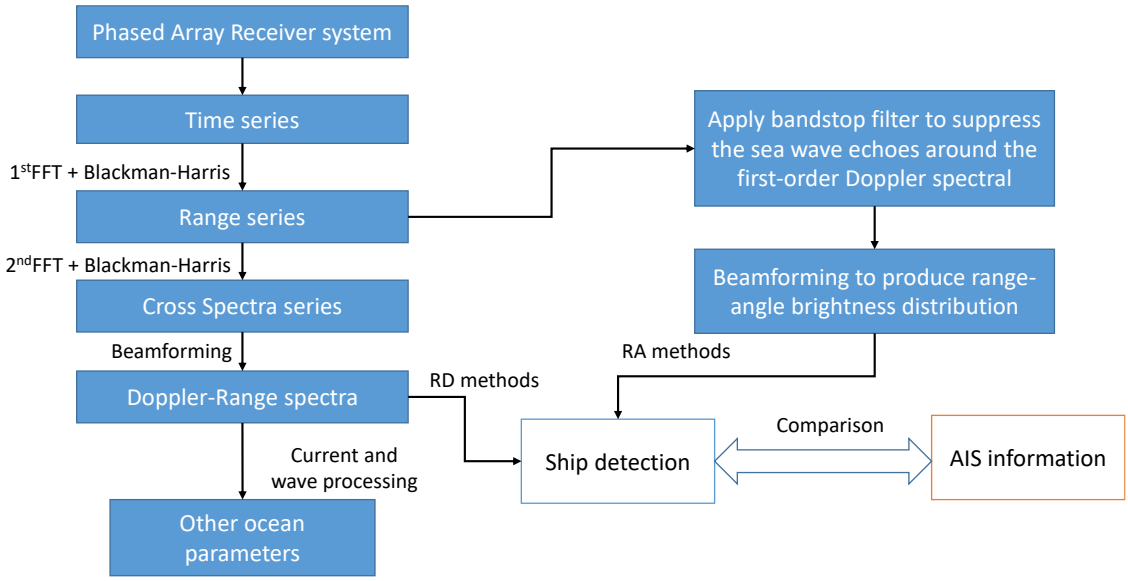

Figure 6-8 The flowchart of data processing for ship detection.

For the AIS information in this study, the ship information is obtained by an AIS device, which was installed at The TUTL station (24° 21.725'N, 120° 34.612'E), which belongs to Taiwan Ocean Radar Observing System (TOROS) (Figure 6-9). In this AIS system, the AIS-3R device is manufactured by Comar Systems Ltd, United Kingdom, and is dual-channel receivers consisting of 87B (161.975MHz) and 88B (162.025MHz) [135]. The system acquires AIS information and saves it into the ASCII raw file. The system can obtain 27 kinds of message types transmitted by AIS Class A and Class B transponders, AIS SARTs and Aids to Navigation, 15 navigation statuses (such as anchored, moored, sailing, …), and 99 ship types, which are Passenger, Freighter, Tanker and beyond [136]. The AIS information includes the

vessel’s name, Maritime Mobile Service Identity (MMSI) number, position and corresponding time, speed (SOG), course (COG), type of vessel, call sign, heading, rate of turn, navigation status, vessel dimensions, and destination. The reporting interval depends on the type of shipborne mobile equipment and the Ship's dynamic condition, and can be referred to in the document of IUT-RM 1371.

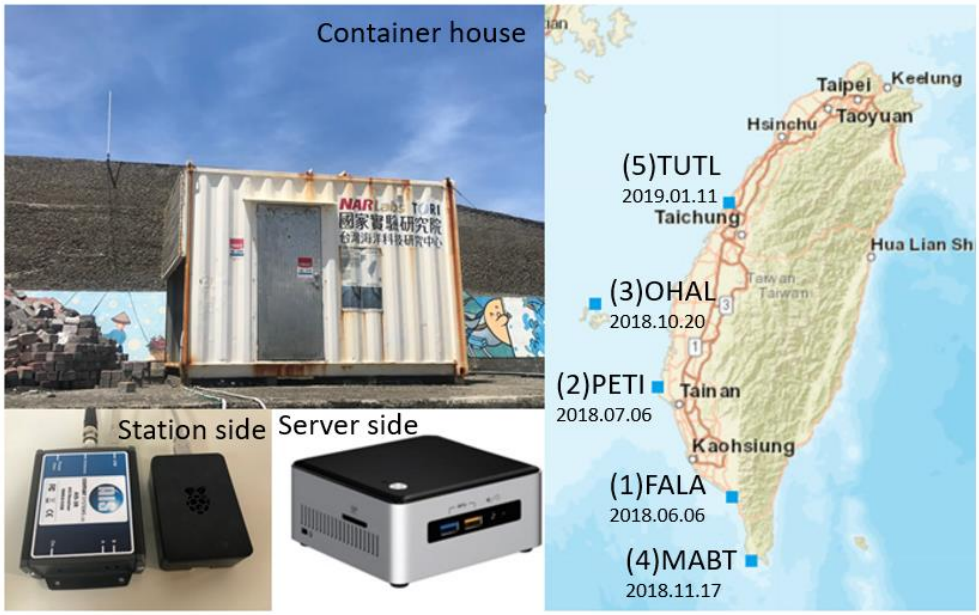

Figure 6-9 The AIS system belongs to TOROS [135].

6.4 Results of Ship Detection Using Radar Echo

6.4.1 Validation of ship echoes

A. Results of RD methods

In order to validate the estimation results, the informed position of coastal ships is shown in Figure 6-10. In this figure, the magenta points show the location of ships recorded into AIS data; the number shows the ship’s Maritime Mobile Service Identity (MMSI); the black dots show the track of vessels within 30 minutes; the yellow points are the target’s location estimated from radar signals at the HTCN station. Figure 6.10 shows that many yellow points have the same location as the AIS

data. It indicated that RD estimators and the CFAR toolbox work well. However, some of them were missed. The main reason is that targets might be identified from strong sea echoes or due to intense noise interference. In addition, there might be a lack of information about AIS due to losing signals or hiding information from the ship. Furthermore, the capability of the HF radar system for ship detection is limited in terms of bearing due to the side lope effect and low signal-to-noise ratio for far fields. Based on many tests, it can be concluded that the performance of RD estimators is still limited in ship detection and tracking.

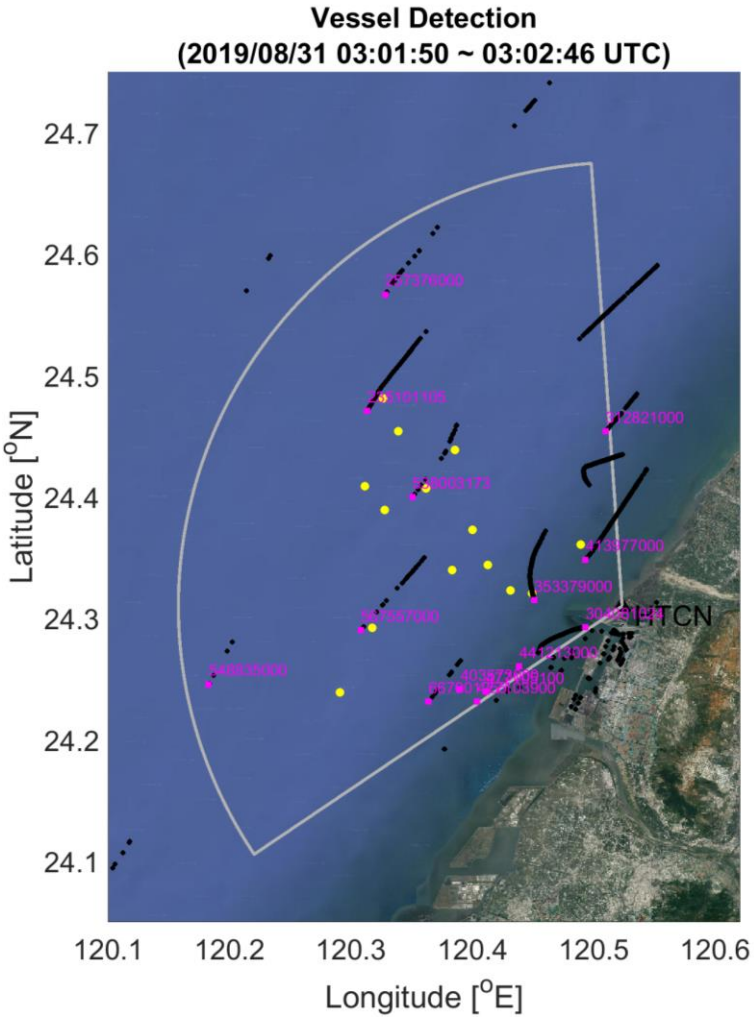

Figure 6-10 The map of ship locations was detected from the D-R methods and those of AIS information. In this figure, the magenta points show the current ship location recorded into AIS data; the number is the ship's MMSI number; the black dots show the track of vessels within 30 minutes; the yellow points are radar-determined ship's locations.

B. Results of RA methods

In order to validate vessel echoes, the brightness distribution over the domain of angle and range is produced. Accordingly, the local maxima in the angular brightness distribution of each range cell can be identified and regarded as possible locations of ships. Indeed, it is possible to consider each echo center to represent a

ship’s location, and the moving of ships can be recognized based on the continuous variation of the echo center in the geographical location. An example is shown in Figure 6-11. Whereby the AIS information is used to validate the possible ship locations denoted by the echo centers (Figure 6-11(a)). This graph shows the ship tracks or object positions obtained from 30-min AIS data near the Taichung Harbor, Taiwan. In this panel, the black and red dotted lines represent the ships heading north and south, respectively, and downward-pointing triangles denote the nearly stationary ships or objects. Panels 6-11(b) and (c) show the locations of the echo centers for five consecutive range cells within the angular range of -80^{o} to 80^{o}, retrieved from the filtered and original radar data, respectively. Notable, the two above panels show the angular location of echo centers (not the ship's location) in the range cell. The radar-determined echo centers are described by six symbols with different colors, sorted by the brightness levels of echo centers. As the example, red circles (ro:1) represent the echo centers at the highest brightness level in each calculation, while green pluses (g+:6) show the minor echo centers at and after the sixth order of brightness level. In addition, the AIS data is represented by the blue circles, which are almost overlapped with some of the determined echo centers. Subsequently, some knowledge is discussed in Figure 6-11 following:

Firstly, the filtering process has removed many sea echoes that are mostly caused by Bragg waves, and significantly clarified the ship/object locations, as shown in the comparison between Figures 6-11(b) and (c).

Secondly, duplicate echoes could exist in adjacent range cells due to the leakage effect of the radar signal. As an example, there was a ship traveling the radar-looking direction transversely in the range cell of 6.0-6.5 km, as marked by the encircled number 1, and the AIS (noted by blue circles) and the radar-determined echo center locations (indicated by red circles) of the ship varied from positive to negative continuously. The duplicate echo centers were usually remarkable in the

above and below-range cells. Nevertheless, the intensity of duplicate echoes in the upper and lower range cells are generally lower than those of the ship-located range cell. This could be useful in the ship tracking process in the following study.

Thirdly, the information of AIS data is used to verify the radar-determined vessel locations and to clarify the duplicate echo centers in adjacent range cells. Figure 6-11(a) shows four ships sailing in the range interval of 5.0 and 7.5 km, as denoted by the encircled numbers ①-④. These ships were identified by the radar, as shown in panel (b) of Figure 6-11. However, the nearly stationary objects, which are represented by the black dots in Figure 6-11(b), were not determined by the radar system. It is possible that these stationary objects were the anchored ships or constructions on the sea, which the radar beamforming cannot obtain for their large angular locations or small radar cross-section (RCS).

Finally, the well-comparable between AIS ship locations and radar-determined echo centers demonstrated the performance of the radar system for ship detection and tracking.

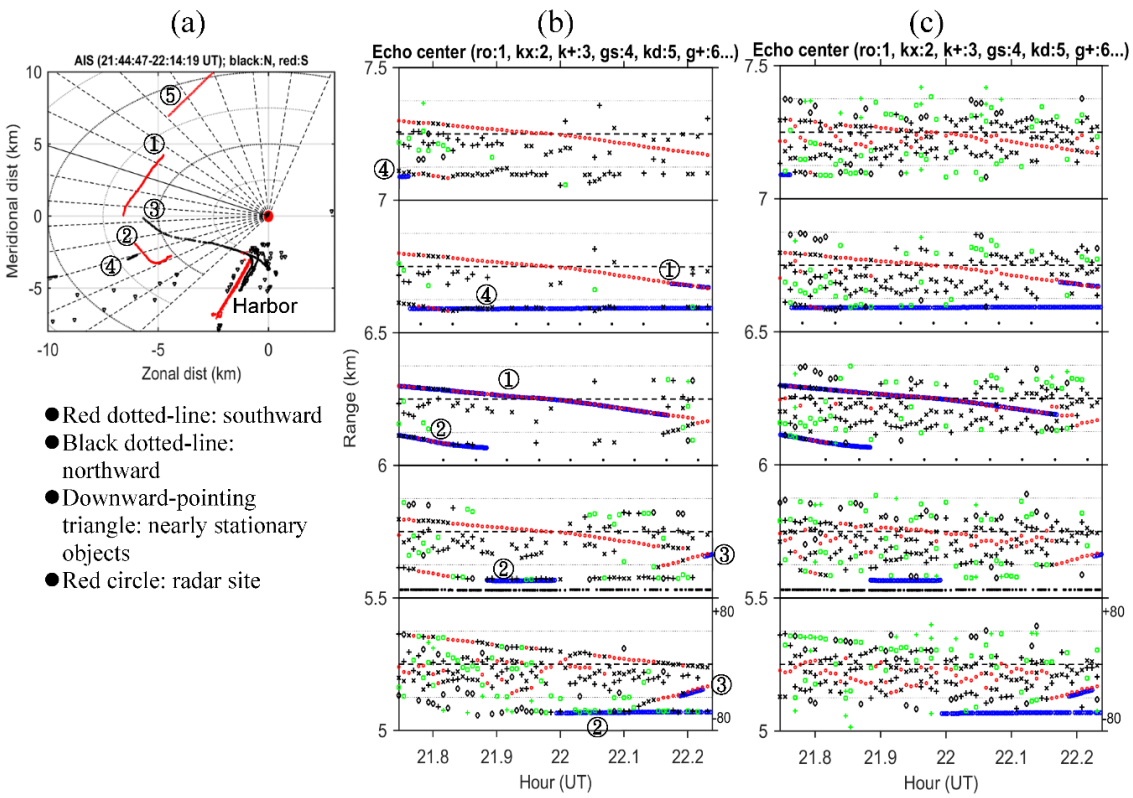

Figure 6-11 Comparison of AIS data and radar-determined echo centers [46]. Herein, panel (a) shows ships/targets tracks/locations obtained from AIS data. Panels (b) and (c) are the echo centers estimated from the range-angle brightness distribution produced by the NC-DCMP algorithm, with filtered and original radar echoes, respectively. In panels (b) and (c), the angular locations of the ships/targets obtained from AIS data are given in their residing range cells, as indicated by blue circles (moving objects) and black dots (nearly stationary objects). Four encircled numbers represent moving ships.

In Figure 6-7(b), the map of RA brightness distribution is a potential approach if the sea echoes are efficiently suppressed. Figure 6-12 shows three of the resultant maps obtained from the NC-DCMP beamformer with nearly the 28s raw data length acquired on August 31, 2019, at the HTCN station. In this study, the brightness values have been compensated by the range to the power of 4. It can be seen that

several brightness spots of ship echoes can be determined, of which locations and intensity varied with time. Accordingly, seven brightness spots are marked by arrows showing moving ships, and a downward-pointing triangle representing a nearly stationary ship or an unknown object, for example. It is noted that the brightness spot in the range of approximately 15 km (noted by No. 4) is challenging to be recognized by eyes in the left panel of Figure 6-12**,** but can be revealed clearly in the two last panels. It may be because that ship echo was suppressed when its radial speed was close to those of Bragg waves. The comparison in Chen et al.'s publication [46] demonstrated that the NC-DCMP beamformer provides the best result for radar-determined ship locations than those of Fourier and Capon beamformers.

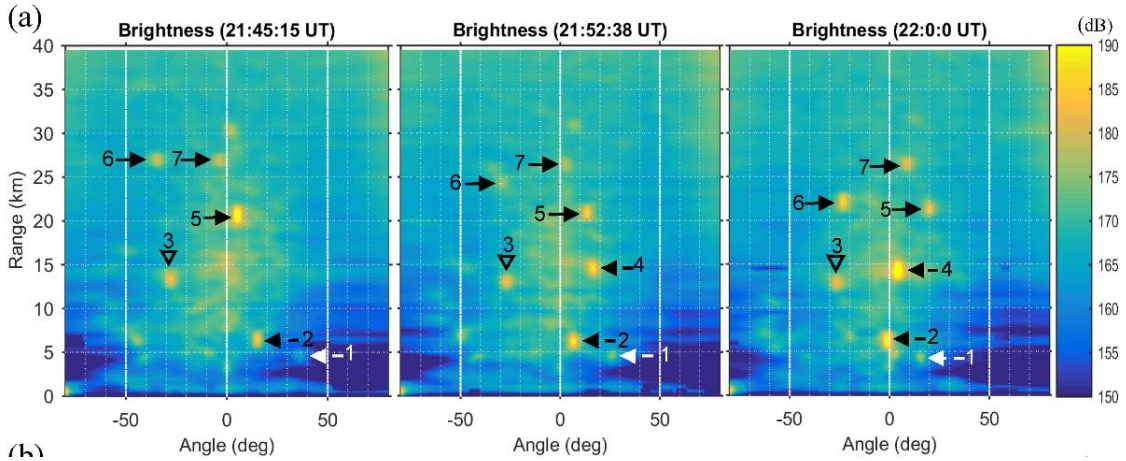

Figure 6-12 Range-angle brightness distributions at three selected periods using the NC-DCMP beamformer with filtered radar echoes [46]. Each map is produced from the approximately 28s raw radar data, and the brightness values have been compensated by the range to the power of 4. The black arrows denote the objects moving with respect to the AIS data. The white arrow shows a moving ship that may not be recorded by the AIS device. A downward-pointing triangle indicates a nearly stationary object. Date: 31 August 2019 (2019243).

A combined brightness distribution map within the 30 minutes radar data is shown in Figure 6-13. The location of ships determined by a locating approach developing for the range-Angle map is shown, as denoted by the white dots in the graph. The locating approach is a contour-based procedure [137] that can help to find the ridged contour centers. Here, the continuity property of vessel locations and echo leakage effect can be assumed for retaining the contour centers, which could be ship echoes with all predetermined contour centers. Regarding comparison, the reported ship locations from the AIS data are shown in red and black dotted curves. The left panel exhibits the RA brightness distribution maps, while the right panel displays the maps in the polar coordinate.

It can be seen that the NC-DCMP beamformer with the filtered radar echoes yielded provides a brightness map of targets that matched with those of the AIS data (Figure 6-13). Nevertheless, some ships or objects were not determined by the radar system. One of the reasons is that those received echoes were not high enough to be visible. Most of those targets are located farther away or larger off-radar boresight. In addition, it is known that the intensity of radar echoes depends on the radar-cross section of objects, and many factors can affect the feature of the object's RCS [128]. As a result, the radar echo intensity varies with the object's RCS and could be too low to be identified occasionally, even when the object is located near the radar boresight. An example case is illustrated by the black arrow in Figure 6-13. In addition, the radar echo intensity of this ship varied over a wide range as the ship sailed through the radar beam.

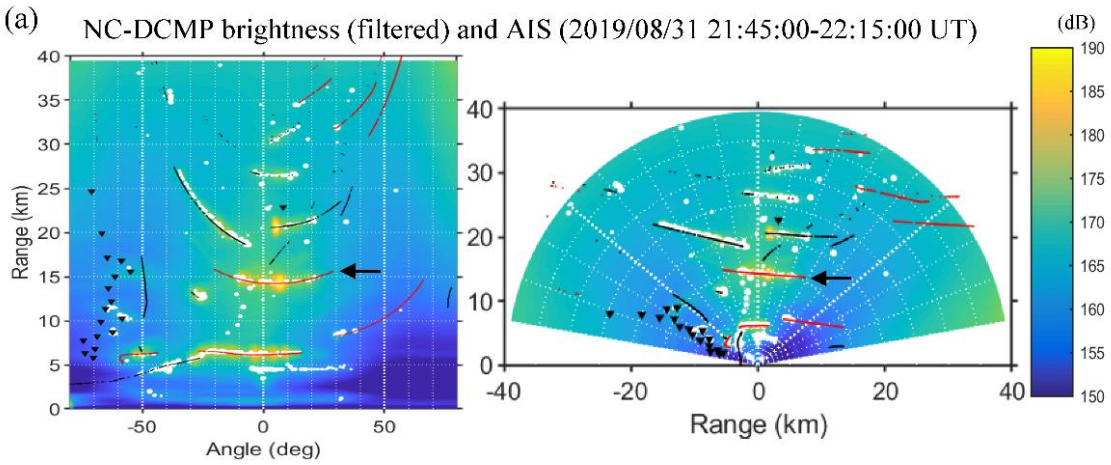

Figure 6-13 Comparison of ship locations obtained from AIS data and integrated brightness distribution within a period of 30 minutes [46]. Herein, the left panel shows the range-angle brightness distribution, while the right panel shows the brightness distribution in the polar coordinate. The ship tracks from AIS data are represented by the dotted curves (red: southward, black: northward) and downward-pointing triangle (nearly stationary object). The white streams and white spots represent the radar-determined object locations. The brightness maps in this graph are obtained from the NC-DCMP beamformer and the filtered radar echoes.

It is also found that the radar sometimes can observe moving ships that do not have information in the AIS data. As an example, a possible ship tracked by the stream of white dots just below 5 km, between -10^o and 40^o is shown in Figure 6-13. The AIS information of this marked point was not retrieved. It could be a small boat or a fishing boat with no AIS system, or its AIS broadcast was turned off on purpose. In Figure 6-13, many isolated white spots can be determined in addition to several white streams. Some of these isolated white spots could be relevant to sea echoes or interferences, which were not removed in our locating approach. It means there is still room for improvement of the locating process to discard doubtful non-ship echoes. After this improvement, it is expected that the radar-determined ship

locations on the RA map can be applied to estimate the velocity and direction of navigations, and provide information on false alarm rates and probability of detection, and so on.

To compare the estimation results of RA and RD methods, the range and angular locations of the seven ships in the right panel of Figure 6-12 are listed in Table 6-1. In that table, the mean AIS information of ships 2, 4, 5, and 6 in the radar data interval (~28 s) is provided, while the AIS information for ships 3 and 7 at the period nearest the radar time is taken. It can be seen that there was a slight difference between the results from RA and Rd methods: the distance and direction differences were within 1 km and 1^{o}, respectively, except for ship #1. In contrast, a larger difference existed between AIS and radar results. It could be attributed to the discontinuity of the AIS information. Indeed, the AIS information was intermittently recorded and sometimes lost data in the radar time interval, which is128 chirps in approximately 28s. Therefore, an average of the AIS information within the radar time interval was given in Table 6-1, or the AIS information nearest the midpoint of the radar time interval was used when the AIS information within the radar time interval was unavailable. In future works, a complete comparison between the results of RA and RD methods and those from AIS data can be conducted to assess the robustness of the RA method.

Table 6-1 Ship locations estimated from RA and RD methods for the seven ships indicated in the right panel of Figure 6-12 and those from AIS information [46].

Ship No. method	1	2	3	4	5	6	7
RA (r, θ_w)	4.24, 15.42°	6.41, -1.05°	13.00, -26.05°	14.27, 3.99°	21.44, 19.77°	22.04, -23.11°	26.50, 8.93°
RD (r, θ_w)	5.24, 17.00°	6.74, -1.00°	13.74, -27.00°	15.24, 4.00°	22.22, 20.00°	22.73, -23.00°	27.22, 9.00°
AIS (r, θ_w) (Ship name, MMSI)	----	6.56, -3.54° (ASIA CEMENT NO.3, 416124000)	14.16, -28.34° (WAN HAI 203, 416260000)	15.13, 0.68° (WAN-HAI 213, 564495000)	22.30, 16.27° (YM EFFICIENCY, 636013698)	24.08, -24.75° (BEAR MOUNTAIN BRIDGE, 354942000)	27.84, 7.99° (SOLAR MAJESTY, 371718000)

In practical operation, we must consider the suitability of the data length used for the ship detection and those for estimating sea surface parameters, such as current, waves, and winds. It is evident that retrieving sea surface parameters is still an essential purpose of the coastal radar. Indeed, a longer data length provides finer frequency bins, which is profitable to produce a better result of the first- and second-order Doppler spectra for sea current and waves retrieval. However, the longer length of radar data (around 10 minutes to an hour) is not beneficial to ship detection because the ship echoes will spread due to a larger variety of ship's radial speed, making the challenge for ship detection from the range-Doppler spectra, and also fewer ship locations are determined, which is not helpful for ship tracking. The same consideration is also required in the RA map, even though the RA map is not subject to the number of Doppler frequencies. It is possible to segment the data stream that is simultaneously used for surface current and wave measurements into short data lengths, which might provide more ship locations on the track. Nevertheless, the radar data length for ship detection should not be too short. It is because the output ship locations may fluctuate, and unreliable echo centers could be provided. In this report, the results in Figure 6-13 can be acceptable, although improvement in the imaging process is still needed. At present, we are testing a new technique that uses the brightness variation value for suppressing sea echoes and highlighting ship echoes in ship tracking.

6.4.2 The influence of ship characteristics and parameters

To estimate the accuracy of the estimation result, the estimated position of targets is compared with the ship location from the AIS data. Around 24 hours of data were used to compare, and the comparison result is shown in Figure 6-14, detailed in [138]. During 24 hours on July 31st, 2019, around 28000 objects were detected by the radar system. Herein, approximately 50% of them are correct

compared with those of the AIS data. Figure 6-14 indicates that there is around a 35% probability for a distance of less than 2 km. However, it is only the preliminary results for the comparison. More comparisons, including different sea states and strongly radio interference, are required to show the detection and tracking performance of the radar system. In addition, the size of the ship has not been taken into account in this statistic.

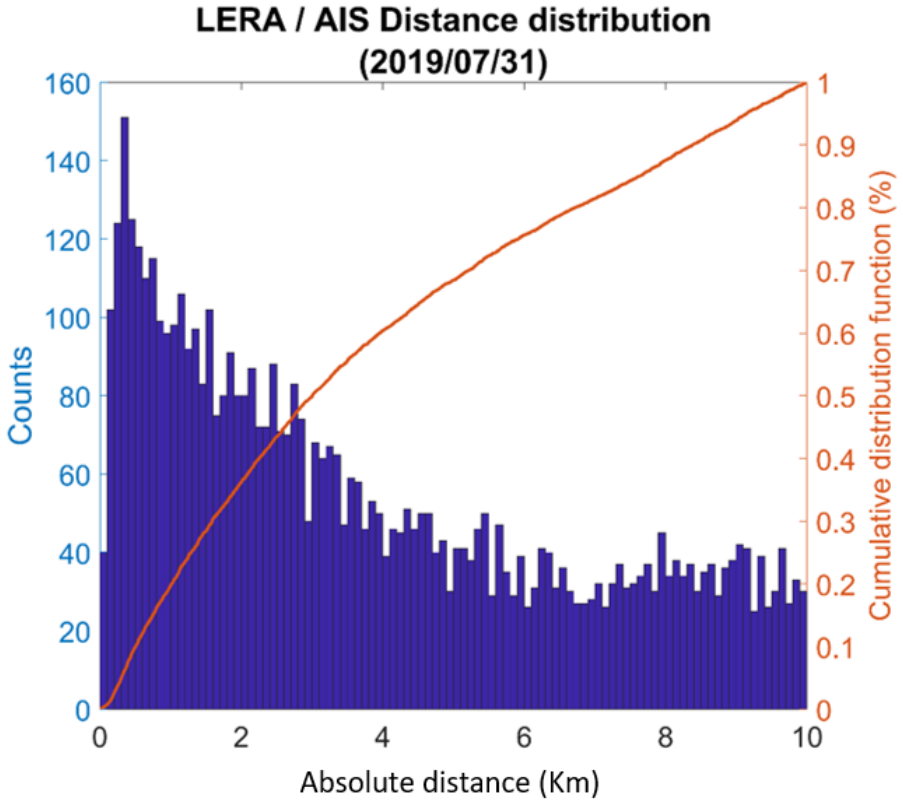

Figure 6-14 The amount (the blue bar) and the cumulative distribution (the orange curve) of the absolute distance between AIS information and radar-determined ship locations. Herein, the blue bar and the orange curve are referenced to the left and right axes, respectively.

The amount and the percentage of ship location detected by the HF radar system with respect to distance are shown in Figure 6-15, detailed in [138]. Less than a 4 km distance between the estimated position and AIS information is considered

co-location. In Figure 6-15, the left vertical axis (blue) shows the percentage of successful detection, while the right vertical axis (orange) shows the number of targets recorded by AIS. The horizontal axis is the observation distance (in kilometers). The data was observed from July 3rd-31st, 2019, with a total of 124080 targets. The result shows that the HF radar system is not efficient for ship detection in a distance of fewer than 4 kilometers and larger than 30 kilometers. This is because the coastal noise influences the estimation result in the near field, while the radar echo signal-to-noise ratio is so low in the far-field. The percentage of detection within the range of 4 to 30 kilometers is steady and approximately 60%. It demonstrated that the performance of the radar system is good enough for ship detection or tracking.

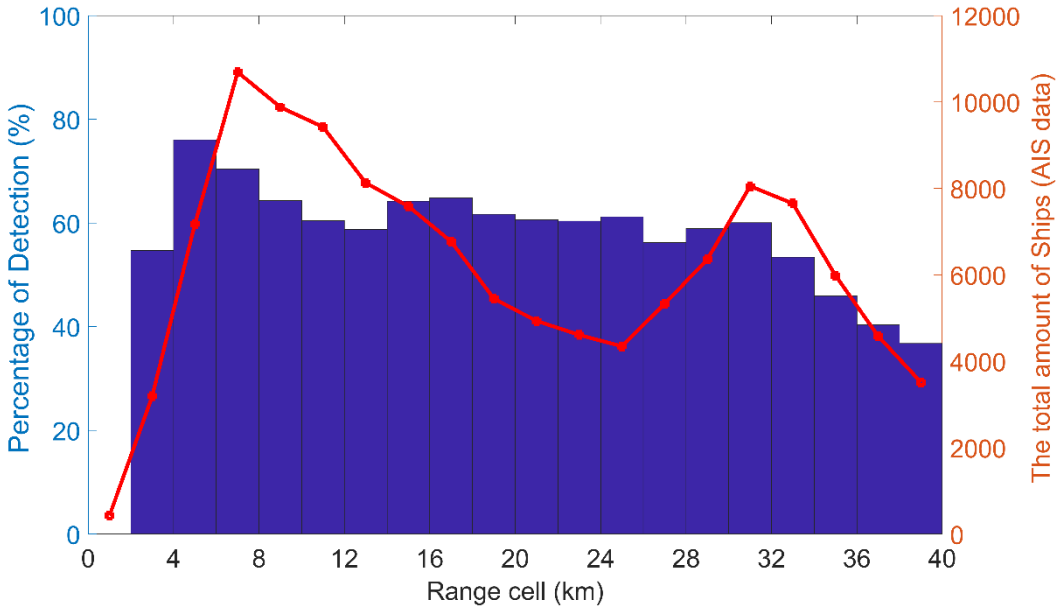

Figure 6-15 The percentage (the blue bar) and the amount (the red line) of radar-determined ship locations with respect to the range of ships. Herein, the blue bar and the red line are referenced to the left and right axes, respectively.

On the other hand, we are going to analyze the influence of ship's characteristics on the percentage of ship detection by HF radar technique. First, to

understand how the ship's signal is in the present under high sea wave conditions, the SNR of the ship's length and sea echoes are shown in terms of distance (Figure 6-16) [138]. The length of vessels is categorized into four levels corresponding to four colors, which are blue, magenta, green and red, while the sea echoes including the first- (black solid and dashed lines) and second-order (black dashed-dotted and dotted lines) Doppler spectra were selected from a special case of severe sea states, which has the significant wave height of 3.8 meters and are driven by winter monsoon winds. It can be seen that larger ships provide stronger intensity, and the ship's power becomes weaker in the far-field compared to those of the near-field. It is true that the intensity of ship echoes decreases with power 4 of the distance, and the sea-echo decays in power 3. The comparison shows that the intensity of ship echoes is generally greater than the sea-echo spectra power. However, there are still a small number of ships whose signals are smaller than the power of Bragg waves. Although the signal power of the ship decreases faster than those of sea echoes, the SNR of the ship's signal remains larger than the wave signal within the range of 40 km. This result is different from the simulated results in [130]. On the other hand, the noise interference in the range of 8 and 16 kilometers causes inconsistent results with other distances. It also shows that it is difficult to identify ship echoes at those range cells under strong interference.

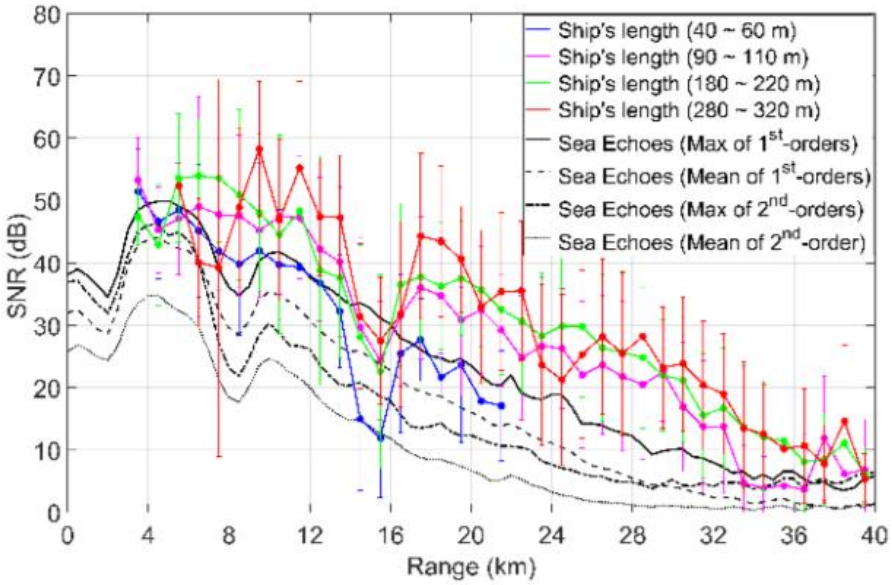

Figure 6-16 The SNR of ship echoes corresponds to various ship lengths and the sea-echo SNR.

Figure 6-17 shows the percentage of ships detected by the HF radar system under different ship lengths. In this figure, the left vertical axis (blue) is the percentage of successfully detected; the right vertical axis (orange) is the number of ships in different sizes recorded by the AIS system [138]. Figure 6-17 indicates that the number of ships larger than 300 meters is small compared to those of other ships' lengths. In addition, the success rate of detection is around 50-60%, which is a great number. The high-frequency radar observations are not significantly affected by the size of the ship. It can also be seen in Figure 6-17 for different ship lengths. The signal can be inferred, which means that the size of the ship may not be an essential factor. The radar performance for ship detection might be significantly influenced by the complex background environment and interference. Besides, the ship's height could be an essential factor affecting the intensity of ship echoes. Unfortunately, there is no ship's height data in the AIS information. Therefore, we cannot implement the analysis for that factor.

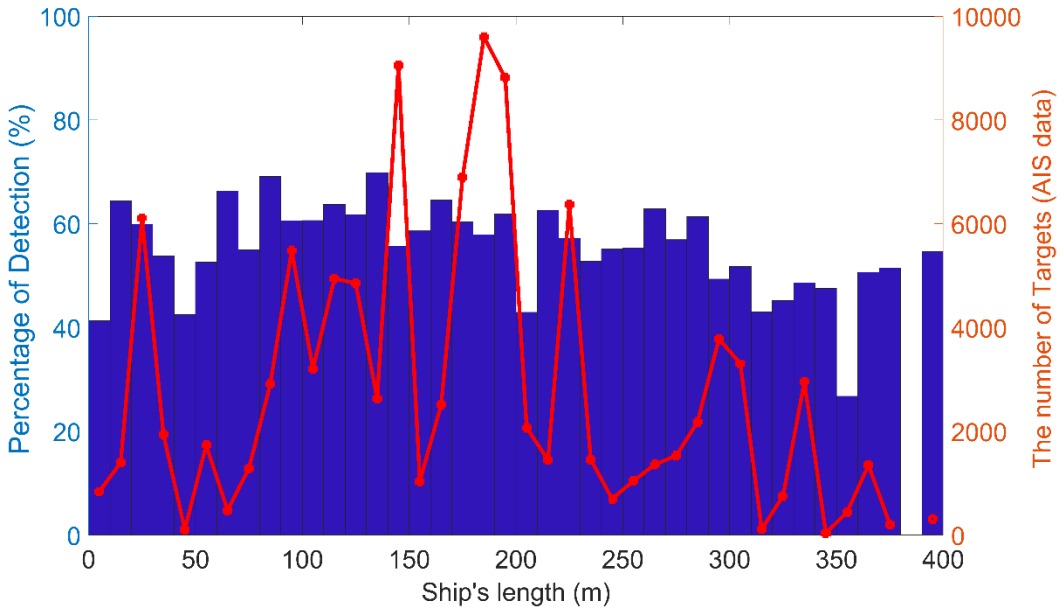

Figure 6-17 The percentage (the blue bar) and the amount (the red line) of radar-determined ship locations with respect to the ship's length. The blue bar and the red line are referenced to the left and right axes, respectively.

In another respect, the influence of the ship's heading and ship's direction on the percentage of detection results is analyzed. Generally, the heading and the direction of ships are slightly different during the movement of ships. It is because the ship's travel vector should be balanced to the sum of the ship's vector and the ocean surface current's vector. The statistical results are shown in Figures 6-18 and 6-19 [138]. In the two those figures, the vertical axis on the left (blue) is the percentage of detection results, while the vertical axis on the right (orange) is the number of ships obtained from the AIS data. The horizontal axis of Figures 6-18 and 6-19 shows the ship's direction and the ship's heading, respectively. For the direction or heading, 0^{o} is north, 180^{o} is south, 120^{o} and 300^{o} are the directions toward and away from the radar station.

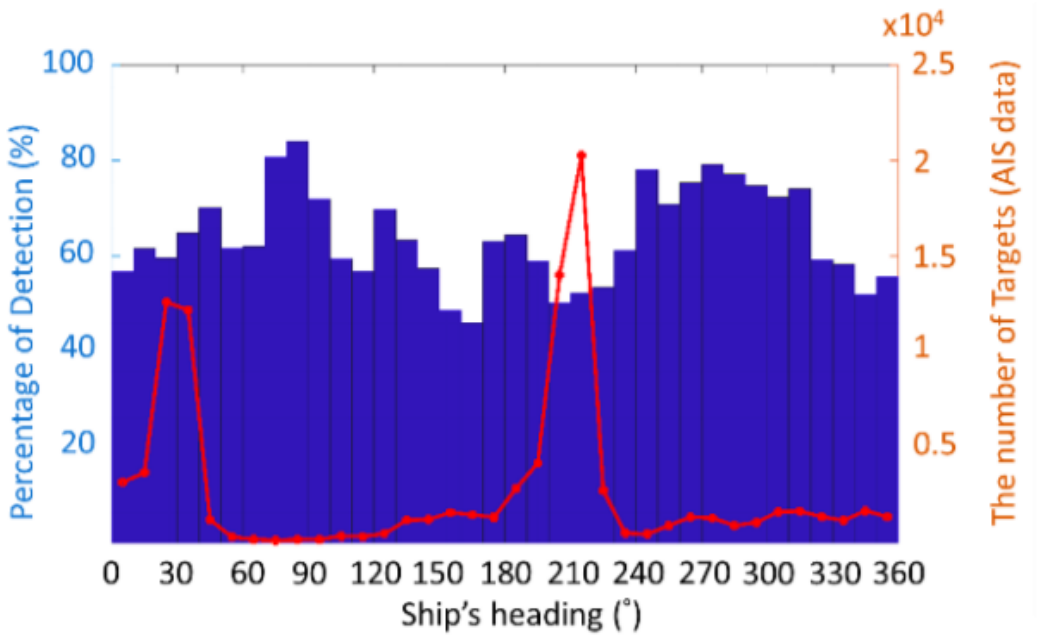

Figure 6-18 The percentage (the blue bar) and the amount (the red line) of radar-determined ship locations with respect to the ship's heading. The blue bar and the red line are referenced to the left and right axes, respectively.

From Figures 6-18 and 6-19, it was found that if the ship is heading or moving toward or away from the radar station, the number of estimation results is low. By contrast, the estimation results become higher when the heading or the traveling direction of ships is parallel to the coastline. It is related to the different radar cross-sections of the ship in different directions. The data shows that the heading or heading direction of the ship here is more concentrated around 30^{o} and 210^{o}, and reduced for other traveling directions. The result of this part may need more information for analysis and verification.

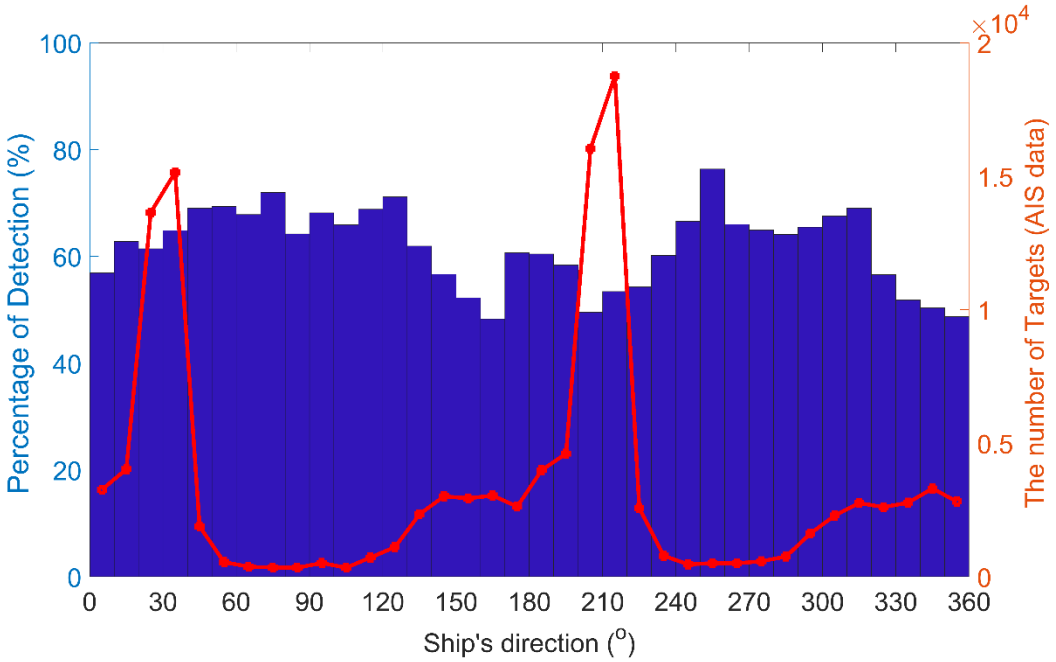

Figure 6-19 The percentage (the blue bar) and the amount (the red line) of radar-determined ship locations with respect to the ship's direction. The blue bar and the orange curve are referenced to the left and right axes, respectively.

6.5 Summary

In this chapter, two approaches for ship detections, including range-Doppler (RD) and range-angle (RA) methods, were introduced and implemented. The results indicated that both estimators perform very well. For the RD methods, common techniques such as the curvilinear regression analysis, 2D moving average filtering, and the corresponding adaptive threshold, are applied to identify ship echos from the range-Doppler spectra maps. In addition, CFAR algorithms are implemented to verify the correctness of possible signals, and it also works well. However, both estimators detected many targets, which is sometimes incorrect. The noise interference is the main factor that influences the uncertainty of estimators. Besides, the value of the adaptive threshold also needs to be carefully selected.

For the RA methods, an alternative approach to detect ship echoes from the data acquired by a phased-array HF coastal radar was proposed. Beamformers with the time series data from multichannel receivers have been executed to produce the horizontal map of range-angle brightness distribution, where ship locations can be directly identified. This approach is totally different from the traditional method using the range-Doppler spectra map, upon which existing algorithms of ship detection using the HF coastal radar are developed. In three beamformers, including linear Fourier, directionally constrained minimum power (DCMP), and norm-constrained DCMP (NC-DCMP) algorithms, the NC-DCMP beamformer provides great confidence for determining ship echoes based on the strength of lower sidelobes and finer angular resolution, yielding more readable and reliable RA map. In addition, the band-stop filter that can effectively suppress the sea echoes is an important technique to improve the detectability of ship echoes. The RA map result illustrated that the ship echoes could be scanned images over the spatial domain as those of microwave radar. It is expected that the image processing toolboxes can be tested to enhance the brightness value of ship echoes.

The radar-determined ship locations using the RD and RA methods have also been verified through Automatic Identification System (AIS) information. It was found that not all ships/objects having the AIS information can be seen by the radar, which could be due to small radar cross-sections or dramatically decreased intensity at large off-beam directions. On the other hand, there exist ships that were detected by the radar system but without AIS information.

Based on the ship detection percentage and ship's characteristics, it was found that the HF radar (LERA MK-III) system performs very well for ship detection. Generally, the intensity of ship echoes is more substantial than those of sea echoes, even under severe sea states. However, it is difficult to detect the ship under strong interference. It means that the environmental background noise and interference

significantly influence ship detection results, whatever methods are used. Also, the heading and the direction of ships affect the strength of ship echoes, which is the most important factor for identifying their location. Later, this radar system performs well in the range of 4 to 30 kilometers from the radar station.

The newly established phased-array HF coastal radar system and our present studies are believed to be a potential tool for monitoring the ships navigating around the harbor. In future work, various methods, including RD spectrum and RA brightness distribution methods, will be improved to establish a convenient operation of ship tracking with the HF coastal radar data, in addition to AIS information.

CHAPTER VII CONCLUSIONS

7.1 General Synopsis and Innovation

Exploiting the applications of high-frequency ocean radar is an exciting topic that is attracted scientists, managers, and politicians for lunching projects, which are used to respond to maritime risks and warning hazards. The HF coastal radar system provides the unique capability to continuously monitor sea surface dynamics and navigate marine traffic within the EEZ. However, due to the lack of knowledge and experience, it is still challenging for research teams in Taiwan to deploy and operate these radar systems for practical applications. In this dissertation, we have clarified and analyzed some issues as well as proposed suitable solutions.

1. We introduced and expressed Barrick's theory that describes the relationship between monostatic radar cross-section and sea-state parameters. Then, a self-developed simulation toolbox is established to simulate the radar Doppler spectra from the given directional wave spectrum. It is an essential tool for analyzing the response of radar cross-sections under various sea-state conditions. It is also helpful for implementing the inversion methods to estimate the directional wave spectrum from HF radar Doppler spectra.

2. Existing methods for wave parameter retrieval are introduced and implemented. A self-developed E2ES toolbox is established to test wave parameter estimators under various ocean wavefields, such as steady homogenous waves, monsoon waves, and typhoon waves. The result indicated that the bias estimation is mainly influenced by radar-to-wave angle and the smallness parameters. Also, it was found that estimators for retrieving wave parameters perform better in typhoon conditions than in monsoon wave conditions.

3. We established a procedure for estimating and validating wave parameters estimated from the Doppler spectra of a single phased-array HF radar system. In this

process, a modification of the FOL method for separating the region of first- and second-order components is proposed. The estimator developed from empirical methods of wave parameter inversion is implemented to determine wave measurements under various weather conditions. Then, the estimation results are compared to in-situ wave data to assess the performance of the HF radar system and the wave estimator's uncertainty. Furthermore, many algorithms are introduced to estimate the wave parameter correction coefficients, which might be the function of radar-to-wave angle, smallness parameters, and spectral width parameters. Finally, the calibrated result is compared to in-situ data to assess the performance of those correction methods. The comparison of error indexes before and after calibration demonstrated the necessity of implementing correction algorithms.

4. To identify marine vessels from the backscattered signal of HF radar systems, detection methods have been implemented and modified. Besides applying traditional methods using the RD spectra map, the range-Angle (RA) method provided the brightness distribution of sea and ship echoes in the two space dimensions (range and azimuthal angle) is first proposed and implemented. Based on the comparison results between the estimated ship location and those of AIS data, the new method has proven effective in ship detection and tracking. It is also represented a new way of actively tracking ship signals from HF coastal radar in addition to AIS. Furthermore, the percentage of ship location detected by the HF radar system is analyzed to respond to the ship's characteristics. The results indicated that the heading or the direction of vessels influences the performance of the HF radar system and the estimator's uncertainty for ship detection.

7.2 Future Works

Implement estimators for retrieving ocean surface wave spectra from the radar Doppler spectra under various weather conditions to assess the uncertainty and

limitations of those existing methods. Then, the method having the best performance will be implemented to retrieve the directional wave spectrum from the ongoing HF radar network.

Develop the method for classifying the wave fields affected by swell and wind-sea under different weather conditions. Thereby, it is able to monitor and predict the appearance of freak waves in the coastal regions.

The RA method for ship detection and tracking is being improved.

BIBLIOGRAPHY

[1] H. Roarty, T. Cook, L. Hazard, D. George, J. Harlan, S. Cosoli, L. Wyatt, E. Alvarez Fanjul, E. Terrill, M. Otero, J. Largier, S. Glenn, N. Ebuchi, B. Whitehouse, K. Bartlett, J. Mader, A. Rubio, L. Corgnati, C. Mantovani, A. Griffa, E. Reyes, P. Lorente, X. Flores-Vidal, K.J. Saavedra-Matta, P. Rogowski, S. Prukpitikul, S.-H. Lee, J.-W. Lai, C.-A. Guerin, J. Sanchez, B. Hansen, and S. Grilli, "The Global High Frequency Radar Network," *Frontiers in Marine Science,* vol. 6, 2019/05/14.

[2] S. Fujii, M. L. Heron, K. Kim, J. W. Lai, S. H. Lee, X. Wu, L.R. Wyatt, and W.C. Yang, "An overview of developments and applications of oceanographic radar networks in Asia and Oceania countries," *Ocean Science Journal,* vol. 48, 2013/03/01, pp. 69-97.

[3] A. Rubio, J. Mader, L. Corgnati, C. Mantovani, A. Griffa, A. Novellino, C. Quentin, L. Wyatt, J. S.-S., J. Horstmann, P. Lorente, E. Zambianchi, M. Hartnett, C. Fernandes, V. Zervakis, P. Gorringe, A. Melet, I. and Puillat, "HF Radar Activity in European Coastal Seas: Next Steps toward a Pan-European HF Radar Network," *Frontiers in Marine Science*, vol. 4, 2017/01/20, pp. 1-20.

[4] K. Hasselmann, "Determination of Ocean Wave Spectra from Doppler Radio Return from the Sea Surface," *Nature Physical Science,* vol. 229, 1971/01/01, pp. 16-17.

[5] D. Barrick, "First-order theory and analysis of MF/HF/VHF scatter from the sea," *IEEE Transactions on Antennas and Propagation,* vol. 20, 1972, pp. 2-10.

[6] D. Barrick, "Remote sensing of sea state by radar," in *Ocean 72 - IEEE International Conference on Engineering in the Ocean Environment*, 1972, pp. 186-192.

[7] D. D. Crombie, "Doppler Spectrum of Sea Echo at 13.56 Mc./s," *Nature,* vol. 175, 1955, pp. 681-682.

[8] E. W. Gill and J. Walsh, "High-frequency bistatic cross sections of the ocean surface," *Radio Science,* vol. 36, 2001, pp. 1459-1475.

[9] J. Walsh, R. Donnelly, and T. Stuart John, "A new technique for studying propagation and scattering for mixed paths with discontinuities," *Proceedings of the Royal Society of London. A. Mathematical and Physical Sciences,* vol. 412, 1987/07/08, pp. 125-167.

[10] J. Walsh, W. Huang, and E. Gill, "The First-Order High Frequency Radar Ocean Surface Cross Section for an Antenna on a Floating Platform," *IEEE Transactions on Antennas and Propagation,* vol. 58, 2010, pp. 2994-3003.

[11] R. L. Hardman, L. R. Wyatt, and C. C. Engleback, "Measuring the Directional Ocean Spectrum from Simulated Bistatic HF Radar Data," *Remote Sensing,* vol. 12, 2020, pp. 1-28.

[12] A. G. Voronovich and V. U. Zavorotny, "Measurement of Ocean Wave Directional Spectra Using Airborne HF/VHF Synthetic Aperture Radar: A Theoretical Evaluation," *IEEE Transactions on Geoscience and Remote Sensing,* vol. 55, 2017, pp. 3169-3176.

[13] F. Ding, C. Zhao, Z. Chen, and J. Li, "Sea Echoes for Airborne HF/VHF Radar: Mathematical Model and Simulation," *Remote Sensing,* vol. 12, 2020.

[14] D. E. Barrick, "Extraction of wave parameters from measured HF radar sea-echo Doppler spectra," *Radio Science,* vol. 12, 1977, pp. 415-424.

[15] Maresca J, J. W., and T. M. Georges, "Measuring rms wave height and the scalar ocean wave spectrum with HF skywave radar," *Journal of Geophysical Research: Oceans*, vol. 85, 1980/05/20, pp. 2759-2771.

[16] Z. Chen, C. Zezong, J. Yanni, F. Lingang, and Z. Gengfei, "Exploration and Validation of Wave-Height Measurement Using Multifrequency HF Radar," *Journal of Atmospheric and Oceanic Technology*, vol. 30, 2013/09/01, pp. 2189-2202.

[17] L. Wyatt, J. Venn, G. Burrows, A. Ponsford, M. Moorhead, and J. V. Heteren, "HF radar measurements of ocean wave parameters during NURWEC," *IEEE Journal of Oceanic Engineering*, vol. 11, 1986, pp. 219-234.

[18] H. C. Graber and M. L. Heron, "Wave height measurements from HF radar," *Oceanography*, vol. 10, 1997, pp. 90-92.

[19] B. K. Haus, L. K. Shay, P. A. Work, G. Voulgaris, R. J. Ramos, and J. Martinez-Pedraja, "Wind Speed Dependence of Single-Site Wave-Height Retrievals from High-Frequency Radars," *Journal of Atmospheric and Oceanic Technology*, vol. 27, 2010/08/01, pp. 1381-1394.

[20] L. Wyatt, "Significant waveheight measurement with h.f. radar," *International Journal of Remote Sensing*, vol. 9, 1988, pp. 1087-1095.

[21] A. Long and D. Trizna, "Mapping of North Atlantic winds by HF radar sea backscatter interpretation," *IEEE Transactions on Antennas and Propagation*, vol. 21, 1973, pp. 680-685.

[22] R. H. Stewart and J. R. Barnum, "Radio measurements of oceanic winds at long ranges: An evaluation," *Radio Science*, vol. 10, 1975, pp. 853-857.

[23] D. M. Fernandez, H. C Graber, J. Paduan, and D. Barrick, "Mapping Wind Directions with HF Radar," *Oceanography*, vol. 10, 1997, pp. 93-95.

[24] W. Huang, E. Gill, S. Wu, B. Wen, Z. Yang, and J. Hou, "Measuring Surface Wind Direction by Monostatic HF Ground-Wave Radar at the Eastern China Sea," *IEEE Journal of Oceanic Engineering,* vol. 29, 2004, pp. 1032-1037.

[25] L. R. Wyatt, "Shortwave Direction and Spreading Measured with HF Radar," *Journal of Atmospheric and Oceanic Technology,* vol. 29, 2012/02/01, pp. 286-299.

[26] E. W. Gill and J. Walsh, "Extraction of ocean wave parameters from HF backscatter received by a four-element array: analysis and application," *IEEE Journal of Oceanic Engineering,* vol. 17, 1992, pp. 376-386.

[27] R. Howell and J. Walsh, "Measurement of ocean wave spectra using narrow-beam HE radar," *IEEE Journal of Oceanic Engineering,* vol. 18, 1993, pp. 296-305.

[28] Y. Hisaki, "Nonlinear inversion of the integral equation to estimate ocean wave spectra from HF radar," *Radio Science,* vol. 31, 1996, pp. 25-39.

[29] L. R. Wyatt, "A relaxation method for integral inversion applied to HF radar measurement of the ocean wave directional spectrum," *International Journal of Remote Sensing,* vol. 11, 1990/08/01, pp. 1481-1494.

[30] N. Hashimoto and M. Tokuda, "A Bayesian Approach for Estimation of Directional Wave Spectra with HF Radar," *Coastal Engineering Journal,* vol. 41, 1999/06/01, pp. 137-149.

[31] Lukijanto, N. Hashimoto, and M. Yamashiro, "An improvement of modified Bayesian method for estimating directional wave spectra from HF radar backscatter," in *Asian and Pacific Coasts 2009,* ed: World Scientific Publishing Company, 2009, pp. 105-111.

[32] R. L. Hardman and L. R. Wyatt, "Inversion of HF Radar Doppler Spectra Using a Neural Network," *Journal of Marine Science and Engineering,* vol. 7, 2019, pp. 1-18.

[33] R. Shahidi and E. W. Gill, "A New Automatic Nonlinear Optimization-Based Method for Directional Ocean Wave Spectrum Extraction From Monostatic HF-Radar Data," *IEEE Journal of Oceanic Engineering*, vol. 46, 2021, pp. 900-918.

[34] A. L. Dzvonkovskaya and H. Rohling, "Target Detection with Adaptive Power Regression Thresholding for HF Radar," in *2006 CIE International Conference on Radar*, 2006, pp. 1-4.

[35] A. L. Dzvonkovskaya and H. Rohling, "HF radar ship detection and tracking using WERA system," in *2007 IET International Conference on Radar Systems*, 2007, pp. 1-5.

[36] F. Jangal, S. Saillant, and M. Helier, "Wavelet Contribution to Remote Sensing of the Sea and Target Detection for a High-Frequency Surface Wave Radar," *IEEE Geoscience and Remote Sensing Letters*, vol. 5, 2008, pp. 552-556.

[37] P. P. Gandhi and S. A. Kassam, "Analysis of CFAR processors in nonhomogeneous background," *IEEE Transactions on Aerospace and Electronic Systems*, vol. 24, 1988, pp. 427-445.

[38] H. Rohling, "Radar CFAR Thresholding in Clutter and Multiple Target Situations," *IEEE Transactions on Aerospace and Electronic Systems*, vol. AES-19, 1983, pp. 608-621.

[39] M. D. E. Turley, "Hybrid CFAR techniques for HF radar," in *Radar 97 (Conf. Publ. No. 449)*, 1997, pp. 36-40.

[40] S. Grosdidier and A. Baussard, "Ship detection based on morphological component analysis of high-frequency surface wave radar images," *IET Radar Sonar Navigation*, vol. 6, 2012, pp. 813–821.

[41] L. Z. H. Chuang, Y. J. Chung, and S. T. Tang, "A Simple Ship Echo Identification Procedure With SeaSonde HF Radar," *IEEE Geoscience and Remote Sensing Letters*, vol. 12, 2015, pp. 2491-2495.

[42] S. Park, C. J. Cho, B. Ku, S. Lee, and H. Ko, "Simulation and Ship Detection Using Surface Radial Current Observing Compact HF Radar," *IEEE Journal of Oceanic Engineering*, vol. 42, 2017, pp. 544-555.

[43] C. Wang, B. Wen, and W. Huang "A Support Vector Regression-Based Method for Target Direction of Arrival Estimation From HF Radar Data," *IEEE Geoscience and Remote Sensing Letters*, vol. 15, 2018, pp. 674-678.

[44] W. Sun, W. Huang, Y. Ji, Y. Dai, P. Ren, P. Zhou, X. Hao, "A Vessel Azimuth and Course Joint Re-Estimation Method for Compact HFSWR," *IEEE Transactions on Geoscience and Remote Sensing*, vol. 58, 2020, pp. 1041-1051.

[45] G. Vivone, P. Braca, and J. Horstmann, "Knowledge-Based Multitarget Ship Tracking for HF Surface Wave Radar Systems," *IEEE Transactions on Geoscience and Remote Sensing*, vol. 53, 2015, pp. 3931-3949.

[46] J. S. Chen, D. T. Dao, and H. Chien, "Ship Echo Identification Based on Norm-Constrained Adaptive Beamforming for an Arrayed High-Frequency Coastal Radar," *IEEE Transactions on Geoscience and Remote Sensing*, vol. PP, 06/19 2020, pp. 1-11.

[47] M. Parker, *Digital Signal Processing 101, Second Edition: Everything You Need to Know to Get Started*: Newnes, 2017.

[48] W. Huang, X. Wu, B. Lund, and K. El-Darymli, "Advances in Coastal HF and Microwave (S- or X-Band) Radars," *International Journal of Antennas and Propagation*, vol. 2017, 2017/02/28.

[49] D. Crombie, "Resonant backscatter from the sea and its application to physical oceanography," in *Ocean 72 - IEEE International Conference on Engineering in the Ocean Environment*, 1972, pp. 174-179.

[50] T. Hilmer, "Radar Sensing of ocean wave heights," Master, University of Hawaii at Manoa, 2010.

[51] S. O. Rice, "Reflection of electromagnetic waves from slightly rough surfaces," *Communications on Pure and Applied Mathematics*, vol. 4, 1951/08/01, pp. 351-378.

[52] E. W. Gill, "The Scattering of High Frequency Electromagnetic Radiation from the Ocean Surface: An Analysis Based on a Bistatic Ground Wave Radar Configuration," PhD, Memorial University of Newfoundland, 1999.

[53] http://radarhf.ismar.cnr.it/HFRadarTech.html.

[54] M. Longuet-Higgins, D. E. Cartwright, and N. D. Smith, "Observations of the directional spectrum of sea waves using the motions of a floating buoy," in *Ocean Wave Spectra, proceedings of a conference, Easton, Maryland*, 1963, pp. 111-136.

[55] B. J. Lipa and D. E. Barrick, "Analysis methods for narrow-beam high-frequency radar sea echo," Technical Report, 1982.

[56] B. J. Lipa and D. E. Barrick, "Extraction of sea state from HF radar sea echo: Mathematical theory and modeling," *Radio Science*, vol. 21, 1986, pp. 81-100.

[57] D. E. Barrick and B. L. Weber, "On the Nonlinear Theory for Gravity Waves on the Ocean's Surface. Part II: Interpretation and Applications," *Journal of Physical Oceanography*, vol. 7, 1977, pp. 11-21.

[58] B. J. Lipa and B. Nyden, "Directional wave information from the SeaSonde," *IEEE Journal of Oceanic Engineering*, vol. 30, 2005, pp. 221-231.

[59] L. R. Wyatt, "High order nonlinearities in HF radar backscatter from the ocean surface," *IEE Proceedings - Radar, Sonar and Navigation*, vol. 142, 1995, pp. 293-300.

[60] W. J. Pierson and L. Moskowitz, "A proposed spectral form for fully developed wind seas based on the similarity theory of S. A. Kitaigorodskii," *Journal of Geophysical Research (1896-1977)*, vol. 69, 1964/12/15, pp. 5181-5190.

[61] K. Hasselmann, T. P. Barnett, E. Bouws, H. Carlson, D. E. Cartwright, K. Enke, *et al.*, "Measurements of wind-wave growth and swell decay during the Joint North Sea Wave Project (JONSWAP)," 1973.

[62] H. Mitsuyasu, F. Tasai, T. Suhara, S. Mizuno, M. Ohkusu, T. Honda, K. Rikiishi, "Observations of the Directional Spectrum of Ocean WavesUsing a Cloverleaf Buoy," *J. Physical Oceanogr.*, vol. 5, 1975/10/01, pp. 750-760.

[63] W. Shen, K.-W. Gurgel, G. Voulgaris, T. Schlick, and D. Stammer, "Wind-speed inversion from HF radar first-order backscatter signal," *Ocean Dynamics*, vol. 62, 2012/01/01, pp. 105-121.

[64] Z. Alattabi, D. Cahl, and G. Voulgaris, "Swell and Wind Wave Inversion Using a Single Very High Frequency (VHF) Radar," *Journal of Atmospheric and Oceanic Technology*, vol. 36, 04/02 2019, pp. 987–1013.

[65] B. Lipa and D. E. Barrick, "Extraction of sea state from HF radar sea echo: Mathematical theory and modeling," *Radio Science*, vol. 21, 1986, pp. 81-100.

[66] L. R. Wyatt, J. J. Green, and A. Middleditch, "HF radar data quality requirements for wave measurement," *Coastal Engineering*, vol. 58, 2011/04/01, pp. 327-336.

[67] Z. Chen, C. Zezong, J. Yanni, F. Lingang, and Z. Gengfei, "Exploration and Validation of Wave-Height Measurement Using Multifrequency HF Radar," *J. Atmos. Ocean. Technol.*, vol. 30, 2013/09/01, pp. 2189-2202.

[68] S. Heron and M. Heron, "A Comparison of Algorithms for Extracting Significant Wave Height from HF Radar Ocean Backscatter Spectra," *Journal of Atmospheric and Oceanic Technology,* vol. 15, 1998, pp. 1157-1163.

[69] M. L. Heron, P. E. Dexter, and B. T. McGann, "Parameters of the air-sea interface by high-frequency ground-wave Doppler radar," *Marine and Freshwater Research,* vol. 36, 1985, pp. 655-670.

[70] L. Cai, S. Shang, G. Wei, Z. He, Y. Xie, K. Liu, T. Zhou, J. Chen, F. Zhang, Y. Li, "Assessment of Significant Wave Height in the Taiwan Strait Measured by a Single HF Radar System," *Journal of Atmospheric and Oceanic Technology,* vol. 36, 2019, pp. 1419-1432.

[71] R. J. Ramos, H. C. Graber, and B. K. Haus, "Observation of Wave Energy Evolution in Coastal Areas Using HF Radar," *Journal of Atmospheric and Oceanic Technology,* vol. 26,01 Sep. 2009, pp. 1891-1909.

[72] G. Lopez, D. Conley, and D. Greaves, "Calibration, validation and analysis of an empirical algorithm for the retrieval of wave spectra from HF radar sea-echo," *Journal of Atmospheric and Oceanic Technology,* ol. 33, 2015, pp. 245-261.

[73] W. Mei and S.-P. Xie, "Intensification of landfalling typhoons over the northwest Pacific since the late 1970s," *Nature Geoscience,* vol. 9, 09/05/online 2016, pp. 753-757.

[74] L. H. Holthuijsen, M. D. Powell, and J. D. Pietrzak, "Wind and waves in extreme hurricanes," *Journal of Geophysical Research: Oceans,* vol. 117, 2012, pp. 1-15.

[75] A. Soloviev, R. Lukas, M. A. Donelan, and I. Ginis, "The Air-Sea Interface and Surface Stress under Tropical Cyclones," *Scientific Reports,* vol. 4, 2013, pp. 1-6.

[76] S. S. Chen, W. Zhao, M. A. Donelan, and H. L. Tolman, "Directional Wind–Wave Coupling in Fully Coupled Atmosphere–Wave–Ocean Models: Results from CBLAST-Hurricane," *Journal of the Atmospheric Sciences,* vol. 70, 2013/10/01, pp. 3198-3215.

[77] F. Ardhuin, A. Roland, F. Dumas, A.-C. Bennis, A. Sentchev, P. Forget, J. Wolf, F. Girard, P. Osuna, M. Benoit, "Numerical Wave Modeling in Conditions with Strong Currents: Dissipation, Refraction, and Relative Wind," *Journal of Physical Oceanography,* vol. 42, 2012/12/01, pp. 2101-2120.

[78] F. Ardhuin, S. T. Gille, D. Menemenlis, C. B. Rocha, N. Rascle, B. Chapron, J. Gula, J. Molemaker, "Small-scale open ocean currents have large effects on wind wave heights," *Journal of Geophysical Research: Oceans,* vol. 122, 2017/06/01, pp. 4500-4517.

[79] W. B. Chen, L. Y. Lin, J. H. Jang, and C. H. Chang, "Simulation of Typhoon-Induced Storm Tides and Wind Waves for the Northeastern Coast of Taiwan Using a Tide–Surge–Wave Coupled Model," *Water,* vol. 9, 2017, pp. 1-24.

[80] J. Walsh, W. Huang, and E. Gill, "The second-order high frequency radar ocean surface cross section for an antenna on a floating platform," *IEEE Transactions on Antennas and Propagation,* vol. 60, 10/01 2012, pp. 4804-4813.

[81] R. Shahidi and E. Gill, "Time-Domain Motion Compensation of HF-Radar Doppler Spectra for an Antenna on a Moving Platform," *2019 IEEE/OES Twelfth Current, Waves and Turbulence Measurement (CWTM)*, 2019, pp. 1-4.

[82] S. J. Anderson, "Remote sensing applications of HF skywave radar: The Australian experience," *Turkish Journal of Electrical Engineering and Computer Sciences,* vol. 18, 05/01 2010, pp. 339-372.

[83] P. E. Dexter and S. Theodoridis, "Surface wind speed extraction from HF sky wave radar Doppler spectra," *Radio Science,* vol. 17, 1982/05/01, pp. 643-652.

[84] J. Parent, "A frequency averaging method to improve sea-state measurements with a HF skywave radar," *IEEE Transactions on Antennas and Propagation,* vol. 35, 1987, pp. 467-469.

[85] S. J. Anderson, "Target Classification , Recognition and Identification with HF Radar," *RTO SET Symposium*, Oslo, Norway, 2004, pp. 1-25.

[86] K. W. Gurgel, G. Antonischki, H. H. Essen, and T. Schlick, "Wellen Radar (WERA): a new ground-wave HF radar for ocean remote sensing," *Coastal Engineering,* vol. 37, 1999/08/01/, pp. 219-234.

[87] P. Flament, D. Harris, M. Flament, I. Q. Fernandez, M. Hlivak, and X. Flores, et al., "A Compact High Frequency Doppler Radio Scatterometer for Coastal Oceanography," Washington, DC, 2016.

[88] H. H. Essen, K. W. Gurgel, and T. Schlick, "Measurement of ocean wave height and direction by means of HF radar: An empirical approach," *Deutsche Hydrografische Zeitschrift,* vol. 51, 1999/12/01, pp. 369-383.

[89] K. Gurgel, H. Essen, and T. Schlick, "An Empirical Method to Derive Ocean Waves From Second-Order Bragg Scattering: Prospects and Limitations," *IEEE Journal of Oceanic Engineering*, vol. 31, 2006, pp. 804-811.

[90] S. Heron and M. L. Heron, "A Comparison of Algorithms for Extracting Significant Wave Height from HF Radar Ocean Backscatter Spectra," *Journal of Atmospheric and Oceanic Technology - J ATMOS OCEAN TECHNOL,* vol. 15, 10/01 1998.

[91] R. Shahidi and E. W. Gill, "Two New Methods for the Extraction of Significant Wave Heights From Received HF-Radar Time Series," *IEEE Geoscience and Remote Sensing Letters*, vol. 17, 2020, pp. 2070-2074.

[92] D. E. Barrick, M. W. Evans, and B. L. Weber, "Ocean Surface Currents Mapped by Radar," *Science*, vol. 198, 1977, pp. 138-144.

[93] B. Lipa and D. Barrick, "Least-squares methods for the extraction of surface currents from CODAR crossed-loop data: Application at ARSLOE," *IEEE Journal of Oceanic Engineering*, vol. 8, 1983, pp. 226-253.

[94] D. Barrick and B. Lipa, "Evolution of Bearing Determination in HF Current Mapping Radars," *Oceanography*, vol. 10, 1997, pp. 72-75.

[95] R. O. Schmidt, "Multiple Emitter Location and Signal Parameter Estimation," *IEEE Transactions on Antennas and Propagation* vol. 34, 1986, pp. 276-280.

[96] J. Capon, "High-resolution frequency-wavenumber spectrum analysis," *Proceedings of the IEEE*, vol. 57, 1969, pp. 1408-1418.

[97] T. Helzel, M. Kniephoff, and L. Petersen, "WERA: Remote ocean sensing for current, wave and wind direction," in *2006 IEEE US/EU Baltic International Symposium*, 2006, pp. 1-8.

[98] S. N. Bhuiya, F. Islam, and M. Matin, "Analysis of Direction of Arrival Techniques Using Uniform Linear Array," *International Journal of Computer Theory and Engineering*, vol. 4, 2012, pp. 931-934.

[99] L. C. Godara, "Application of antenna arrays to mobile communications. II. Beam-forming and direction-of-arrival considerations," *Proceedings of the IEEE*, vol. 85, 1997, pp. 1195-1245.

[100] C. Teague, "Multifrequency HF radar observations of currents and current shears," *IEEE Journal of Oceanic Engineering*, vol. 11, 1986, pp. 258-269.

[101] A. R. Kirincich, T. de Paolo, and E. Terrill, "Improving HF Radar Estimates of Surface Currents Using Signal Quality Metrics, with Application to the MVCO High-Resolution Radar System," *Journal of Atmospheric and Oceanic Technology*, vol. 29, 2012/09/01, pp. 1377-1390.

[102] A. Randazzo, M. A. Abou-Khousa, M. Pastorino, and R. Zoughi, "Direction of Arrival Estimation Based on Support Vector Regression: Experimental Validation and Comparison With MUSIC," *IEEE Antennas and Wireless Propagation Letters*, vol. 6, 2007, pp. 379-382.

[103] H. Cox, R. Zeskind, and M. Owen, "Robust adaptive beamforming," *IEEE Transactions on Acoustics, Speech, and Signal Processing*, vol. 35, 1987, pp. 1365-1376.

[104] J. Li, P. Stoica, and Z. Wang, "On robust Capon beamforming and diagonal loading," *IEEE Transactions on Signal Processing*, vol. 51, 2003, pp. 1702-1715.

[105] C. Liu and G. Liao, "Robust Capon beamformer under norm constraint," *Signal Processing*, vol. 90, 2010/05/01, pp. 1573-1581.

[106] I. R. Young, "The determination of confidence limits associated with estimates of the spectral peak frequency," *Ocean Engineering*, vol. 22, 1995/10/01, pp. 669-686.

[107] I. R. Young and L. A. Verhagen, "The growth of fetch limited waves in water of finite depth. Part 1. Total energy and peak frequency," *Coastal Engineering*, vol. 29, 1996/12/01, pp. 47-78.

[108] B. Lipa, B. Nyden, D. S. Ullman, and E. Terrill, "SeaSonde Radial Velocities: Derivation and Internal Consistency," *IEEE Journal of Oceanic Engineering*, vol. 31, 2006, pp. 850-861.

[109] E. W. Gill, M. L. Khandekar, R. K. Howell, and J. Walsh, "Ocean Surface Wave Measurement Using a Steerable High-Frequency Narrow-Beam Ground Wave Radar," *Journal of Atmospheric and Oceanic Technology*, vol. 13, 01 Jun. 1996, pp. 703-713.

[110] N. Hashimoto, L. R. Wyatt, and S. Kojima, "Verification of a Bayesian Method for Estimating Directional Spectra from HF Radar Surface Backscatter," *Coastal Engineering Journal,* vol. 45, 2003/06/01, pp. 255-274.

[111] L. R. Wyatt, "Limits to the Inversion of HF Radar Backscatter for Ocean Wave Measurement," *Journal of Atmospheric and Oceanic Technology,* vol. 17, 01 Dec. 2000, pp. 1651-1666.

[112] L. R. Wyatt, "Measuring the ocean wave directional spectrum 'First Five' with HF radar," *Ocean Dynamics,* vol. 69, 2019/01/01, pp. 123-144.

[113] G. Lopez, D. C. Conley, and D. Greaves, "Calibration, Validation, and Analysis of an Empirical Algorithm for the Retrieval of Wave Spectra from HF Radar Sea Echo," *Journal of Atmospheric and Oceanic Technology,* vol. 33, 01 Feb. 2016, pp. 245-261.

[114] A. Kirincich, "Improved Detection of the First-Order Region for Direction-Finding HF Radars Using Image Processing Techniques," *Journal of Atmospheric and Oceanic Technology,* vol. 34, 2017/08/01, pp. 1679-1691.

[115] L. R. Wyatt, "An evaluation of wave parameters measured using a single HF radar system," *Canadian Journal of Remote Sensing,* vol. 28, 2002/01/01, pp. 205-218.

[116] Y. Hisaki, "Ocean wave parameters and spectrum estimated from single and dual high-frequency radar systems," *Ocean Dynamics,* vol. 66, 2016/09/01, pp. 1065-1085.

[117] L. Wyatt, B. W. Green, A. Middleditch, M. D. Moorhead, J. Howarth, M. Holt, *et al.*, "Operational Wave, Current, and Wind Measurements With the Pisces HF Radar," *IEEE Journal of Oceanic Engineering,* vol. 31, 2006, pp. 819-834.

[118] L. Wyatt, J. Green, and A. Middleditch, "Signal Sampling Impacts on HF Radar Wave Measurement," *Journal of Atmospheric and Oceanic Technology,* vol. 26, 04/01 2009, pp. 793-805.

[119] G. Lopez and D. Conley, "Comparison of HF Radar Fields of Directional Wave Spectra Against In Situ Measurements at Multiple Locations," vol. 7(8), 08/14 2019, pp. 1-17.

[120] R. Gomez, T. Helzel, L. R. Wyatt, G. Lopez, D. Conley, N. Thomas, *et al.*, "Estimation of wave parameters from HF radar using different methodologies and compared with wave buoy measurements at the Wave Hub," in *OCEANS 2015 - Genova*, 2015, pp. 1-9.

[121] A. Middleditch and S. Cosoli, "The Australian coastal ocean radar network: Temporal and spatial scales of HF radar wave data," in *OCEANS 2016 - Shanghai*, 2016, pp. 1-8.

[122] Z. Tian, Y. Tian, and B. Wen, "Quality Control of Compact High-Frequency Radar-Retrieved Wave Data," *IEEE Transactions on Geoscience and Remote Sensing,* vol. 59, 2021, pp. 929-939.

[123] F. T. Ulaby, D. G. Long, W. J. Blackwell, C. Elachi, A. K. Fung, C. S. Ruf, K. Sarabandi, H. A. Zebker, J. J. Zyl, *Microwave Radar and Radiometric Remote Sensing*: University of Michigan Press, 2014.

[124] C. V. K. Prasada Rao, "Spectral width parameter for wind-generated ocean waves," *Proceedings of the Indian Academy of Sciences - Earth and Planetary Sciences,* vol. 97, 1988/12/01, pp. 173-181.

[125] D. E. Barrick, "Theory of HF and VHF Propagation Across the Rough Sea, 2, Application to HF and VHF Propagation Above the Sea," *Radio Science,* vol. 6, 1971/05/01, pp. 527-533.

[126] J. S. Chen, J. W. Lai, H. Chien, C. Wang, C. Su, K. Lin, M. Chen, Y. Chu, "VHF Radar Observations of Sea Surface in the Northern Taiwan Strait," *Journal of Atmospheric and Oceanic Technology,* vol. 36, 2019, pp. 297-315.

[127] R. Khan, B. Gamberg, D. Power, J. Walsh, B. Dawe, W. Pearson, D. Millan, "Target detection and tracking with a high frequency ground wave radar," *IEEE Journal of Oceanic Engineering*, vol. 19, 1994, pp. 540-548.

[128] A. M. Ponsford and J. Wang, "A review of High Frequency Surface Wave Radar for detection and tracking of ships," *Turkish Journal of Electrical Engineering and Computer Sciences*, vol. 18, 05/01 2010, pp. 409-428.

[129] J. F. Vesecky and K. E. Laws, "Identifying ship echoes in CODAR HF radar data: A Kalman filtering approach," in *OCEANS 2010 MTS/IEEE SEATTLE*, 2010, pp. 1-8.

[130] K. Laws, J. Vesecky, and J. Paduan, "Predicting the capabilities of ship monitoring by HF radar in coastal regions," in *OCEANS'11 MTS/IEEE KONA*, 2011, pp. 1-5.

[131] A. L. Dzvonkovskaya, K. W. Gurgel, H. Rohling, and T. Schlick, "HF Radar WERA Application for Ship Detection and Tracking," *European Journal of Navigation*, vol. 7, 2010, pp. 18-25.

[132] M. G. Kendall, A. Stuart, and J. K. Ord, *The advanced theory of statistics*. London: Charles Griffin and Company Ltd, 1967.

[133] J. J. Jen, "A Study of CFAR Implementation Cost and Performance Tradeoffs in Heterogeneous Environments," Master, Faculty of California State Polytechnic, Pomona, 2011.

[134] F. Bass, I. Fuks, A. Kalmykov, I. Ostrovsky, and A. Rosenberg, "Very high frequency radiowave scattering by a disturbed sea surface Part I: Scattering from a slightly disturbed boundary," *IEEE Transactions on Antennas and Propagation*, vol. 16, 1968, pp. 554-559,

[135] 錢 樺, 楊文榮, 賴堅戊, 徐堂家, 林昆毅, 陶瑞全, *et al.*, "整合 AIS 與海洋陣列雷達系統之航安應用評估," 2019.

[136] https://comarsystems.com/download/ais-3r-datasheet/?wpdmdl=3579&refresh=62aed339aff0a1655624505.

[137] J. S. Chen, P. Hoffmann, M. Zecha, and C. H. Hsieh, "Coherent radar imaging of mesosphere summer echoes: Influence of radar beam pattern and tilted structures on atmospheric echo center," *Radio Science*, vol. 43, 2008/02/01 2008, pp. 1-16.

[138] 錢樺, 陶瑞全, 蘇青和, and 許義宏, "高頻陣列雷達訊號辨識船舶演算法之應用," *港灣季刊*, pp. 9-19, 2020.